Perspectives in Flavour Physics: Neutrino Masses and Experimental Anomalies

Author:
Felkl, Tobias

Publication Date:
2022

DOI:
https://doi.org/10.26190/unsworks/24390

Perspectives in Flavour Physics: Neutrino Masses and Experimental Anomalies

Tobias Felkl

A thesis in fulfilment of the requirements for the degree of

Doctor of Philosophy

School of Physics

Faculty of Science

The University of New South Wales

July 2022

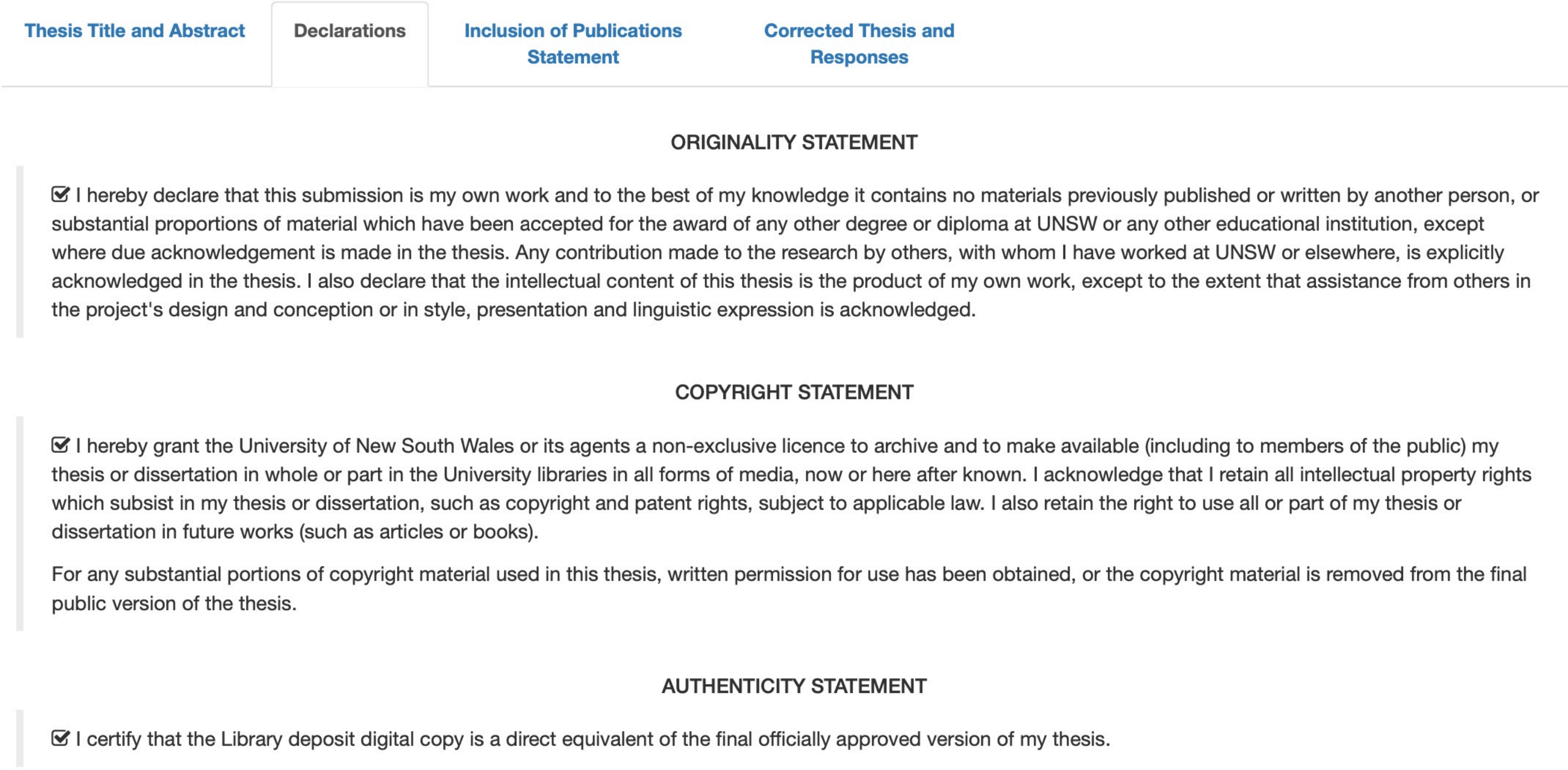

ORIGINALITY STATEMENT

☑ I hereby declare that this submission is my own work and to the best of my knowledge it contains no materials previously published or written by another person, or substantial proportions of material which have been accepted for the award of any other degree or diploma at UNSW or any other educational institution, except where due acknowledgement is made in the thesis. Any contribution made to the research by others, with whom I have worked at UNSW or elsewhere, is explicitly acknowledged in the thesis. I also declare that the intellectual content of this thesis is the product of my own work, except to the extent that assistance from others in the project's design and conception or in style, presentation and linguistic expression is acknowledged.

COPYRIGHT STATEMENT

☑ I hereby grant the University of New South Wales or its agents a non-exclusive licence to archive and to make available (including to members of the public) my thesis or dissertation in whole or part in the University libraries in all forms of media, now or here after known. I acknowledge that I retain all intellectual property rights which subsist in my thesis or dissertation, such as copyright and patent rights, subject to applicable law. I also retain the right to use all or part of my thesis or dissertation in future works (such as articles or books).

For any substantial portions of copyright material used in this thesis, written permission for use has been obtained, or the copyright material is removed from the final public version of the thesis.

AUTHENTICITY STATEMENT

☑ I certify that the Library deposit digital copy is a direct equivalent of the final officially approved version of my thesis.

UNSW is supportive of candidates publishing their research results during their candidature as detailed in the UNSW Thesis Examination Procedure.

Publications can be used in the candidate's thesis in lieu of a Chapter provided:

- The candidate contributed **greater than 50%** of the content in the publication and are the "primary author", i.e. they were responsible primarily for the planning, execution and preparation of the work for publication.
- The candidate has obtained approval to include the publication in their thesis in lieu of a Chapter from their Supervisor and Postgraduate Coordinator.
- The publication is not subject to any obligations or contractual agreements with a third party that would constrain its inclusion in the thesis.

☑ The candidate has declared that **their thesis has publications - either published or submitted for publication - incorporated into it in lieu of a Chapter/s. Details of these publications are provided below.**.

Publication Details #1

Full Title:	The singly-charged scalar singlet as the origin of neutrino masses
Authors:	Tobias Felkl, Juan Herrero-García, Michael A. Schmidt
Journal or Book Name:	Journal of High Energy Physics
Volume/Page Numbers:	05 (2021) 122
Date Accepted/Published:	14 May 2021
Status:	published
The Candidate's Contribution to the Work:	I formulated the algebraic relations on which the work is based, implemented the numerical study, generated the figures which show the results, designed the structure of the manuscript and wrote the bulk of the main text.
Location of the work in the thesis and/or how the work is incorporated in the thesis:	The work is incorporated in lieu of chapter 3 in sections 3.1-3.10.

Publication Details #2

Full Title:	Erratum to: The singly-charged scalar singlet as the origin of neutrino masses
Authors:	Tobias Felkl, Juan Herrero-García, Michael A. Schmidt
Journal or Book Name:	Journal of High Energy Physics
Volume/Page Numbers:	05 (2022) 73
Date Accepted/Published:	11 May 2022
Status:	published
The Candidate's Contribution to the Work:	I formulated the algebraic relations on which the work is based, implemented the numerical study, generated the figures which show the results, designed the structure of the manuscript and wrote the bulk of the main text.
Location of the work in the thesis and/or how the work is incorporated in the thesis:	The work is incorporated in lieu of chapter 3 in section 3.11.

Publication Details #3

Full Title:	A tale of invisibility: constraints on new physics in b → svv
Authors:	Tobias Felkl, Sze Lok Li, Michael A. Schmidt
Journal or Book Name:	Journal of High Energy Physics
Volume/Page Numbers:	12 (2021) 118
Date Accepted/Published:	17 December 2021
Status:	published
The Candidate's Contribution to the Work:	I wrote the code for the inclusive decay mode, helped implement the codes for the other decay channels and the figures which show the results, designed the structure of the manuscript and wrote the bulk of the main text.
Location of the work in the thesis and/or how the work is incorporated in the thesis:	The work is incorporated in lieu of chapter 4.

Candidate's Declaration

I confirm that where I have used a publication in lieu of a chapter, the listed publication(s) above meet(s) the requirements to be included in the thesis. I also declare that I have complied with the Thesis Examination Procedure.

THE UNIVERSITY OF NEW SOUTH WALES
Thesis/Dissertation Sheet

Surname or Family name: **Felkl**

First name: **Tobias** Other name/s:

Abbreviation for degree as given in the University calendar: **PhD**

School: **School of Physics** Faculty: **Faculty of Science**

Title: Perspectives in Flavour Physics: Neutrino Masses and Experimental Anomalies

Abstract

The matter particles which are observed in nature, called fermions, come in three copies that are also referred to as flavours. The properties of the different fermion flavours and their implications constitute the flavour structure of nature. The occurrence of neutrino oscillations is unambiguous proof that the Standard Model of particle physics cannot fully account for this flavour structure. Furthermore, several experiments have revealed hints towards further deviations from the predictions of the Standard Model, especially regarding violations of lepton-flavour universality.

This sets the ground for my thesis which can be split into three parts. Firstly, I scrutinise the hypothesis that neutrino masses are generated via a singly-charged scalar particle which is a singlet under weak interactions, and study its phenomenological implications. As a minimal extension of the Standard Model, this scenario can be very predictive and is in particular not sensitive to the details of how the breaking of lepton-number conservation is achieved. Secondly, I thoroughly analyse existing data on several $b \to s\nu\nu$ decay channels, as well as the prospective sensitivity of the Belle-II experiment regarding a measurement of these decays. The results are fully general and can be matched onto any model in which new degrees of freedom are introduced at or above the electroweak scale. Thirdly, I investigate a concrete new-physics model which aims to explain anomalous experimental data in the lepton-flavour universality ratios $R(D)$ and $R(D^\star)$ and in the magnetic moment of the muon with the help of a scalar leptoquark. An essential feature of the model is the fact that the interactions between the leptoquark and the Standard-Model fermions are completely fixed in terms of a discrete flavour symmetry.

Altogether, in this thesis I highlight different possible approaches towards an improved understanding of the flavour structure of nature, both model-based and model-independent ones.

Declaration relating to disposition of project thesis/dissertation

Signature **Tobias Felkl** Witness Date **29 July, 2022**

FOR OFFICE USE ONLY Date of completion of requirements for Award

Originality Statement

I hereby declare that this submission is my own work and to the best of my knowledge it contains no materials previously published or written by another person, or substantial proportions of material which have been accepted for the award of any other degree or diploma at UNSW or any other educational institution, except where due acknowledgement is made in the thesis. Any contribution made to the research by others, with whom I have worked at UNSW or elsewhere, is explicitly acknowledged in the thesis. I also declare that the intellectual content of this thesis is the product of my own work, except to the extent that assistance from others in the project's design and conception or in style, presentation and linguistic expression is acknowledged.

Tobias Felkl
29 July, 2022

Copyright Statement

Tobias Felkl
29 July, 2022

Authenticity Statement

Tobias Felkl
29 July, 2022

Abstract

The matter particles which are observed in nature, called fermions, come in three copies that are also referred to as flavours. The properties of the different fermion flavours and their implications constitute the flavour structure of nature. The occurrence of neutrino oscillations is unambiguous proof that the Standard Model of particle physics cannot fully account for this flavour structure. Furthermore, several experiments have revealed hints towards further deviations from the predictions of the Standard Model, especially regarding violations of lepton-flavour universality.

This sets the ground for my thesis which can be split into three parts. Firstly, I scrutinise the hypothesis that neutrino masses are generated via a singly-charged scalar particle which is a singlet under weak interactions, and study its phenomenological implications. As a minimal extension of the Standard Model, this scenario can be very predictive and is in particular not sensitive to the details of how the breaking of lepton-number conservation is achieved. Secondly, I thoroughly analyse existing data on several $b \to s\nu\nu$ decay channels, as well as the prospective sensitivity of the Belle-II experiment regarding a measurement of these decays. The results are fully general and can be matched onto any model in which new degrees of freedom are introduced at or above the electroweak scale. Thirdly, I investigate a concrete new-physics model which aims to explain anomalous experimental data in the lepton-flavour universality ratios $R(D)$ and $R(D^\star)$ and in the magnetic moment of the muon with the help of a scalar leptoquark. An essential feature of the model is the fact that the interactions between the leptoquark and the Standard-Model fermions are completely fixed in terms of a discrete flavour symmetry.

Altogether, in this thesis I highlight different possible approaches towards an improved understanding of the flavour structure of nature, both model-based and model-independent ones.

Acknowledgements

First and foremost, I am indebted to my advisor Michael Schmidt. His decision to take me on as a student marked the beginning of my pursuit of a PhD degree. This thesis seeing the light of day would not have been possible without Michael willing to hold countless discussions on particle physics, maintaining a culture of an open (virtual) office door, and continuously providing guidance, feedback and support. My gratitude also goes to Yvonne Wong and Jan Hamann for their generosity and help with administrative matters dating back to when I had not even arrived in Australia until recently.

I am very grateful that I had the opportunity to collaborate with Juan Herrero-García, Claudia Hagedorn, Innes Bigaran and Sze Lok Li during my candidature, which resulted in the scientific work that constitutes this thesis. Special thanks go to Juan for discussing PhD opportunities while it was already clear that he would not be able to take me on as a student, and to Adam Lackner, Michael Schmidt and Seán Gray for proofreading this thesis. Moreover, the members of my PhD review panel, Kim-Vy Tran and Julian Berengut, have my gratitude for their support and encouragement. I would like to thank the Graduate Research School for their administrative support throughout my candidature. I acknowledge that my research has been funded by a Tuition Fee Scholarship.

As a member of the Cosmology and Particle Physics group at UNSW Sydney, I came to get to know a bunch of other PhD students, which proved to be a very rewarding and enriching experience. Indeed, it was a pleasure to meet and spend time with Adam Lackner, Ameek Malhotra, Cosmin Dumitrescu, Giovanni Pierobon, Jack Bennett, Joe Chen, Julius Wons and Yuqi Kang. I am also grateful for the opportunity to meet other students and postdocs at international schools and conferences, of which I had the privilege to attend a few even during my PhD candidature marked by a pandemic. I can call myself lucky for running into Kåre Fridell at two schools and one conference in Europe. Among others I met at the Summer School of Particle Physics 2019 at the ICTP, I would in particular like to acknowledge Innes Bigaran and Matteo Puel. Very recently, getting to know Noah Zipper and Martino Borsato at SUSY 2022 made this conference an even more delightful experience.

Lastly, I am forever grateful to my friends, family and my partner Ale Rios, for their tremendous support, warmth and encouragement over the years.

Publications and Presentations

List of Publications

- I. Bigaran, T. Felkl, C. Hagedorn and M. A. Schmidt, *Flavour anomalies meet flavour symmetry*, `arXiv`: 2207.06197
- T. Felkl, J. Herrero-García, and M. A. Schmidt, *Erratum to: The singly-charged scalar singlet as the origin of neutrino masses*, JHEP **05** (2022) 73
- T. Felkl, S. L. Li, and M. A. Schmidt, *A tale of invisibility: constraints on new physics in* $b \to s\nu\nu$, JHEP **12** (2021) 118, `arXiv`: 2111.04327
- T. Felkl, J. Herrero-García, and M. A. Schmidt, *The singly-charged scalar singlet as the origin of neutrino masses*, JHEP **05** (2021) 122, `arXiv`: 2102.09898

List of Presentations

Oral presentations:

- Flavour anomalies meet flavour symmetry; *29th International Conference on Supersymmetry and Unification of Fundamental Interactions*; University of Ioannina
- Constraints on new physics in $b \to s\nu\nu$; *Sydney-CPPC Seminar Series for Junior Speakers*; University of Sydney & University of New South Wales
- The singly-charged scalar singlet as the origin of neutrino masses; *European Physical Society conference on high energy physics 2021*; DESY, Hamburg University
- The singly-charged scalar singlet as the origin of neutrino masses; *2021 Meeting of the Division of Particles and Fields of the American Physical Society*; Florida State University
- The singly-charged scalar singlet as the origin of neutrino masses; *1st NCTS TG2.1 Hsinchu Hub Workshop*; National Taiwan University

- The singly-charged scalar singlet as the origin of neutrino masses; *26th International Symposium on Particle Physics, String Theory and Cosmology*; Institute for Basic Science, Daejeon, Republic of Korea
- The singly-charged scalar singlet as the origin of neutrino masses; *International Workshop on Weak Interactions and Neutrinos 2021*; University of Minnesota
- The singly-charged scalar singlet as the origin of neutrino masses; *2021 Phenomenology Symposium*; University of Pittsburgh
- The singly-charged scalar singlet as the origin of neutrino masses; *14th International Conference on Interconnections between Particle Physics and Cosmology*; University of Oklahoma
- The singly-charged scalar singlet as the origin of neutrino masses; *First European Consortium for Astroparticle Theory (EuCAPT) Annual Symposium*; CERN
- Probing mechanisms of neutrino-mass generation at next-generation colliders (unpublished work); *2019 TeV Particle Astrophysics conference*; University of Sydney

Poster presentations:

- The singly-charged scalar singlet as the origin of neutrino masses; *17th International Conference on Topics in Astroparticle and Underground Physics*; Instituto de Física Corpuscular, Consejo Superior de Investigaciones Científicas, Universidad de Valencia
- The singly-charged scalar singlet as the origin of neutrino masses; *International Workshop on Weak Interactions and Neutrinos 2021*; University of Minnesota
- The singly-charged scalar singlet as the origin of neutrino masses; *Invisibles 2021 Workshop*; Instituto de Física Teórica, Consejo Superior de Investigaciones Científicas, Universidad Autónoma de Madrid

Contents

Abstract **iii**

Acknowledgements **iv**

Publications and Presentations **v**

Contents **vii**

List of Figures **xii**

List of Tables **xx**

1 Introduction **1**

2 Background **7**

2.1 Aspects of the Standard Model 7

2.1.1 Lorentz Symmetry 7

2.1.2 Particle Content and Weak Interactions 10

2.1.3 Yukawa Sector 12

2.1.4 Global Symmetries 16

2.1.5 Flavour-Changing Neutral Currents 18

2.1.6 Low-Energy QCD 20

2.2 Experimental Status and Prospects 22
2.2.1 Neutrino Masses 22
2.2.2 Lepton Flavour Non-Universality 24
2.3 New-Physics Models 28
2.3.1 Sterile Neutrinos 28
2.3.2 Leptoquarks 29
2.3.3 Colourless Charged Scalars 31
2.3.4 Flavour Symmetries 33
2.4 Effective Field Theory 34
2.4.1 Technical Aspects 35
2.4.2 SMEFT 37
2.4.3 LEFT 38
2.4.4 HQET 39

3 The Singly-Charged Scalar Singlet as the Origin of Neutrino Masses 41

3.1 Introduction 41
3.2 Singly-Charged Scalar Singlet 44
3.2.1 Lagrangian 44
3.2.2 Conventions for the Neutrino Sector 45
3.2.3 Neutrino Mass Matrix 46
3.3 Solving the Neutrino-Mass Constraint 51
3.4 Phenomenology 54
3.4.1 Effective Description of Low-Energy Phenomenology at Tree Level . 54
3.4.2 Charged Lepton Flavour Violation 63
3.4.3 Magnitude of Couplings 68
3.4.4 Decay Channels of the Singly-Charged Scalar Singlet 71

3.5 Multiple Singly-Charged Scalar Singlets 72

3.6 Conclusions 74

3.7 Appendix: Neutrino-Mass Constraint Spelt in Full 77

3.8 Appendix: Effective Four-Lepton Operator 78

3.9 Appendix: $\mu - e$ Conversion in Nuclei 78

3.10 Appendix: Generalised Zee-Babu Model 80

3.11 Erratum to: The Singly-Charged Scalar Singlet as the Origin of Neutrino Masses 81

4 A Tale of Invisibility: Constraints on New Physics in $b \to s\nu\nu$ 86

4.1 Introduction 86

4.2 Effective Field Theory Framework 89

4.3 Observables $b \to s\nu\nu$ 91

4.3.1 $B \to K\nu\nu$ 93

4.3.2 $B \to K^*(\to K\pi)\nu\nu$ 94

4.3.3 $B \to X_s\nu\nu$ 95

4.4 Results 97

4.4.1 One Operator with Massless Neutrinos 98

4.4.2 Two Operators with Massless Neutrinos 102

4.4.3 Massive Neutrinos 108

4.4.4 A Hint for New Physics? 114

4.5 Conclusions 117

4.6 Appendix: Form factors 119

4.7 Appendix: $S, P, V, A, \mathcal{T}$ basis 120

4.8 Appendix: $B \to K\nu_\alpha\nu_\beta$ 121

4.9 Appendix: $B \to K^*\nu_\alpha\nu_\beta$ 123

4.10 Appendix: $B \to X_s \nu_\alpha \nu_\beta$ . . . 126
4.11 Appendix: Matching to SM Effective Field Theory with Sterile Neutrinos . 128

5 Flavour Anomalies Meet Flavour Symmetry 132

5.1 Introduction . . . 132
5.2 Model Setup . . . 135
5.3 Mass Matrices and Leptoquark Couplings . . . 140
  5.3.1 Quark Sector . . . 140
  5.3.2 Charged Lepton Sector . . . 145
  5.3.3 Leptoquark Couplings . . . 146
5.4 Phenomenological Study . . . 148
  5.4.1 Employed Strategy and Parametrisations . . . 149
  5.4.2 $R(D)$ and $R(D^\star)$ . . . 154
  5.4.3 Radiative Lepton Transitions . . . 161
  5.4.4 Simultaneous Explanation of All Anomalies . . . 166
  5.4.5 $R^\nu_{K^{(*)}}$ . . . 172
  5.4.6 $\mu - e$ Conversion in Aluminium . . . 176
  5.4.7 Trilepton Decays . . . 179
  5.4.8 $B_c \to \tau\,\nu$ . . . 185
  5.4.9 $Z \to \tau\tau$ . . . 190
  5.4.10 High-p_T Dilepton Searches . . . 192
  5.4.11 Scalar Charged-Current Wilson Coefficients . . . 194
  5.4.12 Secondary Observables . . . 195
5.5 Conclusions . . . 200
5.6 Appendix: Group Theory of D_{17} . . . 203
5.7 Appendix: Lagrangians . . . 205

5.7.1 Up-Quark Sector 206

5.7.2 Down-Quark Sector 208

5.7.3 Charged Lepton Sector 209

5.7.4 Leptoquark Couplings in Interaction Basis 210

5.8 Appendix: Mass Matrices and Leptoquark Couplings in Scenario A 212

5.8.1 Up-Quark Sector 212

5.8.2 Quark Mixing 213

5.8.3 Leptoquark Couplings 214

5.9 Appendix: Relations between Lagrangian and Effective Parameters 216

5.10 Appendix: Formulae for $R(D)$ and $R(D^\star)$ 221

5.11 Appendix: Matching Results for Leptonic Lagrangian 222

5.12 Appendix: Effective Coupling Constants for $\mu - e$ Conversion 223

6 Conclusion and Future Directions **225**

References **229**

List of Figures

2.1 Feynman diagrams which mediate the decay process $b \to s\nu\overline{\nu}$ in the SM; taken from ref. [1]. 19

2.2 Illustration of the semileptonic decay of a B hadron in the SM, from ref. [2]. 24

2.3 Masses of the SM particles, represented on a logarithmic scale; taken from ref. [3]. 33

2.4 Tree-level contributions to $2 \to 2$ scattering in a toy theory; taken from ref. [4]. 36

3.1 Self-energy diagram responsible for the generation of neutrino masses via a singly-charged scalar singlet: linear case (left) and quadratic case (right). The grey blob represents all other interactions which contribute to the diagram. It could be one effective vertex or a sub-diagram consisting of multiple vertices and propagators. There are at least two insertions of the Higgs vacuum expectation value somewhere in the diagram which are not explicitly shown. 47

3.2 Correlations among deviations of g_μ/g_e, g_τ/g_e (top) and g_τ/g_μ (bottom) from universality for NO (left) and IO (right). All shown sample points explain neutrino masses and respect the bounds arising from the flavour observables considered in this work. For the blue points, the deviation of g_τ/g_e from universality is explained at 2σ in the linear case (Case I), and for the black points at 3σ, but not at 2σ. The red diamonds also explain the flavour anomalies, for which g_τ/g_e must be respected at 2σ. Brown points pertain to the quadratic case (Case II) which only occurs at 2σ for NO and at 3σ for IO. Solid lines indicate current experimental bounds (black for 2σ or 90 % CL, and green for 3σ). 59

3.3 Correlations among M_W and deviations of g_τ/g_e from universality. The colours are the same as in Fig. 3.2. 61

3.4 Non-standard interactions. The colours are the same as in Fig. 3.2. Dashed lines indicate prospected experimental sensitivities. 62

3.5 Branching ratios of radiative charged-lepton decays. The vertical dot-dashed lines correspond to the prospected sensitivities to $\mathrm{Br}(\mu \to e;\ \mathrm{Ti})$ at PRISM/PRIME and to $\mathrm{Br}(\mu \to e;\ \mathrm{Al})$ at Mu2e which were then converted via $\mathrm{Br}(\mu \to e;\ \mathrm{Al}) \approx 0.0079\,\mathrm{Br}(\mu \to e\gamma)$ and $\mathrm{Br}(\mu \to e;\ \mathrm{Ti}) \approx 0.0125\,\mathrm{Br}(\mu \to e\gamma)$, see also App. 3.9. The colours are the same as in Fig. 3.2. 64

3.6 Branching ratios of tri-lepton decays. The colours are the same as in Fig. 3.2. The solid grey lines indicate the respective experimental bounds that would apply to the photon-penguin approximation. Dashed lines indicate prospected experimental sensitivities. 66

3.7 Branching ratio of tri-lepton tau decays as a function of the mass M_h. The colours are the same as in Fig. 3.2. Dashed lines indicate prospected experimental sensitivities. 67

3.8 Plot of the coupling ratios $|y_h^{e\mu}|/|y_h^{\mu\tau}|$ and $|y_h^{e\tau}|/|y_h^{\mu\tau}|$ as obtained in the numerical scan. The colours are the same as in Fig. 3.2. 69

3.9 Plot of the coupling ratios $|y_h^{e\mu}|/|y_h^{e\tau}|$ as a function of the smallest neutrino mass (m_1 for NO, and m_3 for IO). The colours are the same as in Fig. 3.2. 70

3.10 Plot of the coupling ratios $|y_h^{e\mu}|/|y_h^{\mu\tau}|$ and $|y_h^{e\tau}|/|y_h^{\mu\tau}|$ as obtained in the numerical scan if approximately 95.45 % of the overall number of 547991 (542287) sample points generated for NO (IO) are taken into account. Each square shown to be compatible with NO (IO) contains at least 97 (74) sample points. See also main text. 71

3.11 Branching ratios of $h \to \ell\nu$. The colours are the same as in Fig. 3.2. 72

3.12 Branching ratios of the different channels $h \to \ell\nu$ as functions of the Dirac CP phase δ in the quadratic case (Case II). 73

3.3 Correlations among M_W and deviations of g_τ/g_e from universality. The colours are the same as in Fig. 2. 83

3.7 Branching ratio of tri-lepton tau decays as a function of the mass M_h. The colours are the same as in Fig. 2. Dashed lines indicate prospected experimental sensitivities. 84

3.8 Plot of the coupling ratios $|y_h^{e\mu}|/|y_h^{\mu\tau}|$ and $|y_h^{e\tau}|/|y_h^{\mu\tau}|$ as obtained in the numerical scan. The colours are the same as in Fig. 2. 85

4.1 The differential branching ratio distributions (top) and the differential longitudinal polarisation fraction F_L (bottom) generated for different non-zero Wilson coefficients $C^{\text{XLL}}_{\nu d,23sb} = 0.01\,\text{TeV}^{-2}$ for X = V,S,T, and choices of form factors. The blue (red) [black] lines stand for the vector (scalar) [tensor] operator, respectively. The solid lines denote the results for the form factors which are used in the analysis, taken from [5] for the $B \to K^*$ and from [6] for the $B \to K$ form factors. Both sets of form factors are based on a combined fit to LCSR and LQCD data. The dotted lines indicate the form factors based on the LCSR fit in [6] and the dashed lines show the $B \to K^*$ form factors obtained using a combined fit to LCSR and LQCD in [6]. Note that no SM contribution is included here. 101

4.2 The allowed parameter space for the Wilson coefficients under the assumption that the Belle-II results for 5 ab^{-1} (light shaded regions) and for 50 ab^{-1} (dark shaded regions, dashed lines) for several $b \to s\nu\nu$ observables will confirm the SM predictions. In the shown cases, interference with the SM occurs. We use the sensitivities referenced in [7] and assume an experimental uncertainty of 50% (dotted lines) and 20% (dashed lines) for the inclusive decay $B \to X_s\nu\nu$, respectively. The solid dark purple and green lines reflect the current experimental bounds, see Table 4.1. For the neutrino flavor indices, $\alpha \in (1, 2, 3)$, while γ and δ are arbitrary. 103

4.3 Continuation of Figure 4.2, but here the neutrino flavour indices are arbitrary with $\alpha \neq \beta$. 106

4.4 Current (shaded regions) and future sensitivities (lines) on a single Wilson coefficient as a function of the mass of two sterile neutrinos (top panel) and one sterile neutrino (middle panel and bottom plot) in the final state, respectively. We assume that the Belle-II results for 5 ab^{-1} (dashed lines) and for 50 ab^{-1} (solid lines) for several $b \to s\nu\nu$ observables will confirm the SM predictions. We use the sensitivities referenced in [7] and assume an experimental uncertainty of 50% (solid line) and 20% (dashed line) for the inclusive decay $B \to X_s\nu\nu$. Regions with \\ (//) [–] hatching are excluded via the current bounds on $B^+ \to K^+\nu\nu$ ($B^0 \to K^{*0}\nu\nu$) [$B \to X_s\nu\nu$]. The constraints are identical if exchanging the third neutrino flavour $\alpha = 3$ for $\alpha = 1, 2$. 109

4.5 Binned longitudinal polarisation fraction $F_L(K^{*+})$ as a function of one new-physics Wilson coefficient at a time (including the SM contribution). On the left-hand side the blue (red) [black] lines stand for the vector (scalar) [tensor] operator, respectively. Solid [dashed] contours signify $m_{4,5} = 0$ GeV [$m_{4,5} = 1.5$ GeV]. On the right-hand side the blue (purple) lines stand for the Wilson coefficients $C^{\text{VLL}}_{\nu d,33sb}$ ($C^{\text{VLR}}_{\nu d,33sb}$). Note the binned longitudinal polarisation fraction $F_L(K^{*+})$ is obtained by separately binning the numerator and denominator, see Eq. (4.11), and not by integrating the distributions $F_L(q^2; K^{*+})$ shown in Figure 4.1. 111

4.6 Future sensitivity of Belle II for 5 ab^{-1} (light shaded regions) and for 50 ab^{-1} (dark shaded regions, dashed lines) to scalar Wilson coefficients with *sb* and *bs* quark-flavour ordering and massive sterile neutrinos following the same analysis as in Figure 4.2. The solid dark purple and green lines indicate the current experimental bound, see Table 4.1. Left: $m_4 = 0$ GeV; Right: $m_4 = 1.5$ GeV. 113

4.7 Parameter space which is compatible with the non-zero simple weighted average of $\text{Br}(B^+ \to K^+\nu\nu)$ [1,8] at 1σ (2σ) [darker(lighter)-orange shaded region] and the current bounds on $B^+ \to K^+\nu\nu$ and $B^0 \to K^{*0}\nu\nu$. 115

5.1 **Correlation plot for $\hat{m}_\phi = 4$ based on the sample points which explain $R(D^{(\star)})$ at $2\,\sigma$ or $1\,\sigma$ in the primary scan.** The plot visualises Spearman's rank correlation coefficient calculated via the library `seaborn` [9]. A negative (positive) correlation among, say, two coefficient magnitudes indicates that if one of them increases, the other tends to decrease (also increase). Note that sample points not respecting the experimental bounds are taken into account here as well. 158

5.2 **Model predictions for $R(D)$ and $R(D^\star)$. Left:** Results from primary scan. The regions marked by solid lines are compatible with the current experimental world averages for $R(D^{(\star)})$ [10] at the indicated CL; see table 5.4. I use the values output by `flavio`, v2.3 for the SM predictions for $R(D^{(\star)})$ at $1\,\sigma$ [11–13] indicated by the black cross, see section 5.10. The round points (geometric shapes) indicate that current experimental bounds are violated (respected); see also the main text of section 5.4.1.1. **Right:** Results from comprehensive scan. The shown sample points respect the experimental bounds from primary constraints; see also section 5.4.1.2. The dot-dashed purple ellipse shows the $1\,\sigma$ contour about the most recent results for $R(D)$ and $R(D^\star)$ from Belle [14], and the green band indicates the $1\,\sigma$ region about the most recent result for $R(D^\star)$ from LHCb [15, 16]. The black dashed ellipse shows the prospective reach at Belle II [17] at the level of $3\,\sigma$ for 5 ab^{-1} of data under the assumption of the best-fit value and correlation coefficient from the HFLAV collaboration as of 2021 [10]. 160

5.3 **Correlation plot for $\hat{m}_\phi = 4$ based on the sample points which explain Δa_μ at $2\,\sigma$ or $1\,\sigma$ in the primary scan.** The plot visualises Spearman's rank correlation coefficient calculated via the library `seaborn` [9]. A negative (positive) correlation among, say, two coefficient magnitudes indicates that if one of them increases, the other tends to decrease (also increase). Note that sample points not respecting the experimental bounds are taken into account here as well. 162

5.4 **Correlation plot for $\hat{m}_\phi = 4$ based on the sample points which respect all imposed experimental constraints in the primary scan.** The plot visualises Spearman's rank correlation coefficient calculated via the library `seaborn` [9]. A negative (positive) correlation among, say, two coefficient magnitudes indicates that if one of them increases, the other tends to decrease (also increase). The LO contributions to $\mathrm{BR}(\tau \to \mu\gamma)$ and $\mathrm{BR}(\mu \to e\gamma)$ are proportional to $|a_{33}b_{23}|^2$ and $|a_{23}b_{13}|^2$, respectively. 164

5.5 **Model predictions for $R(D)$, $R(D^\star)$ and Δa_μ. Upper panel:** Results from primary scan. The regions marked by solid lines are compatible with the current experimental world averages for $R(D^{(\star)})$ [10] and Δa_μ [18, 19], respectively, at the indicated CL; see table 5.4. The SM predictions for $R(D^{(\star)})$ at $1\,\sigma$ [11–13] are indicated by the green-shaded bands. The round points (geometric shapes) indicate that current experimental bounds are violated (respected); see also the main text of section 5.4.1.1. **Lower panel:** Results from comprehensive scan. The shown sample points respect the experimental bounds from primary constraints; see also section 5.4.1.2. The red-brown band indicates the projected sensitivity of the Muon g−2 experiment [20] at the level of $3\,\sigma$. This (roughly) overlays the present $2\,\sigma$ region under the assumption that the current experimental best-fit value persists (red-brown solid line). 167

5.6 **Constraining power and future reach of $\tau \to \mu\gamma$ and $\mu \to e\gamma$ as found in the primary scan.** The vertical solid (dashed) lines indicate the current bound on (future sensitivity of) $\mathrm{BR}(\tau \to \mu\gamma)$ [7, 21] in the upper panel and the bottom-left plot, and the current bound on (future sensitivity of) $\mathrm{BR}(\mu \to e\gamma)$ [22, 23] in the bottom-right plot; see table 5.4. The round points (geometric shapes) indicate that current experimental bounds are violated (respected); see also the main text of section 5.4.1.1. 169

5.7 **Illustration of the capability of the model to simultaneously explain the anomalies in $R(D)$, $R(D^\star)$ and Δa_μ in the comprehensive scan.** The sample points shown as light-coloured dot points (dark-coloured points with specific shapes) respect the experimental bounds from primary constraints and explain Δa_μ within the $3\,\sigma$ $(2\,\sigma)$ range about the present best-fit value. Apart from that, the plot is to be read in the same way as the right plot in figure 5.2. 171

5.8 **Constraining power and future reach of $R^\nu_{K^\star}$. Left:** Results from primary scan. The vertical solid line indicates (dashed lines indicate) the region compatible with the current experimental bound on (future reach of) $R^\nu_{K^\star}$ [7, 24]; see also table 5.4. For the future reach, a SM-like result and an uncertainty of 10% is assumed. The round points (geometric shapes) indicate that current experimental bounds are violated (respected); see also the main text of section 5.4.1.1. **Right:** Results from comprehensive scan. The shown sample points respect the experimental bounds from primary constraints; see also section 5.4.1.2. The red-brown shaded regions indicate the projected reach for $R^\nu_{K^\star}$ at Belle II for 5 ab^{-1} of data, again under the assumption that the best-fit value is SM-like. 174

5.9 **Results for $R^{\nu}_{K^{(\star)}}$ as a function of the magnitudes of several effective parameters in the comprehensive scan.** The shown sample points respect the experimental bounds from primary constraints; see also section 5.4.1.2. The red-brown shaded regions indicate the projected reach for $R^{\nu}_{K^\star}$ at Belle II for 5 ab^{-1} of data under the assumption that the best-fit value is SM-like. For the bottom-left plot, the dot-dashed lines correspond to the respective upper limit on $|a_{33}|$ for each LQ mass as given in table 5.6, in dark red (orange) [dark blue] for $\hat{m}_\phi = 2(4)[6]$. 175

5.10 **Future reach of $\mu - e$ conversion in Aluminium as found in the primary scan.** The vertical dashed lines indicate the future sensitivity of $\mu - e$ conversion in Al as anticipated by COMET [25] and Mu2e [26]; see table 5.4. The round points (geometric shapes) indicate that current experimental bounds are violated (respected); see also the main text of section 5.4.1.1. 178

5.11 **Constraining power and future reach of $\mu \to 3e$ as found in the primary scan.** The vertical dashed lines indicate the respective projected reach of the phase-1 and phase-2 runs of the future search for $\mu \to 3e$ [27]; see table 5.4. The round points (geometric shapes) indicate that current experimental bounds are violated (respected); see also the main text of section 5.4.1.1. 180

5.12 **Constraining power and future reach of $\tau \to 3\mu$ in relation with $\tau \to \mu\gamma$. Left:** Results from primary scan. The vertical solid (dashed) lines indicate the current bound on (future sensitivity of) $\tau \to 3\mu$ [7, 28]; see table 5.4. The round points (geometric shapes) indicate that current experimental bounds are violated (respected); see also the main text of section 5.4.1.1. **Right:** Results from comprehensive scan. The shown sample points respect the experimental bounds from primary constraints; see also section 5.4.1.2. The purple dot-dashed line (labelled "γ-penguin") illustrates the approximate correlation between $\tau \to 3\mu$ and $\tau \to \mu\gamma$ in the limit of photon-penguin dominance as given in eq. (5.86). . . . 182

5.13 **Constraining power and future reach of $\tau \to 3\mu$ in relation with Δa_μ. Left:** Results from primary scan. The vertical solid (dashed) lines indicate the current bound on (future sensitivity of) $\tau \to 3\mu$ [7, 28]; see table 5.4. The round points (geometric shapes) indicate that current experimental bounds are violated (respected); see also the main text of section 5.4.1.1. **Right:** Results from comprehensive scan. The shown sample points respect the experimental bounds from primary constraints; see also section 5.4.1.2. 183

5.14 **Constraining power and future reach of $\tau \to 3\mu$ in relation with $\mu \to e$ transitions. Top panel:** Results from primary scan. The vertical solid (dashed) lines indicate the current bound on (future sensitivity of) $\tau \to 3\mu$ [7, 28]; see table 5.4. The round points (geometric shapes) indicate that current experimental bounds are violated (respected); see also the main text of section 5.4.1.1. **Bottom-left plot:** Results from comprehensive scan. The shown sample points respect the experimental bounds from primary constraints; see also section 5.4.1.2. 184

5.15 **Constraining power and future reach of $\tau_{Bc}^{\mathbf{SM}}$ in relation with $R(D)$ and $R(D^\star)$. Top panel:** Results from primary scan. The vertical solid lines indicate the region where the inferred contribution to the B_c lifetime in the SM agrees with the measured lifetime at $1\,\sigma$ [10, 29], and the hatched area marks the region in which the BR of $B_c \to \tau\nu$ remains smaller than 0.1, as is implied by eq. (5.99); see also table 5.4. The round points (geometric shapes) indicate that current experimental bounds are violated (respected); see also the main text of section 5.4.1.1. **Lower panel:** Results from comprehensive scan. The shown sample points respect the experimental bounds from primary constraints; see also section 5.4.1.2. The grey-shaded region represents the $1\,\sigma$ range about the current best-fit value for $\tau_{B_c}^{\mathrm{exp}}$, and the red-brown shaded band indicates the region of parameter space that corresponds to $\mathrm{BR}(B_c \to \tau\nu) \leq 0.1$. 188

5.16 **Constraining power and future reach of $\tau_{Bc}^{\mathbf{SM}}$ in relation with Δa_μ. Left:** Results from primary scan. The vertical solid lines indicate the region compatible with current experimental data on the B_c lifetime at $1\,\sigma$ [10, 29], and the hatched areas mark the regions in which the BR of $B_c \to \tau\nu$ remains smaller than 0.1 and 0.3, respectively, as is implied by eq. (5.99); see also table 5.4. The round points (geometric shapes) indicate that current experimental bounds are violated (respected); see also the main text of section 5.4.1.1. **Right:** Results from comprehensive scan. The shown sample points respect the experimental bounds from primary constraints; see also section 5.4.1.2. 189

5.17 **Constraining power and future reach of $g_{\tau_A}/g_A^{\mathbf{SM}}$ as found in the primary scan.** The regions indicated by vertical solid (dashed) lines are compatible with the current experimental world averages for (future sensitivity of) $g_{\tau_A}/g_A^{\mathrm{SM}}$ at the indicated CL [30, 31] (at $3\,\sigma$ [31–33]); see table 5.4. The round points (geometric shapes) indicate that current experimental bounds are violated (respected); see also the main text of section 5.4.1.1. 191

5.18 **Current constraints on and future sensitivity to $|C_{\nu edu,3332}^{SRR}|$ as found in the primary scan.** The scalar WC is computed as in eqs. (5.45) and (5.47), and the displayed results hold at the hadronic scale $\mu = \mu_B$. The round points (geometric shapes) indicate that current experimental bounds are violated (respected); see also the main text of section 5.4.1.1. 193

5.19 **Future reach of secondary leptonic observables in relation with Δa_μ in the comprehensive scan.** The shown sample points respect the experimental bounds from primary constraints; see also section 5.4.1.2. In the left plot, two constraints on the magnitude $|d_\mu|$ of the muon EDM are shown, from the Muon g−2 [34] experiment and the muEDM experiment [35]. For $g_{\mu_A}/g_A^{\mathrm{SM}}$, the red-brown shaded regions represent the projected sensitivities at the ILC [32] under the assumption that the current best-fit values [30, 31] shown herein as red-brown solid lines will persist. 196

5.20 **Future reach of secondary hadronic observables in the comprehensive scan.** The shown sample points respect the experimental bounds from primary constraints; see also section 5.4.1.2. The projected sensitivities at Belle II to $R_D^{\mu/e}$ and $R_{D^\star}^{e/\mu}$ [36] (5 ab^{-1}) and BR($B \to \tau\nu$) [17] are indicated via the respective red-brown shaded regions. Note that the white crosses are omitted in the left plot since they lie uniformly across the coloured region and would thus obstruct a proper visualisation of the data. 199

List of Tables

2.1 Particle content of the SM, together with the transformation properties under the Lorentz and gauge groups. 11

2.2 Coupling strength of SM fermion-antifermion pairs to the Z boson. 12

2.3 Left: Charges of SM fermions under baryon and lepton number, respectively. Right: Charges of SM leptons under electron number, muon number and tau number, respectively. 17

2.4 The six scalar LQ representations under the SM gauge group which admit renormalisable couplings to SM fermions. The individual coupling matrices are omitted for brevity, generation indices are suppressed and the hermitian-conjugate operators are understood to be added. The LQs S_1, $\bar{S}_1$ and $\tilde{R}_2$ may also feature renormalisable interactions with sterile neutrinos if those are introduced. 30

3.1 The table at the top contains the experimental values for input parameters taken from [29,37]; the one in the centre summarises the experimental values for leptonic mixing parameters and neutrino-mass-squared differences taken from NuFIT 5.0 [38]. $\Delta m^2_{31} > 0$ for NO, and $\Delta m^2_{32} < 0$ for IO. Priors and the ranges sampled over in the numerical scan are given in the bottom table. The flavour indices for the antisymmetric Yukawa couplings are $i, j = e$, μ, τ, and $k = \mu$, τ. 53

3.2 The upper table contains the current experimental bounds on and future sensitivities to the relevant observables. The lower table shows the respective maximum contribution found in the scan in the linear case and the quadratic case for either neutrino-mass ordering. 55

3.2 (lower table only) The upper table contains the current experimental bounds on and future sensitivities to the relevant observables. The lower table shows the respective maximum contribution found in the scan in the linear case and the quadratic case for either neutrino-mass ordering. 83

4.1 Observables for $b \to s\nu\nu$. The SM predictions for the exclusive decays and their uncertainties are based on light-cone sum rules (LCSR) and lattice QCD and are taken from [6] for $B \to K\nu\nu$ and from [5] for $B \to K^*\nu\nu$ including a 10% increase of the $B \to K^*$ form factors due to finite-width effects [39]. The last two columns list the Belle-II sensitivities to exclusive B-meson decays to a $K^{(*)}$ meson and active neutrinos [7] if the respective SM predictions are assumed. 92

4.2 Most competitive bounds imposed on the absolute value of the respective Wilson coefficients if only one of them gets (sizeable) contributions from new physics at a time, both for the current situation and for the projections for the 50 ab^{-1} Belle-II data set under the assumption of a confirmation of the SM predictions. Here, $\alpha \in (1, 2, 3)$ and γ and δ arbitrary, but $\gamma \neq \delta$ (only in the case of $\mathcal{O}^{\mathrm{VLL}}_{\nu d,\gamma\delta sb}$, γ and δ may be equal if larger than 3), and neutrino masses are set to zero both for active and sterile states. Generally, the most conservative constraint is provided, with the possibility of interference with the SM taken into account. We also provide rough estimates for the corresponding new-physics scale and the observable from which the respective bound arises. If $B \to K^{(*)}\nu\nu$ is indicated, $B \to K\nu\nu$ and $B \to K^*\nu\nu$ yield similar bounds. 98

4.3 Implication of the non-zero simple weighted average of $\mathrm{Br}(B^+ \to K^+\nu\nu)$ for the contributing WCs and the other decay channels. The indicated upper and lower ranges reflect the uncertainty at 1σ. Note that our new-physics predictions for the inclusive mode do not take into account QCD and HQET corrections, as indicated in Section 4.3, and are thus expected to be overestimated by $\mathcal{O}(10 - 20\%)$. All bounds and SM predictions are the same as in Table 4.1. 114

5.1 **Overview of the three anomalies to be addressed in this chapter and their present significance.** The quoted experimental values for $R(D)$ and $R(D^\star)$ are adopted from the Heavy Flavour Averaging Group (HFLAV) fit *circa* 2021, and the combined significance of these two anomalies is 3.4 σ, with a correlation $\rho = -0.38$ [10]. 134

5.2 **Charges under the residual symmetry $\boldsymbol{Z_{17}^{\mathrm{diag}}}$.** I list the charges of the different fermions, scalars and spurion fields under the residual symmetry Z_{17}^{diag}, preserved by the LO structure of the LQ couplings $\mathbf{x}$ and $\mathbf{y}$; see eq. (5.7). This residual symmetry Z_{17}^{diag} is the diagonal subgroup of the Z_{17} symmetry contained in D_{17} and generated by the generator a, compare appendix 5.6, and the external Z_{17} symmetry. 138

5.3 **Particle content of the model**. The fermions, scalar fields and spurions (flavour-symmetry breaking fields) and their transformation properties under the SM gauge group SU(3) × SU(2) × U(1) as well as the flavour symmetry $G_f = D_{17} \times Z_{17}$ are given. Particles in an irreducible two-dimensional representation of D_{17} are evidenced in terms of two-component vectors. 139

5.4 **List of primary observables**. Herein I list the observables of which the anomalous data ought to be explained, as well as the ones which dominantly constrain this model, together with the respective current measurement/constraint and future reach. The values for $R(D)$ and $R(D^\star)$ reflect the 2021 averages from the HFLAV collaboration. The future reach for BR($\mu \to 3e$) outside (inside) the parentheses refers to Phase 1 (2) of the Mu3E experiment. For CR($\mu \to e$; Al), the first (second) value indicates the future reach of COMET (Mu2E). The future reach for $R^{\nu}_{K^\star}$ holds under the assumption that the result of the measurement will agree with the SM expectation [7]. Regarding the projections for g_{τ_A}, it is assumed that the experimental uncertainty will be reduced by the same factor as $\sin^2\theta_{\text{eff}}$ as in ref. [31]; the unbracketed projection refers to the International Linear Collider (ILC) [32], whereas the bracketed value is for the Future Circular Collider (FCC) [33]. The current experimental constraint on the B_c lifetime is $\tau^{\text{exp}}_{B_c} = (0.510 \pm 0.009)$ ps [10, 29]. Note that the constraint arising from high-p_T $\tau\bar{\tau}$ searches differs from the other constraints in that it is directly imposed in the primary scan via an adequate restriction of the range for $|b_{32}|$ as indicated. . . . 155

5.5 **List of primary observables with the relevant effective parameters**. I list the primary observables together with the effective parameters related to the LQ couplings in the charged fermion mass basis which capture the most relevant contributions, respectively, in line with the analytic estimates performed in this section. The parameters listed in round brackets refer to contributions which are subdominant. 156

5.6 **Inputs for biasing in the comprehensive scan, derived from the samples generated in the primary scan**. I define $\Delta(r_{ij}, s_{kl}) \equiv \text{Arg}(r_{ij}) - \text{Arg}(s_{kl})$. Every sample point found in the primary scan which respects all experimental bounds and explains $R(D^{(\star)})$ or Δa_μ (or both) at $3\,\sigma$ falls into the displayed ranges. The interval bounds are rounded to one decimal place. Since no sample points which explain Δa_μ at $3\,\sigma$ were found for $\hat{m}_\phi = 2$ in the primary scan, the default ranges $[\lambda, 1/\lambda]$ and $[-1.0, 0.0]$ are adopted for $|a_{23}|$ and $\cos[\Delta(a_{23}, b_{23})]$, respectively, in the comprehensive scan. Note that the inequalities in eq. (5.65) and (5.66) are imposed as well, as is explained in the main text. 170

5.7 **List of secondary observables**. I list the observables that can potentially be used to further constrain and test this model, together with their current experimental constraint and future sensitivity. In the case of the muon EDM d_μ, the future projection without brackets refers to the prospective reach of the Muon $g-2$ experiment at Fermilab [34] and a similar experimental effort at J-PARC [40], while the bracketed values are estimates for experimental proposals [35, 41, 42] based on the frozen-spin technique. Furthermore, I assume that the precision of measurements of g_{μ_A} will improve by the same factor as $\sin^2\theta_{\text{eff}}$ as in ref. [31]; the (un)bracketed projection refers to the FCC [33] (ILC [32]). 195

Abbreviations

AMM	Anomalous Magnetic Moment
Br, BR	Branching Ratio
BSM	Beyond the Standard Model
CAA	Cabibbo Angle Anomaly
CKM	Cabibbo-Kobayashi-Maskawa
CL	Confidence Level
cLFV	Charged Lepton Flavour Violating
CMB	Cosmic Microwave Background
CP	Charge Parity
CR	Conversion Ratio
EDM	Electric Dipole Moment
EFT	Effective Field Theory
eV	Electronvolt
FCCC	Flavour-Changing Charged Current
FCNC	Flavour-Changing Neutral Current
GIM	Glashow-Iliopoulos-Maiani
GUT	Grand Unified Theory
h.c.	Hermitian Conjugate
HQET	Heavy-Quark Effective Theory
HVP	Hadronic Vacuum Polarisation
IO	Inverted Ordering

JMS	Jenkins-Manohar-Stoffer
KNT	Krauss-Nasri-Trodden
LCSR	Light-Cone Sum Rules
LEFT	Low-Energy Effective (Field) Theory
LFU	Lepton-Flavour Universality
LFV	Lepton-Flavour Violating
LH	Left-Handed
LQ	Leptoquark
LQCD	Lattice Quantum Chromodynamics
NO	Normal Ordering
NP	New Physics
NSI	Non-Standard Interaction
pc	Parsec
PDG	Particle Data Group
PMNS	Pontecorvo-Maki-Nakagawa-Sakata
QCD	Quantum Chromodynamics
QED	Quantum Electrodynamics
RG	Renormalisation Group
RGE	Renormalisation Group Equation
RH	Right-Handed
SM	Standard Model
SMEFT	Standard Model Effective Field Theory
SO(n)	Special Orthogonal Group of Dimension n
SU(n)	Special Unitary Group of Dimension n
UV	Ultraviolet
VEV	Vacuum Expectation Value
WC	Wilson Coefficient

Chapter 1

Introduction

This thesis is set in flavour physics which is a sub-discipline of the much broader field of particle physics. The modern framework to make quantitative predictions for particle physics is the Standard Model (SM). As a theory, it has been very successful in describing the interactions involving the known fundamental particles, that is, the Higgs boson, the gauge bosons and the fermions. Whereas the former two might be dubbed “interaction” or “force-carrier” particles, the latter constitute the matter particles or “building blocks” of the universe. Fermions come in three different copies which are also commonly called “flavours”. The properties of the different fermion flavours as a whole then constitute what is called the “flavour structure” of nature.

Fermions can be separated into quarks and leptons, distinguished by the fact that the former participate in strong interactions while the latter do not. As mentioned above already, three copies, or flavours, of both quarks and leptons have been observed. Furthermore, there are two types of particles for each generation which are distinguished by isospin: up-type quarks and down-type quarks on the one hand, and neutrinos and charged leptons on the other hand.[1] As spin-$\frac{1}{2}$ particles, fermions constitute the simplest nontrivial representation of the Lorentz group, composed of Weyl spinors which are either

---

[1] One might further notice that each fermion comes with its antiparticle. In the case of neutrinos, particles and antiparticles could be identical.

left-handed (LH) or right-handed (RH).

The SM does not treat quarks and leptons on equal footing, which can be traced back to the fact that it features RH up-type quarks, but lacks RH neutrinos. An obvious reason for this asymmetry is that the existence of RH up-type quarks is well-established, whereas RH neutrinos have never been (conclusively) seen. This is not surprising, given that RH neutrinos are predicted not to participate in gauge interactions, and would thus communicate with the SM only via gravitational or Yukawa interactions. Furthermore, the existence of RH neutrinos is not strictly required by any theoretical argument.

The presence of three fermion generations implies the presence of three physical mixing angles which parametrise the mismatch between the particle states which participate in gauge and/or Yukawa interactions and the physically propagating states. Furthermore, the mixing matrix which translates between the two associated bases features a complex phase, signaling that the symmetry of charge parity (CP) can be violated. This phase as well as the three mixing angles have been measured with percent-level accuracy in the quark sector [29]. In general, the physics of the quark sector as described by the SM is by now fairly well understood.

As a consequence of the absence of RH neutrinos, the lepton sector featuring electrons, muons and tau leptons together with their respective associated neutrinos is less rich in structure in the SM. In fact, it exhibits a symmetry which predicts lepton flavour to be conserved, that is, no net change in the number of particles carrying electron, muon and tau flavour, respectively, can be generated. Still, many experiments, among them those performed at Super-Kamiokande [43] and SNO [44,45], have provided conclusive evidence that neutrinos undergo oscillations and thus lepton flavour is definitely not conserved in nature. Furthermore, at least two neutrinos must be massive, in conflict with the SM. Consequently, we can be certain that the flavour structure of the lepton sector of nature must be more involved than what is implied by the SM.

Another unsatisfactory aspect of the SM is related to the Yukawa sector which describes the interactions between the fermions and the Higgs field. Not accounting for lepton mixing and non-zero neutrino masses, one finds that the Yukawa sector features thirteen physical parameters: three lepton masses and six quark masses as well as three mixing angles and the CP-violating phase in the quark sector. Data on neutrino oscillations evidences the need to introduce at least two non-zero masses in the neutrino sector, together with three mixing angles and one CP-violating phase in the lepton sector. Still, all of these quantities are entirely free parameters which can only be determined from experiment. In particular, there is no explanation for the strong hierarchy among the masses of the charged fermions, the large gap of scales between the electron mass and the largest neutrino mass, or the fact that quark mixing is sizeable only for the first two generations, while there are two large mixing angles in the lepton sector. It is expected that only new physics (NP) can provide insight into the mechanism which gives rise to the flavour structure exhibited by the SM Yukawa interactions.

Besides the large number of unexplained parameters in the SM flavour sector, there is also growing evidence for deviations between the results of specific measurements and the relevant predictions in the SM which depend on (some of) these parameters. In particular, the prediction of lepton-flavour universality (LFU), according to which the masses of the members of the three lepton generations can be the only source of differences in their behaviour, becomes increasingly challenged. This is exemplified by the so-called LFU ratios $R(D)$ and $R(D^\star)$,

$$R(D^{(\star)}) = \frac{\Gamma(B \to D^{(\star)}\tau\overline{\nu})}{\Gamma(B \to D^{(\star)}\ell\overline{\nu})} \tag{1.1}$$

with $\ell = e, \mu$. A combined fit to the data on $R(D)$ and $R(D^\star)$ reveals a tension with the SM prediction at the level of $3.4\,\sigma$ [10]. Furthermore, the measurement of the anomalous magnetic moment (AMM) of the muon $a_\mu = (g-2)_\mu/2$ at Brookhaven National Laboratory [46] has revealed a significant discrepancy with the SM which further solidified with the announcement of the results from the Muon $g-2$ experiment at Fermilab [18]. According to the combined fit to the data, the anomaly currently stands at a significance of $4.2\,\sigma$ in the quantity $\Delta a_\mu = a_\mu^{\mathrm{exp}} - a_\mu^{\mathrm{SM}}$ if the data-driven approach to determine the leading-order hadronic vacuum polarisation is employed; see for instance ref. [19]. Further experimental anomalies have manifested in recent years, for instance in various observables related to $b \to s$ quark transitions.

Let me get back to neutrino masses now, and recall that several questions regarding their nature remain unanswered. For instance, it is still unknown whether neutrinos are Dirac or Majorana particles. The former necessitate the simultaneous existence of (light) RH and LH neutrino fields, whereas for the latter only the known LH neutrinos need to present at low energies. While a Dirac nature of neutrinos is still a perfectly viable possibility, Majorana neutrinos may be seen as more compelling from a theoretical point of view. If induced in a gauge-invariant manner, Majorana neutrino masses are associated with the breaking of the conservation of lepton number which is a symmetry in the SM on the perturbative level. The size of Majorana neutrino masses is set by the (large) scale of lepton-number breaking and thus naturally suppressed, which can be seen explicitly in the context of the non-renormalisable Weinberg operator [47] if the SM is considered an effective field theory (EFT).

Over several decades, many explicit models which give rise to the Weinberg operator have been studied; see for instance the review articles [48–50]. Their sheer number necessitates proper means of classification in order to enable an efficient comparison of the models amongst each other and with experimental data. There are many viable avenues to do so, notably via effective operators which violate the conservation of lepton number by two units ($\Delta L = 2$); see e.g. refs. [51–58]. Still, the relation between contributions to processes which respect the conservation of lepton number and to those which violate it may be very model-dependent, and the former typically constrain the available parameter space more efficiently than the latter. Furthermore, there is an enormous number of possible ultraviolet (UV) completions of effective $\Delta L = 2$ operators.

Building on an approach laid out in ref. [59] which in a way proceeds along an intermediate avenue between EFT and complete models, I investigate a scenario in which Majorana neutrino masses might be generated via a singly-charged scalar singlet which transforms as $h \sim (1, 1, 1)$ under the SM gauge group. It is a case study for "simplified models" in which the SM particle content is enlarged by a single particle which is charged under lepton number, together with a source of lepton-number breaking. The singly-charged scalar singlet plays a vital role in several UV-complete models, including the Zee model [60–62], the Zee-Babu model [63–65] and the Krauss-Nasri-Trodden model [66] and their respective variations. The coupling y_h of h to two LH lepton doublets is antisymmetric in flavour space and thus allows for the derivation of a constraint on the elements y_h^{ij} in terms of neutrino parameters, which sets the ground for a comprehensive numerical study.

Taking a step back, we find ourselves in a situation in which the need to introduce NP is established, while its nature remains elusive. In this light, the odds that a particular model, or even a class of models, correctly describes nature in its entirety might be regarded as relatively small. Thus, interpreting experimental data in a more general and model-independent way is equally important for guiding the search for NP. In this thesis, I thoroughly analyse existing data on and prospective enhanced sensitivities to the decay process $B \to K^{(\star)}$ plus neutrinos at the Belle-II experiment [7]. A recently presented simple weighted average $\mathrm{BR}(B^+ \to K^+\nu\nu) = (1.1 \pm 0.4) \times 10^{-5}$ [1,8] supersedes previously established upper bounds and indicates a possible enhancement with respect to the SM.

The underlying process $b \to s\nu\bar{\nu}$ is suppressed in the SM due to the so-called Glashow-Iliopoulos-Maiani mechanism which may thus increase the chances of detecting a contribution from NP. Besides additional ways to mediate the decay, extensions of the SM may also feature sterile particles, that is, those which do not participate in gauge interactions, that could be produced in the final state and escape without detection. Furthermore, the theoretical description of $b \to s\nu\bar{\nu}$ processes is very clean. Earlier model-independent studies of the decay $B \to K^{(\star)}$ plus neutrinos in terms of EFT can be found in refs. [67–77]. In this thesis, all relevant dimension-6 operators in low-energy effective theory for arbitrarily many neutrino generations are considered, including the possibility of massive sterile neutrinos. The results of the study can be applied to any model of NP introduced at or above the electroweak scale.

Slightly shifting the focus once more, I now turn to the concept of symmetries which have proven extraordinarily successful in describing the gauge interactions of the SM particles. Therefore, it appears reasonable to consider a similar hypothesis for the flavour sector, that is, assume a symmetry which acts on the space of flavours (or generations). It has been demonstrated that the hierarchies among the masses of the charged fermions can be appropriately predicted via an abelian symmetry group, such as U(1) [78], under which the different fermion species carry non-identical charges. Still, in order to accommodate the observed features of mixing in the quark sector and lepton sector and to potentially predict specific patterns, a non-abelian symmetry seems to be preferred.

In ref. [79], a scalar leptoquark (LQ) has been proposed as an explanation of the anomalies in $R(D)$, $R(D^\star)$ and in the AMM of the muon which were introduced above. This scenario was then further studied in subsequent works by different authors, e.g. in ref. [80]. Combining the two aforementioned approaches, I study a model which makes use of a discrete symmetry acting on flavour space to explain the masses of the charged fermions together with quark mixing as well as $R(D)$, $R(D^\star)$ and Δa_μ. The employed symmetry completely determines the interactions among the SM fields in the Yukawa sector as well as those between the SM fermions and the LQ. Similar existing studies may be found in refs. [81–86].

This thesis is structured as follows. In chapter 2, I review some aspects of the SM and possible extensions, as well as effective field theory and current experimental indications of NP. The publication [87] together with the published erratum [88] are used in lieu of chapter 3 wherein I study the simplified model involving the singly-charged scalar singlet, under the assumption that it generates neutrino masses together with an unspecified source of lepton-number violation. Then, I continue in chapter 4 in lieu of which the publication [89] is used. Therein, I provide a model-independent analysis of existing and forecast data on several $b \to s\nu\nu$ decay channels, and the derivation of constraints on different operators contributing to them. Lastly, I scrutinise the above-mentioned concrete NP model which provides an explanation for the measured charged fermion masses and quark mixing parameters, as well as currently observed anomalies in $R(D)$, $R(D^\star)$ and the AMM of the muon. The presentation in chapter 5 has been extensively edited and adapted from ref. [90]. Lastly, I draw conclusions and provide an outlook in chapter 6.

Chapter 2

Background

2.1 Aspects of the Standard Model

In this section, I review some selected aspects of the SM.

2.1.1 Lorentz Symmetry

The stage on which particle physics unfolds in the absence of gravitational effects is Minkowski spacetime. Physical results should not depend on the choice of inertial frame, or put differently, remain unchanged if boosts or rotations are applied which together constitute Lorentz transformations. In technical terms, these can be expressed as 4×4 matrices Λ satisfying $\Lambda^T g \Lambda = g$ where g is the Minkowski metric which is conventionally taken as $g = \mathrm{diag}(1, -1, -1, -1)$ in particle physics [91]. Lorentz transformations give rise to the Lorentz group $\mathrm{SO}(3,1)$. The generators for boosts and rotations can be rearranged in linear combinations such that they satisfy two independent $\mathfrak{su}(2)$ algebras, and thus $\mathrm{SO}(3,1)$ is locally isomorphic to $\mathrm{SU}(2) \times \mathrm{SU}(2)$ [92]. Therefore, the representations of a field under the Lorentz group can be conveniently labeled by a pair of (half-)integers (a, b) with $a, b = 0, \frac{1}{2}, 1, ...$ which are familiar from spin quantisation.

2.1.1.1 Fermion Mass Terms

The presentation in this section mainly draws from ref. [92]. The notation in terms of two-component spinors is aligned with ref. [93], and Lorentz indices are suppressed.

Weyl spinors are the simplest objects which transform non-trivially under the Lorentz group. A Weyl spinor $\chi \sim (\frac{1}{2}, 0)$ is conventionally dubbed LH, whereas $\eta \sim (0, \frac{1}{2})$ then denotes a RH Weyl spinor. The fact that Weyl spinors can transform under either of two SU(2) copies implies that two Lorentz-invariant types of mass terms exist. A *Majorana mass term* involves only one Weyl spinor, that is, in the case of $\chi \sim (\frac{1}{2}, 0)$,

$$m_\chi \chi\chi + \text{h.c.} \tag{2.1}$$

where “h.c.” stands for “hermitian conjugate”. A Weyl fermion with a non-zero Majorana mass is called a *Majorana fermion.* If χ is charged under a pseudo-real or complex representation of an unbroken symmetry, a Majorana mass term is forbidden [92]. Thus, Majorana fermions are in particular electrically neutral and referred to as their own antiparticle.

Still, a Weyl fermion $\chi \sim (\frac{1}{2}, 0)$ which transforms under a pseudo-real or complex representation of an unbroken symmetry can form a *Dirac mass term* with another Weyl fermion $\xi \sim (\frac{1}{2}, 0)$ transforming under the respective complex-conjugate representation,

$$m\chi\xi + \text{h.c.}\ . \tag{2.2}$$

It is conventional to combine χ and ξ into a Dirac spinor $\psi = (\chi, \xi^\dagger)$ which allows the more familiar four-component notation

$$m\overline{\psi}\psi\ . \tag{2.3}$$

If m is non-zero, the Dirac spinor $\psi = (\chi, \xi^\dagger)$ is said to describe a *Dirac fermion.*

Consequently, a major difference between the two types of mass terms is that a Majorana mass only involves one Weyl spinor, whereas a Dirac mass involves two different Weyl spinors and thus twice as many independent degrees of freedom.

2.1.1.2 Lorentz Bilinears

A free Dirac fermion is a solution to the Dirac equation

$$(i\gamma^\mu\partial_\mu - m)\psi = 0 \tag{2.4}$$

where the matrices γ^μ satisfy the Dirac algebra defined by

$$\{\gamma^\mu, \gamma^\nu\} = 2g^{\mu\nu} \tag{2.5}$$

with the anticommutator $\{A, B\} \equiv AB + BA$. The smallest non-trivial representation of the Dirac algebra is four-dimensional. The set of 16 elements $\{1, \gamma^5, \gamma^\mu, \gamma^\mu\gamma^5, \sigma^{\mu\nu}\}$ where

$$\sigma^{\mu\nu} \equiv \frac{i}{2}\left[\gamma^\mu, \gamma^\nu\right] \tag{2.6}$$

constitutes a basis in the space of 4×4 matrices. Given a Dirac spinor ψ, there is a finite number of Lorentz covariants that one can construct out of ψ and its Dirac adjoint $\overline{\psi} \equiv \psi^\dagger\gamma^0$:

$$\begin{aligned}
\overline{\psi}\psi &\qquad \text{scalar} \\
\overline{\psi}\gamma^5\psi &\qquad \text{pseudo-scalar} \\
\overline{\psi}\gamma^\mu\psi &\qquad \text{vector} \\
\overline{\psi}\gamma^\mu\gamma^5\psi &\qquad \text{pseudo-vector} \\
\overline{\psi}\sigma^{\mu\nu}\psi &\qquad \text{tensor}
\end{aligned} \tag{2.7}$$

The designations of these covariants indicate their respective definite behaviour under parity transformations.[1]

In fact, instead considering the basis $\{P_L, P_R, \gamma^\mu P_L, \gamma^\mu P_R, \sigma^{\mu\nu}\}$ often proves more convenient [94]. Here, the chiral projection operators

$$P_L \equiv \frac{1}{2}\left(1 - \gamma^5\right) \;, \qquad P_R \equiv \frac{1}{2}\left(1 + \gamma^5\right) \tag{2.8}$$

enter. Applying a parity transformation then interchanges the Lorentz scalars $\overline{\psi}P_{L,R}\psi \leftrightarrow \overline{\psi}P_{R,L}\psi$ and Lorentz vectors $\overline{\psi}\gamma^\mu P_{L,R}\psi \leftrightarrow \overline{\psi}\gamma^\mu P_{R,L}\psi$, respectively.

---

[1] Note that one can formally also define pseudo-tensors in an equivalent manner, but they can be rewritten in terms of tensors and the Levi-Civita symbol, and are therefore not independent.

2.1.2 Particle Content and Weak Interactions

The particle content of the SM can be grouped into four bosonic representations H, G^a_μ, W^a_μ, B_μ of the Lorentz group, and five fermionic representations Q_{Li}, L_{Li}, u_{Ri}, d_{Ri}, e_{Ri}.[2] Here, the index $i = 1, 2, 3$ counts the three flavours (or generations). Furthermore, all SM particles are organised in multiplets under the gauge group $\mathrm{SU}(3)_c \times \mathrm{SU}(2)_w \times \mathrm{U}(1)_Y$.

Up-type quarks are described by the u_{Ri} as well as the upper components of the representation of Q_L under $\mathrm{SU}(2)_w$, whereas the d_{Ri} and the lower Q_L components are called *down-type quarks*. Similarly, *neutrinos* constitute the upper components of the representation of L_L under $\mathrm{SU}(2)_w$, and the e_{Ri} together with the lower L_L components are called *charged leptons*. The specific transformation properties are summarised in table 2.1. Upon the acquisition of a vacuum expectation value (VEV) by the Higgs doublet, $H = (\phi^+, \phi^0) \to (0, (v + h)/\sqrt{2})$ in unitary gauge, the product $\mathrm{SU}(2)_w \times \mathrm{U}(1)_Y$ is broken to $\mathrm{U}(1)_{\mathrm{EM}}$, where the subscript refers to electromagnetism [95]. Then, the charge of the SM particles under the latter is called *electric charge* and determined from $Q = T_3 + Y$, where T_3 is the eigenvalue under the third generator of $\mathrm{SU}(2)_w$, called *weak isospin*, and Y is the charge under $\mathrm{U}(1)_Y$, called *hypercharge*.

Furthermore, the SM is a *renormalisable* theory, which formally requires that any divergences appearing in results for observable quantities can be removed with a finite number of counterterms [95]. In practice, an operator composed of SM fields is renormalisable in $3 + 1$ dimensions if its mass dimension is smaller than or equal to four. Treating the SM as a weakly coupled theory, one finds that the mass dimension of an operator is simply given by the engineering dimension, that is, the sum of the mass dimensions of the fields and momentum insertions constituting the operator under consideration [4]. In $d = 4$ dimensions, $[p_\mu] = 1$ as well as $[\phi] = 1$ for scalar and vector particles and $[\phi] = 3/2$ for fermions.

---

[2] The four-component notation is consistent with chapters 4 and 5. On the contrary, two-component spinors are employed in chapter 3. In particular, RH spinors $\psi \equiv P_R\psi$ are expressed therein in terms of LH spinors $\bar{\psi} \equiv \psi^c$.

	SU(2) × SU(2)	SU(3)$_c$	SU(2)$_w$	U(1)$_Y$
$H = \left(\phi^+, \phi^0\right)$	$(0,0)$	1	2	$\frac{1}{2}$
$Q_{Li} = \left((u_L, d_L), (c_L, s_L), (t_L, b_L)\right)$	$(\frac{1}{2}, 0)$	3	2	$\frac{1}{6}$
$L_{Li} = \left((\nu_{Le}, e_L), (\nu_{L\mu}, \mu_L), (\nu_{L\tau}, \tau_L)\right)$	$(\frac{1}{2}, 0)$	1	2	$-\frac{1}{2}$
$u_{Ri} = \left(u_R, c_R, t_R\right)$	$(0, \frac{1}{2})$	3	1	$\frac{2}{3}$
$d_{Ri} = \left(d_R, s_R, b_R\right)$	$(0, \frac{1}{2})$	3	1	$-\frac{1}{3}$
$e_{Ri} = \left(e_R, \mu_R, \tau_R\right)$	$(0, \frac{1}{2})$	1	1	-1
G^a_μ	$(\frac{1}{2}, \frac{1}{2})$	8	1	0
$W^a_\mu = \left(W^1_\mu, W^2_\mu, W^3_\mu\right)$	$(\frac{1}{2}, \frac{1}{2})$	1	3	0
B_μ	$(\frac{1}{2}, \frac{1}{2})$	1	1	0

Table 2.1: Particle content of the SM, together with the transformation properties under the Lorentz and gauge groups.

An object of major importance for the following considerations is given by $\overline{\psi}\gamma^\mu\psi$ which is usually called “vector current” or simply “current”. It can be combined with a gauge field to form a Lorentz- and gauge-invariant operator. One distinguishes charged and neutral currents.

Regarding the latter, I consider the (effective) Lagrangian for the interaction between a Z boson and SM fermions, following ref. [96],

$$\mathcal{L}^Z_{\text{eff}} = \frac{g}{c_W} \sum_{i,j} \overline{\psi}_i \gamma^\mu \left[g^{ij}_{\psi_L} P_L + g^{ij}_{\psi_R} P_R\right] \psi_j Z_\mu \ , \tag{2.9}$$

with the sums running over all SM fermion species, the SU(2)$_w$ gauge coupling g, the cosine of the weak mixing angle θ_W denoted by c_W, and

$$g^{ij}_{\psi_{L,R}} = g^{\text{SM}}_{\psi_{L,R}} \delta^{ij} + \delta g^{ij}_{\psi_{L,R}} \ . \tag{2.10}$$

In the SM, the (effective) couplings are given at tree level as in

$$g^0_{\psi_L} = T^\psi_3 - Q^\psi \sin^2\theta_W \ , \qquad g^0_{\psi_R} = -Q^\psi \sin^2\theta_W \tag{2.11}$$

with the electric charge Q^ψ and the weak isospin T^ψ_3 of the fermion $\psi_{L,R}$, see also table 2.2, and $\delta g^{ij}_{\psi_{L,R}} = 0$. At loop level, they are modified according to

$$g^{\text{SM}}_{\psi_L} = \sqrt{\rho_\psi}\,(T^\psi_3 - Q^\psi \sin^2\theta_{\text{eff}}) \ , \qquad g^{\text{SM}}_{\psi_R} = -\sqrt{\rho_\psi}\, Q^\psi \sin^2\theta_{\text{eff}} \tag{2.12}$$

SM fermion ψ	T_3^ψ	Q^ψ	$T_3^\psi - Q^\psi \sin^2\theta_W$
ν_{Le}, $\nu_{L\mu}$, $\nu_{L\tau}$	$\frac{1}{2}$	0	0.50
e_L, μ_L, τ_L	$-\frac{1}{2}$	-1	-0.28
u_L, c_L, t_L	$\frac{1}{2}$	$\frac{2}{3}$	0.35
d_L, s_L, b_L	$-\frac{1}{2}$	$-\frac{1}{3}$	-0.42
e_R, μ_R, τ_R	0	-1	0.23
u_R, c_R, t_R	0	$\frac{2}{3}$	-0.15
d_R, s_R, b_R	0	$-\frac{1}{3}$	0.08

Table 2.2: Coupling strength of SM fermion-antifermion pairs to the Z boson.

where

$$\rho_\psi = 1 + \frac{3G_F m_t^2}{8\sqrt{2}\pi^2} + ... \approx 1.0094 \tag{2.13}$$

with the dominant correction due to electroweak self-energy diagrams with internal top quarks, and $\sin^2\theta_{\text{eff}} \approx 0.2315$ [29]. In the presence of NP, further contributions can get induced which then results in non-zero $\delta g^{ij}_{\psi_{L,R}}$.

2.1.3 Yukawa Sector

A major implication of the representation of the SM particles under the gauge group $\mathrm{SU}(3)_c \times \mathrm{SU}(2)_w \times \mathrm{U}(1)_Y$ is the absence of bare mass terms as introduced in section 2.1.1.1. Still, the *Yukawa interactions*

$$\mathcal{L}_{\text{Yuk}} = -y_u^{ij}\overline{Q_{Li}}\epsilon H^* u_{Rj} - y_d^{ij}\overline{Q_{Li}} H d_{Rj} - y_e^{ij}\overline{L_{Li}} H e_{Rj} + \text{h.c.} \tag{2.14}$$

with $\epsilon \equiv i\sigma^2$ are compatible with the gauge symmetry. The parametrisation above holds in a generic basis in which y_u, y_d and y_e may contain up to 18 (real) parameters each. It might be referred to as the *interaction basis* which alludes to the possibility that the operators in eq. (2.14) are an effective parametrisation of some non-trivial dynamics at high energies. Note that in the interaction basis, the Yukawa matrices account for all the flavour effects.

After electroweak symmetry breaking, the charged fermion mass basis is adopted via biunitary transformations

$$y_i \to y_i^m \equiv L_i^\dagger y_i R_i \quad \text{for } i = u, d, e \tag{2.15}$$

where the matrices y_i^m are diagonal:

$$y_u^m = \operatorname{diag}(y_u, y_c, y_t)\ , \quad y_d^m = \operatorname{diag}(y_d, y_s, y_b)\ , \quad y_e^m = \operatorname{diag}(y_e, y_\mu, y_\tau)\ . \tag{2.16}$$

Regarding the basis transformation of the LH SM fermions, I find

$$u_{Li} = (L_u)_{ij} u_{Lj}^m\ , \quad d_{Li} = (L_d)_{ij} d_{Lj}^m\ , \quad e_{Li} = (L_e)_{ij} e_{Lj}^m\ , \quad \nu_{Li} = (L_e)_{ij} \nu_{Lj}^m \tag{2.17}$$

and for RH SM fermions

$$u_{Ri} = (R_u)_{ij} u_{jR}^m\ , \quad d_{Ri} = (R_d)_{ij} d_{Rj}^m\ , \quad e_{Ri} = (R_e)_{ij} e_{Rj}^m \tag{2.18}$$

where the superscript m indicates the mass basis. In this basis, the elements of the Yukawa matrices are directly proportional to the charged fermion masses, that is,

$$\frac{y_i^m}{\sqrt{2}} = \frac{m_i}{v} \quad \text{for } i = u, d, e \tag{2.19}$$

where the masses are contained in the diagonal matrices m_i.

As the name suggests, charged currents involve a change in the electric charge of the involved fermions by ±1. In the SM, this implies that charged currents are composed of an up-type quark and a down-type quark, or a neutrino and a charged lepton. $W^\pm$ bosons couple to these currents at tree level, since they are linear combinations of the SU$(2)_w$ gauge bosons $W^{1,2}$ associated with the non-diagonal Pauli matrices $\sigma^{1,2}$. The respective weak Lagrangians read

$$\mathcal{L}^W = \frac{g}{\sqrt{2}} \overline{u_{Li}} \gamma^\mu d_{Li} W_\mu^+ + \frac{g}{\sqrt{2}} \overline{\nu_{Li}} \gamma^\mu e_{Li} W_\mu^+ + \text{h.c.}\ . \tag{2.20}$$

Adopting the charged fermion mass basis, one finds

$$\begin{pmatrix} \overline{u_L} & \overline{c_L} & \overline{t_L} \end{pmatrix} \gamma^\mu \begin{pmatrix} d_L \\ s_L \\ b_L \end{pmatrix} = \begin{pmatrix} \overline{u_L^m} & \overline{c_L^m} & \overline{t_L^m} \end{pmatrix} L_u^\dagger\, \gamma^\mu\, L_d \begin{pmatrix} d_L^m \\ s_L^m \\ b_L^m \end{pmatrix}\ , \tag{2.21}$$

$$\begin{pmatrix} \overline{\nu_{Le}} & \overline{\nu_{L\mu}} & \overline{\nu_{L\tau}} \end{pmatrix} \gamma^\mu \begin{pmatrix} e_L \\ \mu_L \\ \tau_L \end{pmatrix} = \begin{pmatrix} \overline{\nu_{L\,e}^m} & \overline{\nu_{L\,\mu}^m} & \overline{\nu_{L\,\tau}^m} \end{pmatrix} L_e^\dagger\, \gamma^\mu\, L_e \begin{pmatrix} e_L^m \\ \mu_L^m \\ \tau_L^m \end{pmatrix} \tag{2.22}$$

where the basis transformation has no effect in the leptonic case since the matrix L_e cancels out. Thus, lepton mixing is unphysical in the SM. On the contrary, the *Cabibbo-Kobayashi-Maskawa (CKM) matrix*

$$V \equiv L_u^\dagger L_d \tag{2.23}$$

is physical and cannot be removed from the theory. Hence, the up-type quarks and the down-type quarks are not fully aligned in the SM. Since L_u and L_d are unitary, so is V. It is commonly parametrised in terms of three mixing angles θ_{12}, θ_{13}, θ_{23} and a complex phase δ. Abbreviating $c_{ij} \equiv \cos(\theta_{ij})$ and $s_{ij} \equiv \sin(\theta_{ij})$, one may write

$$V = \begin{pmatrix} c_{12}c_{13} & s_{12}c_{13} & s_{13}e^{-i\delta} \\ -s_{12}c_{23} - c_{12}s_{23}s_{13}e^{i\delta} & c_{12}c_{23} - s_{12}s_{23}s_{13}e^{i\delta} & s_{23}c_{13} \\ s_{12}s_{23} - c_{12}c_{23}s_{13}e^{i\delta} & -c_{12}s_{23} - s_{12}c_{23}s_{13}e^{i\delta} & c_{23}c_{13} \end{pmatrix} \tag{2.24}$$

where the parameters are determined from the experimental data as follows, according to the Particle Data Group (PDG) [29]:

$$\sin(\theta_{12}) = 0.22650^{+0.00048}_{-0.00048}\,, \qquad \sin(\theta_{13}) = 0.00361^{+0.00011}_{-0.00009}\,, \tag{2.25}$$

$$\sin(\theta_{23}) = 0.04053^{+0.00083}_{-0.00061}\,, \qquad \delta = 1.196^{+0.045}_{-0.043}\,. \tag{2.26}$$

This implies that the magnitudes have the approximate hierarchy [97]

$$|V| \sim \begin{pmatrix} 1 & \lambda & \lambda^3 \\ \lambda & 1 & \lambda^2 \\ \lambda^3 & \lambda^2 & 1 \end{pmatrix} \tag{2.27}$$

where $\lambda \approx 0.2$. Thus, the CKM matrix is close to diagonal. Consequently, flavour-changing charged currents (FCCCs) are generically induced at tree level via couplings to the $W^\pm$ boson, but they are suppressed. Note that since in particular $s_{13} \sim \lambda^3$ is small, the magnitudes $|V_{us}|$, $|V_{ub}|$ and $|V_{cb}|$ can be approximately identified with the (sines of) the mixing angles θ_{12}, θ_{13} and θ_{23}, respectively. In the mass basis, the CKM matrix encodes all the flavour structure, apart from the differences in the charged fermion masses.

A parametrisation-independent way of quantifying CP violation is given by the *Jarlskog* *invariant* J, defined via

$$\mathrm{Im}(V_{ij}V_{kl}V_{il}^*V_{kj}^*) = J \sum_{m,n=1}^{3} \epsilon_{ikm}\epsilon_{jln} \tag{2.28}$$

which for instance implies

$$J = \mathrm{Im}(V_{ud}V_{tb}V_{ub}^*V_{td}^*) = c_{12}\, c_{23}\, c_{13}^2\, s_{12}\, s_{23}\, s_{13}\, \sin(\delta) \tag{2.29}$$

for the parametrisation used above. Note that J has physical meaning only in the presence of three fermion generations and three non-zero mixing angles. This can be easily seen from an alternative definition which involves the determinant [91, 98]

$$\det C = -\frac{16}{v^2}(m_t - m_c)(m_t - m_u)(m_c - m_u)(m_b - m_s)(m_b - m_d)(m_s - m_d)J \tag{2.30}$$

of the traceless matrix $C = i[y_u, y_d]$.

As a brief aside, in order to accommodate lepton mixing and non-zero neutrino masses, one defines the *Pontecorvo-Maki-Nakagawa-Sakata (PMNS) matrix*

$$U \equiv L_e^\dagger L_\nu \tag{2.31}$$

in an analogous manner, where L_ν is a unitary matrix. Then, the LH SM neutrinos transform as in

$$\nu_{Li} = (L_\nu)_{ij}\nu_{Lj}^m\ . \tag{2.32}$$

In stark contrast to the CKM matrix, the PMNS matrix is not close to diagonal and considerably less hierarchical [38]:

$$|U| \approx \begin{pmatrix} 0.82 & 0.55 & 0.15 \\ 0.4 & 0.6 & 0.7 \\ 0.4 & 0.6 & 0.7 \end{pmatrix} \tag{2.33}$$

Hence, lepton mixing is in fact large, and the occurrence of lepton FCCCs is not suppressed. In complete analogy to the CKM matrix, U can be parametrised in terms of three non-zero mixing angles and at least one complex phase.[3] Since the value of the latter is still

---

[3] If neutrinos are Majorana particles, the PMNS matrix necessarily features two further complex phases, commonly referred to as *Majorana phases*; see also section 3.2.3.

beset with a considerable uncertainty, the occurrence of CP violation in the lepton sector is not conclusively established yet; see chapter 3 for more details regarding the current experimental situation.

Note the absence of a suitable partner field N_R for the LH SM neutrinos that would enable a Yukawa interaction with the Higgs field and subsequently a Dirac mass for neutrinos. Various NP models introduce such RH partner fields, called *sterile neutrinos* $N_R \sim (1,1,0)$, some properties of which will be reviewed in section 2.3.1. In addition, in order to give rise to Majorana masses, the object $\overline{L_L^c} L_L + \text{h.c.}$ would need to get contracted into a Lorentz invariant in a suitable manner, which is not possible in the SM on the renormalisable level. Thus, the SM cannot accommodate Majorana masses for neutrinos either, but they are induced by the effective *Weinberg operator* on the non-renormalisable level; see section 2.4.2 for more details.

2.1.4 Global Symmetries

Besides the Yukawa sector, the only instance where fermions enter the SM Lagrangian is the kinetic sector which is described by

$$\mathcal{L}_{\text{kin}} = \sum_{\psi} i\overline{\psi}\gamma^\mu D_\mu \psi \tag{2.34}$$

with the sum running over all fermion species $\psi \in \{Q_L, L_L, u_R, d_R, e_R\}$. In the absence of Yukawa interactions, the SM Lagrangian possesses a large global symmetry [99]

$$G \equiv \left[\mathrm{SU}(3)\right]^5 \times \left[\mathrm{U}(1)\right]^5 \tag{2.35}$$

where the five SU(3) factors are associated with the five different fermion representations, respectively:

$$\mathrm{SU}(3)_Q \times \mathrm{SU}(3)_u \times \mathrm{SU}(3)_d \times \mathrm{SU}(3)_L \times \mathrm{SU}(3)_e \,. \tag{2.36}$$

These groups act on the space of generations, of which there are three for each fermion representation, via unitary matrices. The U(1) factors may be identified in a similar way. In the presence of the Yukawa interactions contained in eq. (2.14), the $\left[\mathrm{SU}(3)\right]^5$ component

	$\mathrm{U}(1)_B$	$\mathrm{U}(1)_L$
Q_{Li}	$\frac{1}{3}$	0
u_{Ri}	$\frac{1}{3}$	0
d_{Ri}	$\frac{1}{3}$	0
L_{Li}	0	1
e_{Ri}	0	1

	$\mathrm{U}(1)_e$	$\mathrm{U}(1)_\mu$	$\mathrm{U}(1)_\tau$
$L_{Le} = (\nu_{Le}, e_L)$	1	0	0
$L_{L\mu} = (\nu_{L\mu}, \mu_L)$	0	1	0
$L_{L\tau} = (\nu_{L\tau}, \tau_L)$	0	0	1
e_R	1	0	0
μ_R	0	1	0
τ_R	0	0	1

Table 2.3: Left: Charges of SM fermions under baryon and lepton number, respectively. Right: Charges of SM leptons under electron number, muon number and tau number, respectively.

of G is completely broken, and the remaining intact symmetry is conventionally expressed as in

$$\mathrm{U}(1)_B \times \mathrm{U}(1)_e \times \mathrm{U}(1)_\mu \times \mathrm{U}(1)_\tau \,. \tag{2.37}$$

Here, $\mathrm{U}(1)_B$ stands for *baryon number*, for which the conventional assignment of charges to the SM fermions is summarised in table 2.3, together with those for *lepton number* denoted by $\mathrm{U}(1)_L$. The three factors $\mathrm{U}(1)_e \times \mathrm{U}(1)_\mu \times \mathrm{U}(1)_\tau$ may be referred to as electron number, muon number and tau number, respectively, with the charge assignment to the SM leptons contained on the right-hand side in table 2.3. A prominent implication of $\mathrm{U}(1)_B$ being conserved is the stability of the proton, that is, decays such as $p \to \overline{e}\pi^0$ are forbidden.[4] As of yet, there is no experimental evidence of $\mathrm{U}(1)_B$ violation, thus it may indeed be an exact symmetry of nature. On the contrary, the occurrence of neutrino oscillations implies that $\mathrm{U}(1)_e \times \mathrm{U}(1)_\mu \times \mathrm{U}(1)_\tau$ can only be approximately realised. Still, the non-observation of charged lepton flavour violating (cLFV) decays such as $\tau \to \mu\gamma$ suggests that it is intact to a large extent [101].

The conservation of baryon number and lepton number in the SM on the classical level is a byproduct of fixing the particle content with its transformation properties under the Lorentz and gauge groups, and the requirement of renormalisability. In that sense, they

---

[4] In fact, only the differences $B/3 - L_i$ where B and L_i are the charges under baryon number and electron, muon or tau number, respectively, are conserved in the SM on the quantum level, which also implies the conservation of $B - L$. However, the rate of the decay of baryons into leptons as mediated by sphalerons is exceedingly tiny at low temperatures [91]. See for instance [100] for a recent discussion.

are widely seen as accidental symmetries. Accordingly, the non-conservation of baryon number and/or lepton number is a generic prediction of physics beyond the Standard Model (BSM). Indeed, if the criterion of renormalisability is relaxed, effective operators composed of SM fields which violate the conservation of lepton number or baryon number emerge already at mass dimension 5 or 6, respectively; see also section 2.4.2.

The invariance of the full SM Lagrangian under G can be formally recovered if one assigns the following transformation properties to the Yukawa couplings:

$$y_u \sim (3, \overline{3}, 1) \text{ under } \mathrm{SU}(3)_Q \times \mathrm{SU}(3)_u \times \mathrm{SU}(3)_d \;, \text{ neutral otherwise,} \tag{2.38}$$

$$y_d \sim (3, 1, \overline{3}) \text{ under } \mathrm{SU}(3)_Q \times \mathrm{SU}(3)_u \times \mathrm{SU}(3)_d \;, \text{ neutral otherwise,} \tag{2.39}$$

$$y_e \sim (3, \overline{3}) \text{ under } \mathrm{SU}(3)_L \times \mathrm{SU}(3)_e \;, \text{ neutral otherwise.} \tag{2.40}$$

In this way, the SM Yukawa matrices are treated as *spurions*, which are typically assumed to be non-dynamical scalar fields. In a broader context, the concept of spurions may be utilised in models which aim to explain specific flavour-dependent hierarchies or interaction patterns via a symmetry which enlarges the SM gauge symmetry at high energies; see also section 2.3.4. In chapter 5, a model which contains several spurion fields is described.

2.1.5 Flavour-Changing Neutral Currents

Contrary to FCCCs, flavour-changing neutral currents (FCNCs) are not induced at tree level in the SM; see for instance ref. [97] for a review. Indeed, gluons and photons are protected from mediating FCNCs at tree level since their respective gauge couplings are by construction flavour-universal, that is, proportional to the unit matrix, which is a basis-independent property. The Higgs-boson couplings are proportional to the respective Yukawa couplings which are diagonal in the charged fermion mass basis, which is the only source of fermion masses in the SM. Lastly, the coupling of the Z boson to any generation of the fermion representations u_{Li}, d_{Li}, e_{Li}, ν_{Li}, u_{Ri}, d_{Ri}, e_{Ri}, is given by $T_{3i} - Q_i \sin\theta_w$. This latter expression is flavour-universal in the SM, effectively implying $T_{3i} = T_3$ and $Q_i = Q$ for all i if a fermion species is fixed, and so the Z-boson couplings remain flavour-universal in the mass basis.

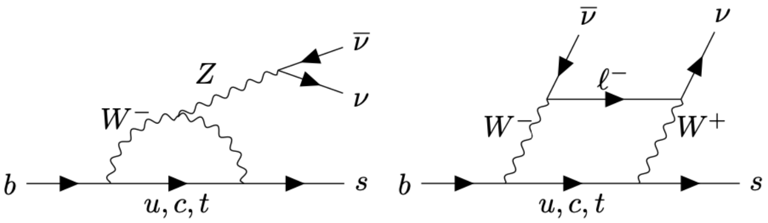

Figure 2.1: Feynman diagrams which mediate the decay process $b \to s\nu\overline{\nu}$ in the SM; taken from ref. [1].

Thus, the SM does not feature a neutral boson which could mediate FCNCs at tree level, but they are induced at loop level. Since only the $W^\pm$ bosons can change fermion flavour, this necessarily involves two $W^\pm$ vertices, and one sums over the flavours of the internal fermion. Figure 2.1 shows two representative one-loop Feynman diagrams which mediate the process $b \to s\nu\overline{\nu}$ process in the SM, a so-called *electroweak penguin diagram* on the left and a *box diagram* on the right. Closely related processes occur due to similar diagrams; one might for instance swap the Z boson on the left-hand side for a hard photon which yields $b \to s\gamma$, or exchange the roles of the charged lepton and the neutrinos on the right-hand side which then corresponds to $b \to s\ell\overline{\ell}$. New mediation mechanisms for both penguin and box diagrams can occur in the presence of NP [102].

In the following, the transition $b \to s$ is specified as it is the most relevant one for this thesis, but similar considerations apply for other FCNC transitions. The amplitude is schematically given as in

$$\mathcal{A}_{b\to s} \sim \sum_{i=u,c,t} V_{ib}^* V_{is} f(x_i), \quad x_i \equiv \frac{m_i^2}{m_W^2} \tag{2.41}$$

with the decay-dependent function $f(x_i)$ [97]. A Taylor expansion yields

$$\mathcal{A}_{b\to s} \sim \sum_{i=u,c,t} V_{ib}^* V_{is} f(0) + \sum_{i=u,c,t} V_{ib}^* V_{is} \frac{m_i^2}{m_W^2} f'(0) \tag{2.42}$$

to leading order (LO) and next-to-leading order. Since $f(0)$ is flavour-independent, the first term is zero by unitarity of the CKM matrix, and the largest non-vanishing term is suppressed by the ratio m_i^2/m_W^2, which is the essence of the Glashow-Iliopoulos-Maiani (GIM) mechanism. Generically, CKM suppression occurs as well, since the product $V_{ib}^* V_{is}$ necessarily involves at least one off-diagonal element. Note that the amplitude would immediately vanish if the internal quark masses were degenerate. Furthermore, if the top-quark contribution dominates the process, GIM suppression is obviously not efficient.

Together with the generic loop-suppression factor $1/(16\pi^2)$, CKM suppression and GIM suppression imply that the SM predicts the rates of FCNC processes to be quite small. So far, no conclusive deviation from this prediction has been observed. Since NP does not have to be subject to any of those suppression mechanisms, there is arguably a good chance for it to be detected in FCNCs, whereas it might be easily swamped in other processes to which the SM contribution is not suppressed. Thus, a precise understanding of how NP could manifest in FCNCs is indicated. In this context, chapter 4 contains a model-independent study of NP which resides at or above the electroweak scale and contributes to $b \to s$ processes with two neutrinos in the final state; see also section 2.2.2.

2.1.6 Low-Energy QCD

In the SM, quantum chromodynamics (QCD) is described in terms of a non-abelian gauge theory governed by the group $\mathrm{SU}(3)_c$ which is coupled to the six different quark flavours u, d, c, s, t and b. The subscript c stands for colour. The associated gauge bosons, called gluons, transform non-trivially under $\mathrm{SU}(3)_c$, thus they undergo self-interactions and source the colour field themselves.

QCD behaves very differently at energies close to or above the electroweak scale, and at lower energies, which is quantitatively captured in terms of *renormalisation group* (RG) running. A straightforward way to appreciate the notion of RG running is to note the appearance of a parameter μ in dimensional regularisation, which arises from the requirement that the coupling parameter of a marginal operator retains a vanishing mass dimension also for a space-time dimension $d \neq 3 + 1$ [95]. In the renormalisation scheme of minimal subtraction, quantities such as couplings and masses or, more generally, Wilson coefficients (WCs) will generally depend on the arbitrary scale μ. Heuristically, the requirement that physical observables do not depend on μ yields the so-called RG equations (RGEs). In practice, incorporating RG running typically implies taking into account the renormalisation of the coupling of a gauge boson to the relevant fermion current. The resulting equations then involve so-called β *functions*

$$\beta(g) \equiv \mu \frac{\mathrm{d}g}{\mathrm{d}\mu} \tag{2.43}$$

which depend on the number of particles charged under g. Specifically, in QCD one finds at the level of one loop

$$\alpha_s(\mu) \equiv \frac{g_s^2(\mu)}{4\pi} = \frac{2\pi}{7} \frac{1}{\ln\left(\frac{\mu}{\Lambda_{\mathrm{QCD}}}\right)} \, . \tag{2.44}$$

Here, the subscript s stands for "strong", and the scale Λ_{QCD} marks the occurrence of the Landau pole in QCD where the coupling formally diverges. Higher-order calculations and measurements of α_s at larger energies indicate $\Lambda_{\mathrm{QCD}} \approx 200$ MeV. Still, one finds $\alpha_s(\mu) \gtrsim \mathcal{O}(1)$ already at energies $E \lesssim 1$ GeV, which implies that perturbative QCD is not predictive anymore in this regime. Instead, the strong dynamics at low energies are more appropriately described in terms of hadrons which are bound states consisting of a specific set of constituent quarks and/or antiquarks.

Matrix elements in low-energy QCD cannot be computed directly, but their functional form can be constrained via symmetry considerations [97]. Restricting to the case of two hadrons involved in the transition, one may generically write

$$\langle H_f | \overline{q} \Gamma q' | H_i \rangle \tag{2.45}$$

with the initial and final hadronic state H_i and H_f, respectively. If the latter is given by the vacuum, the process is described in terms of a *decay constant*, and by a *form factor* otherwise. $\overline{q}\Gamma q'$ consists of (a linear combination of) the Lorentz bilinears in section 2.1.1.2. In the case of semileptonic hadron decays which proves most relevant for this thesis, the relevant form factors are typically computed with the help of so-called light-cone sum rules (LCSR) [5, 6, 103, 104] at low invariant mass q^2 of the final-state lepton pair, and with lattice quantum chromodynamics (LQCD) for large q^2 [105–108].

Thus, a concrete evaluation of the above matrix element must be consistent with its symmetry properties, in particular Lorentz symmetry and discrete symmetries like parity which is conserved by QCD. The vacuum is assumed to be parity-even. In the following, the evaluation of the matrix element of the leptonic decay of a pseudo-scalar meson $B_c^- = b\bar{c}$ is sketched.

In the SM, this decay proceeds via an internal $W^\pm$ boson at tree level. The only observable dynamical quantity is the B_c momentum p_μ which is a Lorentz vector, thus one finds

$$\langle 0|\bar{c}\gamma^\mu\gamma_5 b|B_c^-(p)\rangle = -if_{B_c}p^\mu \tag{2.46}$$

where $-i$ is conventional and the proportionality factor is the decay constant f_{B_c}. Note that the vector part $\bar{c}\gamma^\mu b$ does not contribute due to parity. There is a contribution from pseudo-scalar operators as well,

$$\langle 0|\bar{c}\gamma_5 b|B_c^-(p)\rangle = if_{B_c}\frac{m_{B_c}^2}{m_b + m_c} \tag{2.47}$$

where the proportionality factor can be derived from considering the divergence of the axial-vector current and using the Dirac equation since the quark spinors are on shell [97]. The factor $m_{B_c}^2/(m_b + m_c)$ results in an enhancement of the pseudo-scalar contribution ("scalar dominance") which is however not as pronounced for mesons composed of heavy quarks. In addition, note that neither pseudo-scalar nor tensor contributions are induced at tree level in the SM. See section 4.6 for technical details about form factors for B-meson decays.

2.2 Experimental Status and Prospects

In this section, I review the experimental situation regarding neutrino masses as well as other instances of anomalous data in flavour-sensitive observables, together with future prospects.

2.2.1 Neutrino Masses

Neutrinos are arguably the most elusive particles in the SM. Regarding their three flavours, the electron neutrino ν_e was discovered in the 1950s [109, 110], whereas the existence of

ν_μ [111] and ν_τ [112] was established in 1962 and 2001, respectively. The combined work from several collaborations, notably Super-Kamiokande [43] in 1998 and SNO [44, 45] in 2002, culminated in robust evidence for the occurrence of neutrino oscillations and thus the existence of non-zero neutrino masses, indicating the incompleteness of the SM. The results published by KamLAND, T2K and NOvA, see for instance refs. [113–115], among others, add up to a largely consistent picture of neutrino oscillations. See section 3.2.2 for a convenient parametrisation involving the PMNS matrix, and table 3.1 for the fit results published by the NuFit collaboration in July 2020 [38].[5] Future experiments, among them Hyper-Kamiokande [116] and DUNE [117], are in particular projected to significantly improve upon the determination of the CP-violating phase contained in the PMNS matrix.[6]

A possible means to infer an upper bound on the sum of neutrino masses and thus on the mass m_0 of the lightest neutrino is via cosmic surveys. The trajectory of free-streaming neutrinos is not significantly altered when they pass through matter overdensities in the universe, which results in a delayed growth of perturbations at scales smaller than their free-streaming length scale $1/k_{\text{fs}} \sim 100$ Mpc [120]. Thus, neutrinos do not significantly cluster at length scales smaller than $1/k_{\text{fs}}$, but essentially behave as cold dark matter at larger length scales. A larger neutrino mass would imply further suppression of structure growth at smaller scales which can be constrained by observations. Recent results typically indicate $\Sigma \equiv m_1 + m_2 + m_3 \lesssim \mathcal{O}(0.1 - 0.2)$ eV at 95% CL. In chapter 3, the upper bound $m_1 + m_2 + m_3 \lesssim 0.12$ eV reported by the Planck collaboration in 2018 [121] is used.

Next-generation surveys are anticipated to overcome the currently established upper bounds and detect Σ at a level of almost 3σ or better, assuming the minimal scenario of $m_0 = 0$. Deriving a robust and unambiguous cosmological bound on neutrino mass is difficult since its effect is degenerate with other phenomena, such as the suppression of primordial cosmic microwave background (CMB) fluctuations due to reionisation, or potential contributions

---

[5] Note that there has been an update in October 2021.

[6] The main goal of the experiment JUNO is to detect the mass ordering in the neutrino sector [118], but there are proposals according to which it could also help in measuring leptonic CP violation [119] in conjunction with a superconductive cyclotron.

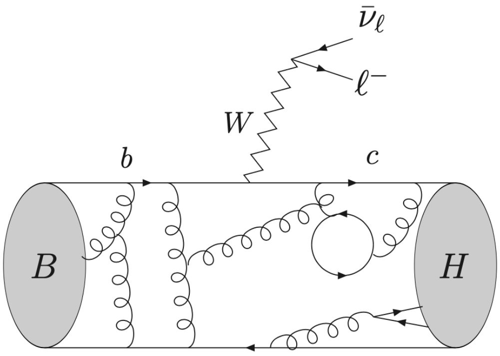

Figure 2.2: Illustration of the semileptonic decay of a B hadron in the SM, from ref. [2].

to the dark-energy equation of state [120]. The tritium-decay experiment KATRIN has already inferred the model-independent bound $\left(\sum_i |U_{ei}|^2 m_i^2\right)^{1/2} \lesssim 0.8$ eV at 90% CL which is projected to get further strengthened to 0.2 eV [122] and will thus be only slightly weaker than the current cosmological one. Furthermore, one can infer an upper bound on the combination $\sum_i U_{ei}^2 m_i^2$ from searches for neutrinoless double beta decay which applies if neutrinos are Majorana particles; see for instance ref. [123] for a recent review.

2.2.2 Lepton Flavour Non-Universality

In the SM, differences in the behaviour of leptons may only arise due to phase-space effects as a consequence of the mass hierarchy in the charged lepton sector, which is referred to as LFU. In particular, gauge bosons couple to all lepton generations with equal strength. Apart from the conclusive establishment of the existence of a non-trivial mass hierarchy in the neutrino sector and of the occurrence of lepton mixing, there is further mounting evidence for deviations from the SM in the form of apparent violations of LFU. In this subsection, I briefly review the current experimental status.

$b \to c$ **transitions.** The transitions $b \to c\ell\overline{\nu}$ where $\ell \in (e, \mu, \tau)$ are of FCCC-type and thus mediated via $W^\pm$ bosons at tree level in the SM; see figure 2.2. Thus, they are in particular not suppressed. As mentioned beforehand, the SM predicts the strength of the coupling of $W^\pm$ bosons to be independent of the involved lepton generation, and it requires the flavours of the final-state charged lepton and neutrino to coincide. The neutrino (and thus also its flavour) is undetected, and so one needs to sum over all three final-state neutrino mass eigenstates, weighted by their overlap with the fixed lepton flavour ℓ as per the PMNS matrix [2]. Since the latter is unitary in the SM extended by three light neutrinos, one finds

$$\sum_{i=1,2,3} |U_{\ell i}|^2 = 1 \tag{2.48}$$

and thus the PMNS matrix plays no role in computations of FCCC processes. Furthermore, the dependence of the amplitude on the CKM-matrix element V_{cb} cancels in the SM if the ratio of the rates involving different charged leptons in the final state is taken. This motivates the consideration of the LFU ratios

$$R(D^{(\star)}) \equiv \frac{\mathrm{BR}(B \to D^{(\star)}\tau\overline{\nu})}{\mathrm{BR}(B \to D^{(\star)}\ell\overline{\nu})} \,, \tag{2.49}$$

where ℓ stands for either an electron or a muon. According to the 2021 results from ref. [10] which incorporates data sets from LHCb [15, 16, 124], Belle [14, 125–127] and BaBar [128, 129], the combined significance of a violation of LFU is about $3\,\sigma$, which sets the ground for chapter 5 wherein a NP model aims to explain this anomaly. Evidence for LFU violation was also found in the $B_c^+ \to J/\psi$ mode [130]. Further quantities of interest are the longitudinal polarisation of the tau lepton [131, 132] and angular distributions in $\overline{B} \to D^\star \ell \overline{\nu}$ transitions [133]. A measurement of the baryonic decay $\Lambda_b^0 \to \Lambda_c^+ \tau \overline{\nu}$ was reported in ref. [134]. Furthermore, the next-generation experiment Belle II is projected to measure $R(D^{(\star)})$ three times more precisely than the current world averages [135].

$b \to s$ transitions. These processes are of FCNC-type, introduced in section 2.1.5, and thus predicted to be suppressed in the SM. The case of two neutrinos in the final state is particularly appealing from a theoretical point of view, since the amplitude can be neatly separated into a hadronic and a leptonic part. In the SM, this decay occurs only if the flavours of the final-state neutrino and antineutrinos match. Furthermore, GIM suppression implies that only the contribution with an internal top quark is relevant, against which the masses of the respective internal charged lepton is negligible in box-diagram contributions. Thus, differences in the decay widths for different flavours of the neutrino-antineutrino pair in the final state are negligible in the SM [136]. This can be seen as an (approximate) manifestation of LFU.

On the experimental side, until very recently, only upper bounds on the branching ratios (BRs) for the decay channel $B \to K^{(\star)}$ plus missing energy existed. Belle II is projected to measure these decays with an uncertainty of only about 10%, based on the full data set which comprises 50 ab^{-1}, if the central values turn out consistent with the respective SM expectation [7]. Furthermore, the process $b \to s\nu\overline{\nu}$ generically also provides a stringent constraint on NP scenarios which aim to explain the anomalous data in $b \to c$ processes, as is the case in chapter 5.

For completeness, the case of charged leptons in the final state is also commented on. Several experiments at LHCb [137–140] and Belle [141, 142] have revealed evidence for deviations from LFU in $b \to s\ell\overline{\ell}$ transitions, notably in the ratio

$$R_{K^{(\star)}} \equiv \frac{\mathrm{BR}(B \to K^{(\star)}\mu\overline{\mu})}{\mathrm{BR}(B \to K^{(\star)}e\overline{e})} \tag{2.50}$$

which is predicted to be equal to 1 in the SM with an uncertainty of less than 1%. The most recent result reports a 3.1σ deviation from the SM in the interval $1.1 < q^2/\mathrm{GeV}^2 < 6$ [139] where q^2 is the invariant mass of the lepton pair.

Magnetic moment of the muon. The so-called gyromagnetic ratio or g-factor parametrises the coupling of a charged fermion to an external magnetic field. The Dirac equation predicts $g = 2$, but one finds $g \neq 2$ due to radiative corrections and thus typically refers to the anomalous magnetic moment (AMM) $a_i \equiv (g-2)_i/2$ with i indicating the fermion under consideration. In quantum electrodynamics (QED), one considers the vertex of a photon of momentum p_μ coupling to an on-shell spinor current (see e.g. refs. [143, 144])

$$\langle p_1|j^\mu(0)|p_2\rangle = \overline{u}(\mathbf{p_1})\left[F_1(q^2)\gamma^\mu + F_2(q^2)\frac{i\sigma^{\mu\nu}}{2m}q_\nu + F_3(q^2)\frac{\sigma^{\mu\nu}}{2m}\gamma_5 q_\nu\right]u(\mathbf{p_2}) \tag{2.51}$$

with the momentum transfer $q^\mu \equiv p_1^\mu - p_2^\mu$. For $q^2 = 0$, one may identify the three form factors with the electric charge $eF_1(0)$, the AMM $a = F_2(0)$, and the electric dipole moment (EDM) $d = -eF_3(0)/2m$, respectively.

The Run-1 results of the $g-2$ experiment at Fermilab [18] are in good agreement with the earlier results obtained at BNL [46] and established a $4.2\,\sigma$ discrepancy with the recommended value for the SM prediction for a_μ [19], that is, $\Delta a_\mu \equiv a_\mu^{\text{exp}} - a_\mu^{\text{SM}} = (2.51 \pm 0.59) \times 10^{-9}$. Improving the precision of the latter is in particular contingent on properly determining the contribution from the hadronic vacuum polarisation (HVP) which is the subject of continuing efforts. Recently, several groups have reported results from lattice studies [145–148] which would significantly reduce the tension with experimental data, and thus challenge the results for the LO HVP obtained from the total cross section for the process $e\bar{e} \to$ hadrons via a dispersion relation. Nonetheless, the tension between experimental data and the SM prediction for a_μ makes a compelling case for the existence of BSM physics sensitive to lepton flavour. There is also evidence for a non-zero Δa_e, but the results of extractions of the electromagnetic fine-structure constant from caesium [149] and rubidium atoms [150] do not agree within the reported uncertainties, thus a further clarification of the experimental situation is indicated in this case.

Unitarity of the CKM matrix. In the SM, the CKM matrix is unitary by construction; see also section 2.1.3. In recent years, testing this premise against experiment has attracted attention in particular for the case of the first row, that is, the assumption that

$$\sum_i |V_{ui}|^2 = |V_{ud}|^2 + |V_{us}|^2 + |V_{ub}|^2 \tag{2.52}$$

adds up to one. In practice, this requires the comparison of independently inferred results for $|V_{ud}|$ and $|V_{us}|$, with the numerical value of the latter being approximately coincident with the (sine of the) Cabibbo angle θ_{12} which parametrises the mixing between the first two generations of quarks. This may be done via considering different decay processes, the results of which seem to not entirely agree and constitute the so-called *Cabibbo angle anomaly* (CAA); see for instance [151] for a recent review. A possible source of the anomaly are modifications of the Fermi constant G_F due to NP. G_F can be inferred indirectly, for instance via global fits [152], but is importantly also directly extracted from muon decay. Contributions to the latter imply a deviation from LFU in the leptonic gauge couplings. See chapter 3 for further information and a possible realisation of this scenario.

2.3 New-Physics Models

In the following, several concrete extensions of the SM in terms of new particles which are relevant for this thesis are reviewed.

2.3.1 Sterile Neutrinos

Sterile neutrinos are a very well-motivated extension of the SM; see for instance refs. [153–155] for reviews. Their presence would fix up the apparent asymmetry between the quark sector and the lepton sector in the sense that they would provide a Dirac partner for the active LH SM neutrinos. A sterile neutrino or RH neutral fermion singlet is a field $N_R \sim (1, 1, 0)$, where "sterile" refers to the fact that this particle does not participate in SM gauge interactions. The Yukawa sector as described in eq. 2.14 gets extended by the term

$$\mathcal{L}^{\nu}_{\text{Yuk}} = -y^{ij}_{\nu} \overline{L_{Li}} \epsilon H^* N_{Rj} + \text{h.c.} \tag{2.53}$$

which is the only renormalisable coupling between sterile neutrinos and SM particles. Upon the acquisition of a non-zero VEV by the Higgs doublet, the neutrinos would receive a Dirac mass in the same way the charged fermions in the SM do. Thereby, neutrinos and up-type quarks would formally be treated on similar footing. A non-zero Yukawa interaction induces mass mixing between the active SM neutrinos and sterile neutrinos, which is however relatively stringently constrained. Moreover, since N_R is sterile, the Majorana mass term

$$m^{ij}_N \overline{N^c_{Ri}} N_{Rj} + \text{h.c.} \tag{2.54}$$

is trivially compatible with the SM gauge symmetry. In the minimal scenario of extending the SM by sterile neutrinos, the Majorana mass term is the only source of lepton-number breaking, and a small m_N would thus be technically natural. Still, since the Majorana mass is not necessarily related to any other SM scale, it may also be very large. The case $m_N \gg v$ implies the compelling seesaw scenario in which the scale of the small active neutrino masses is induced as per $m_\nu \sim (v\, y_\nu)^2/m_N$, which naïvely implies $m_N \sim 10^{15}$

GeV if the couplings y_ν^{ij} are $\mathcal{O}(1)$ numbers. In this case, a description in terms of the effective Weinberg operator applies; see section 2.4.2.

Another viable reason to assume the existence of sterile neutrinos is due to their prominent role in scenarios of leptogenesis, which rather motivates a mass scale around $m_N \sim 10^{10}$ GeV. Heavy sterile neutrinos may undergo out-of-equilibrium decay in the early universe, thereby generating a lepton-number asymmetry which can be transferred into a baryon-number asymmetry via sphalerons [156]. Much lighter sterile neutrinos with masses in the keV range represent an attractive candidate for warm dark matter. Lastly, eV-scale sterile neutrinos have been proposed to ameliorate several short-baseline anomalies, which is however problematic in the light of results from MicroBooNE, see e.g. refs. [157, 158], as well as cosmological constraints, as is reviewed for instance in ref. [159]. Since the number of generations of sterile neutrinos is not constrained a priori, they could also exist with largely different mass scales. In addition, the presence of three sterile neutrinos is required in scenarios in which $B - L$ is promoted to a gauge symmetry due to anomaly cancellation [95].

2.3.2 Leptoquarks

As their name suggests, LQs directly couple quarks to leptons, thus they may be either scalar or vector particles. The SM Yukawa couplings strictly separate the quark and lepton sectors. For both scalar and vector LQ, respectively, only a small number of representations under the SM gauge group exist which allow for renormalisable couplings to SM fermions [160]. A gauge-invariant description of massive vector bosons requires an adequate enlargement of the SM gauge group, which implies that minimal extensions of the SM by a single vector LQ are not predictive per se. Hence, vector LQs will not be discussed further.

The six representations of scalar LQs under the SM gauge group and the allowed renormalisable interactions with matter fields are given in Table 2.4. Note the appearance of diquark operators in the presence of both the weak singlet LQs and the weak triplet S_3.

	Gauge Representation	Renormalisable Matter Couplings
S_1	$(\overline{3}, 1, \frac{1}{3})$	$\overline{L^c_L} Q_L S_1 + \overline{e^c_R} u_R S_1 + \overline{Q_L} Q^c_L S_1 + \overline{u_R} d^c_R S_1$
$\tilde{S}_1$	$(\overline{3}, 1, \frac{4}{3})$	$\overline{e^c_R} d_R \tilde{S}_1 + \overline{u_R} u^c_R \tilde{S}_1$
$\bar{S}_1$	$(\overline{3}, 1, -\frac{2}{3})$	$\overline{d_R} d^c_R \bar{S}_1$
R_2	$(3, 2, \frac{7}{6})$	$\overline{e^c_R} Q^c_L R_2 + \overline{u_R} L_L R_2$
$\tilde{R}_2$	$(3, 2, \frac{1}{6})$	$\overline{d_R} L_L \tilde{R}_2$
S_3	$(\overline{3}, 3, \frac{1}{3})$	$\overline{L^c_L} Q_L S_3 + \overline{Q_L} Q^c_L S_3$

Table 2.4: The six scalar LQ representations under the SM gauge group which admit renormalisable couplings to SM fermions. The individual coupling matrices are omitted for brevity, generation indices are suppressed and the hermitian-conjugate operators are understood to be added. The LQs S_1, $\bar{S}_1$ and $\tilde{R}_2$ may also feature renormalisable interactions with sterile neutrinos if those are introduced.

Combinations of diquark and Yukawa-like LQ couplings must be sufficiently constrained in order not to give rise to large rates of proton decay. LQs are generically also expected to couple to the SM Higgs boson and gauge bosons. They are appealing candidates for an explanation of the anomalous data on $b \to s\ell\bar{\ell}$ and $b \to c\ell\bar{\nu}$ processes, see section 2.2.2, since they do not contribute to meson mixing at tree level [3]:

- S_1 is well suited to explain the $b \to c\ell\bar{\nu}$ anomalies via tree-level contributions which sets the ground for chapter 5, whereas $b \to s\ell\bar{\ell}$ transitions are only sourced at one-loop level.
- S_3 induces both $b \to s\ell\bar{\ell}$ and $b \to c\ell\bar{\nu}$ transitions at tree level, but it can explain the anomalous data only in the former case [161, 162].
- R_2 can explain the anomalies in $b \to s\mu\bar{\mu}$ via loop-level contributions if the tree-level processes are switched off. A tree-level explanation of the $b \to c\ell\bar{\nu}$ data by R_2 is also possible, but incompatible with the aforementioned scenario.[7]

---

[7] A different avenue was followed in ref. [163] where R_2 was shown to allow for an explanation of the anomaly in $R_{K^{(\star)}}$ due to a tree-level contribution to $b \to se\bar{e}$, compatible with a simultaneous explanation of $R(D^{(\star)})$. Nonetheless, this (minimal) scenario bars the amelioration of anomalous data in other $b \to s\mu\bar{\mu}$ processes and predicts a largish BR for the process $B_c \to \tau\bar{\nu}$.

2.3.3 Colourless Charged Scalars

The only physical scalar particle in the SM is the CP-even neutral Higgs boson. Still, the existence of further scalar particles is well-motivated due to conceptual difficulties of the SM scalar sector, such as the apparent meta-stability of the electroweak vacuum, see for instance refs. [164, 165] for reviews, or the absence of a phase transition in the early universe which is strongly first-order [166]. Of particular relevance for this thesis is the singly-charged scalar singlet $h \sim (1, 1, 1)$. This field has the appealing property that its only renormalisable coupling to SM fermions is given by

$$\mathcal{L}_{\text{Yuk}} = y_h^{ij} \overline{L^c_{Li}} L_{Lj} h + \text{h.c.} \tag{2.55}$$

where the matrix y_h is antisymmetric in flavour space. Thus, y_h only contains three free parameters, which renders this SM extension very predictive. If supplemented with a source of lepton-number violation, h can induce Majorana masses for neutrinos. A comprehensive model-independent study of this scenario is presented in chapter 3.[8] In the following, a few explicit models featuring h are briefly reviewed. See ref. [50] for a very comprehensive overview over radiative neutrino mass models.

Zee Model. A simple radiative neutrino mass model is given by the Zee model [60] which enlarges the SM particle content by a second Higgs doublet Φ and a singly-charged scalar singlet h. It is customary to adopt the so-called Higgs basis [167] in which the Higgs doublets are parametrised as in

$$H = \begin{pmatrix} \eta^+ \\ \frac{1}{\sqrt{2}}(v + h + i\eta^0) \end{pmatrix} , \qquad \Phi = \begin{pmatrix} \xi^+ \\ \frac{1}{\sqrt{2}}(\phi' + iA) \end{pmatrix} . \tag{2.56}$$

Here, η^+ and η^0 are the Goldstone bosons, h and ϕ' are CP-even neutral scalars, A is a CP-odd neutral scalar and ξ^+ is a singly-charged scalar.[9] The lepton Yukawa sector of

---

[8] Therein, two-component spinors are employed, so that the above Yukawa coupling reads $L_L L_L h$ + h.c.. Furthermore, a different sign convention is used for the Yukawa sector in general.

[9] Writing h for both the CP-even neutral Higgs boson and the singly-charged scalar singlet may be seen as undesirable clash of notation. Still, in order to maintain consistency

the theory is enlarged to

$$\mathcal{L}_{\text{Yuk,lept}} = -y_e^{ij}\overline{L_{Li}}He_{Rj} - y_{e,\Phi}^{ij}\overline{L_{Li}}\Phi e_{Rj} - y_h^{ij}\overline{L^c_{Li}}L_{Lj}h + \text{h.c.}\,. \tag{2.57}$$

The breaking of lepton-number conservation is contingent on the simultaneous presence of these three couplings as well as the tri-linear term $H\Phi h^* + \text{h.c.}$. In this way, Majorana masses for neutrinos are induced at one-loop level. The Zee model is a realisation of a class of models dubbed the *linear case* which is introduced and studied in section 3.

Zee-Babu Model. Another simple radiative neutrino mass model is given by the Zee-Babu model [63–65] which enlarges the SM particle content by a singly-charged scalar singlet $h \sim (1,1,1)$ and a doubly-charged scalar singlet $k \sim (1,1,2)$. The lepton Yukawa sector of the theory is enlarged to

$$\mathcal{L}_{\text{Yuk,lept}} = -y_e^{ij}\overline{L_{Li}}He_{Rj} - y_h^{ij}\overline{L^c_{Li}}L_{Lj}h - y_k^{ij}\overline{e^c_{Ri}}e_{Rj}k + \text{h.c.}\,. \tag{2.58}$$

Then, lepton-number conservation is violated if the tri-linear term $h^2k^* + \text{h.c.}$ is present as well, and Majorana masses for neutrinos are induced at two-loop level. In section 3, the Zee-Babu model is identified as a realisation of a class of models dubbed the *quadratic case*.

Krauss-Nasri-Trodden Model. The Krauss-Nasri-Trodden model (KNT) model [66] extends the SM particle content by two singly-charged scalar singlets h_1 and h_2 and a neutral fermion singlet $N_R \sim (1,1,0)$. The lepton Yukawa sector of the theory is enlarged to

$$\mathcal{L}_{\text{Yuk,lept}} = -y_e^{ij}\overline{L_{Li}}He_{Rj} - y_h^{ij}\overline{L^c_{Li}}L_{Lj}h - y_{Nh}^{i}\overline{N^c_R}e_{Ri}h_2 + \text{h.c.}\,. \tag{2.59}$$

Note that both h_2 and N_R are assumed to be odd under a Z_2 symmetry, in order to prevent the canonical type-I seesaw mechanism from becoming effective. Together with the Majorana mass term $m_N\overline{N^c_R}N_R + \text{h.c.}$ violating the conservation of lepton number

---

with chapter 3, I opt not to change the conventions at this point, and note that from the context it should be clear which particle is referred to.

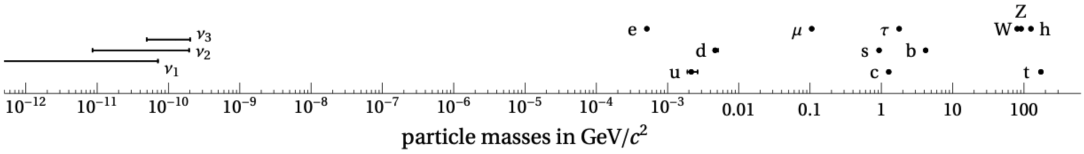

Figure 2.3: Masses of the SM particles, represented on a logarithmic scale; taken from ref. [3].

and the scalar-potential term $(h_1 h_2^*)^2$ + h.c., Majorana masses for neutrinos appear at three-loop level. Furthermore, if N_R is lighter than the singly-charged scalar singlets, it can be a viable candidate for dark matter since it is stable as a result of the unbroken Z_2 symmetry. The KNT model is a further example of the quadratic case.

2.3.4 Flavour Symmetries

Lastly, a brief introduction to the concept of *flavour symmetries* is given. This does not refer to the extension of the SM by a specific particle, but rather provides a framework for predicting the interaction structure of a model via the assignment of the particle content to representations under a specific symmetry group, or products thereof.

Symmetries have proven a most elegant and successful concept in different fields of physics. Via the Lorentz and gauge groups, they give rise to the structure of the SM. Thus, it might appear reasonable to assume that the flavour structure of nature is also dictated in terms of a symmetry. The different masses in all respective charged fermion sectors, especially for the up-type quarks, display a hierarchical pattern; see figure 2.3 for an illustration on a logarithmic scale.

This suggests the existence of a (spontaneously broken) flavour symmetry which extends the SM gauge group and under which fermions of different generations carry in general different charges. Arguably, the simplest case is given by *Froggatt-Nielsen* models [168] which employ a U(1) symmetry and typically feature a SM singlet scalar ϕ and heavy vector-like fermions [3]. One may then assign -1 unit of the U(1) charge to ϕ and assume that it condenses at a high scale. Thus, ϕ takes up the role of a spurion field; see also section 2.1.4. At low energies, the elements of the SM Yukawa matrices will then schematically scale as

$$y^{ij} \sim \left(\frac{\langle \phi \rangle}{m_\Psi} \right)^{|n_{ij}|} \tag{2.60}$$

where m_Ψ is a large vector-like fermion mass and n_{ij} is the (added) U(1) charge of a SM Yukawa operator, say $\overline{L_{Li}} H e_{Rj}$. If $\langle \phi \rangle / m_\Psi < 1$, a larger $|n_{ij}|$ will imply a larger suppression of the coefficient of the respective Yukawa operator. In general, both the radial mode and the modulus of ϕ can give rise to constraints. If U(1) is a global symmetry, the modulus is a (pseudo-)Goldstone boson and may help solve the strong CP problem or provide a viable dark matter candidate [169–174].

A viable alternative to U(1) is given by non-abelian symmetry groups. For instance, U(2) provides a natural framework to unify the first two generations in the quark sector, respectively, in the fundamental (2-dimensional) representation, which might be beneficial since the mixing among either of the first two generations and the third one is suppressed. In addition, the presence of two large mixing angles in the lepton sector motivates a symmetry group which admits three-dimensional irreducible representations. Moreover, note that the appearance of Goldstone modes as a result of spontaneous symmetry breaking can be naturally avoided if discrete symmetries are utilised instead of continuous ones; see refs. [175–178] for reviews. Still, the spontaneous breaking of discrete symmetries can result in the formation of domain walls [179]. Another approach related to flavour symmetries is based on so-called modular forms which were first utilised in ref. [180] for model building in the context of neutrino masses.

2.4 Effective Field Theory

The capability of quantum field theories to yield predictions of astonishing precision is inherently connected to the premise of taking into account the effect of each and every particle on an intermediate, that is, virtual level. Thus, the final result will in general depend on a variety of (mass) scales of potentially largely different numerical values [29]. Efforts to reduce this complexity are pursued within the framework of EFTs.

2.4.1 Technical Aspects

The first step in constructing an EFT typically consists of identifying the relevant degrees of freedom in the theory. In the simplest case, this implies a separation of the theory spectrum into light states, here collectively denoted by ϕ, and heavy states Φ. The latter cannot be produced at the energies which are probed by experiments relevant for the problem under consideration. In a path-integral context, *integrating out* the heavy states then schematically implies

$$\int \mathcal{D}\phi\,\mathcal{D}\Phi\, e^{iS_{\text{full}}[\phi,\Phi]} = \int \mathcal{D}\phi\, e^{iS_{\text{eff}}[\phi]}\,. \tag{2.61}$$

Here, the effective theory described by S_{eff} only contains the lighter states ϕ. Its Lagrangian formally reads

$$\mathcal{L}_{\text{eff}} = \mathcal{L}_{d\leq 4} + \sum_i \frac{O_i}{\Lambda^{d_{O_i}-4}} \tag{2.62}$$

where the sum contains local non-renormalisable operators O_i of dimension d_{O_i}. Locality implies that all fields contained in an operator are evaluated at the same space-time point. In the case of weakly interacting theories considered here, the coefficients of operators with larger d_{O_i} will be further suppressed, which provides a simple example of power counting. The set of operators contained in the (a priori infinite) sum above may be further restricted, for instance upon the imposition of a symmetry, or simply by fixing the precision to which a specific observable needs to be computed.

At energy scales $E \lesssim \Lambda$, the effective theory is predictive and equivalent to the full theory described by S_{full} above. The effects of the heavier states Φ are entirely captured via the WCs of the non-renormalisable operators O_i composed of ϕ and momentum insertions. The technical procedure of achieving this is known as *matching*, for which a simple explicit example drawn from section 2.1 in ref. [4] will be provided in the following.

Consider a toy theory describing a massless fermion ψ and a heavy (real) scalar Φ:

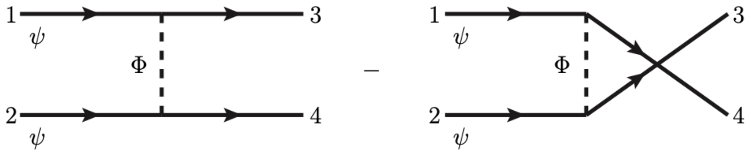

Figure 2.4: Tree-level contributions to 2 → 2 scattering in a toy theory; taken from ref. [4].

$$\mathcal{L}_{\text{full}} = i\overline{\psi}\gamma^\mu\partial_\mu\psi - \frac{1}{2}\Phi(\Box + M^2)\Phi - \lambda\overline{\psi}\psi\Phi\ . \tag{2.63}$$

There are two diagrams which contribute to the scattering process $\psi\psi \to \psi\psi$ at tree-level; see figure 2.4. This yields the amplitude

$$\mathcal{M} = \overline{u}(p_3)u(p_1)\overline{u}(p_4)u(p_2)(-i\lambda)^2\frac{i}{(p_3-p_1)^2 - M^2} - (3 \leftrightarrow 4) \tag{2.64}$$

where the indices 1,2 (3,4) label the incoming (outgoing) particles. Expanding the propagator in the ratio p^2/M^2, one finds

$$\frac{i}{(p_3-p_1)^2 - M^2} = \frac{i}{M^2}\frac{1}{1-\frac{(p_3-p_1)^2}{M^2}} \approx \frac{i}{M^2}\left(1 + \frac{(p_3-p_1)^2}{M^2} + \mathcal{O}(p^4/M^4)\right)\ . \tag{2.65}$$

If one instead considers the theory containing only the massless fermion, the lowest-order terms in the pertinent Lagrangian read

$$\mathcal{L}_{\text{eff}} = i\overline{\psi}\sigma^\mu\partial_\mu\psi + \frac{c}{2}\overline{\psi}\psi\overline{\psi}\psi \tag{2.66}$$

from which one obtains for the scattering amplitude

$$\mathcal{M} = \overline{u}(p_3)u(p_1)\overline{u}(p_4)u(p_2)(ic) - (3 \leftrightarrow 4)\ . \tag{2.67}$$

Now, matching dictates that the effective theory is equivalent to the full theory up to some order in the expansion parameters, given by λ and the ratio p^2/M^2 in this case. At the lowest possible order, that is, at tree level and vanishing external momenta, one thus finds

$$c = \frac{\lambda^2}{M^2}\ . \tag{2.68}$$

Note that the set of all operators in an EFT (say, up to a fixed mass dimension) is generally not unique, since some operators can be expressed as linear combinations of others upon the application of field redefinitions, Fierz identities, integration by parts or other transformations. Importantly, redundant operators may occur due to off-shell matching to the EFT, and then vanish on-shell, that is, if the equations of motion are invoked; see for instance refs. [4, 181].

On a more formal level, the difference between renormalisable and non-renormalisable theories consists in the fact that the UV divergences appearing in the latter cannot be removed with a finite number of counterterms [95]. Still, as mentioned above already, higher-dimensional (counter)terms are suppressed by more powers of the cutoff scale Λ, and thus non-renormalisable theories are perfectly predictive at sufficiently low energies. Moreover, the formal consistency of renormalisable theories may also be challengeable, for instance regarding the occurrence of Landau poles as in QED.

In the remainder of this section, several examples of EFTs will be introduced.

2.4.2 SMEFT

As the name suggests, *Standard Model Effective Field Theory* (SMEFT) arises from taking the particle content of the complete SM as it is and promoting it to an EFT, that is, dropping the requirement of renormalisability. It is a widely accepted view that the SM should only be regarded as the low-energy effective version of a more complete theory. This is indicated by several shortcomings, for instance its incapability to accommodate inflation [182, 183] or baryogenesis [184], among other phenomena. Lastly, gravitational effects become relevant around the Planck scale which signals the need to UV-complete the SM into a theory which incorporates the assumed quantum nature of gravity. SMEFT is invariant under the full SM gauge group $\mathrm{SU}(3)_c \times \mathrm{SU}(2)_w \times \mathrm{U}(1)_Y$.

At dimension 5, SMEFT features the unique Lorentz- and gauge-invariant Weinberg operator [47]

$$\frac{c^{ij}}{\Lambda}\overline{L^c_{Li}}\epsilon H H \epsilon L_{Lj} + \text{h.c.}\ . \tag{2.69}$$

which gives rise to small Majorana masses upon the acquisition of a non-zero VEV by the Higgs doublet in a gauge-invariant manner. This appearance of Majorana neutrino masses at the lowest non-renormalisable level of SMEFT is not a proof for the Majorana nature of neutrino masses, albeit a very appealing and suggestive hint towards it. If neutrino masses can indeed be described via the Weinberg operator, their smallness implies that the associated scale Λ may be very large, potentially close to the scale of grand unified theories (GUTs), thus $\Lambda \sim 10^{15}$ GeV if $c^{ij} \sim O(1)$. This large suppression is unproblematic from an experimental point of view, since there is no further evidence of lepton-number violation so far. Note that in order to accommodate neutrino oscillations, the Weinberg operator also necessarily breaks the accidental global symmetry $\mathrm{U}(1)_e \times \mathrm{U}(1)_\mu \times \mathrm{U}(1)_\tau$ which is intact in the SM; see section 2.1.4.

A complete basis of SMEFT operators at dimension 6, commonly referred to as the Warsaw basis, was first presented in ref. [185]. The dimension of a SM operator is even (odd) if $(\Delta B - \Delta L)/2$ is even (odd), as it was shown in ref. [186]. Thus, dimension-6 operators with $\Delta B - \Delta L = 0$ can be grouped into two categories:

- Operators like $\left(\overline{L_{Li}}\gamma^\mu L_{Lj}\right)\left(\overline{Q_{Lk}}\gamma_\mu Q_{Ll}\right)$ which individually conserve both B and L. They may be generated at a comparatively low scale.
- Operators like $\left(\overline{Q^c_{Li}}Q_{Lj}\right)\left(\overline{Q^c_{Lk}}L_{Ll}\right) + \text{h.c.}$ which individually violate both B and L. Since there is no evidence of baryon number not being intact in nature so far, naïvely they can be expected to be very suppressed.

Lastly, I note that extending the particle content of SMEFT by including sterile neutrinos results in a theory which is commonly referred to as SMNEFT or νSMEFT [187–191].

2.4.3 LEFT

If the scales relevant for a particular process are substantially smaller than the electroweak scale, the heavier SM particles, that is, the $W^\pm$ bosons, the Z boson, the h boson and the top quark cannot be produced on shell and thus effectively play no role for the dynamics under consideration. Importantly, this is typically the case for observables which are utilised to accurately determine the flavour structure of the SM and constrain possible extensions. The theory which results from integrating out the aforementioned particles from SMEFT is commonly referred to as *Low-Energy Effective Field Theory* (LEFT), with a comprehensive description and analysis first provided by Jenkins, Manohar and Stoffer in ref. [192]. Regarding its physical content, it may be viewed as a systematised version of Fermi theory.

The lowest-dimensional operators in LEFT are Majorana mass terms for neutrinos at dimension 3, and dipole operators for quarks, charged leptons and neutrinos at dimension 5. Sterile neutrinos can be readily accounted for in LEFT by describing them in terms of the charge-conjugate of LH neutrinos and extending the number of generations beyond three, that is, by writing $\nu_{Li}^c \equiv C\overline{\nu_{Li}}^T$ with $i = 1, 2, 3, 4, ...$ This yields a theory commonly referred to as LNEFT or νLEFT.

The complete operator basis for LEFT with the three active SM neutrinos ν_{Li} explicitly distinguished from (an arbitrary number of) sterile neutrinos N_{Rj} has been presented in refs. [190, 191]. Since LEFT is governed by the gauge group $\mathrm{SU}(3)_c \times \mathrm{U}(1)_{\mathrm{EM}}$ associated with QCD and QED, respectively, with the latter being weakly coupled at all accessible energies, only accounting for one-loop RG running under QCD is a reasonable approximation which is adopted in chapter 4 and 5. Since the bottom quark is the heaviest (coloured) particle contained in LEFT, no threshold effects need to be accounted for when performing QCD running from the electroweak scale down to scales relevant for B-meson physics. See section 4.2 for more details.

2.4.4 HQET

Because of the pronounced hierarchy of their masses, quarks of different flavours are studied with the help of conceptually different techniques. The masses of the lightest quarks, that is, the up, down and strange quark are small compared to Λ_{QCD}. They are described within chiral perturbation theory which effectively operates around the $m_q = 0$ limit and yields reliable results at energies $E \lesssim 1$ GeV; see for instance refs. [193–195]. At the other end of the spectrum, the top quark can efficiently be studied within perturbative QCD, since $\alpha_s(m_t)$ is small. Lastly, the charm and bottom quarks take up intermediate roles, since they hadronise unlike the top, but are heavy compared to Λ_{QCD}. Thus, the scale separation $\Lambda_{\text{QCD}} \ll m_{c,b}$ indicates the possibility of efficiently studying the properties of B and D mesons within *Heavy-Quark Effective Theory* (HQET) which formalises an expansion in the ratio Λ_{QCD}/m_q for $q = c, b$. In mesons comprising a heavy quark and a light quark, such as $B^- = b\overline{u}$ or $B^0 = d\bar{b}$, the heavy quark may to LO qualitatively be seen as a static source of gluons [95].

An aspect of HQET which is particularly relevant for this thesis is its application to inclusive hadron decays. If the initial-state hadron is constituted by a heavy quark and a light quark, the expansion in Λ_{QCD}/m_q is predictive, and the inclusiveness of the decay erases the dependence on a specific final state. The notion of *quark-hadron duality* implies that upon integrating out a sufficiently large portion of the phase space, the decay process of the hadron becomes calculable in QCD [29, 97]. For more technical details, see section 4.3.3.

Chapter 3

The Singly-Charged Scalar Singlet as the Origin of Neutrino Masses

In this chapter I study a scenario in which the main contribution to Majorana neutrino masses originates from the coupling of two LH lepton doublets to a singly-charged scalar singlet h. The analysis is performed in the context of a "simplified model" as laid out in ref. [59], that is, the SM is not further extended than by h, and I remain agnostic about the source of lepton-number violation. Thereby, the approach followed in this chapter proceeds along a partly model-independent line. Sections 3.1 to 3.10 are a verbatim adoption of the publication [87]. Section 3.11 is a verbatim adoption of the published erratum [88] to the aforementioned publication.

3.1 Introduction

The Standard Model (SM) of particle physics has been extraordinarily successful. It describes all observed fundamental particles and their gauge interactions and accounts for the masses of the charged fermions. However, the picture painted by the SM is incomplete since it predicts neutrinos to be massless. Several neutrino-oscillation experiments including Super-Kamiokande [43] and SNO [44, 45] established conclusive evidence that neutrinos are massive, which substantiates the need for new physics.

Introducing a Dirac mass term may be considered the most straightforward way to generate neutrino masses, however, it does not provide an explanation for their smallness. Thus, Majorana neutrinos are generally favoured from a theoretical point of view. A Majorana mass term is generated once the SM is considered a low-energy Effective Field Theory (EFT) via the Weinberg operator [47], which is the lowest-dimensional non-renormalisable operator and violates the conservation of lepton number by two units. Then, neutrino masses are suppressed by the associated new-physics scale and hence are naturally small. Among the numerous ultraviolet (UV) completions of the Weinberg operator are the different seesaw mechanisms [196–206] at tree level. The first one- and two-loop neutrino mass models have been proposed more than 30 years ago [60–65] and in the past 20 years many more models have been designed, as detailed in various reviews on neutrino mass models [48–50].

In recent years, several groups followed different avenues to systematically study neutrino mass models, based on simplicity [207–209], topology [210–218], effective operators of the form $LLHH(H^\dagger H)^n$ with $n = 0, 1, \dots$ [215, 219, 220] and more generally effective operators which violate lepton number by two units ($\Delta L = 2$) [51–58]. The last option allows for an efficient classification of a large number of models and their phenomenology associated with lepton-number violation. However, processes which do not violate lepton number generally require us to resort to explicit models which are the origin of the different $\Delta L = 2$ operators. There are systematic ways to use a $\Delta L = 2$ operator as a starting point to construct a UV-complete model [51, 54–56]. A complete set of tree-level UV completions of $\Delta L = 2$ operators up to dimension 11 has been constructed in [56]. The vast number of UV completions, however, make a systematic study difficult. Lastly, some of us thus proposed a classification based on simplified models [59] and identified 20 different particles which carry lepton number and generate neutrino masses.

In this work, we focus on a singly-charged scalar singlet h which transforms under the

SM gauge-symmetry group $SU(3)_c \times SU(2)_L \times U(1)_Y$ as $h \sim (1,1,1)$.[1] It features in a large number of models, including the well-known Zee model [60–62] which has recently been studied in [223], the Zee-Babu model [63–65] of which the phenomenology has been studied in [224–226], the Krauss-Nasri-Trodden (KNT) model [66] and a number of other models [55, 214, 214, 227, 228]. Our approach is based on the *most general form of the Majorana neutrino mass matrix if at least one of the external neutrinos couples via the antisymmetric Yukawa coupling y_h of h to two left-handed SM lepton doublets.* We focus on the case of only one singly-charged scalar singlet which may be light, for which there are only two possible forms of the neutrino mass matrix. The antisymmetry of the Yukawa coupling matrix y_h allows us to derive model-independent constraints for the elements y_h^{ij} in terms of neutrino parameters.[2] Under the assumption that low-energy effects of new physics are dominantly governed by h, we then perform a phenomenology study and derive conservative bounds on parameter space which are applicable to any model of neutrino mass generation that satisfies the above criterion. We also outline generalisations of our framework to multiple singly-charged scalar singlets.

The paper is organised as follows. In Sect. 3.2 we discuss the structure of the neutrino mass matrix in models with a singly-charged scalar singlet and derive constraints for its Yukawa couplings. The procedure to solve the latter is elaborated on in Sect. 3.3. The resulting phenomenological predictions are discussed in Sect. 3.4. In Sect. 3.5 we briefly comment on the possibility of multiple singly-charged singlet scalars. In Sect. 3.6 we summarise our findings and draw a conclusion. Technical details are presented in the appendices.

---

[1] Motivated by the cocktail model [221], the phenomenology of the doubly-charged scalar singlet has been studied in [222].

[2] For the Casas-Ibarra parametrisation in seesaw models see [229], and for a general parametrisation of the neutrino mass matrix see [230, 231].

3.2 Singly-Charged Scalar Singlet

3.2.1 Lagrangian

In the following, it is assumed that the SM is extended by singly-charged scalar particle h which in particular is a singlet under $SU(2)_L$. The kinetic part of the Lagrangian pertaining to h is given by

$$\mathcal{L}_{\text{kin}} = -h^*(D^\mu D_\mu + M_h^2)h \tag{3.1}$$

with the covariant derivative D_μ containing the hypercharge gauge boson in the unbroken phase. After electroweak symmetry breaking, tree-level couplings to the photon and the Z boson are generated, but not to $W^\pm$ bosons. There are also a bi-quadratic coupling $|h|^2 H^\dagger H$ to the SM Higgs doublet and a quartic self-coupling $|h|^4$ at tree level, however, their respective coefficients are free parameters and they are unrelated to neutrino masses. Hence, these interactions are disregarded in the following. There is no tri-linear term involving the Higgs doublet. The overall lepton sector is now enlarged to

$$\mathcal{L}_{\text{lept}} = y_e^{ij}\bar{e}_i L_j H^* + y_h^{ij} L_i L_j h + \text{h.c.} \tag{3.2}$$

with the left-handed SM lepton doublet $L_i \equiv (\nu_i, \ell_i)^T$, the charge-conjugate $\bar{e}_i$ of the right-handed SM charged leptons and the SM lepton Yukawa coupling matrix y_e which can be assumed to be diagonal, see also Sect. 3.3.[3] Repeated flavour indices i, j are summed over.

Besides electric charge and baryon number, this theory features another continuous global $U(1)$ symmetry that can be identified with lepton number and is conserved by the Lagrangian in Eq. (3.2) if one assigns $+1$ unit to L_i, -1 unit to $\bar{e}_i$ and in particular -2 units to h. Crucial for the following analyses is the fact that the 3×3 Yukawa coupling matrix

$$y_h = \begin{pmatrix} 0 & y_h^{e\mu} & y_h^{e\tau} \\ -y_h^{e\mu} & 0 & y_h^{\mu\tau} \\ -y_h^{e\tau} & -y_h^{\mu\tau} & 0 \end{pmatrix} \tag{3.3}$$

---

[3] Note that expanding the contraction of weak-isospin indices yields $2y_h^{ij}\nu_i\ell_j h$, hence the physical coupling matrix is given by $2y_h$.

is antisymmetric in flavour space and therefore features a non-trivial eigenvector

$$v_h = (y_h^{\mu\tau}, -y_h^{e\tau}, y_h^{e\mu})^T \tag{3.4}$$

with eigenvalue zero, $y_h v_h = 0$.

3.2.2 Conventions for the Neutrino Sector

Majorana masses for the active SM neutrinos are described by a symmetric complex 3×3 matrix M_ν. In line with the conventions in [232], we relate neutrino mass eigenstates ν_i and flavour eigenstates ν_α via

$$\nu_\alpha = \sum_{i=1}^{3} U_{\alpha i} \nu_i \tag{3.5}$$

with the unitary Pontecorvo-Maki-Nakagawa-Sakata (PMNS) mixing matrix U, and thus $m_{\text{diag}} \equiv U^T M_\nu U$. Since three generations of active neutrinos are assumed, $m_{\text{diag}} = \text{diag}(m_1, m_2, m_3)$ contains two or three non-vanishing eigenvalues. We have

$$U = P U_{23} U_{13} U_{12} U_{\text{Maj}} \tag{3.6}$$

with

$$U_{23} = \begin{pmatrix} 1 & 0 & 0 \\ 0 & c_{23} & s_{23} \\ 0 & -s_{23} & c_{23} \end{pmatrix}, \quad U_{13} = \begin{pmatrix} c_{13} & 0 & s_{13}e^{-i\delta} \\ 0 & 1 & 0 \\ -s_{13}e^{i\delta} & 0 & c_{13} \end{pmatrix}, \quad U_{12} = \begin{pmatrix} c_{12} & s_{12} & 0 \\ -s_{12} & c_{12} & 0 \\ 0 & 0 & 1 \end{pmatrix}, \tag{3.7}$$

$U_{\text{Maj}} \equiv \text{diag}(e^{i\eta_1}, e^{i\eta_2}, 1)$ and $P = \text{diag}(e^{i\alpha_1}, e^{i\alpha_2}, e^{i\alpha_3})$. The three phases α_k will eventually be removed from U upon a phase redefinition of the left-handed charged leptons ℓ_i, as described in Section 3.3. $\eta_{1,2}$ are the physical Majorana phases in the case of three massive neutrinos, and $c_{ij} \equiv \cos(\theta_{ij})$ and $s_{ij} \equiv \sin(\theta_{ij})$ with the leptonic mixing angles θ_{12}, θ_{13} and θ_{23}. The individual neutrino masses can be expressed in terms of the lightest neutrino mass m_0 and the relevant squared-mass differences $\Delta m_{ij}^2 \equiv m_i^2 - m_j^2$,

$$m_1 = m_0, \quad m_2 = \sqrt{\Delta m_{21}^2 + m_0^2}, \quad m_3 = \sqrt{\Delta m_{31}^2 + m_0^2} \tag{3.8}$$

in the case of Normal Ordering (NO) $m_1 < m_2 \ll m_3$, and

$$m_1 = \sqrt{|\Delta m_{32}^2| - \Delta m_{21}^2 + m_0^2}, \quad m_2 = \sqrt{|\Delta m_{32}^2| + m_0^2}, \quad m_3 = m_0 \tag{3.9}$$

in the case of Inverted Ordering (IO) $m_3 \ll m_1 < m_2$ of neutrino masses. The ranges of the different parameters entering U and m_{diag} which are compatible with current experimental data are listed in Tab. 3.1.

3.2.3 Neutrino Mass Matrix

In the following, we will discuss the two possible structures for the neutrino mass matrix that are obtained in the presence of one singly-charged scalar singlet h. *The main assumption is that the dominant contribution to neutrino masses is generated by a diagram in which one or both of the external neutrinos couple via y_h.* This is schematically depicted in Fig. 3.1 where the grey blob represents unspecified physics which involves the breaking of the conservation of lepton number. Hence, we require that there are no sizeable contributions to neutrino masses which are independent of the one stemming from the singly-charged scalar singlet h. This scenario is naturally realised in an effective field theory (EFT) for which the grey blob represents an effective operator, but it is not limited to it. Examples are provided below when discussing the two cases. The case of multiple singly-charged scalar singlets which generate similarly large contributions to neutrino masses is commented on in Sect. 3.5.

3.2.3.1 Case I: Neutrino Masses Linear in y_h

If the main contribution to neutrino masses is generated by a diagram in which only one of the external neutrinos couples via y_h, as schematically shown on the left in Fig. 3.1, neutrino masses are approximately given by

$$U^* m_{\text{diag}} U^\dagger = M_\nu = X y_h - y_h X^T. \tag{3.10}$$

Here, the coupling matrix X contains the information about the rest of the loop structure, that is, particle masses, couplings, loop factors and further unknown parameters.

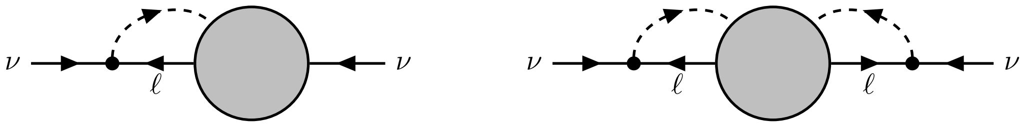

Figure 3.1: Self-energy diagram responsible for the generation of neutrino masses via a singly-charged scalar singlet: linear case (left) and quadratic case (right). The grey blob represents all other interactions which contribute to the diagram. It could be one effective vertex or a sub-diagram consisting of multiple vertices and propagators. There are at least two insertions of the Higgs vacuum expectation value somewhere in the diagram which are not explicitly shown.

It is stressed again that the main assumption that there are no sizeable contributions to neutrino masses which cannot be parametrised as above is essential for what follows. Multiplying Eq. (3.10) by v_h defined in Eq. (3.4) from the left- and the right-hand side, one obtains

$$v_h^T U^* m_{\text{diag}} U^\dagger v_h = 0\,, \tag{3.11}$$

which we identify as a *necessary condition* for neutrino masses being correctly explained by h. Eq. (3.11) is very predictive in the sense that is does not involve X and hence the mechanism of the breaking of lepton-number conservation does not have to be specified. Instead, we maintain a model-independent approach throughout the analysis and do not explicitly construct the neutrino mass matrix. Treating the elements of X as essentially free parameters also implies that in general the determinant of M_ν does not vanish and hence all three active neutrinos are massive.[4] Nevertheless, one may impose $\det(M_\nu) = 0$ as a further condition which then necessarily also involves the elements of X. In this case, the smallest neutrino mass and one of the Majorana phases vanish, the consequences of which will be briefly commented on in Sect. 3.4.3. See App. 3.7 for the expression in Eq. (3.11) explicitly written out.

In case X is generated by some heavy new physics, one may use EFT to parametrise its

---

[4] Linear combinations of the elements X^{ij} are constrained in the sense that Eq. (3.10) has to be satisfied, however, this does not uniquely determine the X^{ij} in terms of the y_h^{kl} since M_ν is symmetric, whereas X can be a general matrix.

effect. As an example, let us consider the non-renormalisable dimension-5 operator [59]

$$\frac{c^{ij}}{\Lambda} h^* \bar{e}_i L_j H + \text{h.c.} \tag{3.12}$$

which violates lepton number by two units. Here, the lepton-number breaking scale Λ is assumed to be much larger than M_h, and c is a general complex 3×3 matrix. Then, neutrino masses are generated at one-loop level and can be approximately written as

$$M_\nu \propto \frac{v^2}{(4\pi)^2 \Lambda} \left(c\, y_e\, y_h - y_h y_e\, c^T \right) . \tag{3.13}$$

Hence, in this case

$$X \approx \frac{c\, y_e}{(4\pi)^2 \Lambda} v^2 . \tag{3.14}$$

There is in principle an infinite number of potential realisations of this effective description of neutrino masses in terms of concrete models. Among them, several simple examples in which neutrino masses are generated at three-loop level are discussed in [214].[5] In addition, the constraint in Eq. (3.11) also applies to some of the minimal UV completions of lepton-number violating effective operators discussed in [55]. Still, the most prominent realisation of the general structure in Eq. (3.10) is given by the Zee model and its variants [50, 60–62, 223, 233, 234]. Here, the SM particle content is enlarged by h and a new Higgs doublet $\Phi \sim (1, 2, 1/2)$ which in particular allows for a tri-linear term $H\Phi h^* + \text{h.c.}$ at tree level which violates lepton number. Then,

$$X = y_e'\, m_e \, \frac{\sin(2\varphi)}{16\pi^2} \, \log \left(\frac{M^2_{h_2^+}}{M^2_{h_1^+}} \right) , \tag{3.15}$$

with m_e the SM charged-lepton masses, φ the angle parametrising the mixing of the singly-charged scalar mass eigenstates $h^+_{1,2}$ with masses $M_{h^+_{1,2}}$, and y_e' the Yukawa coupling of Φ (in the so-called Higgs basis) to the SM leptons. Together with the tri-linear term, the latter generates the effective operator in Eq. (3.12) at tree level when the second Higgs doublet Φ is integrated out.

---

[5] They are dubbed ‘Model 3’ and ‘Model 4’ therein. Another possibility mentioned is to take h as accompanied by the scalar doublet $\sim (1, 2, 3/2)$ and generate neutrino masses at two-loop level. This can be seen as a modification of the Zee model in the sense that one of the loops generates the tri-linear term $HHh + \text{h.c.}$ which vanishes at tree level.

3.2.3.2 Case II: Neutrino Masses Quadratic in y_h

If neutrino masses are dominantly generated by a diagram in which both external neutrinos couple via y_h, respectively, as shown on the right in Fig. 3.1, one obtains

$$U^* m_{\text{diag}} U^\dagger = M_\nu = y_h \, S \, y_h \,, \tag{3.16}$$

where S is a complex symmetric matrix. This can be considered as a special realisation of the linear case (Case I) with $X = y_h S'$, where S' is a general complex matrix and thus $S \equiv S' + S'^T$. Still, this identification is trivial if the main contribution to neutrino masses is inherently flavour-symmetric. The lightest neutrino will be massless at this order, because the determinant of M_ν vanishes by construction due to y_h being antisymmetric. Also, this implies that there is only one physical Majorana phase.[6]

As in the linear case, the relevant assumption is that the model under consideration does not generate any sizeable contribution to neutrino masses which is not given by the structure in Eq. (3.16). Then, one identifies the condition

$$m_{\text{diag}} U^\dagger v_h = 0 \tag{3.17}$$

which trivially implies the one in Eq. (3.11), but the converse statement is not true in general. Explicitly, Eq. (3.17) yields the two relations

$$\frac{y_h^{e\tau}}{y_h^{\mu\tau}} = \tan(\theta_{12}) \frac{\cos(\theta_{23})}{\cos(\theta_{13})} + \tan(\theta_{13}) \sin(\theta_{23}) e^{i\delta}, \tag{3.18}$$

$$\frac{y_h^{e\mu}}{y_h^{\mu\tau}} = \tan(\theta_{12}) \frac{\sin(\theta_{23})}{\cos(\theta_{13})} - \tan(\theta_{13}) \cos(\theta_{23}) e^{i\delta} \tag{3.19}$$

in the case of NO and

$$\frac{y_h^{e\tau}}{y_h^{\mu\tau}} = -\frac{\sin(\theta_{23})}{\tan(\theta_{13})} e^{i\delta}, \tag{3.20}$$

$$\frac{y_h^{e\mu}}{y_h^{\mu\tau}} = \frac{\cos(\theta_{23})}{\tan(\theta_{13})} e^{i\delta} \tag{3.21}$$

---

[6] We choose $\eta_1 = 0$ in the quadratic case which matches the convention in [224].

for IO.[7] Note that these relations only depend on the leptonic mixing angles and the Dirac CP phase and are independent of the Majorana phases and individual neutrino masses, and thus they are more constraining than the one in Eq. (3.11).

For a concrete example for S in terms of an EFT, one may consider the non-renormalisable dimension-5 operator

$$\frac{d^{ij}}{\Lambda}(h^*)^2\bar{e}_i\bar{e}_j + \text{h.c.} \tag{3.22}$$

which violates lepton number by two units. Here, the lepton-number breaking scale Λ is assumed to be much larger than M_h, and d is a complex symmetric 3×3 matrix. Then, neutrino masses are generated at two-loop level and can be approximately written as

$$M_\nu \propto \frac{v^2}{(4\pi)^4\Lambda} y_h\, y_e\, d\, y_e\, y_h\,. \tag{3.23}$$

Hence, in this case

$$S \approx \frac{y_e d y_e}{(4\pi)^4\Lambda} v^2\,. \tag{3.24}$$

The constraint in Eq. (3.17) has been previously discussed [224–226, 235] in the context of the Zee-Babu model [63–65]. Here, the SM particle content gets enlarged by h and a doubly-charged scalar singlet $k \sim (1,1,2)$ with mass M_k which in particular allows for a tri-linear term $\mu h^2 k^* + \text{h.c.}$ at tree level which violates lepton number. Then, neutrino masses are generated at two-loop level and one may write [224, 226, 236]

$$S = 16\, m_e\, y_k\, m_e\, \mu\, F\left(\frac{M_k^2}{M_h^2}\right)\,, \tag{3.25}$$

with y_k the symmetric Yukawa coupling matrix of k to right-handed SM leptons and F a loop function. The effective operator in Eq. (3.22) is induced at tree level when k is integrated out. However, the constraint also applies to the KNT model [66] which features a second singly-charged scalar singlet $\sim (1,1,1)$ and a fermionic singlet $\sim (1,1,0)$ both of which are charged under a Z_2 symmetry, as well as to some variants of it discussed

---

[7] Eq. (3.17) formally implies three equations, but one of them is trivially satisfied due to $\det(M_\nu) = 0$. Also, the expressions differ from the ones in [224] by a complex conjugation as per how the PMNS matrix U is defined.

in [214, 227, 228] or to the extension of the Zee-Babu model by another heavy singly-charged scalar singlet, see App. 3.10. Analogous to X in the linear case, the constraint in Eq. (3.17) does not involve S itself and hence is independent of the details of the breaking of lepton-number conservation.

3.3 Solving the Neutrino-Mass Constraint

In this section, the procedure of solving the constraint in Eq. (3.11) is elaborated on. Both the real part and the imaginary part of $v_h^T U^* m_{\text{diag}} U^\dagger v_h$ have to identically vanish which yields two real conditions. We decompose the couplings into their respective magnitudes and phases and use the constraint to determine two of the $|y_h^{ij}|$ in terms of the third one, the phases and the active-neutrino parameters which enter m_{diag} and U. This amounts to finding the roots of a single expression that is quartic in two of the y_h^{ij} since both the real and imaginary part of $v_h^T U^* m_{\text{diag}} U^\dagger v_h$ can be taken as quadratic in either of the couplings y_h^{ij}. Therefore, the constraint is numerically solved and one can obtain up to four solutions. In the quadratic case, Eq. (3.17) implies four real conditions which then also determine two phases of the Yukawa couplings y_h^{ij} in terms of neutrino data.

The smallest neutrino mass m_0 can be arbitrarily small or even zero, whereas upper bounds arise from cosmological surveys as well as experimental searches for tritium beta decay and neutrino-less double beta decay. The cosmological bound is the strongest one and, while model-dependent, it is assumed to apply in the scenario under consideration since no new physics is introduced below the electroweak scale. The latest results published by the Planck Collaboration in 2018 [121] comprise the upper bound $m_1 + m_2 + m_3 \leq 0.12\,\text{eV}$ which implies $m_0 = m_1 \lesssim 30\,\text{meV}$ for NO and $m_0 = m_3 \lesssim 15\,\text{meV}$ for IO. $|y_h^{ij}|$ can in principle also be arbitrarily small, whereas $|y_h^{ij}| \lesssim 2\pi$ due to perturbativity constraints with the normalisation of the Yukawa coupling taken into account.[8] Notwithstanding, both the coupling magnitude assigned a value and the magnitudes obtained as solutions

---

[8] The constraint $|y_h^{ij}| \lesssim 2\pi$ may for instance be derived from requiring that the one-loop correction to the physical coupling $2y_h^{ij}$ remains smaller than $2y_h^{ij}$ itself.

to Eq. (3.11) are required to satisfy $|y_h^{ij}| > 1\times10^{-4}$ in order to limit the orders of magnitude sampled over.

The flavour observables discussed in the following section also depend on the mass M_h which is not constrained by Eq. (3.11). A model-independent lower bound $M_h \gtrsim 200\,\text{GeV}$ has recently been derived in [237] from the reinterpretation of a collider search for smuons and selectrons [238]. Depending on the relative magnitudes $|y_h^{ij}|$, the constraint is actually slightly more stringent. Hence, we require $M_h \geq 350\,\text{GeV}$ to safely operate beyond any mass region potentially excluded. This is consistent with the earlier analysis in [239]. The assumed upper bound $M_h \leq 100\,\text{TeV}$ arises from an order-of-magnitude estimate based on requiring the absence of unnaturally large corrections to the SM Higgs-boson mass [59].

Furthermore, a careful determination of the physical phases in the theory is in order. Before electroweak symmetry breaking, unitary basis transformations applied to $\bar{e}_i$ and L_i can be used to diagonalise y_e with real and positive eigenvalues, and the phases in y_h can be eliminated upon redefinitions of $\bar{e}_i$ and L_i. After electroweak symmetry breaking, the charged-lepton masses are already diagonal by construction, and the neutrino mass matrix is diagonalised via the PMNS matrix U. Then, three phases in U can be eliminated via redefining the left-handed charged leptons ℓ_i which reintroduces three phases in y_h. One of these can be set to zero upon exploiting the phase freedom of h. Therefore, $y_h^{\mu\tau}$ is taken real while $\arg(y_h^{e\mu})$ and $\arg(y_h^{e\tau})$ are randomly sampled over. As a side note, the presence of complex couplings indicates that the singly-charged scalar singlet, accompanied by a source of lepton-number violation, will in general contribute to leptonic electric dipole moments. However, as these are linked to the violation of lepton-number conservation and hence no strong constraints are to be expected, electric dipole moments are not explored further. As of yet, the physical Majorana phases $\eta_{1,2}$ are completely unconstrained experimentally and hence also randomly sampled over. Note that the ranges of $\eta_{1,2}$ can be restricted to $[0, \pi]$ without loss of generality since the sign of the Majorana field is unphysical.

The leptonic mixing parameters and neutrino-mass-squared differences which have been constrained by experiments are assigned pseudo-random variates from normal distributions of which the respective mean values and standard deviations are taken from the latest fit

m_e [keV]	m_μ [MeV]	m_τ [GeV]	$G_F\,[\frac{1}{\mathrm{GeV}^2}]$	$\alpha_{\mathrm{EM}}^{-1}$	M_Z [GeV]
510.9989	105.6584	1.777	1.16638×10^{-5}	137.035999	91.1535

	$\Delta m^2_{3l}\,[1 \times 10^{-3}\,\mathrm{eV}^2]$	$\Delta m^2_{21}\,[1 \times 10^{-5}\,\mathrm{eV}^2]$	δ [rad]
NO	2.517 ± 0.026	7.42 ± 0.20	3.44 ± 0.42
IO	-2.498 ± 0.028	7.42 ± 0.20	4.92 ± 0.45
	$\sin^2(\theta_{12})$	$\sin^2(\theta_{13})$	$\sin^2(\theta_{23})$
NO	0.304 ± 0.012	0.02219 ± 0.00062	0.573 ± 0.016
IO	0.304 ± 0.012	0.02238 ± 0.00062	0.575 ± 0.016

	$\lvert y_h^{ij}\rvert$	$\arg(y_h^{ek})$	$\arg(y_h^{\mu\tau})$	m_0 [meV]	$\eta_{1,2}$ [rad]	M_h [GeV]
Prior	Log-Flat	Flat	Fixed	Log-Flat	Flat	Log-Flat
Range	$[1 \times 10^{-4}, 2\pi]$	$[0, 2\pi]$	0	$[1 \times 10^{-4},\ 30]$ (NO) $[1 \times 10^{-4},\ 15]$ (IO)	$[0, \pi]$	$[350,\ 1 \times 10^5]$

Table 3.1: The table at the top contains the experimental values for input parameters taken from [29,37]; the one in the centre summarises the experimental values for leptonic mixing parameters and neutrino-mass-squared differences taken from NuFIT 5.0 [38]. $\Delta m^2_{31} > 0$ for NO, and $\Delta m^2_{32} < 0$ for IO. Priors and the ranges sampled over in the numerical scan are given in the bottom table. The flavour indices for the antisymmetric Yukawa couplings are $i, j = e$, μ, τ, and $k = \mu$, τ.

results provided by the NuFIT collaboration [38]. Symmetric distributions are assumed for simplicity. The numerical values used for the charged-lepton masses (m_e, m_μ, m_τ) and the electroweak input parameters $(G_F, \alpha_{\mathrm{EM}}, M_Z)$ are summarised in Tab. 3.1. For the numerical scan we generated approximately 5×10^5 sample points for each neutrino-mass ordering.

3.4 Phenomenology

In the following, the contributions of h to various flavour observables are presented under the assumption that the couplings y_h^{ij} satisfy the constraints in Eq. (3.11) or Eq. (3.17) and hence neutrino masses are dominantly generated by the singly-charged scalar singlet. The considered observables together with the current experimental bound, prospected sensitivities for future experiments as well as the maximum contribution found in the numerical scan are summarised in Tab. 3.2. Note that the bounds on several observables can be (nearly) saturated. Large tuning of the ratios of coupling magnitudes $|y_h^{ij}|$ is necessarily absent due to the constraints in Eq. (3.11) and Eq. (3.17), see Sect. 3.4.3, thus in particular the bounds on $\mu \to e\gamma$ and $\mu \to 3e$ cannot be evaded and hence they efficiently shape the available parameter space.

We assume that further new particles are weakly coupled or heavy enough not to generate sizeable contributions to any of the observables under consideration. In particular, particles which induce flavour-changing decays of charged leptons at tree level have to be sufficiently decoupled, as the singly-charged scalar singlet generates these processes at one-loop level. Significant destructive interference or fine-tuned cancellations are taken as absent. Succinctly, we assume that low-energy effects of new physics are dominantly governed by h. In that sense, the bounds on parameter space which is compatible with neutrino masses as discussed in the following are conservative.

3.4.1 Effective Description of Low-Energy Phenomenology at Tree Level

As derived in App. 3.8, the Wilson coefficient of the effective dimension-6 four-lepton operator

$$\mathcal{O}_{LL,ijkl} \equiv L_i^{\dagger\alpha} \bar{\sigma}^\mu L_{j\alpha} L_k^{\dagger\beta} \bar{\sigma}_\mu L_{l\beta} \tag{3.26}$$

	Experimental Data	
Observable	Current Bound	Future Sensitivity
$\mathrm{Br}(\mu \to e\gamma)$	4.2×10^{-13} (90% CL) [22]	6×10^{-14} [240]
$\mathrm{Br}(\tau \to e\gamma)$	3.3×10^{-8} (90% CL) [241]	3×10^{-9} [7]
$\mathrm{Br}(\tau \to \mu\gamma)$	4.4×10^{-8} (90% CL) [241]	1×10^{-9} [7]
$\mathrm{Br}(\mu \to 3e)$	1×10^{-12} (90% CL) [242]	1×10^{-16} [243]
$\mathrm{Br}(\tau \to 3e)$	2.7×10^{-8} (90% CL) [28]	4.3×10^{-10} [7]
$\mathrm{Br}(\tau \to 3\mu)$	2.1×10^{-8} (90% CL) [28]	3.3×10^{-10} [7]
$\lvert g_\mu/g_e \rvert$	[0.9986, 1.0050] (2σ) [244]	
$\lvert g_\tau/g_\mu \rvert$	[0.9981, 1.0041] (2σ) [244]	
$\lvert g_\tau/g_e \rvert$	[1.0000, 1.0060] (2σ) [244] [0.9985, 1.0075] (3σ) [244]	
$\lvert \delta M_W \rvert$[GeV]	0.018 (3σ) [29]	

	Numerical Analysis			
	Linear Case		Quadratic Case	
Observable	NO	IO	NO	IO
$\mathrm{Br}(\mu \to e\gamma)$	4.2×10^{-13}	4.2×10^{-13}	4.2×10^{-13}	4.2×10^{-13}
$\mathrm{Br}(\tau \to e\gamma)$	6.4×10^{-11}	4.9×10^{-11}	3.1×10^{-13}	6.8×10^{-14}
$\mathrm{Br}(\tau \to \mu\gamma)$	1.6×10^{-11}	1.6×10^{-11}	2.9×10^{-14}	1.5×10^{-12}
$\mathrm{Br}(\mu \to 3e)$	1×10^{-12}	1×10^{-12}	1×10^{-12}	1×10^{-12}
$\mathrm{Br}(\tau \to 3e)$	6.6×10^{-9}	1.3×10^{-8}	7.7×10^{-13}	1.6×10^{-13}
$\mathrm{Br}(\tau \to 3\mu)$	3.0×10^{-9}	1.2×10^{-8}	6.1×10^{-13}	8.8×10^{-13}
$\lvert g_\mu/g_e \rvert$	1.0050	1.0047	1.0002	1.0000
$\lvert g_\tau/g_\mu \rvert$	1.0009	1.0014	1.0000	1.0001
$\lvert g_\tau/g_e \rvert$	1.0048	1.0043	1.0002	1.0000
$\lvert \delta M_W \rvert$[GeV]	0.018	0.018	0.002	0.007

Table 3.2: The upper table contains the current experimental bounds on and future sensitivities to the relevant observables. The lower table shows the respective maximum contribution found in the scan in the linear case and the quadratic case for either neutrino-mass ordering.

receives a contribution at tree level from integrating out the singly-charged scalar singlet h:[9]

$$C_{LL}^{ijkl} = \frac{(y_h^{ik})^* y_h^{jl}}{M_h^2} \,. \tag{3.27}$$

In the low-energy effective theory, this leads to the neutral-current Lagrangian

$$\mathcal{L}_{d=6}^{\mathrm{NSI}} = -2\sqrt{2} G_F \epsilon_{ij}^{kl} \left(\nu_i^\dagger \bar{\sigma}^\mu \nu_j\right) \left(\ell_k^\dagger \bar{\sigma}_\mu \ell_l\right) \,, \tag{3.28}$$

(see also [226]) with the Wilson coefficients

$$\epsilon_{ij}^{kl} \equiv -\frac{1}{2\sqrt{2} G_F} \left(C_{LL}^{ijkl} + C_{LL}^{klij}\right) = -\frac{1}{\sqrt{2} G_F} \frac{(y_h^{ik})^* y_h^{jl}}{M_h^2} \tag{3.29}$$

which are commonly called non-standard interaction (NSI) parameters. They are antisymmetric under the exchange of an upper index and the corresponding lower index, $\epsilon_{ij}^{kl} = -\epsilon_{il}^{kj} = -\epsilon_{kj}^{il}$, and their complex conjugates are obtained via swapping the upper and lower indices among themselves: $\epsilon_{ij}^{kl} = (\epsilon_{ji}^{lk})^*$. Note that there are no effective operators with four neutrinos or four charged leptons due to the antisymmetry of y_h and thus in particular no tree-level contributions to flavour-violating charged-lepton decays.

Fermi Constant and CKM Matrix

Singly-charged scalar singlets affect the partial decay widths $\Gamma_{a\to b}$ associated to the different leptonic channels $\ell_a^- \to \ell_b^- \nu_a \bar{\nu}_b$ and $\ell_a^+ \to \ell_b^+ \bar{\nu}_a \nu_b$ [224,237,246] and hence in particular modify the extraction of the Fermi constant G_F from measurements of the muon lifetime. In the framework of treating the SM as an effective field theory (SMEFT), one defines (see e.g. [247])

$$G_F = G_F^{\mathrm{SM}} - \frac{\sqrt{2}}{4} \left(C_{LL}^{\mu ee\mu} + C_{LL}^{e\mu\mu e}\right) \tag{3.30}$$

with the Wilson coefficient C_{LL}^{ijkl} given in Eq. (3.27) and G_F^{SM} denotes the Fermi constant in the SM.[10] Hence,

$$G_F = G_F^{\mathrm{SM}} - \frac{\sqrt{2}}{4} \left(\frac{(y_h^{e\mu})^* y_h^{\mu e}}{M_h^2} + \frac{(y_h^{\mu e})^* y_h^{e\mu}}{M_h^2} \right) = G_F^{\mathrm{SM}} + \frac{1}{\sqrt{2}} \frac{|y_h^{e\mu}|^2}{M_h^2} \,, \tag{3.31}$$

---

[9] See [245] for integrating out h at one-loop level.

[10] Additional contributions from other operators to G_F are omitted.

where we have used the antisymmetry of the Yukawa coupling matrix y_h. Equivalently, we can express it as $G_F = G_F^{\rm SM} + \sqrt{2} G_F \delta G_F$ with

$$\delta G_F = \frac{1}{2G_F}\frac{|y_h^{e\mu}|^2}{M_h^2} \equiv -\frac{\epsilon_{ee}^{\mu\mu}}{\sqrt{2}}. \tag{3.32}$$

Another observable which has recently attracted attention (see for instance [248–255]) and is of interest for the scenario under consideration is the sum of the squares of the absolute values of the first-row elements of the Cabibbo-Kobayashi-Maskawa (CKM) matrix:

$$\sum_i |V_{ui}|^2 = |V_{ud}|^2 + |V_{us}|^2 + |V_{ub}|^2 \,. \tag{3.33}$$

The magnitude of the element V_{us} can be extracted directly from kaon and tau decays [256, 257], and indirectly via $|V_{ud}|$ from nuclear beta decays (see for instance [258, 259] for recent theoretical progress) and the assumption of the sum in Eq. (3.33) being equal to one which in the SM is a built-in consequence of unitarity.[11] The fact that there is significant tension between the results is referred to as the Cabibbo Angle Anomaly (CAA). The discrepancy between the “true" value of $|V_{us}|$ and the one obtained from beta decays and CKM unitarity in the SM can be explained via new contributions to muon decay and subsequently the Fermi constant [237].

Universality of Leptonic Gauge Couplings

One defines the lepton-flavour universality ratios via the “effective Fermi constants" $G_{ab} \sim g_a g_b$ associated to the different leptonic channels: [224, 246]

$$\sqrt[4]{\frac{\Gamma_{\tau\to\mu}}{\Gamma_{\tau\to e}}} \propto \frac{G_{\tau\mu}}{G_{\tau e}} = \frac{g_\mu}{g_e} \approx 1 + \frac{1}{\sqrt{2}G_F}\frac{|y_h^{\mu\tau}|^2 - |y_h^{e\tau}|^2}{M_h^2} \equiv 1 + \epsilon_{ee}^{\tau\tau} - \epsilon_{\mu\mu}^{\tau\tau}, \tag{3.34}$$

$$\sqrt[4]{\frac{\Gamma_{\tau\to\mu}}{\Gamma_{\mu\to e}}} \propto \frac{G_{\tau\mu}}{G_{\mu e}} = \frac{g_\tau}{g_e} \approx 1 + \frac{1}{\sqrt{2}G_F}\frac{|y_h^{\mu\tau}|^2 - |y_h^{e\mu}|^2}{M_h^2} \equiv 1 + \epsilon_{ee}^{\mu\mu} - \epsilon_{\mu\mu}^{\tau\tau}, \tag{3.35}$$

$$\sqrt[4]{\frac{\Gamma_{\tau\to e}}{\Gamma_{\mu\to e}}} \propto \frac{G_{\tau e}}{G_{\mu e}} = \frac{g_\tau}{g_\mu} \approx 1 + \frac{1}{\sqrt{2}G_F}\frac{|y_h^{e\tau}|^2 - |y_h^{e\mu}|^2}{M_h^2} \equiv 1 + \epsilon_{ee}^{\mu\mu} - \epsilon_{ee}^{\tau\tau} \,. \tag{3.36}$$

The experimental best-fit values of all three universality ratios are currently larger than one, $|g_\mu/g_e| = 1.0018 \pm 0.0032$, $|g_\tau/g_e| = 1.0030 \pm 0.0030$, $|g_\tau/g_\mu| = 1.0011 \pm 0.0030$ with

---

[11] The magnitude of V_{ub} is negligibly small in this context.

errors given at 2σ [244]. In particular, the channel $\tau \to \mu$ appears to receive sizeable contributions from new physics.

In [237] it has been shown that the deviations of g_μ/g_e and g_τ/g_e from one and the CAA, which will be collectively referred to as the “flavour anomalies" henceforth, can be simultaneously explained with a singly-charged scalar singlet. Adopting the results for the best-fit regions and using the terminology as in [237], for simplicity we take the anomalies to be explained if both $\delta(\mu \to e\nu\nu) \in [0.0005, 0.0008]$ and $\delta(\tau \to \mu\nu\nu) \in [0.0016, 0.004]$ are satisfied[12], with

$$\delta(\ell_i \to \ell_j \nu\nu) \equiv \frac{1}{\sqrt{2}G_F} \frac{|y_h^{ij}|^2}{M_h^2} = -\epsilon_{ii}^{jj} . \tag{3.37}$$

This immediately implies an upper bound $M_h \lesssim 39\,\text{TeV}$ if h explains the flavour anomalies, given that perturbativity constraints require $|y_h^{ij}| \lesssim 2\pi$. The experimental values used in [237] are taken from [257].

In the top panel of Fig. 3.2 we show $g_\tau/g_e - 1$ as a function of $g_\mu/g_e - 1$ for NO (left) and IO (right). The results of the numerical scan for the linear case are represented by blue sample points which explain g_τ/g_e at 2σ, and by black sample points which explain g_τ/g_e at 3σ, but not at 2σ, see also the caption of Fig. 3.2 for details. The 3σ region for g_τ/g_e has been included to accommodate the SM prediction. If not indicated otherwise, “at 2σ" and “at 3σ" always refer to this distinction. Red sample points in diamond shape also explain the flavour anomalies which are briefly discussed below. The quadratic case is shown in brown. In Tab. 3.2 we summarise the respective confidence levels at which further experimental bounds are imposed. For the sample points, the same colour code is used throughout this work, except for Figs. 3.10 and 3.12.

We find that there are solutions to the linear-case constraint in Eq. (3.11) *for both neutrino-mass orderings which simultaneously explain the flavour anomalies introduced above and respect the bounds from the considered flavour observables.* One does in particular not have

---

[12] These ranges are located within the region preferred at 1σ as presented in [237]. We refrain from parametrising its elliptic shape.

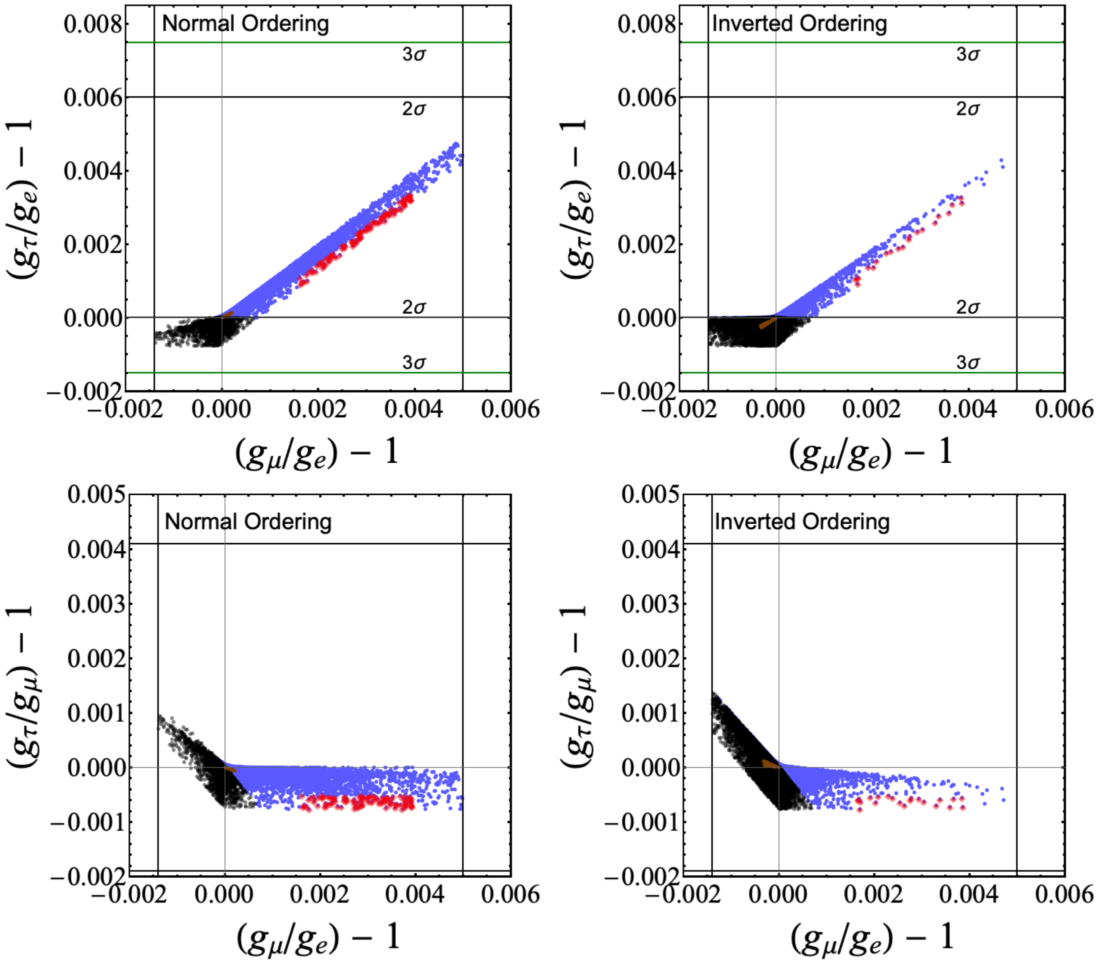

Figure 3.2: Correlations among deviations of g_μ/g_e, g_τ/g_e (top) and g_τ/g_μ (bottom) from universality for NO (left) and IO (right). All shown sample points explain neutrino masses and respect the bounds arising from the flavour observables considered in this work. For the blue points, the deviation of g_τ/g_e from universality is explained at 2σ in the linear case (Case I), and for the black points at 3σ, but not at 2σ. The red diamonds also explain the flavour anomalies, for which g_τ/g_e must be respected at 2σ. Brown points pertain to the quadratic case (Case II) which only occurs at 2σ for NO and at 3σ for IO. Solid lines indicate current experimental bounds (black for 2σ or 90 % CL, and green for 3σ).

to assume that $|y_h^{e\tau}|$ is negligibly small.[13] *Contrariwise, explaining the flavour anomalies in the quadratic case is not possible.*

In the quadratic case, no large deviations from universality can be generated. In particular, none of the respective 1σ regions for the g_a/g_b which are currently preferred by experiments can be reached. Still, the corrections to both $g_\mu/g_e - 1$ and $g_\tau/g_e - 1$ are strictly positive (negative) for Normal (Inverted) Ordering in the quadratic case, hence a conclusive experimental determination of one of the signs would rule out one of the mass orderings being generated by h. Similarly, positive (negative) corrections to $g_\tau/g_\mu - 1$ are severely disfavoured for NO (IO).

In the linear case, large contributions to g_μ/g_e (g_τ/g_e) are disfavoured for IO as they enforce $|y_h^{\mu\tau}| \gg |y_h^{e\tau}|(|y_h^{e\mu}|)$, see Sect. 3.4.3 for more details. On the contrary, for IO we find more sample points with $g_\tau/g_\mu > 1$ as shown in the bottom panel of Fig. 3.2. This is due to the fact that a hierarchy between $|y_h^{e\mu}|$ and $|y_h^{e\tau}|$ is easier to achieve in this case. Still, the deviation of g_τ/g_μ from universality is measured to be smaller and an explanation of its best-fit value via h would imply a further deviation from the best-fit values of the other two ratios. A given mass M_h fixes the ranges of magnitude of $|y_h^{\mu\tau}|$ and $|y_h^{e\mu}|$ for which the flavour anomalies are explained, as in Eq. (3.37). Together with the strict experimental limit on $\mathrm{Br}(\mu \to e\gamma)$ which bounds $|y_h^{e\tau}|$ in terms of $|y_h^{\mu\tau}|$, this determines the relative positions of the red and blue sample points in Fig. 3.2.

A more precise determination of the lepton-flavour universality ratios g_a/g_b mainly relies on reducing the uncertainties in measurements of the branching ratios $\mathrm{Br}(\tau \to \mu(e)\nu\nu)$ and of the tau lifetime [260]. An improvement of a factor of ten is suggested in [261]. Further improvement would rely on determining the tau mass at higher precision, for instance upon running a future tau factory at the production threshold [260–263]. Nonetheless, shifts in the measured values g_a/g_b themselves cannot be predicted and we refrain from showing estimates for prospective sensitivities in Fig. 3.2.

---

[13] In order to avoid the bound from $\mu \to e\gamma$, $y_h^{e\tau}$ was set to zero in [237] which in general is not a viable solution to the constraint in Eq. (3.11) and hence is incompatible with neutrino masses.

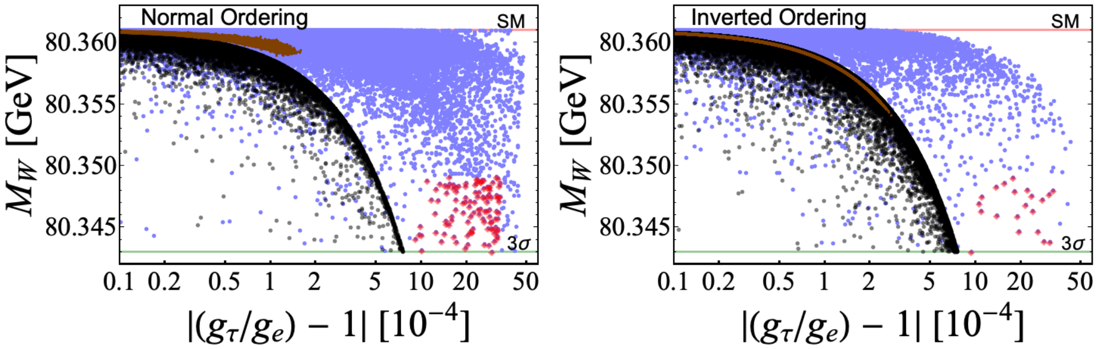

Figure 3.3: Correlations among M_W and deviations of g_τ/g_e from universality. The colours are the same as in Fig. 3.2.

W-Boson Mass

The contribution to the Fermi constant induced by h results in a necessarily negative correction [264]

$$\delta M_W^2 = -\frac{M_W^2}{\sqrt{2}G_F}\left|1-\frac{M_W M_Z}{2M_W^2-M_Z^2}\right|\frac{|y_h^{e\mu}|^2}{M_h^2} \tag{3.38}$$

to the W-boson mass which exacerbates the existing 1.5σ tension among the SM prediction $M_W \pm \Delta M_W = (80.361 \pm 0.005)$ GeV and the world average of measurements given by $M_W^{\mathrm{exp}} \pm \Delta M_W^{\mathrm{exp}} = (80.379 \pm 0.012)$ GeV [29, 37, 265]. In order to accommodate an explanation of the flavour anomalies, we allow for a 3σ discrepancy which implies $M_W \geq 80.343$ GeV and gives rise to the constraint $|y_h^{e\mu}|^2/M_h^2 \lesssim 1.25\times 1\times 10^{-2}/\mathrm{TeV}^2$. To compare, the best-fit value presented in [237] corresponds to $|y_h^{e\mu}|^2/M_h^2 \approx 1.07\times 1\times 10^{-2}/\mathrm{TeV}^2$. In Fig. 3.3 the prediction for the W-boson mass is shown as a function of the absolute value of the deviation of the universality ratio g_τ/g_e from one. Note that in the quadratic case the maximum correction to M_W is much larger for IO than for NO, and there is a non-trivial correlation in the linear case especially for $|y_h^{e\mu}| > |y_h^{\mu\tau}|$. A large effect in $g_\tau/g_e - 1$ together with a conclusive determination of M_W close to its current SM prediction would severely disfavour the scenario of h explaining neutrino masses with IO, but not with NO. Furthermore, a result $M_W \gtrsim 80.35$ GeV would currently rule out an explanation of the flavour anomalies via h. In proposals for next-generation lepton colliders, a reduction of the uncertainty in the experimental determination of M_W by a factor of roughly $10-20$ [261, 266] is suggested. As for the universality ratios g_a/g_b, any shifts in the obtained value M_W itself, be it determined at colliders or via electroweak fits, cannot be predicted though.

Leptonic Non-Standard Interactions

As it can be seen from Eq. (3.28), the singly-charged scalar singlet induces leptonic non-standard interactions at tree level, whereas NSIs with quarks only arise at loop level. Hence, we disregard the latter. The fact that the constraint in Eq. (3.11) disfavours large hierarchies among the coupling magnitudes (see Sect. 3.4.3 for more details) implies that the results found in studies in which only one NSI parameter was switched on at a time (see for instance [267]) are not directly applicable here. We obtain magnitudes of up to $|\epsilon^{\rho\sigma}_{\alpha\beta}| \sim 1 \times 10^{-3}$ in the linear case which to our knowledge is below all current bounds and also appears to be challenging to observe in near-future experiments. For instance, depending on the flavour channel, DUNE is prospected to be sensitive to magnitudes down to $|\epsilon^{\rho\sigma}_{\alpha\beta}| \sim 1 \times 10^{-2}$ at 90 % CL [268]. Still, at a future neutrino factory it might be possible to probe some of the NSI parameters relevant for neutrino production in the $\nu_e \to \nu_\tau$ and

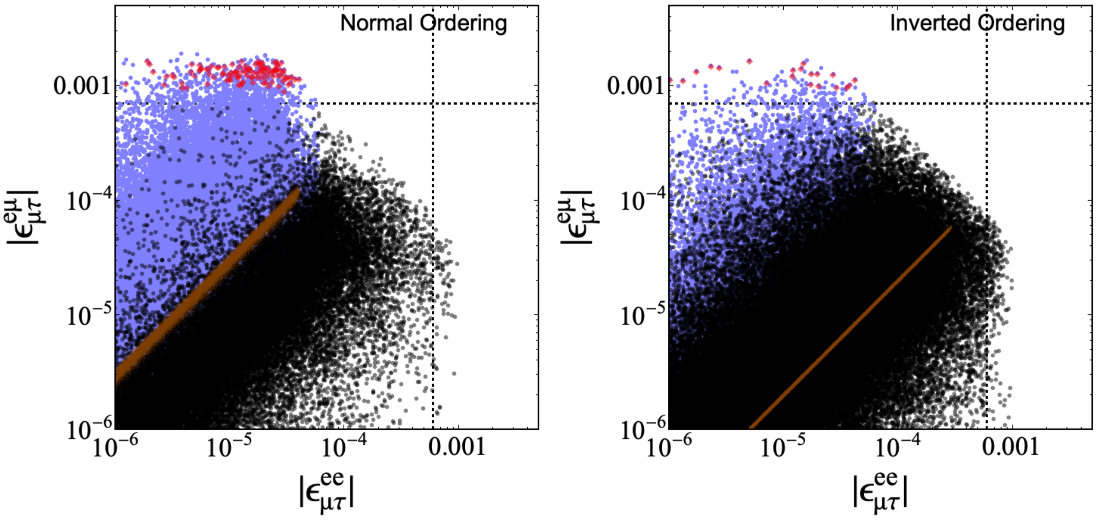

Figure 3.4: Non-standard interactions. The colours are the same as in Fig. 3.2. Dashed lines indicate prospected experimental sensitivities.

$\nu_\mu \to \nu_\tau$ channels [226]:

$$\epsilon^{e\mu}_{\tau e} \equiv \frac{(y_h^{e\tau})^* y_h^{e\mu}}{\sqrt{2} G_F M_h^2} = -(\epsilon^{ee}_{\mu\tau})^*, \qquad \epsilon^{e\mu}_{\mu\tau} \equiv -\frac{(y_h^{e\mu})^* y_h^{\mu\tau}}{\sqrt{2} G_F M_h^2}\,. \tag{3.39}$$

Upon using a 2 kt OPERA-like near tau detector a sensitivity to $|\epsilon^{e\mu}_{\mu\tau}| \sim 7 \times 10^{-4}$ and $|\epsilon^{e\mu}_{\tau e}| \sim 6 \times 10^{-4}$ is prospected to be achievable [225, 269]. In that case, the simultaneous explanation of neutrino masses and the flavour anomalies via h in the linear case could be conclusively tested at a neutrino factory for both neutrino-mass orderings. The contributions in the quadratic case will remain beyond reach. This is illustrated in Fig. 3.4. As indicated in Eq. (3.39), the NSI parameter $\epsilon^{e\mu}_{\tau e}$ is trivially related to the corresponding one for the propagation of ν_μ and ν_τ neutrinos in matter.

3.4.2 Charged Lepton Flavour Violation

The leading-order contributions to flavour-violating charged-lepton decays from singly-charged scalar singlets occur at one-loop level. In fact, finite contributions to radiative charged-lepton decays $\ell_i \to \ell_j \gamma$ are sourced by a single diagram with a neutrino ν_k, $i \neq j$ and $i \neq k \neq j$, in the loop. The branching ratios are given by [224, 237, 270–272]

$$\mathrm{Br}(\mu \to e\gamma) = \mathrm{Br}(\mu \to e\nu\bar{\nu}) \frac{\alpha_{\mathrm{EM}}}{48\pi G_F^2} \frac{|y_h^{e\tau} y_h^{\mu\tau}|^2}{M_h^4}, \tag{3.40}$$

$$\mathrm{Br}(\tau \to e\gamma) = \mathrm{Br}(\tau \to e\nu\bar{\nu}) \frac{\alpha_{\mathrm{EM}}}{48\pi G_F^2} \frac{|y_h^{e\mu} y_h^{\mu\tau}|^2}{M_h^4}, \tag{3.41}$$

$$\mathrm{Br}(\tau \to \mu\gamma) = \mathrm{Br}(\tau \to \mu\nu\bar{\nu}) \frac{\alpha_{\mathrm{EM}}}{48\pi G_F^2} \frac{|y_h^{e\mu} y_h^{e\tau}|^2}{M_h^4}\,, \tag{3.42}$$

with $\mathrm{Br}(\mu \to e\nu\bar{\nu}) \approx 1$, $\mathrm{Br}(\tau \to e\nu\bar{\nu}) \approx 0.178$ and $\mathrm{Br}(\tau \to \mu\nu\bar{\nu}) \approx 0.174$ [29]. As it can be seen in Fig. 3.5, any signal in radiative tau decays showing up at Belle II cannot be induced by h alone, see Table 3.2. For instance, one would need two singly-charged scalar singlets which conspire to circumvent the strong bounds arising from flavour-violating muon decays. Also the sizeable contributions to $\tau \to e\gamma$ implied by simultaneously generating neutrino mass and explaining the flavour anomalies will be beyond reach [237]. Instead, a future search for $\mu \to e\gamma$ [240] efficiently probes parts of the parameter space pertaining to h generating neutrino masses both in the linear case and in the quadratic case, as well

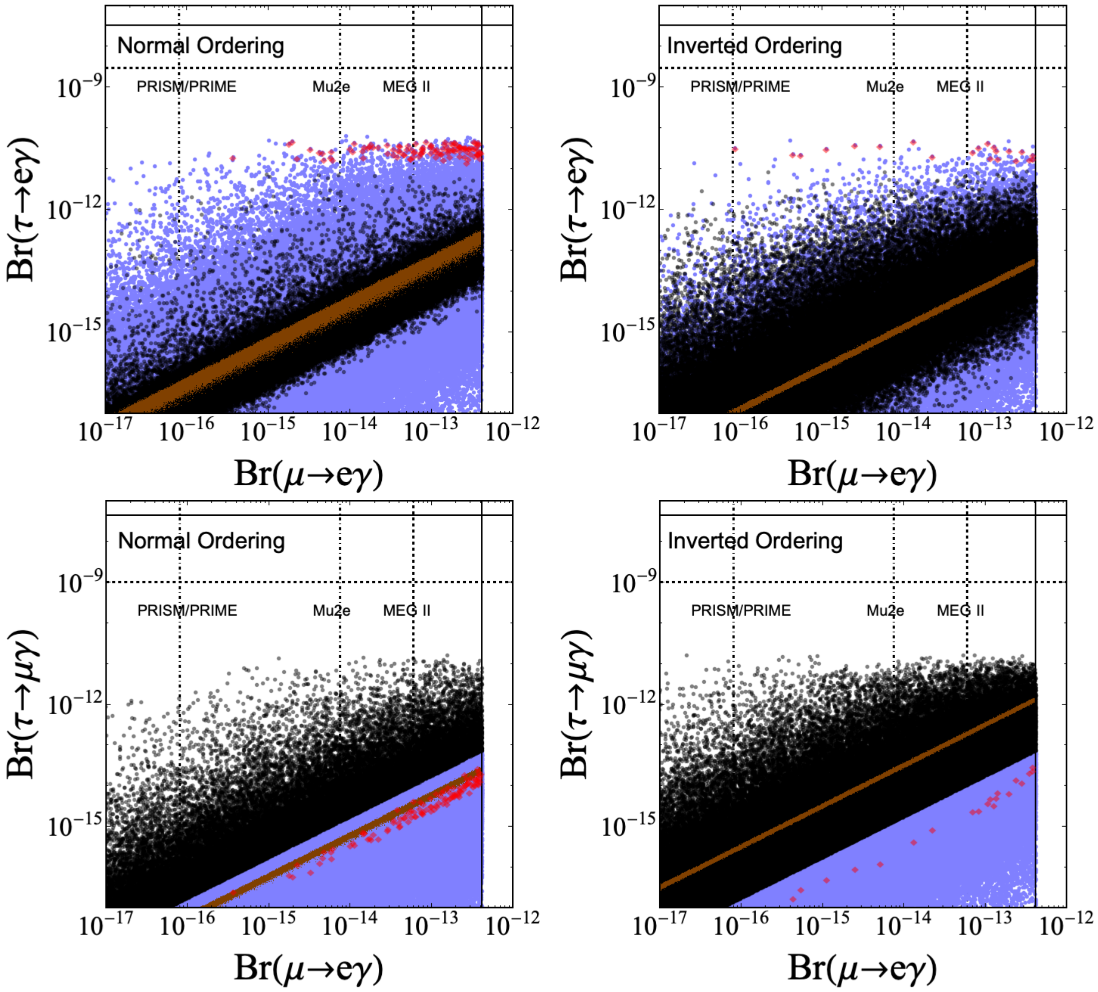

Figure 3.5: Branching ratios of radiative charged-lepton decays. The vertical dot-dashed lines correspond to the prospected sensitivities to $\mathrm{Br}(\mu \to e;\, \mathrm{Ti})$ at PRISM/PRIME and to $\mathrm{Br}(\mu \to e;\, \mathrm{Al})$ at Mu2e which were then converted via $\mathrm{Br}(\mu \to e;\, \mathrm{Al}) \approx 0.0079\,\mathrm{Br}(\mu \to e\gamma)$ and $\mathrm{Br}(\mu \to e;\, \mathrm{Ti}) \approx 0.0125\,\mathrm{Br}(\mu \to e\gamma)$, see also App. 3.9. The colours are the same as in Fig. 3.2.

as the combined scenario in which also the flavour anomalies are explained in the linear case.

As it is well-known, if the contributions from on-shell photon penguin diagrams dominate, the branching ratios for tri-lepton decays with only one flavour in the final state are entirely fixed as functions of $\mathrm{Br}(\ell_i \to \ell_j \gamma)$ and SM parameters:[14] [273, 274]

$$\frac{\mathrm{Br}(\mu \to 3e)}{\mathrm{Br}(\mu \to e\gamma)} \approx \frac{\alpha_{\mathrm{EM}}}{3\pi}\left(\log\left(\frac{m_\mu^2}{m_e^2}\right) - \frac{11}{4}\right) \approx \frac{1}{163}, \tag{3.43}$$

$$\frac{\mathrm{Br}(\tau \to 3e)}{\mathrm{Br}(\tau \to e\gamma)} \approx \frac{\alpha_{\mathrm{EM}}}{3\pi}\left(\log\left(\frac{m_\tau^2}{m_e^2}\right) - \frac{11}{4}\right) \approx \frac{1}{95}, \tag{3.44}$$

$$\frac{\mathrm{Br}(\tau \to 3\mu)}{\mathrm{Br}(\tau \to \mu\gamma)} \approx \frac{\alpha_{\mathrm{EM}}}{3\pi}\left(\log\left(\frac{m_\tau^2}{m_\mu^2}\right) - \frac{11}{4}\right) \approx \frac{1}{446}\,. \tag{3.45}$$

For masses close to the lower bound $M_h = 350\,\mathrm{GeV}$, the photon-penguin approximation is perfectly valid. In the quadratic case, the relative magnitudes of the couplings y_h^{ij} are quite sensitive to the neutrino-mass ordering, as dictated in Eq. (3.17). Together with the flavour-dependent suppression factors $\sim \log(m_k/m_l)$, this efficiently determines the relative size of the different radiative charged-lepton decay channels in the photon-penguin limit. On the contrary, note how the contributions from box diagrams outperform those from photon penguins for $\tau \to 3\mu$ in the case of NO, as can be seen in Fig. 3.6.

The vertical solid grey lines in Fig. 3.6 indicate the bound induced by $\mu \to e\gamma$ which is the relevant one both for the the linear case and for the quadratic case as long as the photon penguin dominates $\mu \to 3e$. In the numerical scan, the full expression as given in [237] is used, because larger masses M_h generally render larger magnitudes $|y_h^{ij}|$ compatible with the different experimental bounds, which in turn implies that the contributions from box diagrams to tri-lepton decays become increasingly dominant. Since box diagrams are proportional to the product of four Yukawa couplings, they can thus induce contributions to tri-lepton decays which in fact grow if the mass increases beyond $M_h \approx 1\,\mathrm{TeV}$ and further. Thus, h will decouple from the phenomenology at low energy only for even larger masses $M_h \gg 100\,\mathrm{TeV}$. This is distinctively visible in Fig. 3.7 where we show $\tau \to 3e(\mu)$ as

---

[14] We do not expect more stringent constraints from tri-lepton decays with different flavours in the final state and hence we do not consider them.

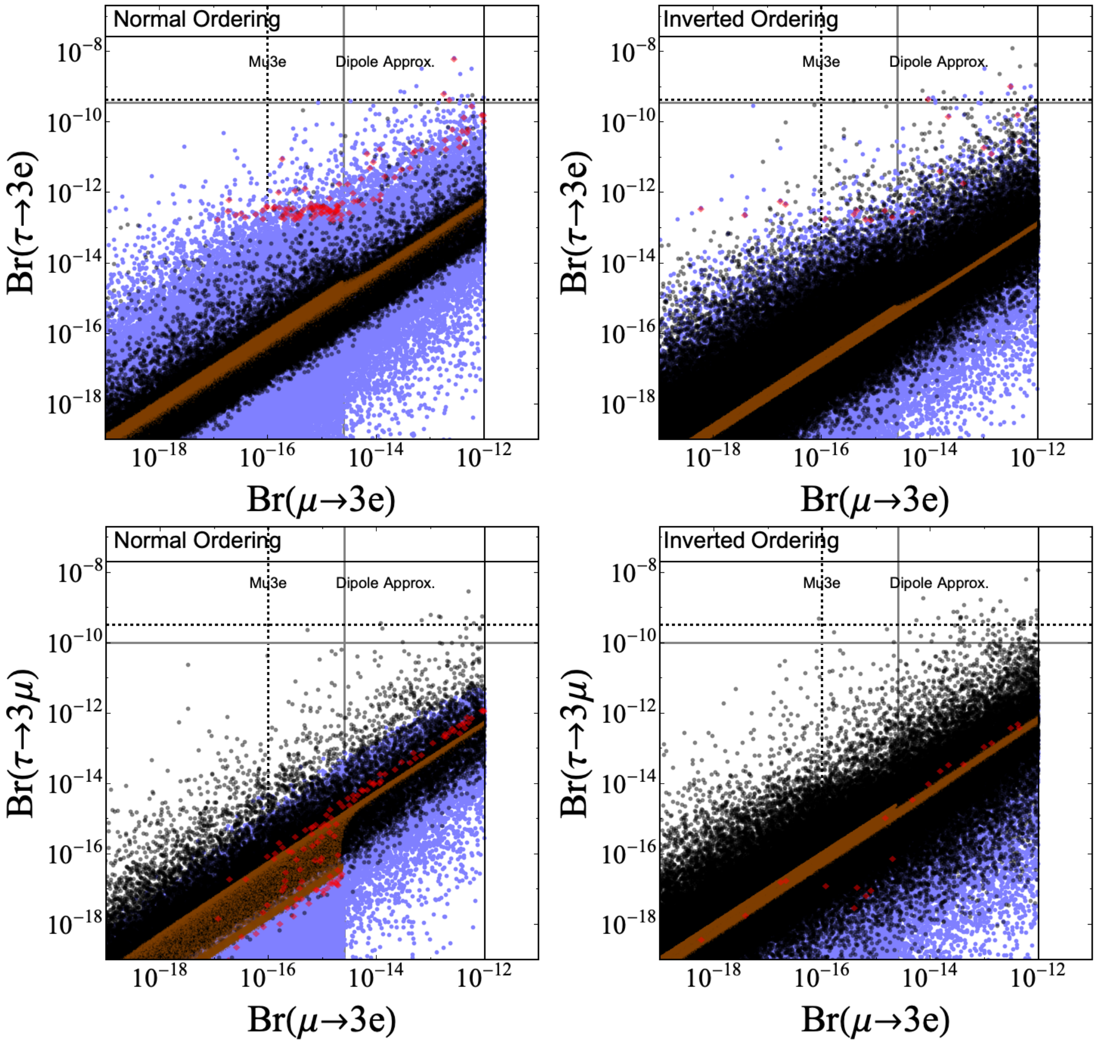

Figure 3.6: Branching ratios of tri-lepton decays. The colours are the same as in Fig. 3.2. The solid grey lines indicate the respective experimental bounds that would apply to the photon-penguin approximation. Dashed lines indicate prospected experimental sensitivities.

a function of the singly-charged scalar singlet mass M_h. As the figures illustrate, masses larger than $M_h \gtrsim 11$ TeV and $M_h \gtrsim 15$ TeV can induce an observable signal in $\tau \to 3e$ and $\tau \to 3\mu$, respectively, at Belle II [7].

Besides $\mu \to 3e$ [243] which will be sensitive both to the linear case and the quadratic case, tri-lepton tau decay thus offer another avenue for testing the generation of neutrino masses via h at larger masses M_h in the linear case, complementary to $\mu \to e\gamma$ for which

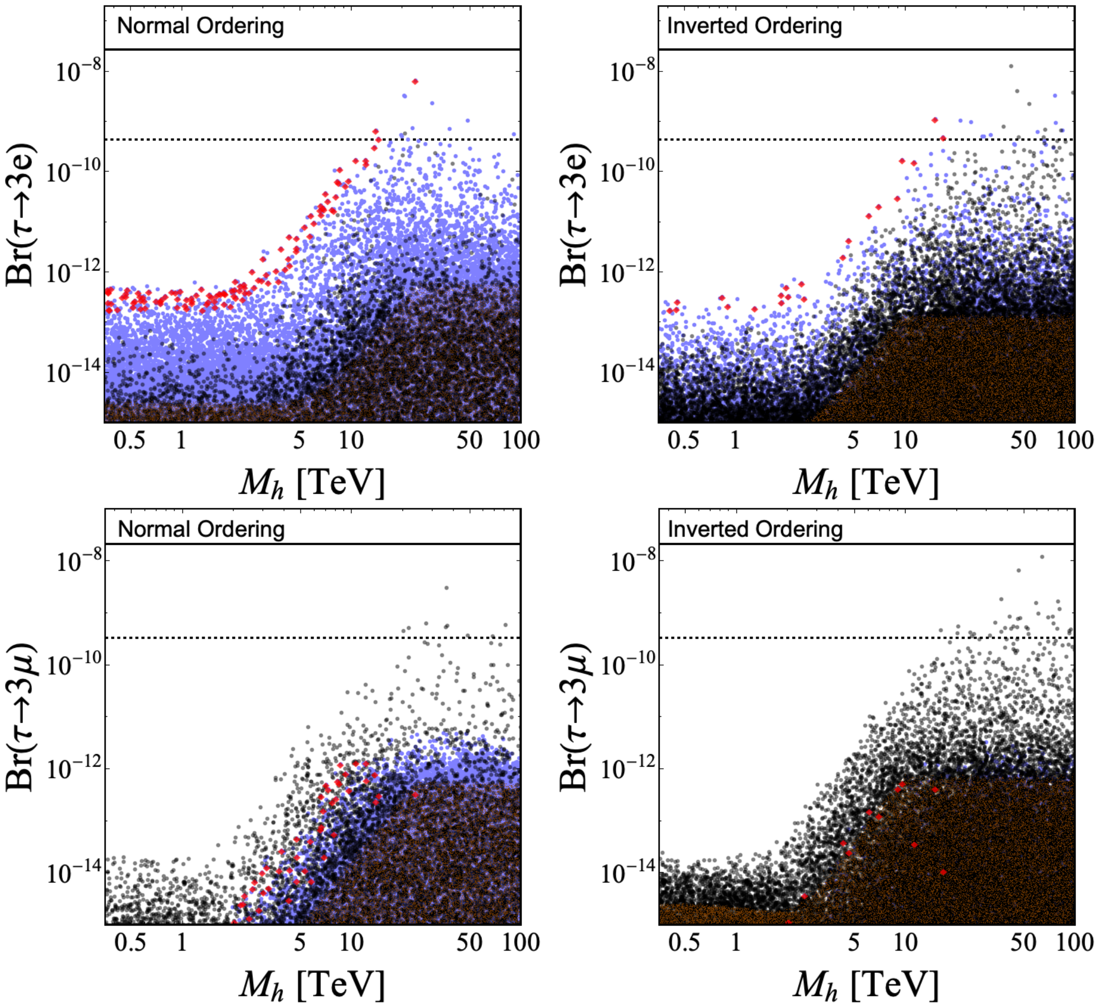

Figure 3.7: Branching ratio of tri-lepton tau decays as a function of the mass M_h. The colours are the same as in Fig. 3.2. Dashed lines indicate prospected experimental sensitivities.

the contributions start to decrease before the assumed upper limit $M_h \leq 100\,\text{TeV}$ is reached. Via $\tau \to 3e$ we are even sensitive to parts of the parameter space for which the flavour anomalies are explained as well [237]. Still, the constraint in Eq. (3.11) disfavours the solutions y_h^{ij} which induce large contributions to $\tau \to 3e(\mu)$ as there needs to be a hierarchy among the coupling magnitudes $|y_h^{e\mu}|$ and $|y_h^{\mu\tau}|$ $(|y_h^{e\tau}|)$ entering the relevant box diagram and $|y_h^{e\tau}|$ $(|y_h^{\mu\tau}|)$ which must be smaller in order not to violate the experimental bound on $\text{Br}(\mu \to e\gamma)$.

A further relevant process is $\mu - e$ conversion in nuclei which probes the same parameter combination as $\mu \to e\gamma$ and is dominated by photon-penguin diagrams. As of today, the strongest constraint arises from the SINDRUM-II experiment in which a gold target was used [275]. Taking into account both the short-range and the long-range contribution (see App. 3.9), one finds $\text{Br}(\mu \to e;\,\text{Au}) \equiv \omega_{\text{conv}}^{\text{Au}}/\omega_{\text{capt}}^{\text{Au}} \approx 0.0130\,\text{Br}(\mu \to e\gamma)$ for $\mu - e$ conversion in gold [237, 276, 277]. Hence, the process does not yield a competitive constraint yet, still, in the photon-penguin approximation it is less suppressed with respect to $\mu \to e\gamma$ than $\mu \to 3e$. In addition, future experiments on $\mu - e$ conversion are prospected to outperform current and future searches for radiative charged-lepton decays in sensitivity by far [278–280]. For instance, PRISM/PRIME can be expected to almost conclusively test the simultaneous explanation of neutrino masses and the flavour anomalies.

As a side note, the singly-charged scalar singlet also generates contributions to anomalous magnetic moments. However, the contribution is always negative [224, 281–283], hence it is not possible to explain the long-standing anomaly $\delta a_\mu \equiv a_\mu^{\text{exp}} - a_\mu^{\text{SM}} \approx 3 \times 10^{-9}$ [284, 285] in the first place. Contributions up to $\delta a_\mu \approx -1 \times 10^{-11}$ and $\delta a_e \approx -1 \times 10^{-16}$ are possible, which is however too small to explain the measured value $\delta a_e \approx -9 \times 10^{-13}$ [286].

3.4.3 Magnitude of Couplings

The constraint in Eq. (3.11) tends to correlate the couplings y_h^{ij} in such a way that in many cases at least two of them are comparable in magnitude, as it can be seen in Fig. 3.8. We show the ratios because the magnitudes $|y_h^{ij}|$ of the elements of v_h in Eq. (3.11) can always

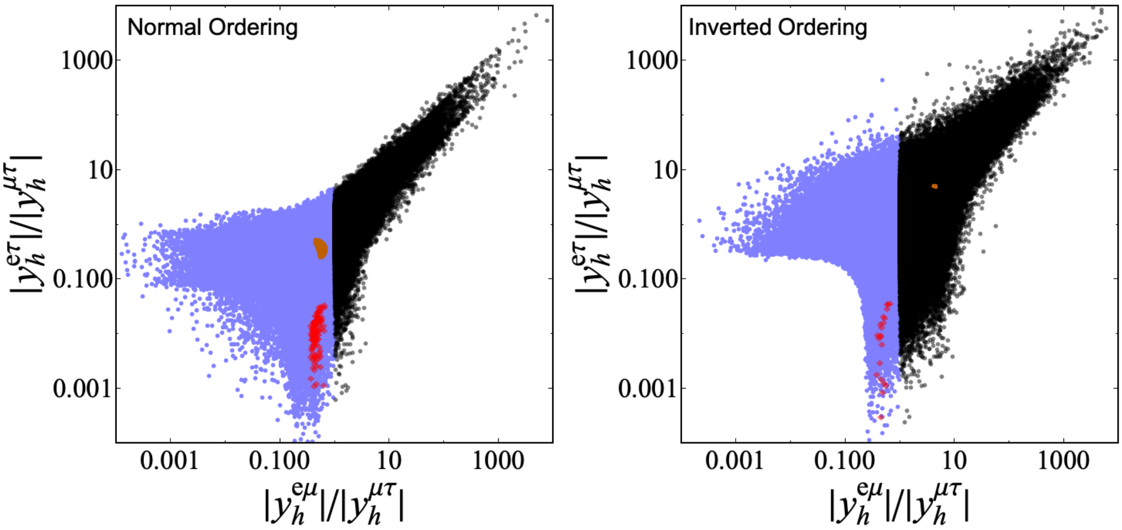

Figure 3.8: Plot of the coupling ratios $|y_h^{e\mu}|/|y_h^{\mu\tau}|$ and $|y_h^{e\tau}|/|y_h^{\mu\tau}|$ as obtained in the numerical scan. The colours are the same as in Fig. 3.2.

.

be rescaled by a common factor and hence only the relative magnitudes are determined via the constraint. It is distinctively visible how viable parameter space opens up upon replacing the condition in Eq. (3.17) by the more general one in Eq. (3.11).

For NO, solutions with $|y_h^{\mu\tau}|$ larger than both $|y_h^{ei}|$, $i = \mu, \tau$ are most abundant and in particular the hierarchies $|y_h^{e\mu}| < |y_h^{\mu\tau}| < |y_h^{e\tau}|$ and $|y_h^{e\tau}| < |y_h^{\mu\tau}| < |y_h^{e\mu}|$ are rather disfavoured, hence, there is a tendency for $|y_h^{\mu\tau}| \gtrsim |y_h^{e\mu}| \approx |y_h^{e\tau}|$. On the contrary, for IO there are smaller differences in how often the different hierarchies are obtained. Note that while the viable regions in parameter space in Fig. 3.8 do in general not feature a sharp contour, the most distinctive deviation from that tendency occurs if both $|y_h^{e\mu}|/|y_h^{\mu\tau}| \lesssim 0.1$ and $|y_h^{e\tau}|/|y_h^{\mu\tau}| \lesssim 0.1$ for which viable solutions seem to be rigorously excluded in the case of IO. Hence, if the coupling $y_h^{\mu\tau}$ was experimentally confirmed to sufficiently dominate over the electron-flavoured ones in magnitude, this would appear to leave us only with the possibility of h generating the main contribution to neutrino masses with NO. The corresponding experimental signature would be a vanishingly small branching ratio for the decay channel $h \to e\nu$, see also Sect. 3.4.4.

Besides, as it can be seen in Fig. 3.9, if $|y_h^{e\mu}| > |y_h^{\mu\tau}|$, which corresponds to black sample

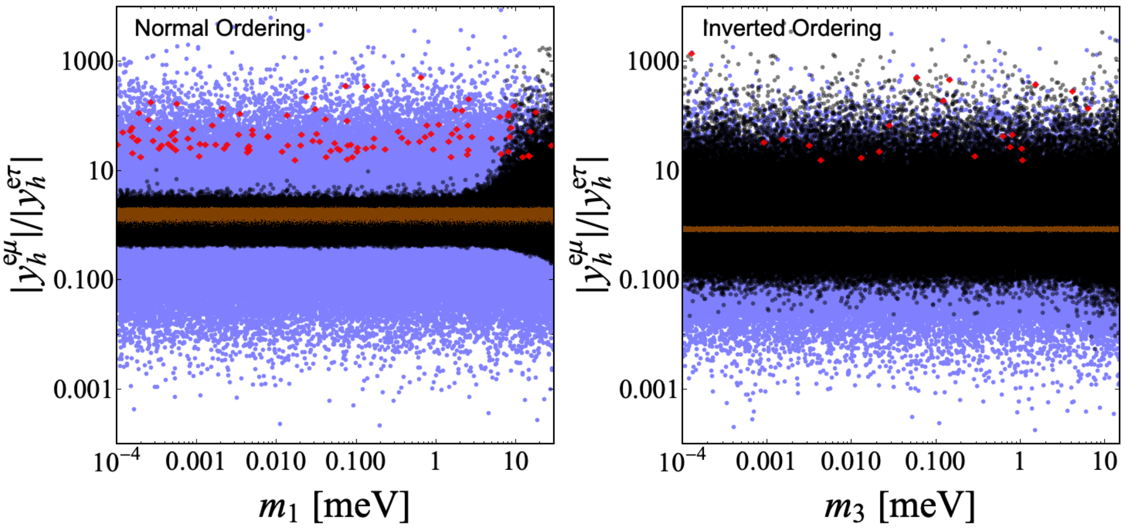

Figure 3.9: Plot of the coupling ratios $|y_h^{e\mu}|/|y_h^{e\tau}|$ as a function of the smallest neutrino mass (m_1 for NO, and m_3 for IO). The colours are the same as in Fig. 3.2.

points, the constraint in Eq. (3.11) further disfavours solutions with $|y_h^{e\mu}|/|y_h^{e\tau}| \lesssim 0.1$. In addition, if the lightest neutrino is not much heavier than $m_0 = m_1 \approx 1\,\text{meV}$ in the case of NO, $|y_h^{e\mu}| > |y_h^{\mu\tau}|$ is only viable for $|y_h^{e\mu}|/|y_h^{e\tau}| \lesssim 10$. We trace this back to the fact that for NO the neutrino mass matrix is known to feature a slight hierarchy between the magnitudes of the components in the first row (and column) and those in the 23-block, which only diminishes if the smallest neutrino mass m_1 becomes large.

Of course, these solutions are not obtained if one solves the constraint in Eq. (3.11) with the additional condition of one Majorana phase and the smallest neutrino mass vanishing. Still, there are no major differences in the obtained phenomenology compared to the general case with three massive neutrinos. In particular, one does not enjoy the same predictive power as in the quadratic case for which the smallest neutrino mass vanishes, $m_0 = 0$, automatically. On the contrary, for IO the $|M_\nu^{ij}|$ are more similar in magnitude and less sensitive to m_3, and thus so are the $|y_h^{ij}|$.

Furthermore, a determination of the relative size of the regions in the parameter space of coupling magnitudes which are compatible only with NO or with IO, or with both is performed. The strategy is to discretise the parameter space into a grid structure and to count the sample points contained in each grid square, starting with the square containing

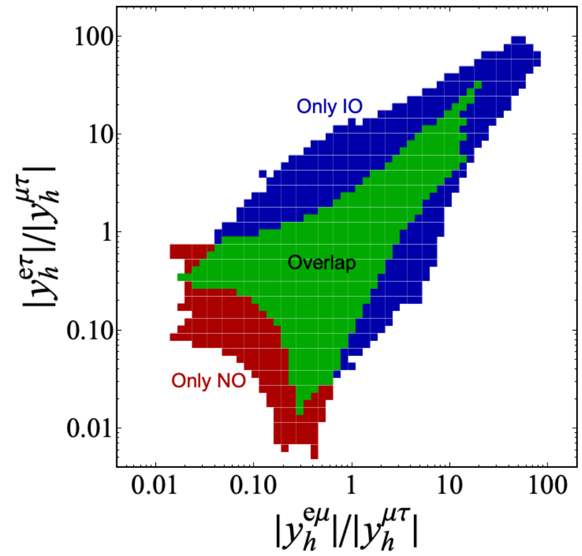

Figure 3.10: Plot of the coupling ratios $|y_h^{e\mu}|/|y_h^{\mu\tau}|$ and $|y_h^{e\tau}|/|y_h^{\mu\tau}|$ as obtained in the numerical scan if approximately 95.45 % of the overall number of 547991 (542287) sample points generated for NO (IO) are taken into account. Each square shown to be compatible with NO (IO) contains at least 97 (74) sample points. See also main text.

the largest number of points and then gradually moving on to those with fewer points, until a specified portion of the overall number of sample points is taken into account. Fig. 3.10 shows the region of approximately 95.45 % of the sample points.

3.4.4 Decay Channels of the Singly-Charged Scalar Singlet

The partial width of the decay of a singly-charged scalar singlet into a charged lepton ℓ and a neutrino ν is given by [224]

$$\Gamma(h \to \ell_a \nu_b) = \Gamma(h \to \ell_b \nu_a) = \frac{|y_h^{ab}|^2}{4\pi} M_h \,. \tag{3.46}$$

Leaving the undetected neutrino flavour unspecified, one obtains the branching ratio for the decay of h into a charged lepton of flavour a and a neutrino:

$$\mathrm{Br}(h \to \ell_a \nu) = \frac{\sum_{b\neq a} |y_h^{ab}|^2}{2(|y_h^{e\mu}|^2 + |y_h^{e\tau}|^2 + |y_h^{\mu\tau}|^2)} \,. \tag{3.47}$$

Regardless of whether the magnitudes $|y_h^{ij}|$ are constrained in some way or not, the individual branching ratios always take a value between 0 and 0.5.

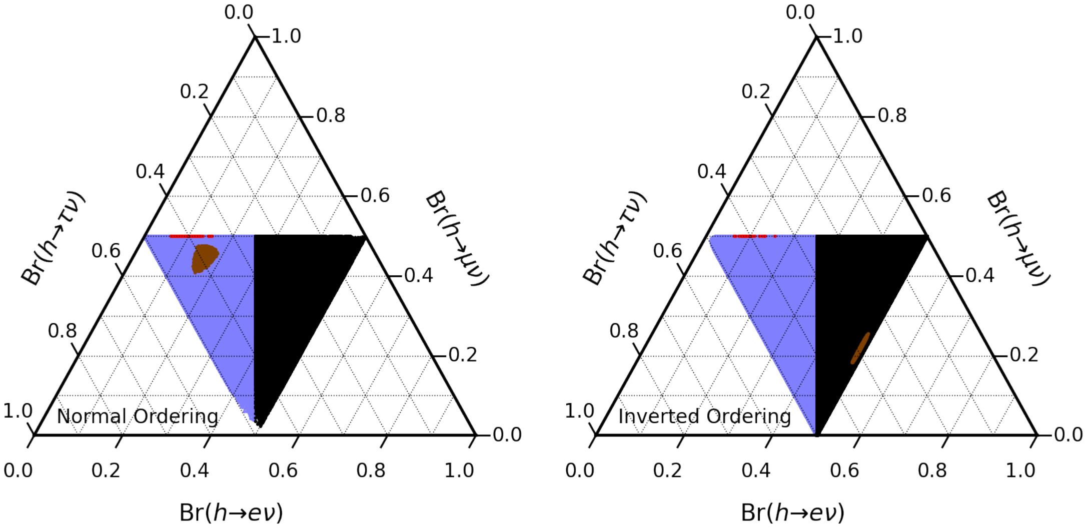

Figure 3.11: Branching ratios of $h \to \ell\nu$. The colours are the same as in Fig. 3.2.

A very small or vanishing branching ratio for the electron channel (and consequently $\mathrm{Br}(h \to \mu\nu) \approx \mathrm{Br}(h \to \tau\nu) \approx 0.5$) is supported in NO, but severely disfavoured for IO, as it can be seen in Fig. 3.11. Contrariwise, obtaining a (near-)maximal branching to taus and a small one to muons is disfavoured by NO, but compatible with IO. For the more restrictive constraint in Eq. (3.17), the muon and tau channels exhibit a slight correlation with the CP-violating phase δ in the case of NO which is illustrated in Fig. 3.12 and has been discussed before in [226] for the Zee-Babu model. It is due to the fact that for IO δ only fixes the phases $\arg(y_h^{ei})$, while it also determines $|y_h^{\mu\tau}|$ in the case of NO.

3.5 Multiple Singly-Charged Scalar Singlets

Lastly, we comment on the possibility of generating $1, ..., n$ sizeable contributions to neutrino masses via multiple singly-charged scalar singlets $h_1, ..., h_n$ and focus on $n = 2$ for simplicity.

The overall lepton sector for two singly-charged singlet scalars is given by

$$\mathcal{L}_{\text{lept}} = y_e^{ij} \bar{e}_i L_j H^* + y_{h_1}^{ij} L_i L_j h_1 + y_{h_2}^{ij} L_i L_j h_2 + \text{h.c.}. \tag{3.48}$$

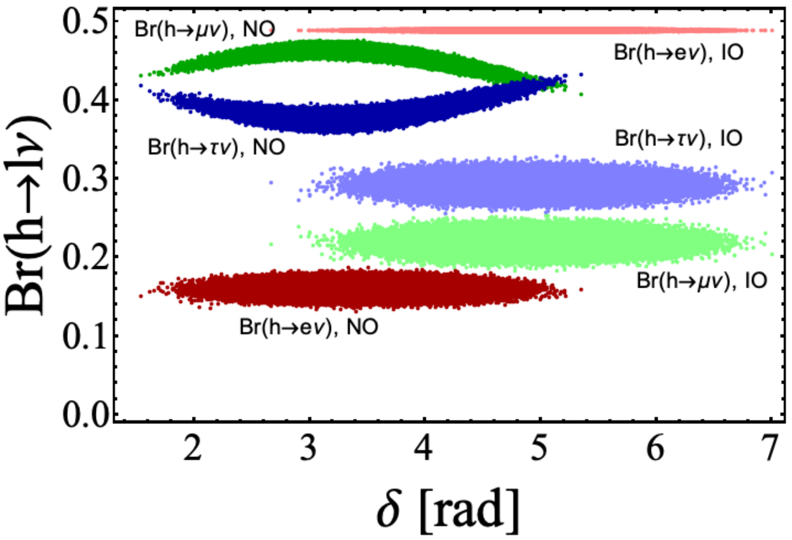

Figure 3.12: Branching ratios of the different channels $h \to \ell\nu$ as functions of the Dirac CP phase δ in the quadratic case (Case II).

We again can distinguish the linear and the quadratic case and focus on the latter first. We assume that the main contribution to neutrino masses consists of diagrams in which both external neutrinos couple to the respective loop structure via y_{h_1} or y_{h_2}. Then, the most general neutrino mass matrix reads

$$U^* m_{\text{diag}} U^\dagger = M_\nu = y_{h_1}^T S_1 y_{h_1} + y_{h_2}^T S_2 y_{h_2} + y_{h_1}^T Z y_{h_2} + y_{h_2}^T Z^T y_{h_1} \,, \tag{3.49}$$

with the symmetric coupling matrices $S_{1,2}$ and a general matrix Z. Multiplying Eq. (3.49) by the respective eigenvectors $v_{h_{1,2}}$ of $y_{h_{1,2}}$ with eigenvalue zero, one obtains three inequivalent complex conditions:

$$v_{h_1}^T U^* m_{\text{diag}} U^\dagger v_{h_1} = v_{h_1}^T y_{h_2}^T S_2 y_{h_2} v_{h_1} \,, \tag{3.50a}$$

$$v_{h_2}^T U^* m_{\text{diag}} U^\dagger v_{h_1} = v_{h_2}^T y_{h_1}^T Z y_{h_2} v_{h_1} \,, \tag{3.50b}$$

$$v_{h_2}^T U^* m_{\text{diag}} U^\dagger v_{h_2} = v_{h_2}^T y_{h_1}^T S_1 y_{h_1} v_{h_2} \,. \tag{3.50c}$$

Contrary to the linear case and the quadratic case discussed for one singly-charged scalar singlet before, here the constraint explicitly involves the matrices $S_{1,2}$ and Z which parametrise the breaking of lepton-number conservation. In that sense, Eqs. (3.50a)-(3.50c) are in general model-dependent and hence less predictive. In App. 3.10 we present one possible neutrino mass model with two singly-charged scalar singlets as an example.

In explicit models, some of the matrices $S_{1,2}, Z$ may vanish in the case of an additional symmetry. Then, the respective expressions above would simplify accordingly and one could solve them as in the linear case. Still, irrespective of the specific structures in $S_{1,2}$ and Z, all Eqs. (3.50a)-(3.50c) have to be individually satisfied. Thus, the contributions $y_{h_1}^T S_1 y_{h_1}$ and $y_{h_2}^T S_2 y_{h_2}$ are not independent, but the elements of y_{h_1} and y_{h_2} are intertwined via each of the right-hand sides and in particular also via the left-hand side of Eq. (3.50b) even if Z is taken to zero. Only if both Z and one of the matrices S_1 and S_2 are absent, one trivially recovers the quadratic case for one singly-charged scalar singlet. The same limit is obtained for a large hierarchy between the masses of h_1 and h_2 since one may integrate out the heavier singlet and attain more predictive power. Lastly, it is straightforward to generalise Eq. (3.49) towards the case of n singly-charged scalar singlets generating sizeable contributions to neutrino masses.[15]

In the linear case, one would generalise the structure of the neutrino mass matrix towards

$$U^* m_{\text{diag}} U^\dagger = M_\nu = X_1 y_{h_1} - y_{h_1} X_1^T + X_2 y_{h_2} - y_{h_2} X_2^T \,. \tag{3.51}$$

Still, there is no non-trivial limit in which the derived constraints would become independent of the model-dependent physics in $X_{1,2}$.

3.6 Conclusions

We have presented a classification and phenomenological study for scenarios in which a singly-charged scalar singlet particle h generates the main contribution to neutrino masses. Among the SM fermions, h interacts only with the left-handed lepton doublets via an antisymmetric Yukawa coupling $y_h LLh + \text{h.c.}$ at tree level. It is possible to assign charges of lepton number to h and the SM leptons in a way such that it is respected by all renormalisable terms in the Lagrangian. Thus, in order to generate Majorana masses for neutrinos, one needs to introduce a source of lepton-number breaking. Our approach

---

[15] See for instance [287, 288] for studies of variants of the Zee-Babu model which contain three singly-charged scalar singlets.

is independent of the details of this breaking. *The only assumption is that the main contribution of neutrino masses is generated by a diagram in which one or both of the external neutrinos couples via y_h.*

For the minimal case of just one singlet state, this gives rise to only two possible structures for the neutrino mass matrix. Regarding the Feynman diagram which generates the main contribution to neutrino masses, we distinguish between the “linear case" in which only one external neutrino is linked to the loop structure via y_h, and the “quadratic case" in which both external neutrinos are. Several well-known models of neutrino-mass generation fall into those two categories: The Zee model [60–62] is an example for the linear case and the Zee-Babu [63–65] and KNT models [66] are examples for the quadratic case.

For each of the cases, we employ the antisymmetry of y_h in flavour space to derive a model-independent constraint which has to be satisfied to guarantee the correct description of the measured mixing and mass hierarchy of neutrinos. In the linear case, the constraint determines two of the magnitudes of the Yukawa coupling matrix elements $|y_h^{ij}|$ in terms of the third one, the two phases of y_h^{ei}, $i = \mu, \tau$, neutrino masses, leptonic mixing angles and phases. In the quadratic case, the two constraints are independent of the neutrino masses and Majorana phases and thus more predictive.

This enables us to perform a phenomenological study applicable to many different types of models. The study is conservative in the sense that no other contributions to the considered observables beyond the ones induced by h are taken into account. If the other new particles involved in a specific model are sufficiently decoupled in the sense that they are very heavy or very weakly coupled to the SM, the phenomenological bounds obtained will approximately coincide with those of the actual model, otherwise the bounds will be weaker. This is trivially satisfied in an effective field theory framework, in which the singly-charged scalar singlet is much lighter than all other new particles.

For the linear case, the constraint disfavours large hierarchies among the coupling magnitudes y_h^{ij} and hence the available parameter space is mostly shaped by $\mu \to e\gamma$ and $\mu \to 3e$ and other low-energy processes are generally not competitive. The relative magnitudes

$|y_h^{ij}|$ display some sensitivity to the neutrino-mass ordering. Furthermore, we demonstrate that the region in parameter space where the Cabibbo Angle Anomaly and the deviation of leptonic gauge couplings from universality, collectively dubbed the “flavour anomalies", are explained by h is compatible with, albeit not preferred by neutrino masses. A conclusive measurement of $M_W > 80.35\,\text{GeV}$ would imply that h cannot explain the flavour anomalies.

For the quadratic case, the parameter space is strongly constrained by neutrino masses and thus the scenario is very predictive. The leptonic gauge couplings do not receive large contributions and thus it is not possible to explain their deviation from universality as indicated by current data and neither the Cabibbo Angle Anomaly. Furthermore, there is a tight correlation between the different radiative charged-lepton decays and hence any signal of a radiative flavour-violating tau decay at Belle II would imply that low-energy effects of new physics cannot be assumed to be dominated by h. Also, one may derive sharp predictions for the branching ratios of the different decay channels to satisfy $\text{Br}(h \to \tau\nu) \simeq \text{Br}(h \to \mu\nu) \sim 0.4$ and $\text{Br}(h \to e\nu) \lesssim 0.2$ for NO and $\text{Br}(h \to \tau\nu) \sim 0.3$, $\text{Br}(h \to \mu\nu) \sim 0.2$ and $\text{Br}(h \to e\nu) \sim 0.5$ for IO. The branching ratios $\text{Br}(h \to \tau\nu)$ and $\text{Br}(h \to \mu\nu)$ exhibit a slight dependence on the Dirac CP phase δ for NO.

Finally, we commented on the generalisation of our framework to multiple singly-charged scalar singlets. One may also derive constraints in that case, but they depend on the breaking of lepton number and thus do not allow for a model-independent study.

To conclude, this study of the singly-charged scalar singlet h is a neat example of a model-independent towards neutrino masses and their phenomenological implications. The constraints originate only from the form of the neutrino mass matrix and the antisymmetry of the Yukawa coupling of h to left-handed lepton doublets. We leave the discussion of other simplified neutrino mass scenarios for future work.

3.7 Appendix: Neutrino-Mass Constraint Spelt in Full

Written out, the constraint in Eq. (3.11) explicitly reads

$$
\begin{aligned}
&\Bigg(\Big(c_{13}^2 m_3 c_{23}^2 + e^{-2i\eta_2} m_2 \left(e^{-i\delta} c_{23} s_{12} s_{13} + c_{12} s_{23}\right)^2 + \\
&\quad e^{-2i\eta_1} m_1 \left(e^{-i\delta} c_{12} c_{23} s_{13} - s_{12} s_{23}\right)^2 \Big) y_h^{\mathrm{e}\mu} \\
&-\Big(c_{23} m_3 s_{23} c_{13}^2 + e^{-2i\eta_1} m_1 \left(e^{-i\delta} c_{12} c_{23} s_{13} - s_{12} s_{23}\right) \left(c_{23} s_{12} + e^{-i\delta} c_{12} s_{13} s_{23}\right) \\
&-e^{-2i\eta_2} m_2 \left(e^{-i\delta} c_{23} s_{12} s_{13} + c_{12} s_{23}\right) \left(c_{12} c_{23} - e^{-i\delta} s_{12} s_{13} s_{23}\right) \Big) y_h^{\mathrm{e}\tau} \\
&+c_{13}\Big(e^{i\delta} c_{23} m_3 s_{13} - e^{-2i\eta_2} m_2 s_{12} \left(e^{-i\delta} c_{23} s_{12} s_{13} + c_{12} s_{23}\right) \\
&+e^{-2i\eta_1} c_{12} m_1 \left(s_{12} s_{23} - e^{-i\delta} c_{12} c_{23} s_{13}\right) \Big) y_h^{\mu\tau} \Bigg) y_h^{\mathrm{e}\mu} \\
&-\Bigg(\Big(c_{23} m_3 s_{23} c_{13}^2 + e^{-2i\eta_1} m_1 \left(e^{-i\delta} c_{12} c_{23} s_{13} - s_{12} s_{23}\right) \left(c_{23} s_{12} + e^{-i\delta} c_{12} s_{13} s_{23}\right) \\
&-e^{-2i\eta_2} m_2 \left(e^{-i\delta} c_{23} s_{12} s_{13} + c_{12} s_{23}\right) \left(c_{12} c_{23} - e^{-i\delta} s_{12} s_{13} s_{23}\right) \Big) y_h^{\mathrm{e}\mu} \\
&-\Big(c_{13}^2 m_3 s_{23}^2 + e^{-2i\eta_1} m_1 \left(c_{23} s_{12} + e^{-i\delta} c_{12} s_{13} s_{23}\right)^2 \\
&\quad + e^{-2i\eta_2} m_2 \left(c_{12} c_{23} - e^{-i\delta} s_{12} s_{13} s_{23}\right)^2 \Big) y_h^{\mathrm{e}\tau} \\
&-e^{i\delta} c_{13}\Big(e^{-2i(\delta+\eta_1)} m_1 s_{13} s_{23} c_{12}^2 + e^{-i\delta} c_{23} \left(e^{-2i\eta_1} m_1 - e^{-2i\eta_2} m_2\right) s_{12} c_{12} \\
&- \left(m_3 - e^{-2i(\delta+\eta_2)} m_2 s_{12}^2\right) s_{13} s_{23}\Big) y_h^{\mu\tau} \Bigg) y_h^{\mathrm{e}\tau} \\
&+\Bigg(c_{13}\Big(e^{i\delta} c_{23} m_3 s_{13} - e^{-2i\eta_2} m_2 s_{12} \left(e^{-i\delta} c_{23} s_{12} s_{13} + c_{12} s_{23}\right) \\
&+e^{-2i\eta_1} c_{12} m_1 \left(s_{12} s_{23} - e^{-i\delta} c_{12} c_{23} s_{13}\right) \Big) y_h^{\mathrm{e}\mu} \\
&+e^{i\delta} c_{13}\Big(e^{-2i(\delta+\eta_1)} m_1 s_{13} s_{23} c_{12}^2 + e^{-i\delta} c_{23} \left(e^{-2i\eta_1} m_1 - e^{-2i\eta_2} m_2\right) s_{12} c_{12} \\
&- \left(m_3 - e^{-2i(\delta+\eta_2)} m_2 s_{12}^2\right) s_{13} s_{23}\Big) y_h^{\mathrm{e}\tau} \\
&+ \left(e^{-2i\eta_2} m_2 s_{12}^2 c_{13}^2 + e^{-2i\eta_1} c_{12}^2 m_1 c_{13}^2 + e^{2i\delta} m_3 s_{13}^2\right) y_h^{\mu\tau} \Bigg) y_h^{\mu\tau} = 0\,,
\end{aligned}
\tag{3.52}
$$

with the abbreviations $s_{ij} \equiv \sin(\theta_{ij})$ and $c_{ij} \equiv \cos(\theta_{ij})$.

3.8 Appendix: Effective Four-Lepton Operator

Starting from the full theory as defined via Eqs. (3.1) and (3.2), one obtains the lowest-order solution to the classical equation of motion for h:

$$h = -\frac{(y_h^{ij})^*}{M_h^2} L_j^\dagger L_i^\dagger \,. \tag{3.53}$$

The resulting effective Lagrangian reads

$$\mathcal{L}_{\text{eff}} = \frac{(y_h^{ij})^* y_h^{kl}}{M_h^2} L_j^\dagger L_i^\dagger L_k L_l = \frac{(y_h^{ik})^* y_h^{jl}}{M_h^2} L_i^{\dagger\alpha} \bar\sigma^\mu L_{j\alpha} L_k^{\dagger\beta} \bar\sigma_\mu L_{l\beta}. \tag{3.54}$$

In order to derive this result, one first observes that

$$L_j^\dagger L_i^\dagger L_k L_l = L_j^{\dagger\alpha} L_i^{\dagger\beta} L_{k\beta} L_{l\alpha} - L_j^{\dagger\alpha} L_i^{\dagger\beta} L_{k\alpha} L_{l\beta}. \tag{3.55}$$

Together with the antisymmetry of y_h, this implies

$$\frac{(y_h^{ij})^* y_h^{kl}}{M_h^2} L_j^\dagger L_i^\dagger L_k L_l = 2\frac{(y_h^{ij})^* y_h^{kl}}{M_h^2} L_j^{\dagger\alpha} L_i^{\dagger\beta} L_{k\beta} L_{l\alpha}. \tag{3.56}$$

Then, applying a Fierz transformation and relabeling flavour indices yields the result

$$\begin{aligned} \frac{(y_h^{ij})^* y_h^{kl}}{M_h^2} L_j^\dagger L_i^\dagger L_k L_l &= \frac{(y_h^{ij})^* y_h^{kl}}{M_h^2} L_j^{\dagger\alpha} \bar\sigma^\mu L_{l\alpha} L_i^{\dagger\beta} \bar\sigma_\mu L_{k\beta} \\ &= \frac{(y_h^{ik})^* y_h^{jl}}{M_h^2} L_i^{\dagger\alpha} \bar\sigma^\mu L_{j\alpha} L_k^{\dagger\beta} \bar\sigma_\mu L_{l\beta} \equiv C_{LL}^{ijkl} \mathcal{O}_{LL,ijkl}. \end{aligned} \tag{3.57}$$

3.9 Appendix: $\mu - e$ Conversion in Nuclei

We consider the photon-penguin contribution to the effective Lagrangian for $\mu - e$ conversion in nuclei and neglect all other contributions following [237]. In addition to the short-range contribution which has been discussed in [237] we also include the relevant long-range contribution. Following [277], we identify the relevant terms

$$\mathcal{L}_{\text{eff}} = -4\sqrt{2} G_F \left(m_\mu A_R \bar\mu \sigma^{\mu\nu} e F_{\mu\nu} + \text{h.c.}\right) - \frac{G_F}{\sqrt{2}} \sum_{q=u,d,s} \left[g_{LV(q)}\, e^\dagger \bar\sigma^\mu \mu \left(q^\dagger \bar\sigma_\mu q + \bar q \sigma_\mu \bar q^\dagger\right) \right] \tag{3.58}$$

in the effective Lagrangian, where the “barred" fields denote the charge-conjugates of the respective right-handed fields and we employ the 2-component notation for spinors as detailed in [93]. The Wilson coefficients are given by [237]

$$A_R = -\frac{1}{2\sqrt{2}G_F}\frac{\sqrt{4\pi\alpha_{\mathrm{EM}}}}{96\pi^2 M_h^2} y_h^{e\tau}(y_h^{\mu\tau})^*, \qquad g_{LV(q)} = -\frac{\sqrt{2}}{G_F}\frac{4\pi\alpha_{\mathrm{EM}}Q_q}{72\pi^2 M_h^2}(y_h^{e\tau})^* y_h^{\mu\tau}\,, \tag{3.59}$$

where Q_q denotes the electric quark charge, $Q_u = \frac{2}{3}$ and $Q_d = -\frac{1}{3}$. The resulting conversion rate is [277]

$$\omega_{\mathrm{conv}} = 2G_F^2 m_\mu^5 \left| A_R^* D + \tilde{g}_{LV}^{(p)} V^{(p)} + \tilde{g}_{LV}^{(n)} V^{(n)} \right|^2 \tag{3.60}$$

in terms of the couplings to protons and neutrons. The coupling to neutrons vanishes, $\tilde{g}_{LV}^{(n)} = g_{LV(u)} + 2g_{LV(d)} = 0$, because the photon-penguin contribution is proportional to the electric charge of the nucleon, and the effective coupling to the proton is

$$\tilde{g}_{LV}^{(p)} = 2g_{LV(u)} + g_{LV(d)} = -\frac{\sqrt{2}\alpha_{\mathrm{EM}}}{18\pi G_F M_h^2}(y_h^{e\tau})^* y_h^{\mu\tau}\,. \tag{3.61}$$

Hence we find the conversion rate

$$\omega_{\mathrm{conv}} = \left|(y_h^{e\tau})^* y_h^{\mu\tau}\right|^2 \left| \frac{\alpha_{\mathrm{EM}}^{1/2} D}{96\pi^{3/2}} + \frac{\alpha_{\mathrm{EM}} V^{(p)}}{9\pi} \right|^2 \frac{m_\mu^5}{M_h^4}\,. \tag{3.62}$$

The experimental limits for $\mu - e$ conversion are generally quoted in terms of the ratio of the conversion rate ω_{conv} over the capture rate ω_{capt} [277, 289], $\mathrm{Br}(\mu \to e;\, \mathrm{X}) \equiv \omega_{\mathrm{conv}}^{\mathrm{X}}/\omega_{\mathrm{capt}}^{\mathrm{X}}$. For $X = \mathrm{Au}, \mathrm{Al}, \mathrm{Ti}$ we use

$$\omega_{\mathrm{capt}}^{\mathrm{Au}} = 13.06 \times 10^6\,\frac{1}{\mathrm{s}}, \qquad \omega_{\mathrm{capt}}^{\mathrm{Al}} = 0.7054 \times 10^6\,\frac{1}{\mathrm{s}}, \qquad \omega_{\mathrm{capt}}^{\mathrm{Ti}} = 2.59 \times 10^6\,\frac{1}{\mathrm{s}}. \tag{3.63}$$

Currently, the SINDRUM II experiment places the strongest limit on $\mu - e$ conversion in gold [275] with $\mathrm{Br}(\mu \to e;\, \mathrm{Au}) \equiv \omega_{\mathrm{conv}}^{\mathrm{Au}}/\omega_{\mathrm{capt}}^{\mathrm{Au}} < 7 \times 10^{-13}$. In the coming years, several experiments with improved sensitivity will probe unexplored parameter space using $\mu - e$ conversion: The Mu2e experiment at Fermilab [278] and the COMET experiment [279] are expected to reach a sensitivity of 6×10^{-17} and 2.6×10^{-17}, respectively, for an aluminum target. Ultimately, PRISM/PRIME [280] is projected to reach a sensitivity of 10^{-18} for a titanium target. The relevant overlap integrals for the long-range and short-range photon-penguin contributions to $\mu - e$ conversion in gold, aluminum and titanium are given by

D, $V^{(n)}$ and $V^{(p)}$:

$$\begin{aligned} D_{\rm Au} &= 0.189\ , & V^{(p)}_{\rm Au} &= 0.0974\ , & V^{(n)}_{\rm Au} &= 0.146\ , \\ D_{\rm Al} &= 0.0362\ , & V^{(p)}_{\rm Al} &= 0.0161\ , & V^{(n)}_{\rm Al} &= 0.0173\ , \\ D_{\rm Ti} &= 0.0864\ , & V^{(p)}_{\rm Ti} &= 0.0396\ , & V^{(n)}_{\rm Ti} &= 0.0468\ . \end{aligned} \tag{3.64}$$

3.10 Appendix: Generalised Zee-Babu Model

A natural example of the quadratic case with two singly-charged scalar singlets is given by a generalised version of the Zee-Babu model. Hence, consider the extension of the SM particle content by two singly-charged scalar singlets h_1 and h_2 and a doubly-charged scalar singlet k. Assuming the mass basis for the singly-charged scalar singlets and neglecting all terms in the scalar potential which are unrelated to the breaking of lepton-number conservation, one finds the following Lagrangian:

$$\begin{aligned} \mathcal{L} = &-h_1^*(D^\mu D_\mu + M_1^2)h_1 - h_2^*(D^\mu D_\mu + M_2^2)h_2 - k^*(D^\mu D_\mu + M_k^2)k \\ &- \Big(\Big(\mu_1 h_1^2 + \mu_2 h_2^2 + \mu_{12} h_1 h_2\Big)\, k^* + \text{h.c.}\Big) \\ &- \Big(y_e^* L^\dagger H \bar{e}^\dagger + y_{h_1} LL h_1 + y_{h_2} LL h_2 + y_k \bar{e}^\dagger \bar{e}^\dagger k + \text{h.c.}\Big)\ . \end{aligned} \tag{3.65}$$

The contribution to neutrino masses corresponding to S_1 (S_2) which is defined in Eq. (3.49) can be obtained as in the Zee-Babu model and is proportional to μ_1/M_k^2 (μ_2/M_k^2) in the limit $M_k/M_h \gg 1$.[16] To our knowledge, a similar limit for the contribution corresponding to Z has not been considered yet, but in analogy it may be expected to be proportional to μ_{12}/M_k^2. There are up to fifteen parameters in the model which are directly linked to neutrino masses: μ_1, μ_2, μ_{12}, six couplings in y_k and three couplings both in y_{h_1} and in y_{h_2}. In general, up to six of them can be determined via the constraint in Eqs. (3.50a)-(3.50c) upon fixing the other parameters. A detailed study of the full generalised Zee-Babu model is left for future work.

---

[16] This assumption may be relaxed without altering the form of the dominant contribution to neutrino masses. Still, the relevant loop function acquires a simple form only in the limits $M_k/M_h \gg 1$ and $M_k/M_h \to 0$ [224, 226, 236].

In the case of a further hierarchy between the masses M_1 and M_2 (which is assumed not to be cancelled by another hierarchy in $|\mu_1|$ and $|\mu_2|$), such that the contribution of the heavier singly-charged scalar singlet both to neutrino masses and to other flavour observables can be neglected with respect to the lighter one, one may integrate out the former. Hence, assuming $M_2 \gg M_{1,k}$ and integrating out h_2, we obtain the following effective Lagrangian up to dimension-6 terms:

$$\begin{aligned}\mathcal{L}_{\text{eff}} \supseteq & -h_1^*(D^\mu D_\mu + M_1^2)h_1 - k^*(D^\mu D_\mu + M_k^2)k - \left(\mu_1 h_1^2 k^* + \text{h.c.}\right) - \left(y_{h_1}^{ij} L_i L_j h_1 + \text{h.c.}\right) \\ & - \left(\frac{\mu_2^* y_{h_2}^{ij} y_{h_2}^{kl}}{M_2^4} k L_i L_j L_k L_l + \text{h.c.}\right) + \left(\frac{\mu_{12}^* y_{h_2}^{ij}}{M_2^2} k h_1^* L_i L_j + \text{h.c.}\right) + \frac{(y_{h_2}^{ij})^* y_{h_2}^{kl}}{M_2^2} L_k L_l L_j^\dagger L_i^\dagger \\ & - \left(y_k \bar{e}^\dagger \bar{e}^\dagger k + \text{h.c.}\right) . \end{aligned} \tag{3.66}$$

This corresponds to the Zee-Babu model extended by effective interactions. Thus, in the effective field theory limit $M_2 \gg M_{1,k}$ the dominant contribution to neutrino masses is given by the renormalisable terms and therefore the same as in Eq. (3.25) for $h \to h_1$.

3.11 Erratum to: The Singly-Charged Scalar Singlet as the Origin of Neutrino Masses

Taking only contributions to the Fermi constant into account, the correction to the gauge coupling $g_2 = e/s_\theta$ reads

$$\delta g_2 = -\frac{g_2}{c_{2\theta}} \frac{1}{\sqrt{2}} c_\theta^2 \, \delta G_F$$

which corrects for a missing factor c_θ in the first line of Eq. (A.11) in [264]. Thus a singly-charged scalar singlet $h \sim (1,1,1)$ of mass M_h which couples to left-handed leptons as per $y_h^{ij} L_i L_j h + \text{h.c.}$ results in the following correction to the squared W-boson mass at tree level:

$$\delta M_W^2 = -\frac{M_W^2}{\sqrt{2} G_F} \left| 1 - \frac{M_W^2}{2M_W^2 - M_Z^2} \right| \frac{|y_h^{e\mu}|^2}{M_h^2} \, . \tag{4.13}$$

According to this, $|\delta M_W^2|$ is roughly a factor of 2/3 smaller than implied by Eq. (4.13) in [87]. Since we require agreement with the world average of measurements[17] of M_W at 3σ, Eq. (4.13) implies a weaker bound on $|y_h^{e\mu}|/M_h$ and thus a small growth of the available parameter space. Consequently, two quantitative statements in [87] are changed as follows:

- We find that a result $80.348\,\text{GeV} \lesssim M_W \lesssim 80.353\,\text{GeV}$ can be compatible with an explanation of the flavour anomalies at 1σ, as can be seen in Fig. 3.3.
- The coupling $y_h^{e\mu}$ enters box-diagram contributions to trilepton tau decays, and so we find that the minimum mass M_h required to induce an observable signal in $\tau \to 3e$ and $\tau \to 3\mu$ at Belle II is given by $M_h \gtrsim 9$ TeV and $M_h \gtrsim 13$ TeV, respectively, as illustrated in Fig. 3.7. Note that we display the brown sample points on top of the other ones to improve contrast, unlike in Fig. 7 in [87].

More generally, since $y_h^{e\mu}$ is correlated with $y_h^{e\tau}$ and $y_h^{\mu\tau}$ via the neutrino-mass constraint, is it slightly easier to generate viable sample points. Still, their overall distribution in parameter space is not noticeably affected, see Fig. 3.8. The figures shown in this erratum are based on a sample comprising roughly 6.5×10^5 points for each neutrino-mass ordering. As detailed in the caption of Fig. 2 in [87], the colours distinguish between the quadratic case (brown) and the linear case in which the deviation of g_τ/g_e from universality can be explained either only at 3σ (black), or at 2σ (blue) for which an explanation of the flavour anomalies at 1σ (red) is also possible. For completeness, we also provide an updated version of the lower part of Tab. 3.2.

---

[17] As $\delta M_W^2 < 0$ in Eq. (4.13), the singly-charged scalar singlet is not able to explain the recent CDF result [290]. Here, we do not attempt to include the latter in the world average for the W-boson mass, but use the value reported in [29] like in [87].

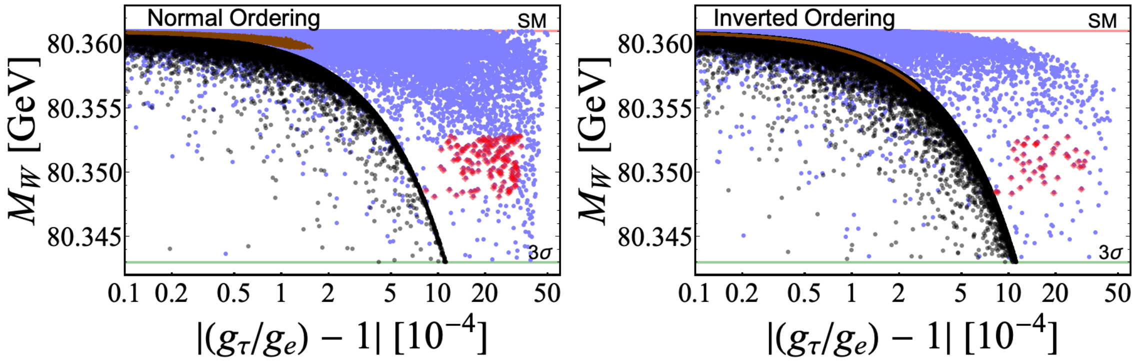

Figure 3.3: Correlations among M_W and deviations of g_τ/g_e from universality. The colours are the same as in Fig. 2.

	Numerical Analysis			
	Linear Case		Quadratic Case .	
Observable	NO	IO	NO	IO
$\mathrm{Br}(\mu \to e\gamma)$	4.2×10^{-13}	4.2×10^{-13}	4.2×10^{-13}	4.2×10^{-13}
$\mathrm{Br}(\tau \to e\gamma)$	9.5×10^{-11}	8.2×10^{-11}	3.3×10^{-13}	6.6×10^{-14}
$\mathrm{Br}(\tau \to \mu\gamma)$	2.4×10^{-11}	2.4×10^{-11}	3.1×10^{-14}	1.5×10^{-12}
$\mathrm{Br}(\mu \to 3e)$	1×10^{-12}	1×10^{-12}	1×10^{-12}	1×10^{-12}
$\mathrm{Br}(\tau \to 3e)$	1.3×10^{-8}	4.3×10^{-9}	7.1×10^{-13}	1.5×10^{-13}
$\mathrm{Br}(\tau \to 3\mu)$	4.2×10^{-9}	6.9×10^{-9}	5.9×10^{-13}	8.5×10^{-13}
$\lvert g_\mu/g_e \rvert$	1.0050	1.0050	1.0002	1.0000
$\lvert g_\tau/g_\mu \rvert$	1.0010	1.0014	1.0000	1.0001
$\lvert g_\tau/g_e \rvert$	1.0050	1.0047	1.0002	1.0000
$\lvert\delta M_W\rvert$[GeV]	0.018	0.018	0.001	0.005

Table 3.2: (lower table only) The upper table contains the current experimental bounds on and future sensitivities to the relevant observables. The lower table shows the respective maximum contribution found in the scan in the linear case and the quadratic case for either neutrino-mass ordering.

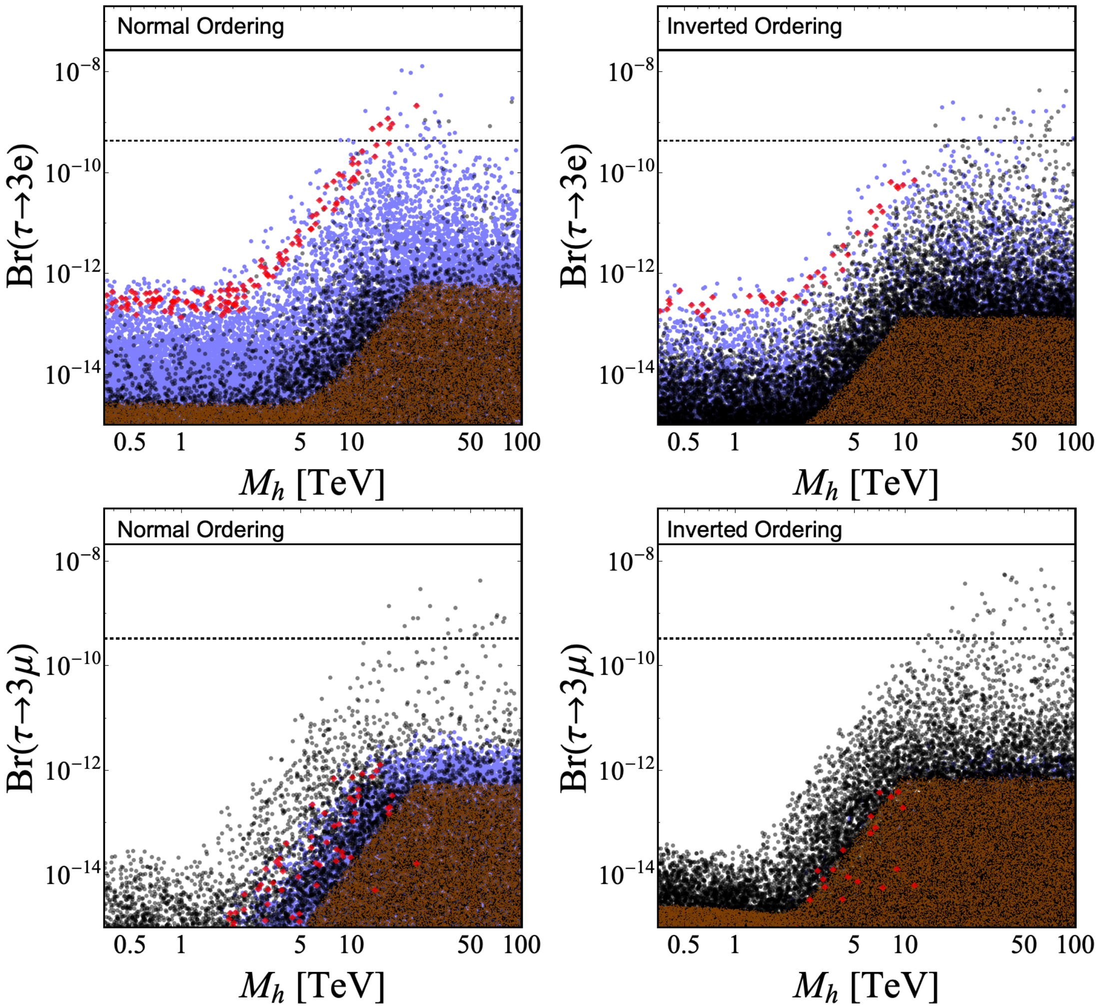

Figure 3.7: Branching ratio of tri-lepton tau decays as a function of the mass M_h. The colours are the same as in Fig. 2. Dashed lines indicate prospected experimental sensitivities.

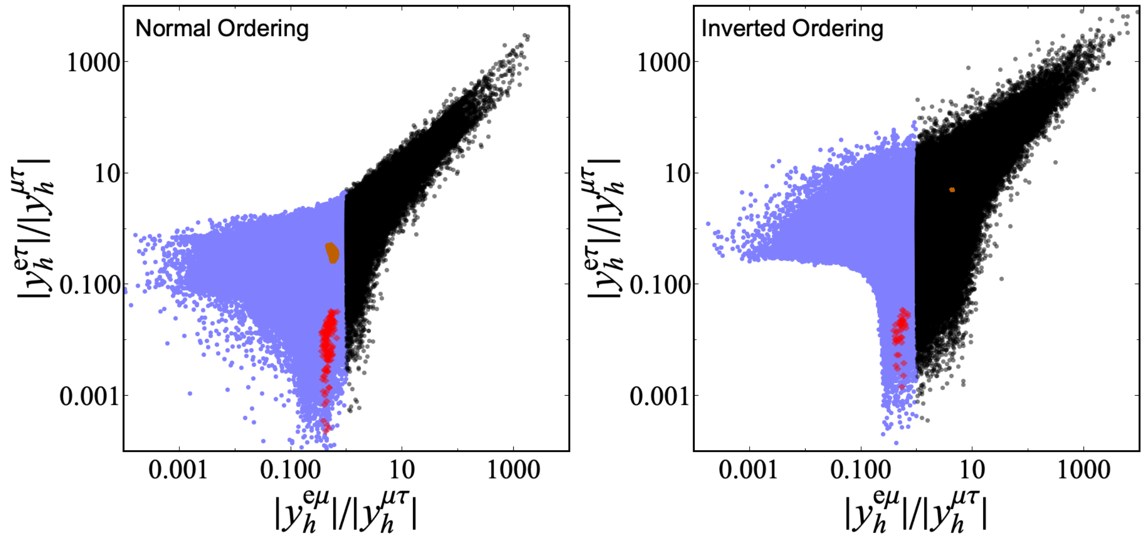

Figure 3.8: Plot of the coupling ratios $|y_h^{e\mu}|/|y_h^{\mu\tau}|$ and $|y_h^{e\tau}|/|y_h^{\mu\tau}|$ as obtained in the numerical scan. The colours are the same as in Fig. 2.

Chapter 4

A Tale of Invisibility: Constraints on New Physics in $b \to s\nu\nu$

After having investigated a simplified neutrino mass model in the last chapter, I now turn to a genuinely model-independent study of existing and prospective data on $b \to s\nu\nu$ decay processes. Working in the context of LEFT and taking into account several decay channels, I derive constraints on contributions from different operators. The results can be matched onto any concrete BSM model which introduces new degrees of freedom close to or above the electroweak scale. The presentation in this chapter is a verbatim adoption of the publication [89].

4.1 Introduction

As of today, we know for sure that the flavour structure of nature is more complicated than what is implied by the Standard Model (SM) of particle physics. This has first become manifest with the measurement of neutrino oscillations which provide conclusive evidence that lepton flavour is not exactly conserved. Currently observed anomalies such as the long-standing tensions between the SM predictions for and measurements of the magnetic dipole moment of the muon [18] as well as in observables related to lepton-flavour universality in semi-leptonic B-meson decays like $R(D^{(*)})$ and $R(K^{(*)})$ (see for instance Ref. [10]) suggest the existence of new physics.

A particularly promising avenue to probe and constrain extensions of the SM is via the investigation of rare processes. In the search for light and weakly-interacting particles, rare processes with missing energy are particularly interesting, because they may not only be enhanced via new intermediate states, but also via exotic sterile final states which escape undetected.

Furthermore, the amplitudes for $b \to s\nu\nu$ transitions completely factorise into a hadronic and a leptonic part and are therefore under very good theoretical control. Indeed, quantum chromodynamics (QCD) involved in exclusive decays is entirely captured via an appropriate set of form factors, whereas the inclusive decay mode is at leading order given by the underlying parton-level process which is calculable in perturbation theory and receives corrections only at quadratic order in the heavy-quark effective theory (HQET) expansion. Processes like $b \to s\nu\nu$ are mediated by flavour-changing neutral currents (FCNCs) which in the SM are suppressed in a rather accidental manner via the Glashow-Iliopoulos-Maiani (GIM) mechanism, which however generically does not hold anymore if flavour-sensitive new physics is introduced. In this paper, we exploit this feature and study the constraining power of measurements of several observables related to the $b \to s\nu\nu$ transition in the light of the expected sensitivity of Belle II [7].

Indeed, due to the large suppression of $b \to s$ transitions as predicted by the SM, currently only experimental upper bounds on the decay channels $B \to K^{(*)}\nu\nu$ and $B \to X_s\nu\nu$ exist. Most recently, the Belle-II collaboration presented a new analysis for $B^+ \to K^+\nu\nu$ [8] and reported an upper bound $\mathrm{Br}(B^+ \to K^+\nu\nu) < 4.1 \times 10^{-5}$ at the 90% confidence level. A simple weighted average of their result with earlier results [24, 291, 292] leads to $\mathrm{Br}(B^+ \to K^+\nu\nu) = (1.1 \pm 0.4) \times 10^{-5}$ [1, 8]. If substantiated further, this would imply an enhancement on top of the SM expectation $\mathrm{Br}(B^+ \to K^+\nu\nu) = (4.4 \pm 0.7) \times 10^{-6}$ [11], which has been interpreted in terms of leptoquarks and Z' bosons [293, 294].

Moreover, if the aforementioned observed tensions in $b \to s\ell\ell$ processes are confirmed as being induced by new physics, this may intriguingly also imply effects in the decay channels with neutrinos, since the latter are part of the same weak-isospin doublets as left-handed charged leptons. Recently, the interplay of the observed anomalies in $b \to s\mu^+\mu^-$ and rare decays such as $B \to K^{(*)}\nu\nu$ and $K \to \pi\nu\nu$ was studied in [295, 296], and [77] provides a more general analysis of the interplay of di-neutrino and di-charged-lepton modes based on the relevant four-fermion vector operators. Finally, an observation of $b \to s\nu\nu$ may place constraints on semi-leptonic B-meson decays with τ leptons in the final state which are currently less precisely determined by experimental data.

There are several earlier model-independent studies of semi-leptonic B-meson decays with final-state neutrinos in terms of effective field theory for different classes of operators. Vector operators with left-handed massless neutrinos have been studied in [70, 71, 74–77]. Contributions from scalar and tensor operators were taken into account in [72, 73], but no dependence on (sterile) neutrino mass and consequently neither any interference between scalar, vector and tensor operators. The inclusive mode $B \to X_s\nu\nu$ was studied earlier in [67–69, 74] where only vector operators were taken into account. Reference [297] contains an investigation of the process $B \to X_s\ell^+\ell^-$ including contributions from scalar and tensor operators which can be applied to $B \to X_s\nu\nu$.

We go beyond previous work by considering the full set of dimension-6 operators in low-energy effective theory (LEFT) which contribute to $b \to s\nu\nu$ [192, 298] for an arbitrary number of generations to account for the possible existence of massive sterile neutrinos. Right-handed sterile neutrinos ν_R are included as left-handed fields $\nu_R^c \equiv C\overline{\nu_R}^T$. There are only five operators at dimension 6, i.e. vector and scalar operators with left-handed and right-handed quark bilinears, respectively, and tensor operators with left-handed quark bilinears. The dimension-5 dipole operators are already strongly constrained from searches for neutrino magnetic dipole moments [299, 300] (see [301] for a recent review) and are thus not considered.

In this work, we investigate the current constraints on the dimension-6 LEFT operators and their improvement in the light of the future sensitivity of Belle II. We discuss the implications of an interpretation of the aforementioned simple weighted average of $\mathrm{Br}(B^+ \to K^+ \nu\nu)$ in terms of an additional sterile neutrino. We also provide the leading-order result for the inclusive decay mode $B \to X_s \nu\nu$ with all contributing operators including interference terms and arbitrary masses for both final-state neutrinos. Our results are entirely general and can be matched onto any specific new-physics model yielding non-zero contributions to one or several of the considered operators.

The paper is organised as follows. The effective field theory framework is explained in Sec. 4.2. In Sec. 4.3 we introduce the considered observables and present compact expressions for massless neutrinos. In Sec. 4.4 we discuss the results of our phenomenological study and conclude in Sec. 4.5. Expressions for the observables in the case of massive neutrinos as well as further technical details are summarised in the appendices.

4.2 Effective Field Theory Framework

We consider the Standard Model extended by an arbitrary number of sterile neutrinos and work entirely within LEFT [192]. The matching of the LEFT operators to SM effective field theory (SMEFT) operators is presented in App. 4.11. Throughout the paper, we assume massless SM neutrinos $\nu_{1,2,3}$, i.e. they refer both to flavour eigenstates and to mass eigenstates. We neglect mixing between active $\nu_{1,2,3}$ and sterile neutrinos $\nu_{4,\ldots}$, thus we also treat the latter as well-defined mass and flavour eigenstates. The relevant interactions for $b \to s\nu\nu$ processes are described by the Lagrangian [192, 298]

$$\mathcal{L} = \sum_{X=L,R} C_{\nu d}^{\mathrm{VLX}} \mathcal{O}_{\nu d}^{\mathrm{VLX}} + \left(\sum_{X=L,R} C_{\nu d}^{\mathrm{SLX}} \mathcal{O}_{\nu d}^{\mathrm{SLX}} + C_{\nu d}^{\mathrm{TLL}} \mathcal{O}_{\nu d}^{\mathrm{TLL}} + \text{h.c.} \right) \tag{4.1}$$

with the effective operators

$$\begin{aligned} \mathcal{O}_{\nu d}^{\mathrm{VLL}} &= (\overline{\nu_L} \gamma_\mu \nu_L)(\overline{d_L} \gamma^\mu d_L) & \mathcal{O}_{\nu d}^{\mathrm{VLR}} &= (\overline{\nu_L} \gamma_\mu \nu_L)(\overline{d_R} \gamma^\mu d_R) \\ \mathcal{O}_{\nu d}^{\mathrm{SLL}} &= (\overline{\nu_L^c} \nu_L)(\overline{d_R} d_L) & \mathcal{O}_{\nu d}^{\mathrm{SLR}} &= (\overline{\nu_L^c} \nu_L)(\overline{d_L} d_R) \\ \mathcal{O}_{\nu d}^{\mathrm{TLL}} &= (\overline{\nu_L^c} \sigma_{\mu\nu} \nu_L)(\overline{d_R} \sigma^{\mu\nu} d_L) \,, \end{aligned} \tag{4.2}$$

where the superscripts indicate the chirality and $\nu_L^c \equiv C \overline{\nu_L}^T$ with the charge conjugation matrix $C = i\gamma^2\gamma^0$. Note that the scalar operators $\mathcal{O}_{\nu d}^{\mathrm{SLL}}$, $\mathcal{O}_{\nu d}^{\mathrm{SLR}}$ are symmetric in the neutrino flavours and the tensor operator $\mathcal{O}_{\nu d}^{\mathrm{TLL}}$ is antisymmetric in the neutrino flavours as shown in Eq. (4.57). The vector operators $\mathcal{O}_{\nu d}^{\mathrm{VLL}}$, $\mathcal{O}_{\nu d}^{\mathrm{VLR}}$ do not exhibit any manifest symmetry properties. As the dimension-5 neutrino dipole operator $\overline{\nu_L^c}\sigma^{\mu\nu}\nu_L F_{\mu\nu}$ only contributes together with the dipole operator $\overline{d_L}\sigma^{\mu\nu}d_R F_{\mu\nu}$ for down-type quarks, it effectively contributes at the same order in the LEFT expansion. Still, both dipole operators are only generated at loop-level and thus further suppressed. Moreover, the neutrino dipole operator is strongly constrained by searches for magnetic dipole moments of neutrinos [299,300] (see [301] for a recent review). Hence we do not include contributions from the neutrino dipole operator in this study.

The Weyl fermions ν_L for the neutrino fields and their respective charge conjugate can be combined to form Majorana neutrino fields $\nu \equiv \nu_L + \nu_L^c$, e.g. the scalar operator $\mathcal{O}_{\nu d}^{\mathrm{SLL}}$ can be rewritten as $\mathcal{O}_{\nu d}^{\mathrm{SLL}} = (\overline{\nu} P_L \nu)(\overline{d_R} d_L)$ where we explicitly included the chiral projection operators $P_{L,R} = \frac{1}{2}(1 \mp \gamma_5)$. The vector and axial-vector Majorana neutrino bilinears are antisymmetric and symmetric in the neutrino flavours, respectively. In App. 4.7 we present the matching to a basis in terms of (pseudo)scalar, (axial)vector and tensor neutrino bilinears which we use for the exclusive decays following [302].

Most of the relevant Wilson coefficients (WCs) are zero in the SM. The only sizeable non-vanishing WC which contributes to $b \to s\nu_\alpha\overline{\nu_\alpha}$ is

$$C_{\nu d,\alpha\alpha sb}^{\mathrm{VLL,SM}} = -\frac{4G_F}{\sqrt{2}}\frac{\alpha}{2\pi}V_{ts}^* V_{tb}\left(\frac{X}{\sin^2\theta_W}\right) , \tag{4.3}$$

including two-loop electroweak corrections induced by top quarks as captured by the function X. The latter has been calculated in [303] and is numerically given by [11] $X = 6.402\sin^2\theta_W$.

In LEFT the dominant quantum corrections originate from QCD running. The vector (and axial-vector) current operators do not run at one-loop order because of the Ward identity. However, the scalar and tensor currents do exhibit renormalisation group (RG) running and their one-loop RG equations for the corresponding Wilson coefficients are well-known (see e.g. [298,304])

$$\mu\frac{d}{d\mu}C_{\nu d}^{\mathrm{SLL}} = -3C_F\,\frac{\alpha_s}{2\pi}\,C_{\nu d}^{\mathrm{SLL}}, \quad \mu\frac{d}{d\mu}C_{\nu d}^{\mathrm{TLL}} = C_F\,\frac{\alpha_s}{2\pi}\,C_{\nu d}^{\mathrm{TLL}} \tag{4.4}$$

where $C_F = (N_c^2 - 1)/2N_c = 4/3$ and $N_c = 3$ is the second Casimir invariant of the colour group $SU(3)_c$ and $\alpha_s = g_s^2/(4\pi)$ is the strong fine structure constant. Here, one may exchange SLL ↔ SLR. The solutions to the above equations are given by

$$C_{\nu d}^{\rm SLL}(\mu_1) = \left(\frac{\alpha_s(\mu_2)}{\alpha_s(\mu_1)}\right)^{3C_F/b} C_{\nu d}^{\rm SLL}(\mu_2) \,, \qquad C_{\nu d}^{\rm TLL}(\mu_1) = \left(\frac{\alpha_s(\mu_2)}{\alpha_s(\mu_1)}\right)^{-C_F/b} C_{\nu d}^{\rm TLL}(\mu_2) \tag{4.5}$$

between two scales μ_1 and μ_2. Here $b = -11 + \frac{2}{3}n_f$ with n_f being the number of active quark flavors between μ_1 and μ_2, and one may exchange $C_{\nu d}^{\rm SLL} \leftrightarrow C_{\nu d}^{\rm SLR}$. We use RunDec [305] to obtain precise values for the strong fine structure constant at the different scales. Numerically, we find for the Wilson coefficients at the hadronic scale $\mu = 4.8$ GeV as a function of the Wilson coefficients at the scale $\mu = m_Z$

$$\begin{aligned} &C_{\nu d}^{\rm SLL}(4.8{\rm GeV}) = 1.370\, C_{\nu d}^{\rm SLL}(m_Z) \,, \quad C_{\nu d}^{\rm TLL}(4.8{\rm GeV}) = 0.900\, C_{\nu d}^{\rm TLL}(m_Z) \,, \\ &C_{\nu d}^{\rm SLR}(4.8{\rm GeV}) = 1.370\, C_{\nu d}^{\rm SLR}(m_Z) \,. \end{aligned} \tag{4.6}$$

4.3 Observables $b \to s\nu\nu$

In our analysis we consider the two exclusive decays $B \to K^{(*)}\nu\nu$ and the inclusive decay $B \to X_s\nu\nu$ decay. While the only observable for $B \to K\nu\nu$ is the differential branching ratio because the final-state neutrinos escape the detector unobserved, the decay to a vector meson $B \to K^*(\to K\pi)\nu\nu$ provides additional angular information which is contained in the K^* longitudinal polarisation fraction F_L [74, 76]. Belle II is anticipated to measure the different branching ratios for $B \to K^{(*)}\nu\nu$ at the level of 10% with the full integrated luminosity and will also be sensitive to F_L [7]. Throughout this work we use the $B \to K$ form factors in [6] and the $B \to K^*$ form factors in [5], the analytical expressions for which are summarised in App 4.6. Both of them are based on a combined fit to data extracted from light-cone sum rules (LCSR) and lattice QCD (LQCD). We summarise the SM predictions[1], current constraints and future sensitivities in Tab. 4.1. There is no

---

[1] We used `flavio` [11,12] to determine the SM uncertainties of the exclusive decays. Our results for the central values of the SM prediction are the same. Using $B \to K^*$ form factors based on the LCSR+LQCD in [6] yields slightly smaller values for the branching ratio and the longitudinal polarisation fraction F_L, but within the quoted theoretical errors. Our

Observable	SM prediction	current constraint	Belle II [7]	
	LQCD+LCSR		5 ab^{-1}	50 ab^{-1}
$\text{Br}(B^0 \to K^0\nu\nu)$	$(4.1 \pm 0.5) \times 10^{-6}$ [12]	$< 2.6 \times 10^{-5}$ [24][2]		
$\text{Br}(B^+ \to K^+\nu\nu)$	$(4.4 \pm 0.7) \times 10^{-6}$ [12]	$< 1.6 \times 10^{-5}$ [292]	30%	11%
$\text{Br}(B^0 \to K^{*0}\nu\nu)$	$(11.6 \pm 1.1) \times 10^{-6}$ [12]	$< 1.8 \times 10^{-5}$ [24]	26%	9.6%
$\text{Br}(B^+ \to K^{*+}\nu\nu)$	$(12.4 \pm 1.2) \times 10^{-6}$ [12]	$< 4.0 \times 10^{-5}$ [291]	25%	9.3%
$F_L(B^0 \to K^{*0}\nu\nu)$	0.49 ± 0.04 [12]			0.079
$F_L(B^+ \to K^{*+}\nu\nu)$	0.49 ± 0.04 [12]			0.077
$\text{Br}(B \to X_s\nu\nu)$	$(2.7 \pm 0.2) \times 10^{-5}$ [74]	$< 6.4 \times 10^{-4}$ [306]		

Table 4.1: Observables for $b \to s\nu\nu$. The SM predictions for the exclusive decays and their uncertainties are based on light-cone sum rules (LCSR) and lattice QCD and are taken from [6] for $B \to K\nu\nu$ and from [5] for $B \to K^*\nu\nu$ including a 10% increase of the $B \to K^*$ form factors due to finite-width effects [39]. The last two columns list the Belle-II sensitivities to exclusive B-meson decays to a $K^{(*)}$ meson and active neutrinos [7] if the respective SM predictions are assumed.

projection for the inclusive decay $B \to X_s\nu\nu$ [7].

Recently, the Belle II collaboration presented a new analysis with a new upper bound $\text{Br}(B^+ \to K^+\nu\nu) < 4.1 \times 10^{-5}$ [1, 8]. A simple weighted average of the result with previous analyses [24, 291, 292] results in $\text{Br}(B^+ \to K^+\nu\nu) = (1.1 \pm 0.4) \times 10^{-5}$ [1, 8] which suggests an enhancement over the SM expectation. We discuss its implications in terms of new physics in Sec. 4.4.4.

For the discussion of the exclusive decays $B \to K^{(*)}\nu\nu$ we employ the helicity formalism [307] and make use of the general discussion in [302] which employs the narrow-width approximation. Finite-width effects have been considered for $B \to K^*$ form factors in [39, 308]. Following [39] we increase all $B \to K^*$ form factors by 10% to take these effects into account. In order to check our results, we performed independent calculations for $B \to K\nu\nu$ without the use of helicity amplitudes [309] and for $B \to K^*\nu\nu$ using transversity amplitudes [310]. Finally, we find agreement when comparing our results to a

---

result for the inclusive decay slightly overestimates the branching ratio by about 20%, because it does not take into account QCD and subleading HQET corrections, and hence we refer to [74] for the SM prediction.

[2] Reference [24] quotes the upper bound on the branching ratio for $B^0 \to K^0_S\nu\nu$ which we translated to $B^0 \to K^0\nu\nu$.

calculation of exclusive decays in the SM extended with vector operators with `flavio` [12] and the calculation of the inclusive decay in [74].

4.3.1 $B \to K\nu\nu$

After integrating over the phase space of the final state neutrinos which escape the detector unobserved, the differential decay width reads [302]

$$\frac{d\Gamma(B \to K\nu_\alpha\nu_\beta)}{dq^2} = \frac{1}{4}\bar{G}^{(0)}(q^2)\ , \tag{4.7}$$

where q^2 denotes the square of the 4-momentum of the neutrino pair and $\bar{G}^{(0)}(q^2)$ is the coefficient of the Wigner-D function $D^0_{0,0}(\Omega_\nu) = 1$[3]. In App. 4.8 we report the function $G^{(0)}(q^2)$ which describes the CP-conjugate process $\bar{B} \to \bar{K}\nu_\alpha\nu_\beta$. It is related to $\bar{G}^{(0)}$ via replacing all Wilson coefficients by their complex conjugates.

We refer the reader to App. 4.8 for the full expression with massive neutrinos as it is lengthy, and only quote the differential decay rate for massless neutrinos

$$\begin{aligned}\frac{d\Gamma(B \to K\nu_\alpha\nu_\beta)}{dq^2} =& \frac{\sqrt{\lambda_{BK}}q^2}{(4\pi)^3 m_B^3(1+\delta_{\alpha\beta})}\Bigg[\frac{\lambda_{BK}}{24q^2}|f_+|^2\left|C^{\mathrm{VLL}}_{\nu d,\alpha\beta sb} + C^{\mathrm{VLR}}_{\nu d,\alpha\beta sb}\right|^2 \\ &+ \frac{(m_B^2-m_K^2)^2}{8(m_b-m_s)^2}|f_0|^2\Big(\left|C^{\mathrm{SLL}}_{\nu d,\alpha\beta sb} + C^{\mathrm{SLR}}_{\nu d,\alpha\beta sb}\right|^2 + \left|C^{\mathrm{SLL}}_{\nu d,\alpha\beta bs} + C^{\mathrm{SLR}}_{\nu d,\alpha\beta bs}\right|^2\Big) \\ &+ \frac{2\lambda_{BK}}{3(m_B+m_K)^2}|f_T|^2\left(\left|C^{\mathrm{TLL}}_{\nu d,\alpha\beta sb}\right|^2 + \left|C^{\mathrm{TLL}}_{\nu d,\alpha\beta bs}\right|^2\right) + (\alpha \leftrightarrow \beta)\Bigg]\end{aligned} \tag{4.8}$$

where λ_{BK} is an abbreviation for the Källén function evaluated as $\lambda_{BK} \equiv \lambda(m_B^2, m_K^2, q^2)$.

Note that there is no interference between scalar, vector and tensor operators for massless neutrinos due to the different chiralities of the final-state neutrinos and the symmetry properties of the scalar and tensor operators. As expected, the differential decay rate is symmetric under exchange of the final-state neutrinos and also under exchange of the quark-flavour indices $sb \leftrightarrow bs$ for the scalar and tensor operators. The same exchange symmetries hold for massive neutrinos.

---

[3] Ω_ν denotes the solid angle of ν_α in the centre of mass frame of the neutrino pair.

4.3.2 $B \to K^*(\to K\pi)\nu\nu$

As the final-state neutrinos escape unobserved from the detector, there are two independent observables which can be parameterised in terms of the coefficients $\bar{G}_0^{0,0}$ and $\bar{G}_0^{2,0}$ of the Wigner-D functions in the differential decay rate [302]

$$\frac{d\Gamma(B \to K^*\nu_\alpha\nu_\beta)}{dq^2 d\cos\theta_K} = \frac{3}{8}\left[\bar{G}_0^{0,0}(q^2)D^0_{0,0}(\Omega_K) + \bar{G}_0^{2,0}(q^2)D^2_{0,0}(\Omega_K)\right] \tag{4.9}$$

where q^2 denotes the square of the 4-momentum of the neutrino pair. The relevant Wigner-D functions are $D^0_{0,0}(\Omega_K) = 1$ and $D^2_{0,0}(\Omega_K) = \frac{1}{2}\left(3\cos^2\theta_K - 1\right)$[4] and their coefficients $\bar{G}$ are given in App. 4.9. The CP conjugate process $\bar{B} \to \bar{K}^*\nu_\alpha\nu_\beta$ is obtained by replacing the $\bar{G}$ functions with the corresponding G functions $G_0^{0,0}$ and $G_0^{2,0}$ for which all Wilson coefficients are replaced by their complex conjugates.

As there are two observable final-state particles K and π in addition to the missing energy of the neutrino pair, there are two independent observables, the differential decay rate $d\Gamma/dq^2$ and the longitudinal polarisation fraction $F_L(q^2)$ [311],

$$\frac{d\Gamma}{dq^2} = \frac{3}{4}\bar{G}_0^{0,0}(q^2)\,, \qquad F_L(q^2) = \frac{\bar{G}_0^{0,0}(q^2) + \bar{G}_0^{2,0}(q^2)}{3\bar{G}_0^{0,0}(q^2)}\,. \tag{4.10}$$

The corresponding transverse polarisation fraction F_T is related to the longitudinal polarisation fraction by $F_L + F_T = 1$. Experiments measure the integrated longitudinal polarisation fraction

$$F_L = \frac{\left\langle \bar{G}_0^{0,0}(q^2)\right\rangle + \left\langle \bar{G}_0^{2,0}(q^2)\right\rangle}{3\left\langle \bar{G}_0^{0,0}(q^2)\right\rangle}\,, \tag{4.11}$$

where angle brackets denote the binning over q^2 including a summation over the final-state neutrino flavours[5]

$$\langle X \rangle \equiv \sum_{\alpha,\beta} \frac{1}{(q_1^2 - q_0^2)} \int_{q_0^2}^{q_1^2} dq^2 X\,. \tag{4.12}$$

The analytic expressions in the general case of massive neutrinos are lengthy and reported in App. 4.9, but there are compact expressions for massless neutrinos. In this case, the

---

[4] Ω_K denotes the solid angle of the final-state K meson in the K^* rest frame.

[5] If no endpoints $q_{0,1}$ are specified, the full kinematic range is integrated over.

differential decay rate is given by

$$\begin{aligned}
\frac{d\Gamma(B\to K^*\nu_\alpha\nu_\beta)}{dq^2} =& \frac{\sqrt{\lambda_{BK^*}}q^2}{(4\pi)^3 m_B^3(1+\delta_{\alpha\beta})}\left[\frac{\lambda_{BK^*}|V|^2}{12(m_B+m_{K^*})^2}\left|C^{\mathrm{VLL}}_{\nu d,\alpha\beta sb}+C^{\mathrm{VLR}}_{\nu d,\alpha\beta sb}\right|^2\right.\\
&+\left(\frac{8m_B^2m_{K^*}^2}{3q^2}|A_{12}|^2+\frac{(m_B+m_{K^*})^2|A_1|^2}{12}\right)\left|C^{\mathrm{VLL}}_{\nu d,\alpha\beta sb}-C^{\mathrm{VLR}}_{\nu d,\alpha\beta sb}\right|^2\\
&+\frac{\lambda_{BK^*}}{8(m_b+m_s)^2}|A_0|^2\Big(\left|C^{\mathrm{SLR}}_{\nu d,\alpha\beta sb}-C^{\mathrm{SLL}}_{\nu d,\alpha\beta sb}\right|^2+\left|C^{\mathrm{SLR}}_{\nu d,\alpha\beta bs}-C^{\mathrm{SLL}}_{\nu d,\alpha\beta bs}\right|^2\Big)\\
&+\left(\frac{32m_B^2m_{K^*}^2|T_{23}|^2}{3(m_B+m_{K^*})^2}+\frac{4\lambda_{BK^*}|T_1|^2+4(m_B^2-m_{K^*}^2)^2|T_2|^2}{3q^2}\right)\\
&\left.\times\left(\left|C^{\mathrm{TLL}}_{\nu d,\alpha\beta bs}\right|^2+\left|C^{\mathrm{TLL}}_{\nu d,\alpha\beta sb}\right|^2\right)+(\alpha\leftrightarrow\beta)\right]
\end{aligned} \tag{4.13}$$

where $\lambda_{BK^*}=\lambda(m_B^2,m_{K^*}^2,q^2)$. The longitudinal polarisation fraction reads

$$\begin{aligned}
F_L = 1-&\sum_{\alpha,\beta}\frac{1}{3(4\pi)^3m_B^3(1+\delta_{\alpha\beta})\Gamma(B\to K^*\nu\nu)}\int dq^2\sqrt{\lambda_{BK^*}}\\
&\times\left(\frac{\lambda_{BK^*}|V|^2q^2}{4(m_B+m_{K^*})^2}\left|C^{\mathrm{VLL}}_{\nu d,\alpha\beta sb}+C^{\mathrm{VLR}}_{\nu d,\alpha\beta sb}\right|^2+\frac{(m_B+m_{K^*})^2q^2|A_1|^2}{4}\left|C^{\mathrm{VLL}}_{\nu d,\alpha\beta sb}-C^{\mathrm{VLR}}_{\nu d,\alpha\beta sb}\right|^2\right.\\
&\left.+\Big(2\lambda_{BK^*}|T_1|^2+2(m_B^2-m_{K^*}^2)^2|T_2|^2\Big)\left(\left|C^{\mathrm{TLL}}_{\nu d,\alpha\beta sb}\right|^2+\left|C^{\mathrm{TLL}}_{\nu d,\alpha\beta bs}\right|^2\right)+(\alpha\leftrightarrow\beta)\right),
\end{aligned} \tag{4.14}$$

where we integrate over the full kinematic range in q^2. As it is the case for $B\to K\nu\nu$ there is no interference between the scalar, vector, and tensor operators because of the different chiralities and the symmetry properties of the scalar and tensor Wilson coefficients.

4.3.3 $B \to X_s \nu\nu$

Formally, the inclusive decay rate of a hadron H is related to its full propagator in the relevant effective theory described by a Hamiltonian $\mathcal{H}_{\mathrm{eff}}$ via the optical theorem [312]

$$\Gamma(H)=\frac{1}{m_H}\mathrm{Im}\left\langle H\left|i\int d^4x\ \mathrm{T}\{\mathcal{H}_{\mathrm{eff}}(x)\mathcal{H}_{\mathrm{eff}}(0)\}\right|H\right\rangle\ . \tag{4.15}$$

In the case of B hadrons, the comparatively large b-quark mass allows for an efficient expansion of the time-ordered product in terms of local operators defined in heavy-quark effective theory (HQET). The leading term in this expansion is determined by the decay width of a free b quark, and corrections only appear at $\mathcal{O}(\Lambda^2_{\rm QCD}/m_b^2)$ in the heavy-quark limit as it was first demonstrated in [313]. The fact that, at leading order, inclusive hadron decays are equivalent to the underlying partonic processes is seen as a manifestation of the notion of “quark-hadron duality" (see for instance Ref. [97] for a review). For semi-leptonic inclusive decays, this enforces integrating out the phase space to a sufficiently large extent which is often referred to as a “smearing procedure".

The rate of the inclusive decay $B \to X_s\nu\nu$ is very sensitive to m_b. Besides the HQET corrections, there are also radiative QCD corrections to the leading-order result, the size of which depends on the scheme one chooses for the b-quark mass. It has been argued that a so-called “threshold mass" definition is favourable [314, 315] as this avoids renormalon ambiguities associated with the pole mass which does not directly correspond to a measurable quantity, and the QCD corrections are smaller and exhibit better convergence behaviour compared to the case of the $\overline{\rm MS}$ mass. We will employ the 1S mass as originally proposed in [314] and use the more recently determined value $m_b^{1S} = 4.75 \pm 0.04$ GeV [316].

The leading-order result for the differential decay rate of the inclusive decay $B \to X_s\nu_\alpha\nu_\beta$ reads

$$\begin{aligned}\frac{d\Gamma(B \to X_s\nu_\alpha\nu_\beta)}{dq^2} = & \frac{\sqrt{\lambda(m_b^2, m_s^2, q^2)\lambda(m_\alpha^2, m_\beta^2, q^2)}}{384\pi^3 q^4(1+\delta_{\alpha\beta})} \\ & \times \left(\frac{d\Gamma^{\nu_\alpha\nu_\beta}_{\rm incl,V}}{dq^2} + \frac{d\Gamma^{\nu_\alpha\nu_\beta}_{\rm incl,S}}{dq^2} + \frac{d\Gamma^{\nu_\alpha\nu_\beta}_{\rm incl,T}}{dq^2} + \frac{d\Gamma^{\nu_\alpha\nu_\beta}_{\rm incl,VS}}{dq^2} + \frac{d\Gamma^{\nu_\alpha\nu_\beta}_{\rm incl,VT}}{dq^2}\right)\end{aligned} \tag{4.16}$$

with the different terms given in Appendix 4.10 for arbitrary neutrino masses. Subleading HQET contributions will lead to a slight suppression by $\mathcal{O}(10\%)$ [74] compared to the leading-order result presented here. In the limit of massless neutrinos, the expression simplifies as follows:

$$
\begin{aligned}
\frac{d\Gamma(B\to X_s\nu_\alpha\nu_\beta)}{dq^2} = {} & \frac{\sqrt{\lambda(m_b^2,m_s^2,q^2)}}{768\pi^3 m_b(1+\delta_{\alpha\beta})}\Bigg(\left(3\frac{q^2}{m_b^2}(m_b^2+m_s^2-q^2)+\frac{1}{m_b^2}\lambda(m_b^2,m_s^2,q^2)\right) \\
& \times\Big[\left|C^{\mathrm{VLL}}_{\nu d,\alpha\beta sb}\right|^2+\left|C^{\mathrm{VLL}}_{\nu d,\beta\alpha sb}\right|^2+\left|C^{\mathrm{VLR}}_{\nu d,\alpha\beta sb}\right|^2+\left|C^{\mathrm{VLR}}_{\nu d,\beta\alpha sb}\right|^2\Big] \\
& -12q^2\frac{m_s}{m_b}\mathrm{Re}(C^{\mathrm{VLL}}_{\nu d,\alpha\beta sb}C^{\mathrm{VLR}*}_{\nu d,\alpha\beta sb}+C^{\mathrm{VLL}}_{\nu d,\beta\alpha sb}C^{\mathrm{VLR}*}_{\nu d,\beta\alpha sb}) \\
& +2\Big[3\frac{q^2}{m_b^2}(m_b^2+m_s^2-q^2)\Big[\left|C^{\mathrm{SLL}}_{\nu d,\alpha\beta sb}\right|^2+\left|C^{\mathrm{SLR}}_{\nu d,\alpha\beta sb}\right|^2+\left|C^{\mathrm{SLL}}_{\nu d,\alpha\beta bs}\right|^2+\left|C^{\mathrm{SLR}}_{\nu d,\alpha\beta bs}\right|^2\Big] \\
& +12q^2\frac{m_s}{m_b}\mathrm{Re}(C^{\mathrm{SLL}}_{\nu d,\alpha\beta sb}C^{\mathrm{SLR}*}_{\nu d,\alpha\beta sb}+C^{\mathrm{SLL}}_{\nu d,\alpha\beta bs}C^{\mathrm{SLR}*}_{\nu d,\alpha\beta bs})\Big] \\
& +32\left(3\frac{q^2}{m_b^2}(m_b^2+m_s^2-q^2)+\frac{2}{m_b^2}\lambda(m_b^2,m_s^2,q^2)\right)\Big[\left|C^{\mathrm{TLL}}_{\nu d,\alpha\beta sb}\right|^2+\left|C^{\mathrm{TLL}}_{\nu d,\alpha\beta bs}\right|^2\Big]\Bigg)\,.
\end{aligned}
\tag{4.17}
$$

Note that the result does not include QCD corrections and subleading HQET corrections which generally lead to a suppression of the differential decay rate. For the SM prediction it amounts to a suppression of $\mathcal{O}(20\%)$. As there are currently no projected sensitivities for the inclusive decay mode at Belle II, QCD and subleading HQET corrections are left for future work.

4.4 Results

In this section we present our results, of which the discussion is split in four parts. In the first three subsections, we demonstrate the reach for new physics in $b\to s\nu\nu$ processes at Belle II under the assumption of no experimental evidence of an enhancement or suppression of the SM expectation. In the fourth subsection, we consider the recently reported simple weighted average [1,8] $\mathrm{Br}(B^+\to K^+\nu\nu)=(1.1\pm0.4)\times10^{-5}$ and discuss how it could be explained in terms of a sterile neutrino.

We generally use [6] for the $B\to K$ form factors and [5] for the $B\to K^*$ form factors which are both based on a combined fit to LCSR and LQCD data. We increase the $B\to K^*$ form factors by 10% to include finite-width effects following [39]. Note that only the leading-order contribution to the inclusive decay is taken into account in the following, which in particular overestimates the contributions to vector operators (and thus the SM contribution) by $\mathcal{O}(20\%)$. All results are presented as constraints on real Wilson coefficients evaluated at the electroweak scale $\mu = m_Z$. Note that the scalar (tensor) Wilson coefficients are (anti)symmetric in the neutrino flavours, and thus the presence of a Wilson coefficient with neutrino flavours $\alpha\beta$ always implies the simultaneous presence of the Wilson coefficient with neutrino flavours $\beta\alpha$ in these cases.

We typically only refer to $B \to K\nu\nu$ and $B \to K^*\nu\nu$ in the main text, but we generally imply $B^+ \to K^+\nu\nu$ and $B^0 \to K^{*0}\nu\nu$ for the current bounds as they are the most stringent ones, and the charged modes for the future sensitivity due to a slightly better new-physics reach, unless differently specified. The results for the neutral mode would be essentially the same in the latter case, since any discrepancy is only due to the slightly different lifetimes and masses. Furthermore, as indicated in the caption in Figure 4.2, α refers to a fixed value $\in (1, 2, 3)$ in general, thus no summation is implied.

4.4.1 One Operator with Massless Neutrinos

	Current Bound			Future Sensitivity (50 ab^{-1})		
Operator	Value [TeV^{-2}]	NP scale [TeV]	Observable	Value [TeV^{-2}]	NP scale [TeV]	Observable
$\mathcal{O}^{\rm VLL,NP}_{\nu d,\alpha\alpha sb}$	0.028	6	$B \to K^*\nu\nu$	0.023	7	$B \to K^{(*)}\nu\nu$
$\mathcal{O}^{\rm VLR}_{\nu d,\alpha\alpha sb}$	0.021	7	$B \to K\nu\nu$	0.002	25	$B \to K^{(*)}\nu\nu$
$\mathcal{O}^{\rm VLL}_{\nu d,\gamma\delta sb}$	0.014	9	$B \to K^*\nu\nu$	0.006	13	$B \to K^{(*)}\nu\nu$
$\mathcal{O}^{\rm SLL}_{\nu d,\gamma\gamma sb}$	0.012	10	$B \to K^{(*)}\nu\nu$	0.002	25	$B \to K\nu\nu$
$\mathcal{O}^{\rm SLL}_{\nu d,\gamma\delta sb}$	0.009	10	$B \to K^{(*)}\nu\nu$	0.002	25	$B \to K\nu\nu$
$\mathcal{O}^{\rm TLL}_{\nu d,\gamma\delta sb}$	0.002	25	$B \to K^*\nu\nu$	0.0009	35	$B \to K^*\nu\nu$

Table 4.2: Most competitive bounds imposed on the absolute value of the respective Wilson coefficients if only one of them gets (sizeable) contributions from new physics at a time, both for the current situation and for the projections for the 50 ab^{-1} Belle-II data set under the assumption of a confirmation of the SM predictions. Here, $\alpha \in (1, 2, 3)$ and γ and δ arbitrary, but $\gamma \neq \delta$ (only in the case of $\mathcal{O}^{\rm VLL}_{\nu d,\gamma\delta sb}$, γ and δ may be equal if larger than 3), and neutrino masses are set to zero both for active and sterile states. Generally, the most conservative constraint is provided, with the possibility of interference with the SM taken into account. We also provide rough estimates for the corresponding new-physics scale and the observable from which the respective bound arises. If $B \to K^{(*)}\nu\nu$ is indicated, $B \to K\nu\nu$ and $B \to K^*\nu\nu$ yield similar bounds.

In this section we discuss the current constraints on and future sensitivities to new physics under the assumption that it contributes (dominantly) only to one of the considered operators, as summarised in Table 4.2. The first column contains a representative selection of relevant operators which are bounded in different ways. The operators $\mathcal{O}_{\nu d,\alpha\alpha sb}^{\mathrm{VLL,NP}}$ and $\mathcal{O}_{\nu d,\alpha\alpha sb}^{\mathrm{VLR}}$ both interfere with the SM, but since $B \to K^*\nu\nu$ and F_L depend on $|C_{\nu d,\alpha\alpha sb}^{\mathrm{VLL}} + C_{\nu d,\alpha\alpha sb}^{\mathrm{VLR}}|^2$ and $|C_{\nu d,\alpha\alpha sb}^{\mathrm{VLL}} - C_{\nu d,\alpha\alpha sb}^{\mathrm{VLR}}|^2$ with different q^2 dependencies each, contributions from $\mathcal{O}_{\nu d,\alpha\alpha sb}^{\mathrm{VLR}}$ cannot efficiently cancel the SM contribution and thus it is subject to stronger bounds. The operator $\mathcal{O}_{\nu d,\gamma\delta sb}^{\mathrm{VLL}}$ and the scalar operators could be replaced by the respective right-handed operators[6] without changing the constraints.

The second and fifth columns contain the current bounds on and future sensitivities to the Wilson coefficients in TeV^{-2}, respectively. The values for the future sensitivities are obtained under the assumption that the central value of the Belle II measurement exactly coincides with the SM prediction. In each case, the given experimental uncertainty then translates into a constraint on the Wilson coefficient. We generally provide the most conservative bound on the absolute value, with the possibility of interference with the SM contribution taken into account. Due to the latter, the current bounds on $\mathcal{O}_{\nu d,\alpha\alpha sb}^{\mathrm{VLL,NP}}$ and $\mathcal{O}_{\nu d,\alpha\alpha sb}^{\mathrm{VLR}}$ are the least stringent ones.

Scalar operators are more strongly constrained, both in the case of contributions to diagonal elements and those to off-diagonal elements, and tensor operators exhibit the tightest bounds. This general trend can be expected to remain so in the future as well, with the only exception given by $\mathcal{O}_{\nu d,\alpha\alpha sb}^{\mathrm{VLR}}$. The bound on this operator is projected to outperform the one on $\mathcal{O}_{\nu d,\gamma\delta sb}^{\mathrm{VLL}}$ due to interference with the SM, because of which there is a comparatively large contribution $\propto C_{\nu d,\alpha\alpha sb}^{\mathrm{VLL,SM}} C_{\nu d,\alpha\alpha sb}^{\mathrm{VLR}}$ to the relevant observables.

Therefore, the future sensitivity to $\mathcal{O}_{\nu d,\alpha\alpha sb}^{\mathrm{VLR}}$ may become about ten times as strong as the current bound, whereas the improvement factor for scalar operators is roughly five, and about or less than two for the other operators. Besides the numerical values of the bounds on the Wilson coefficients, we also provide an approximate lower bound for the associated

---

[6] In general, a “left-handed (right-handed) operator" is to be understood as an operator which contains a left-handed (right-handed) projector in the quark bilinear.

scale

$$\Lambda \approx \frac{1}{\sqrt{|C^{\mathrm{XLY}}_{\nu d,\alpha\beta sb}|}} \tag{4.18}$$

at which new physics contributing to the respective operator might reside. Here, tree-level mediation and $\mathcal{O}(1)$ couplings are assumed, and potential (unknown) enhancement or suppression factors are neglected.

Currently, depending on the operator under consideration, new physics scales between a few TeV and roughly 25 TeV may be seen as (partly) constrained. In the fourth and seventh column of Table 4.2, we provide the process which gives rise to the indicated bound. If $B \to K^{(*)}\nu\nu$ is indicated, both processes are very similarly competitive. We find that $B \to K\nu\nu$ is most sensitive to scalar operators, whereas tensor operators receive the most stringent constraint from $B \to K^*\nu\nu$. For vector operators, there is no overall trend towards one clearly most competitive observable.

Lastly, we discuss the differential branching ratios as functions of the transferred momentum q^2. Figure 4.1 shows the contours for vector (blue), scalar (red) and tensor (black) operators. For each of the curves, one representative non-zero Wilson coefficient is introduced. We have set $C^{\mathrm{XLL}}_{\nu d,23sb} = 0.01\,\mathrm{TeV}^{-2}$ in all cases X = V,S,T. The different linestyles correspond to different choices for the form factors as detailed in the caption of Figure 4.1. One finds that vector operators dominantly contribute to the small-q^2 region in the case of $B \to K\nu\nu$, whereas the tensor and scalar operators source this decay more efficiently at intermediate and large q^2, respectively. For $B \to K^*\nu\nu$, one instead finds that the contributions from tensor operators are quite large for small and intermediate q^2 and then decrease. Here, vector and scalar operators become most efficient for larger q^2 values. As we use a logarithmic scale on the vertical axes in the top plots of Figure 4.1, we cannot show the behaviour of the respective curves at the kinematic endpoints which can be intuitively understood in terms of helicity conservation, see for instance Ref. [72] for a discussion. Three q^2 bins would most likely already help distinguish potential contributions from different operators for either decay channel. As for the form factors, the different sets are generally in good agreement for each operator. The largest discrepancies arise for $B \to K\nu\nu$ in the case of scalar operators.

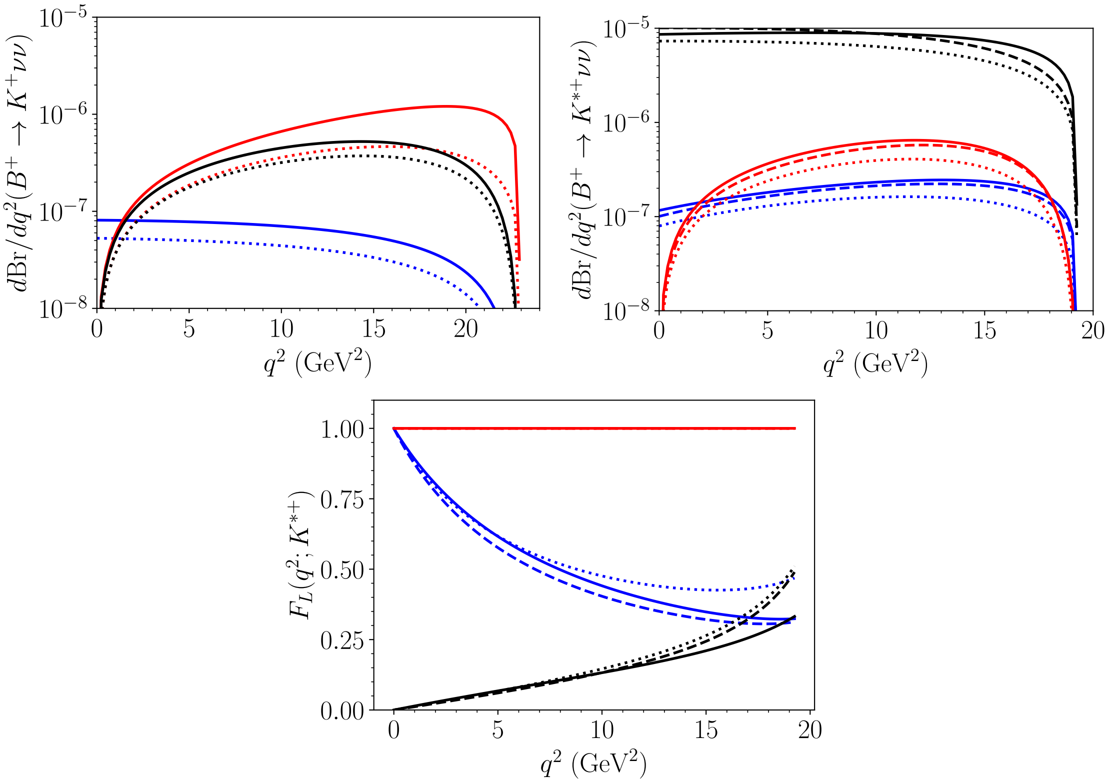

Figure 4.1: The differential branching ratio distributions (top) and the differential longitudinal polarisation fraction F_L (bottom) generated for different non-zero Wilson coefficients $C^{\mathrm{XLL}}_{\nu d,23sb} = 0.01\,\mathrm{TeV}^{-2}$ for X = V,S,T, and choices of form factors. The blue (red) [black] lines stand for the vector (scalar) [tensor] operator, respectively. The solid lines denote the results for the form factors which are used in the analysis, taken from [5] for the $B \to K^*$ and from [6] for the $B \to K$ form factors. Both sets of form factors are based on a combined fit to LCSR and LQCD data. The dotted lines indicate the form factors based on the LCSR fit in [6] and the dashed lines show the $B \to K^*$ form factors obtained using a combined fit to LCSR and LQCD in [6]. Note that no SM contribution is included here.

As can be seen from the definition in Eq. (4.43), the (unbinned) longitudinal polarisation fraction is not sensitive to the value of the contributing Wilson coefficient if only one is switched on at a time. Scalar-operator contributions do generally not enter the numerator of $F_T \equiv 1 - F_L$ and thus imply $F_L(q^2; K^{*+}) = 1$ (without taking into account the SM contribution). The behaviour of vector and tensor operators is complementary in the sense that the former gradually reduce the value of $F_L(q^2; K^{*+})$ if q^2 increases, whereas the effect of the latter is a complete cancellation of $F_L(q^2; K^{*+})$ for small q^2 which then becomes less efficient for larger q^2. This is related to the normalisation of the relevant helicity amplitudes with respect to q^2, i.e., one has $q^2|H^{V(A)}_{\pm\alpha\beta}|^2 \to 0$ and $q^2|H^{T(T_t)}_{0\alpha\beta}|^2 \to 0$, but $q^2|H^{V(A)}_{0\alpha\beta}|^2 \to$ const. and $q^2|H^{T(T_t)}_{\pm\alpha\beta}|^2 \to$ const. for $q^2 \to 0$, see Eqs. (4.40), since A_{12}, T_1 and T_2 do not vanish at $q^2 = 0$. In general, the distributions pertaining to scalar and tensor operators (approximately) converge at the kinematic endpoint of the distribution, only for the ones based on the form-factor set in Ref. [6] which employs a combined fit to LQCD and LCSR data there is a slight discrepancy.

4.4.2 Two Operators with Massless Neutrinos

In the following, we discuss the parameter space compatible with non-zero contributions from two operators induced by new physics under the assumption of massless neutrinos, both for sterile states and as an approximation for the very small masses of the active SM neutrinos. The case of massive neutrinos is discussed in Sect. 4.4.3.

Depending on the observable and whether the two operators shown in a plot interfere with each other, the parameter space compatible with that observable will in most cases have the shape of an ellipse or of straight bands. Straight bands indicate the possibility of exact cancellations among two operators. This occurs if the observable under consideration depends only on the sum or the difference of the two Wilson coefficients shown. If there is no interference between the two operators, the viable parameter space will in general be elliptic. The same shape arises if the observable under consideration receives contributes both from the sum and from the difference. The cases can be distinguished based on the orientation of the ellipses in parameter space. The occurrence of parabola in the case of $F_L(K^{*+})$ is due to its insensitivity to contributions from a single vector operator or due to cancellations between contributions to the numerator and the denominator, see the bottom-right plot in Figure 4.3.

In the plots in Figure 4.3, no interference with the SM contribution occurs. In the plots in Figure 4.2, the Wilson coefficient shown on the horizontal axis interferes with the SM contribution. This implies an overall shift of the centre of the resulting viable parameter space, i.e. the intersection of the regions pertaining to the different observables, from

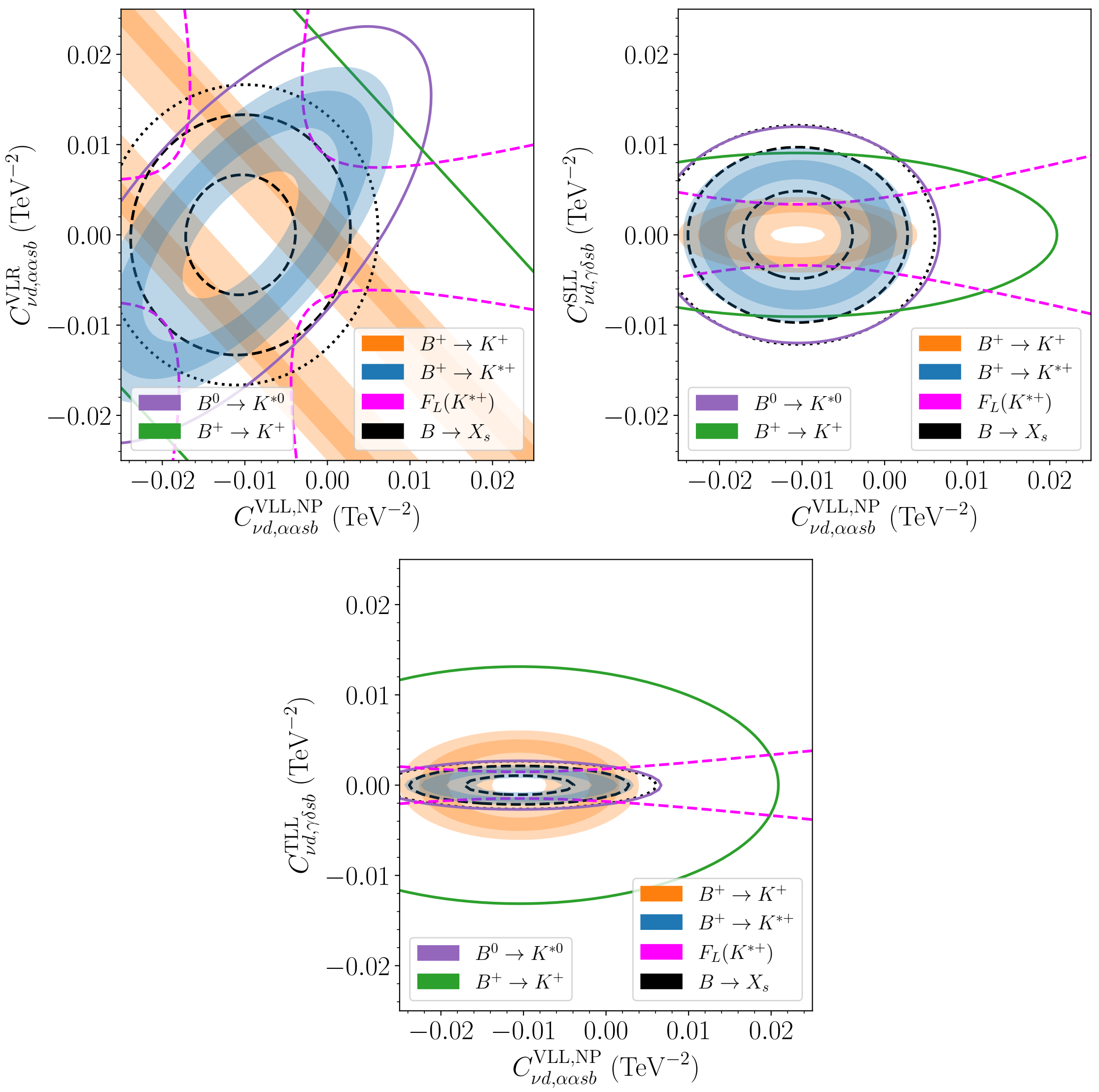

Figure 4.2: The allowed parameter space for the Wilson coefficients under the assumption that the Belle-II results for 5 ab^{-1} (light shaded regions) and for 50 ab^{-1} (dark shaded regions, dashed lines) for several $b \to s\nu\nu$ observables will confirm the SM predictions. In the shown cases, interference with the SM occurs. We use the sensitivities referenced in [7] and assume an experimental uncertainty of 50% (dotted lines) and 20% (dashed lines) for the inclusive decay $B \to X_s\nu\nu$, respectively. The solid dark purple and green lines reflect the current experimental bounds, see Table 4.1. For the neutrino flavor indices, $\alpha \in (1, 2, 3)$, while γ and δ are arbitrary.

$(0, 0)$ to $(-1, 0)$ in units of $|C^{\rm VLL,SM}_{\nu d,\alpha\alpha sb}| \approx 0.01\,\text{TeV}^{-2}$. Moreover, a region containing that point will be excluded as well, since destructive interference would render the respective decays unobservable in there, contrary to our assumption that Belle II will confirm the

SM predictions. If instead the measured branching ratios turned out to be larger than expected, the viable regions would in general get inflated, since there would necessarily have to be non-zero contributions from new physics to induce the measured excess. In the case of no interference with the SM, an excluded region containing $(0, 0)$ would appear. The excluded region containing $(-|C^{\mathrm{VLL,SM}}_{\nu d,\alpha\alpha sb}|, 0)$ in the plots in Figure 4.2 would also grow, since a cancellation of the SM contribution would be even more strongly disfavoured. On the contrary, if Belle II turned out to measure smaller branching ratios than expected, this would imply that there has to be cancellation of the SM contribution. Thus, the viable region in the plots would generally shrink towards their respective centre points.

If the constraints from all decay channels are combined, there trivially is at least one single connected viable region in parameter space containing $(0, 0)$. If neither of the shown operators interferes with the SM contribution, it is the only viable region. In the case of interference, a region enclosing the point $(-2, 0)$ in units of $|C^{\mathrm{VLL,SM}}_{\nu d,\alpha\alpha sb}|$ will be viable as well. This is because the new-physics contribution will result only in a sign flip of $C^{\mathrm{VLL}}_{\nu d,\alpha\alpha sb}$ which has no observable effect.[7]

In the case of vector operators, a region compatible with $B \to K\nu\nu$ has the shape of a straight band as can be seen in the top-left plot of Figure 4.2 and the bottom-left plot in Figure 4.3, because the observable only depends on the (squared) sum of $\mathcal{O}^{\mathrm{VLL}}_{\nu d,\alpha\beta sb}$ and $\mathcal{O}^{\mathrm{VLR}}_{\nu d,\alpha\beta sb}$ where β may be equal to α. Thus, there are exact cancellations between opposite-sign contributions from new physics to these two Wilson coefficients. Put differently, $B \to K\nu\nu$ bounds new-physics contributions to left- and right-handed vector operators of equal sign. On the contrary, $B \to K^*\nu\nu$ depends both on the sum and on the difference of $\mathcal{O}^{\mathrm{VLL}}_{\nu d,\alpha\beta sb}$ and $\mathcal{O}^{\mathrm{VLR}}_{\nu d,\alpha\beta sb}$, each being multiplied by different combinations of form factors and constants. Hence, the parameter space compatible with $B \to K^*\nu\nu$ is always elliptic in the case of vector operators, see the top-left plot in Figure 4.2 and the bottom-left plot in Figure 4.3.

Interference between $\mathcal{O}^{\mathrm{VLL}}_{\nu d,\alpha\alpha sb}$ and $\mathcal{O}^{\mathrm{VLR}}_{\nu d,\alpha\alpha sb}$ as visible in the top-left plot in Figure 4.2 can

---

[7] Throughout this work, $C^{\mathrm{VLL}}_{\nu d,\alpha\alpha sb} = C^{\mathrm{VLL,SM}}_{\nu d,\alpha\alpha sb} + C^{\mathrm{VLL,NP}}_{\nu d,\alpha\alpha sb}$ is understood.

slightly weaken the current single-operator constraints listed in Table 4.2 to $-0.033\ \text{TeV}^{-2} \lesssim C^{\text{VLL,NP}}_{\nu d,\alpha\alpha sb} \lesssim 0.012\ \text{TeV}^{-2}$ or $-0.022\ \text{TeV}^{-2} \lesssim C^{\text{VLR}}_{\nu d,\alpha\alpha sb} \lesssim 0.022\ \text{TeV}^{-2}$ which amounts to an effect of roughly 18% and 5%, respectively, and the implied lower bounds on the new-physics scale become $\Lambda \gtrsim 6$ TeV and $\Lambda \gtrsim 7$ TeV. Note, though, that the future sensitivities are not noticeably affected in a similar way in the case of vector operators due to the fact that $B \to K\nu\nu$ and $B \to K^*\nu\nu$ will become almost equally competitive.

For $\mathcal{O}^{\text{VLL}}_{\nu d,\alpha\alpha sb}$ and $\mathcal{O}^{\text{VLR}}_{\nu d,\alpha\alpha sb}$, regions containing the point $(-1, \pm 1)$ in units of $|C^{\text{VLL,SM}}_{\nu d,\alpha\alpha sb}|$ are viable as well, see the top-left plot in Figure 4.2. Thus, for these two operators, an experimental “confirmation" of the SM will restrict any deviation of the new-physics contribution from the points $(0, 0)$, $(0, -2)$ and $(-1, \pm 1)$ in units of $|C^{\text{VLL,SM}}_{\nu d,\alpha\alpha sb}|$ to less than roughly $0.002\ \text{TeV}^{-2}$, respectively. If the sign of this deviation is the same (opposite) for $C^{\text{VLL,NP}}_{\nu d,\alpha\alpha sb}$ and $C^{\text{VLR}}_{\nu d,\alpha\alpha sb}$, the relevant bound will be set by $B \to K\nu\nu$ ($B \to K^*\nu\nu$). For the region containing $(0, 0)$, this would infer a prospective bound on $C^{\text{VLL,NP}}_{\nu d,\alpha\alpha sb}$ which is numerically very similar to the one on $C^{\text{VLR}}_{\nu d,\alpha\alpha sb}$ in Table 4.2. A region containing $(-1, \pm 1)|C^{\text{VLL,SM}}_{\nu d,\alpha\alpha sb}|$ means that sizeable $\mathcal{O}(|C^{\text{VLL,SM}}_{\nu d,\alpha\alpha sb}|)$ new-physics contributions to two Wilson coefficients effectively relocate the source of the processes under consideration from $\mathcal{O}^{\text{VLL}}_{\nu d,\alpha\alpha sb}$, as it is the case in the SM, to $\mathcal{O}^{\text{VLR}}_{\nu d,\alpha\alpha sb}$ without altering the experimentally accessible signal. Thus, the possibility of the existence of two further relatively small, disjoint windows for new physics will persist, distinguished by the sign of $C^{\text{VLR}}_{\nu d,\alpha\alpha sb}$, with an associated scale of roughly 10 TeV.

The bottom-left plot in Figure 4.3 shows a situation where two vector operators interfere among themselves, but not with the SM. Here, it is sufficient to discuss the constraints for non-negative $C^{\text{VLR}}_{\nu d,\alpha\beta sb}$ where $\alpha \neq \beta$ for $\alpha < 4$ or $\beta < 4$, as there is no change under swapping $C^{\text{VLL}}_{\nu d,\alpha\beta sb} \leftrightarrow C^{\text{VLR}}_{\nu d,\alpha\beta sb}$ or a sign flip of the contributions. The current constraint may weaken to $-0.018\ \text{TeV}^{-2} \lesssim C^{\text{VLL}}_{\nu d,\alpha\beta sb} \lesssim 0.018\ \text{TeV}^{-2}$ if $C^{\text{VLR}}_{\nu d,\alpha\beta sb} \approx (-)0.011\ \text{TeV}^{-2}$ at the upper (lower) bound, which amounts to a relaxation of the constraint on $\mathcal{O}^{\text{VLL}}_{\nu d,\gamma\delta sb}$ in Table 4.2 by roughly 30%, and may be interpreted as the possibility of new physics residing at roughly 7 TeV.

Vector operators are a suitable instance to make a case for efforts to experimentally access

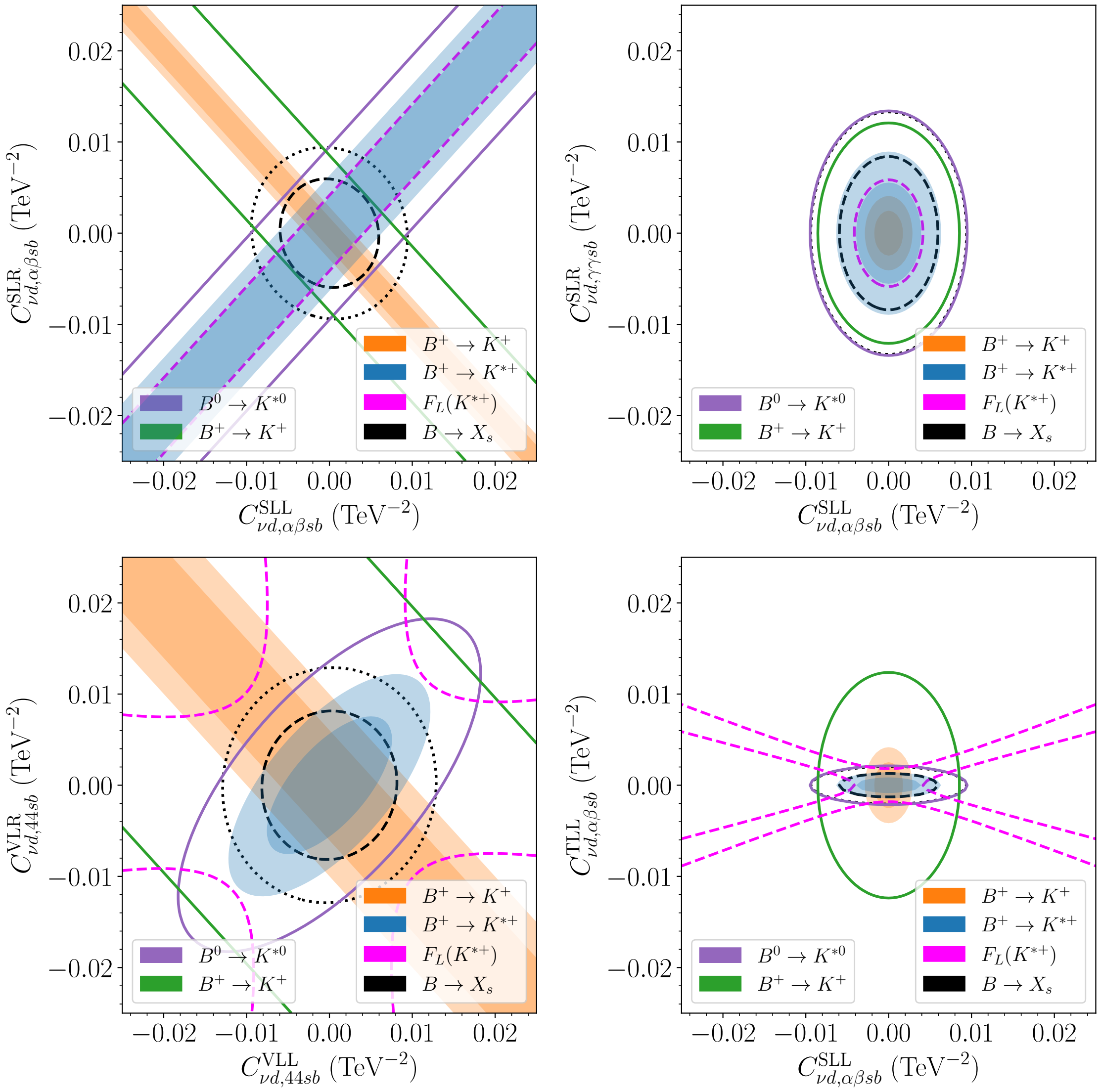

Figure 4.3: Continuation of Figure 4.2, but here the neutrino flavour indices are arbitrary with $\alpha \neq \beta$.

the inclusive mode $B \to X_s\nu\nu$. While this is very challenging, our results show that with an assumed sensitivity of 50% one can already expect to (almost) exclusively probe parameter space which has been inaccessible so far. Also, note that the inclusive mode is less prone to cancellations among contributions from left- and right-handed operators than $B \to K^*\nu\nu$ in parts of parameter space.

In the case of scalar operators, $B \to K^*\nu\nu$ only depends on the difference of $\mathcal{O}^{\mathrm{SLL}}_{\nu d,\alpha\beta sb}$ and

$\mathcal{O}^{\rm SLR}_{\nu d,\alpha\beta sb}$. Thus, the region compatible with this observable also has the shape of a straight band, as it can be seen in the top-left plot in Figure 4.3. $B \to K^*\nu\nu$ ($B \to K\nu\nu$) hence provides a bound on new-physics contributions to left- and right-handed scalar operators of opposite (equal) sign.

Note that interference between contributions to $O^{\rm SLL}_{\nu d,\alpha\beta sb}$ and $O^{\rm SLR}_{\nu d,\alpha\beta sb}$ cannot significantly relax the relevant current constraints indicated in Table 4.2, but $|C^{\rm SLL}_{\nu d,\alpha\beta sb}| \lesssim 0.003$ TeV^{-2} and a corresponding new-physics scale of roughly 20 TeV, which amounts to a loosening of the single-operator bounds by roughly 50%, may still be viable in the future. This is due to the fact that the new-physics reach of $B \to K\nu\nu$ will become clearly dominant in the case of scalar operators, whereas currently $B \to K^*\nu\nu$ is only slightly inferior. In that sense, the situation is contrary to the one for vector operators where interference can only noticeably affect the current constraints.

Generally, the observable $F_L(K^{*+})$ is very suitable to test contributions to scalar operators because they only modify the denominator in $F_T \equiv 1 - F_L$, see Eq. (4.44), whereas vector and tensor operators also alter the numerator. Furthermore, note that a single contribution to $\mathcal{O}^{\rm VLL}_{\nu d,\alpha\alpha sb}$ can be removed from the q^2 integral in the numerator and the denominator and thus $F_L(K^{*+})$ is not sensitive to its value. If new physics contributes to $\mathcal{O}^{\rm SLL}_{\nu d,\alpha\beta sb}$ and $\mathcal{O}^{\rm SLR}_{\nu d,\alpha\beta sb}$ with opposite signs, $B \to K^*\nu\nu$ (for 50 ab^{-1}) and $F_L(K^{*+})$ provide similarly competitive constraints, as can be seen in the top-left plot of Figure 4.3. The top-right plot in Figure 4.2 demonstrates that combining $F_L(K^{*+})$ with $B \to K^*\nu\nu$ would prove efficient in probing the scenario of new physics contributing to $\mathcal{O}^{\rm VLL}_{\nu d,\alpha\alpha sb}$ and a scalar operator (or a tensor operator as shown in the bottom diagram). In this case, both observables related to $B \to K^*$ can already considerably tighten the existing bounds, and leveraging $B \to K\nu\nu$ as well would imply only a moderate further improvement especially in the case of tensor operators.

The current single-operator bound on, say, $\mathcal{O}^{\rm SLR}_{\nu d,\alpha\beta sb}$ does not significantly loosen if at the same time the SM contribution would be (partly) cancelled by new physics. In fact, an efficient cancellation of the SM contribution and a simultaneous contribution to scalar operators would already come under severe pressure if the 5 ab^{-1} data set confirmed the respective SM predictions for $B \to K\nu\nu$ and $B \to K^*\nu\nu$, as there is only little overlap between the relevant light-shaded regions in the top-right plot in Figure 4.3. On the contrary, in the top-left plot the intersection of the viable regions pertaining to the 5 ab^{-1} data set is even disconnected in parameter space, but cancellations of the SM contribution could not be excluded at all. Still, a scenario with $|C^{\mathrm{SLR}}_{\nu d,\alpha\beta sb}| \lesssim 0.004\ \mathrm{TeV}^{-2}$ and a less efficient cancellation of the SM contribution could only be ruled out with the 50 ab^{-1} data set. This illustrates that Belle II can be expected to be quite efficient in constraining new physics which sources only one scalar operator with different final-state neutrinos, hence, more contributions would be necessary to “mimic" the SM expectation.

For the $b \to s\nu\nu$ processes, tensor operators only exist with left-handed projectors in the fermion bilinears (together with their hermitean conjugates), thus they can never interfere with one another. As in the case of scalar operators, the 5 ab^{-1} data set will not entirely suffice either to rule out the scenario that $|C^{\mathrm{VLL,SM}}_{\nu d,\alpha\alpha sb}|$ gets (partially) cancelled by new physics and the relevant decays under consideration are instead induced by tensor operators, but 50 ab^{-1} will provide a conclusive answer, see the bottom plot in Figure 4.2. Note that if $\mathcal{O}^{\mathrm{VLL,NP}}_{\nu d,\alpha\alpha sb}$ and $\mathcal{O}^{\mathrm{TLL}}_{\nu d,\gamma\delta sb}$ contribute together, instead of $B \to K^*\nu\nu$ one could consider $F_L(K^{*+})$ together with $B \to K\nu\nu$ without a significant loss of constraining power.

4.4.3 Massive Neutrinos

For the discussion of the impact of non-zero neutrino masses, we start with the current constraints on and future sensitivities to a single Wilson coefficient, respectively, as a function of the mass of a sterile neutrino, as shown in Figure 4.4. In each case, all other operators are switched off. It is assumed that the SM is extended by only one sterile neutrino, that is, there cannot be two sterile neutrinos in the final state with different masses. We study the entire range from massless neutrinos up to the respective kinematic threshold for each process. Regarding the final-state neutrino flavours, we consider a representative off-diagonal element as well as the diagonal one with two sterile neutrinos with identical masses in the final state for the vector and scalar operator.

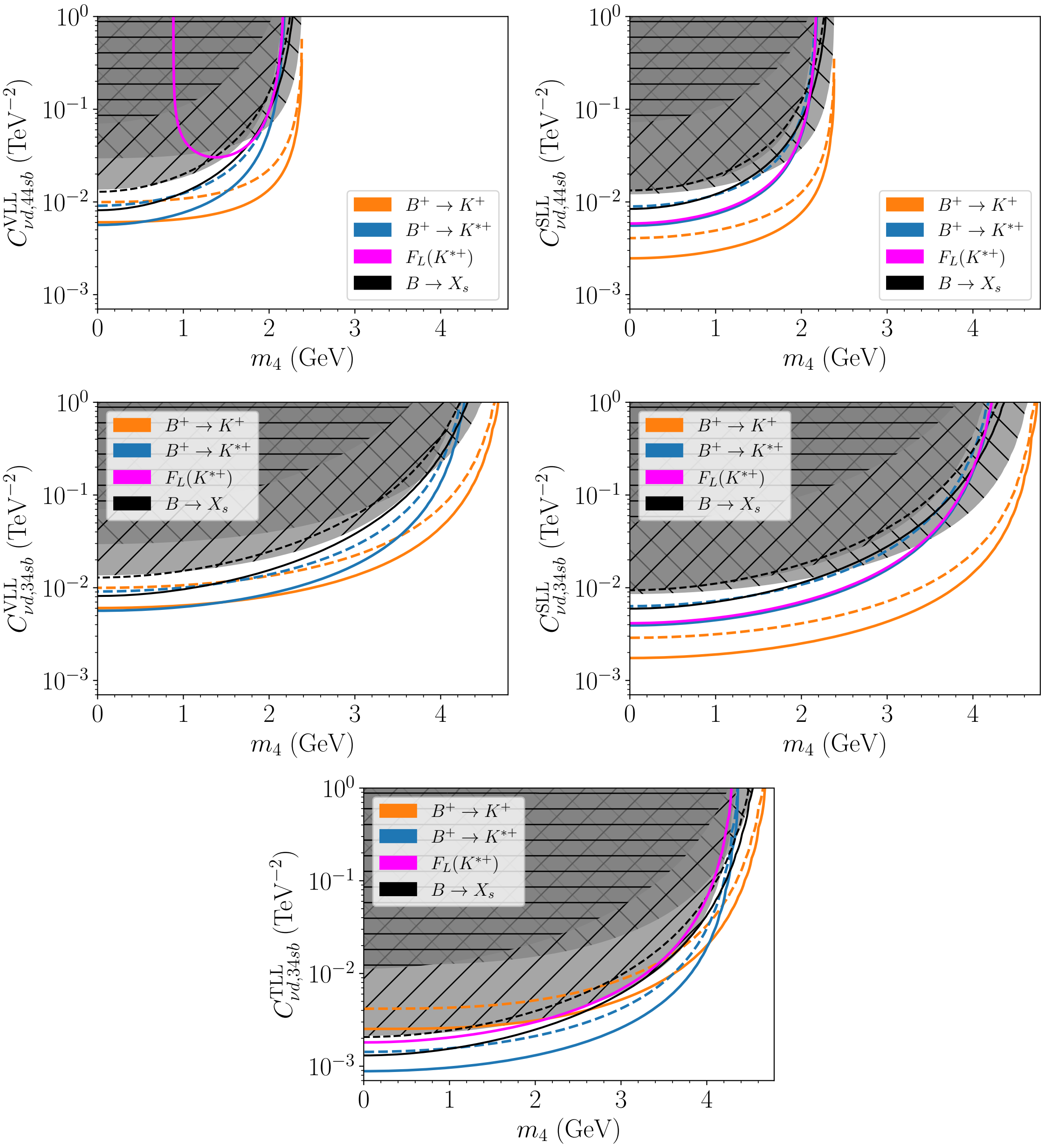

Figure 4.4: Current (shaded regions) and future sensitivities (lines) on a single Wilson coefficient as a function of the mass of two sterile neutrinos (top panel) and one sterile neutrino (middle panel and bottom plot) in the final state, respectively. We assume that the Belle-II results for 5 ab^{-1} (dashed lines) and for 50 ab^{-1} (solid lines) for several $b \to s\nu\nu$ observables will confirm the SM predictions. We use the sensitivities referenced in [7] and assume an experimental uncertainty of 50% (solid line) and 20% (dashed line) for the inclusive decay $B \to X_s\nu\nu$. Regions with \\ (//) [–] hatching are excluded via the current bounds on $B^+ \to K^+\nu\nu$ ($B^0 \to K^{*0}\nu\nu$) [$B \to X_s\nu\nu$]. The constraints are identical if exchanging the third neutrino flavour $\alpha = 3$ for $\alpha = 1, 2$.

Note that for a sterile-neutrino mass larger than $m_4 \gtrsim 1.7$ (3.7) GeV for (off-)diagonal elements of vector operators, $B \to K\nu\nu$ is currently more constraining than $B \to K^*\nu\nu$. In terms of future sensitivities, $B \to K\nu\nu$ and $B \to K^*\nu\nu$ are very similarly competitive in the (approximately) massless case, but for heavier sterile neutrinos $B \to K^*\nu\nu$ also grows more and more inferior. Indeed, for $m_4 \gtrsim 1.5$ (3.5) GeV for (off-)diagonal vector-operator elements, even the results for $B \to K\nu\nu$ based on the 5 ab^{-1} data set are projected to outperform the bounds imposed by all other observables. The plots in Figure 4.4 also reflect the previously made observation that $F_L(K^{*+})$ is not sensitive to a single contribution to $\mathcal{O}^{\text{VLL}}_{\nu d,\alpha\beta sb}$ in the case of massless neutrinos. A sizeable deviation from that only occurs for two massive neutrinos in the final state as can be seen in Eqs. (4.38) and (4.39), and thus $F_L(K^{*+})$ cannot impose a constraint on $C^{\text{VLL}}_{\nu d,34sb}$ where the mass only reduces the available phase space. For $\mathcal{O}^{\text{VLL}}_{\nu d,44sb}$, a prospective constraint arises for $m_4 \gtrsim 0.9$ GeV which nonetheless will only imply a (moderate) improvement over the current bounds in the range 1.5 GeV $\lesssim m_4 \lesssim$ 1.9 GeV, and is generally not competitive.

For the entire accessible neutrino-mass range, $B \to K\nu\nu$ accounts for the highest future sensitivity to as well as the most stringent current bound on scalar operators, although this dominant role is not very pronounced in the latter case for very small or zero neutrino masses. Furthermore, irrespective of their symmetry properties, scalar operators are always more strongly constrained than vector operators also for non-zero neutrino masses. In the case of tensor operators, $B \to K^*\nu\nu$ imposes the most competitive bound for almost the entire neutrino-mass range. Indeed, for 1.1 GeV $\lesssim m_4 \lesssim$ 3.6 GeV, even the results for $B \to K^*\nu\nu$ based on the 5 ab^{-1} data set will outperform the bounds imposed by all other observables. Only if the sterile neutrino is heavier than $m_4 \gtrsim 4$ GeV, $B \to K\nu\nu$ becomes more competitive, and in this range the tensor operator will also be slightly less stringently constrained than the scalar operator. Hence, $B \to K\nu\nu$ is indeed a very powerful probe of new physics in $b \to s\nu\nu$ processes for all considered operators. Note that up to $m_4 \lesssim 2.6$ GeV, we find that the inclusive mode is more sensitive to tensor-operator contributions than $B \to K\nu\nu$.

Linearly adding up the theoretical and experimental uncertainties for $F_L(K^{*+})$ as given

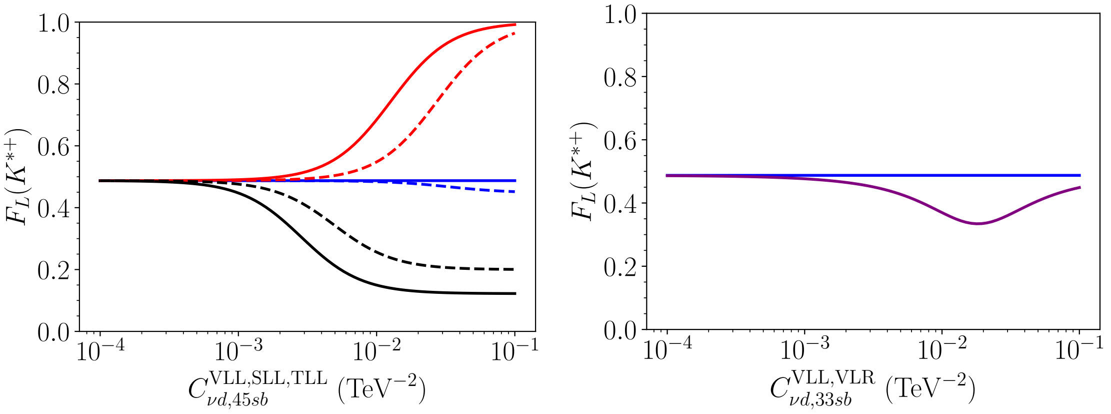

Figure 4.5: Binned longitudinal polarisation fraction $F_L(K^{*+})$ as a function of one new-physics Wilson coefficient at a time (including the SM contribution). On the left-hand side the blue (red) [black] lines stand for the vector (scalar) [tensor] operator, respectively. Solid [dashed] contours signify $m_{4,5} = 0$ GeV [$m_{4,5} = 1.5$ GeV]. On the right-hand side the blue (purple) lines stand for the Wilson coefficients $C^{\text{VLL}}_{\nu d,33sb}$ ($C^{\text{VLR}}_{\nu d,33sb}$). Note the binned longitudinal polarisation fraction $F_L(K^{*+})$ is obtained by separately binning the numerator and denominator, see Eq. (4.11), and not by integrating the distributions $F_L(q^2; K^{*+})$ shown in Figure 4.1.

in Table 4.1, one finds that only a result in the range $(0.37, 0.61)$ would be compatible with the SM expectation at 1σ. Hence, a measurement of $F_L(K^{*+})$ in principle allows for a sharp distinction between the case of dominant contributions to only the scalar operator, or only the tensor operator, as can be seen in Figure 4.5 on the left-hand side. As scalar operators do only contribute to the denominator, but not to the numerator of F_T, increasing the Wilson coefficient only implies a shrinkage of the difference of $F_L(K^*)$ from 1. Note that with one massive neutrino in the final state, $F_L(K^{*+})$ is affected by new physics contributing to $\mathcal{O}^{\text{VLL}}_{\nu d,\alpha\alpha sb}$ only via phase-space suppression which does not result in a competitive bound, see Eqs. (4.38) and (4.39). While $F_L(K^{*+})$ is sensitive to new-physics contributions to left-handed vector operators with two massive neutrinos, unambiguously discerning a deviation from the SM expectation might be challenging in this case. On the contrary, a contribution to a right-handed vector operator can induce a signal in $F_L(K^{*+})$ also for massless neutrinos, see the plot on the right in Figure 4.5, which should be distinguishable from the SM case at least for a Wilson coefficient value close to $C^{\text{VLR}}_{\nu d,\alpha\alpha sb} \approx 0.02\ \text{TeV}^{-2}$.

A generic effect of the introduction of sterile-neutrino masses is a larger phase-space suppression and thus a relaxation of the implied bounds on the new-physics Wilson coefficients. Note that the masses have to be quite large to induce a noticeable deviation, for instance, a decrease of the bounds on the respective Wilson coefficients by a factor of 2 occurs only for sterile-neutrino masses of at least roughly $m_4 = 1$ (2) GeV or larger in the case of (off-)diagonal operator elements, that is, for about half of the kinematically allowed range there is only a small effect. Indeed, the structure of the respective viable regions for two non-zero operators does not substantially change either if massive neutrinos are considered. In particular, neutrino masses do not spoil the possibility of exact cancellations between contributions from vector and scalar operators of opposite chirality, respectively, to $B \to K\nu\nu$ and $B \to K^*\nu\nu$.

Non-zero neutrino masses allow for interference between vector operators and scalar or tensor operators. Still, as the contributions are proportional to (the sum or difference of) the final-state neutrino masses, the discussion of potential interference of new physics with the SM contribution in the last section will not be noticeably impacted if the tiny masses of the active SM neutrinos were taken into account. A non-trivial consequence of two massive sterile neutrinos in the final state, though, are non-vanishing contributions from interference among scalar operators with different quark-flavour orderings, sb and bs. This can also occur for tensor operators.[8] As the amplitudes for the decays under consideration receive contributions from the Hermitian conjugates of the bs operators which amounts to a chirality flip in the neutrino bilinears, interference with sb operators only occurs if both neutrinos in the final state are massive.

The plots in Figure 4.6 indicate that the interference effect could in principle be exploited to distinguish between interfering contributions from sb and bs quark-flavour scalar operators with of the same quark chirality from those of opposite chirality. In particular, the orientation of the ellipses indicating the parameter space compatible with $B \to K^*\nu\nu$ and $F_L(K^{*+})$ changes. Note that especially for two operators of the same chirality, a

---

[8] Vector operators with the quark-flavour ordering bs are trivially related to those with sb via Hermitian conjugation.

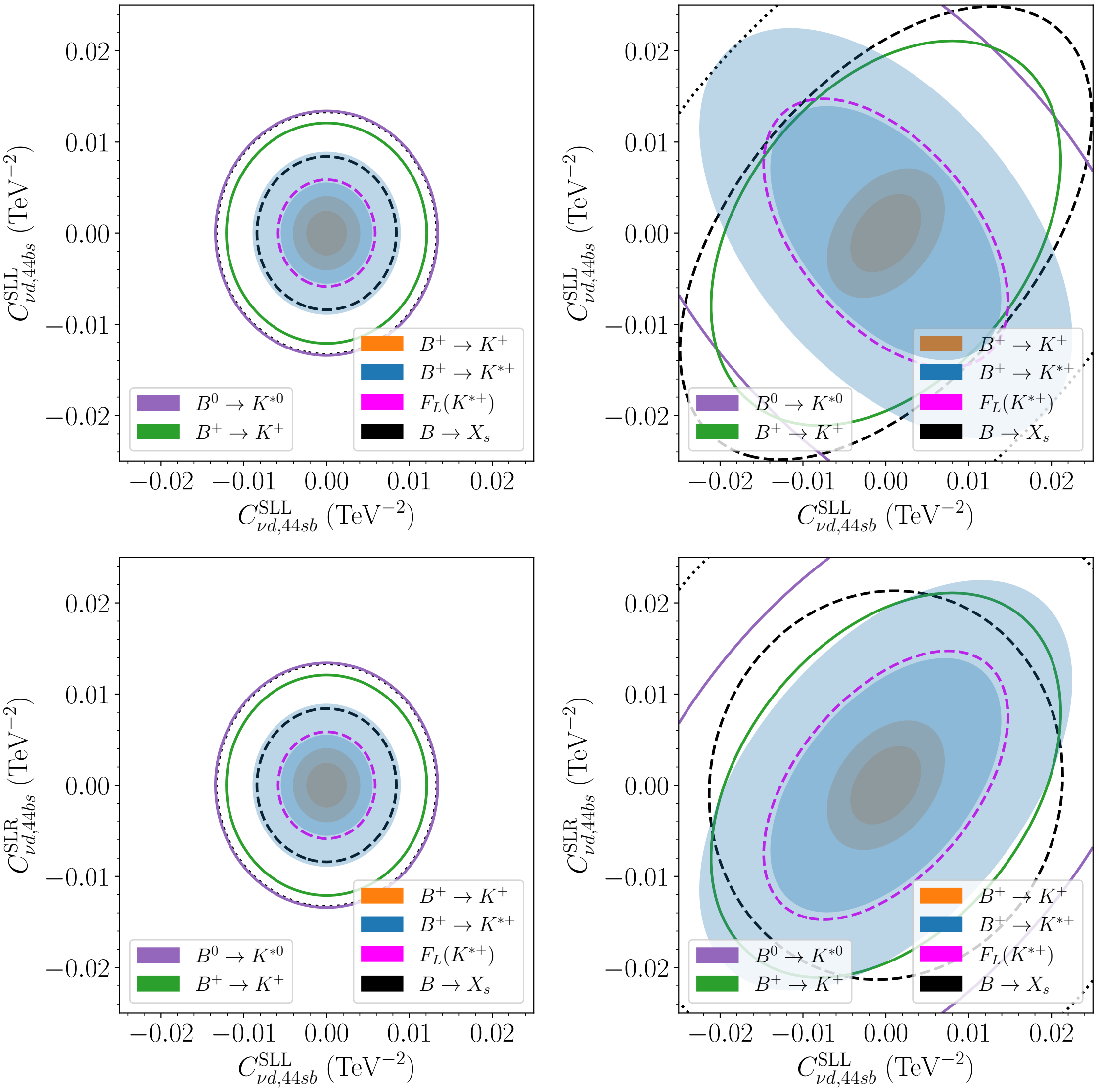

Figure 4.6: Future sensitivity of Belle II for 5 ab^{-1} (light shaded regions) and for 50 ab^{-1} (dark shaded regions, dashed lines) to scalar Wilson coefficients with sb and bs quark-flavour ordering and massive sterile neutrinos following the same analysis as in Figure 4.2. The solid dark purple and green lines indicate the current experimental bound, see Table 4.1. Left: $m_4 = 0$ GeV; Right: $m_4 = 1.5$ GeV.

measurement of either observable can be expected to already imply a substantial improvement over the current bound imposed by $B \to K\nu\nu$. Still, in the considered scenario with only two contributing operators, the latter will retain the best future sensitivity to new physics. Nonetheless, $B \to K\nu\nu$ lacks the feature of distinguishing between chiralities of scalar operators. Thus it is conceivable that in scenarios with more contributions, for in-

	$\mathcal{O}^{\text{VLL}}_{\nu d,44sb}$	$\mathcal{O}^{\text{SLL}}_{\nu d,44sb}$	$\mathcal{O}^{\text{SLL}}_{\nu d,34sb}$	$\mathcal{O}^{\text{TLL}}_{\nu d,34sb}$	Bound	SM
WC (10^{-3} TeV^{-2})	$22.3^{+5.97}_{-8.31}$	$9.12^{+2.44}_{-3.40}$	$6.45^{+1.72}_{-2.40}$	$9.33^{+2.50}_{-3.48}$		0
$\text{Br}(B^0 \to K^{*0}\nu\nu)/10^{-5}$	2.89 ± 1.05	1.45 ± 0.18		13.5 ± 7.5	1.8	1.16 ± 0.11
$\text{Br}(B^+ \to K^{*+}\nu\nu)/10^{-5}$	3.11 ± 1.13	1.57 ± 0.20		14.6 ± 8.1	4.0	1.24 ± 0.12
$\text{Br}(B \to X_s\nu\nu)/10^{-4}$	1.01 ± 0.37	0.494 ± 0.055		4.57 ± 2.53	6.4	0.27 ± 0.02

Table 4.3: Implication of the non-zero simple weighted average of $\text{Br}(B^+ \to K^+\nu\nu)$ for the contributing WCs and the other decay channels. The indicated upper and lower ranges reflect the uncertainty at 1σ. Note that our new-physics predictions for the inclusive mode do not take into account QCD and HQET corrections, as indicated in Section 4.3, and are thus expected to be overestimated by $\mathcal{O}(10 - 20\%)$. All bounds and SM predictions are the same as in Table 4.1.

stance also to $C^{\text{SLR}}_{\nu d,44sb}$ with the sign opposite to that of $C^{\text{SLL}}_{\nu d,44sb}$, interference effects render $B \to K^*\nu\nu$ and/or $F_L(K^{*+})$ entirely competitive with $B \to K\nu\nu$ and the shape of the combined viable parameter space carries information about the chiralities.

4.4.4 A Hint for New Physics?

Recently, the Belle-II collaboration reported an upper limit $\text{Br}(B^+ \to K^+\nu\nu) < 4.1 \times 10^{-5}$ [8] at the 90% confidence level. As part of the analysis a simple weighted average of the branching ratio with previous analyses [24, 291, 292] was presented with $\text{Br}(B^+ \to K^+\nu\nu) = (1.1 \pm 0.4) \times 10^{-5}$ [1, 8] which is above the SM expectation $\text{Br}(B^+ \to K^+\nu\nu) = (4.4 \pm 0.7) \times 10^{-6}$ [11]. In this section, we interpret it as a hint for new physics and discuss its implication for and interplay with the existing bounds on the other decay channels. With the sets of form factors employed in this work, the SM prediction is contained in the 2σ region of the average. At 3σ, the latter is still well compatible with zero.

We take the SM to be extended by one massless sterile neutrino which accounts for the non-zero branching ratio $\text{Br}(B^+ \to K^+\nu\nu)$. We further assume one non-zero Wilson coefficient at a time, and compute the resulting branching ratios for the other decay channels. The results (at the scale $\mu = m_Z$) are summarised in Table 4.3. The constraints for the right-handed vector and scalar operators would be the same.

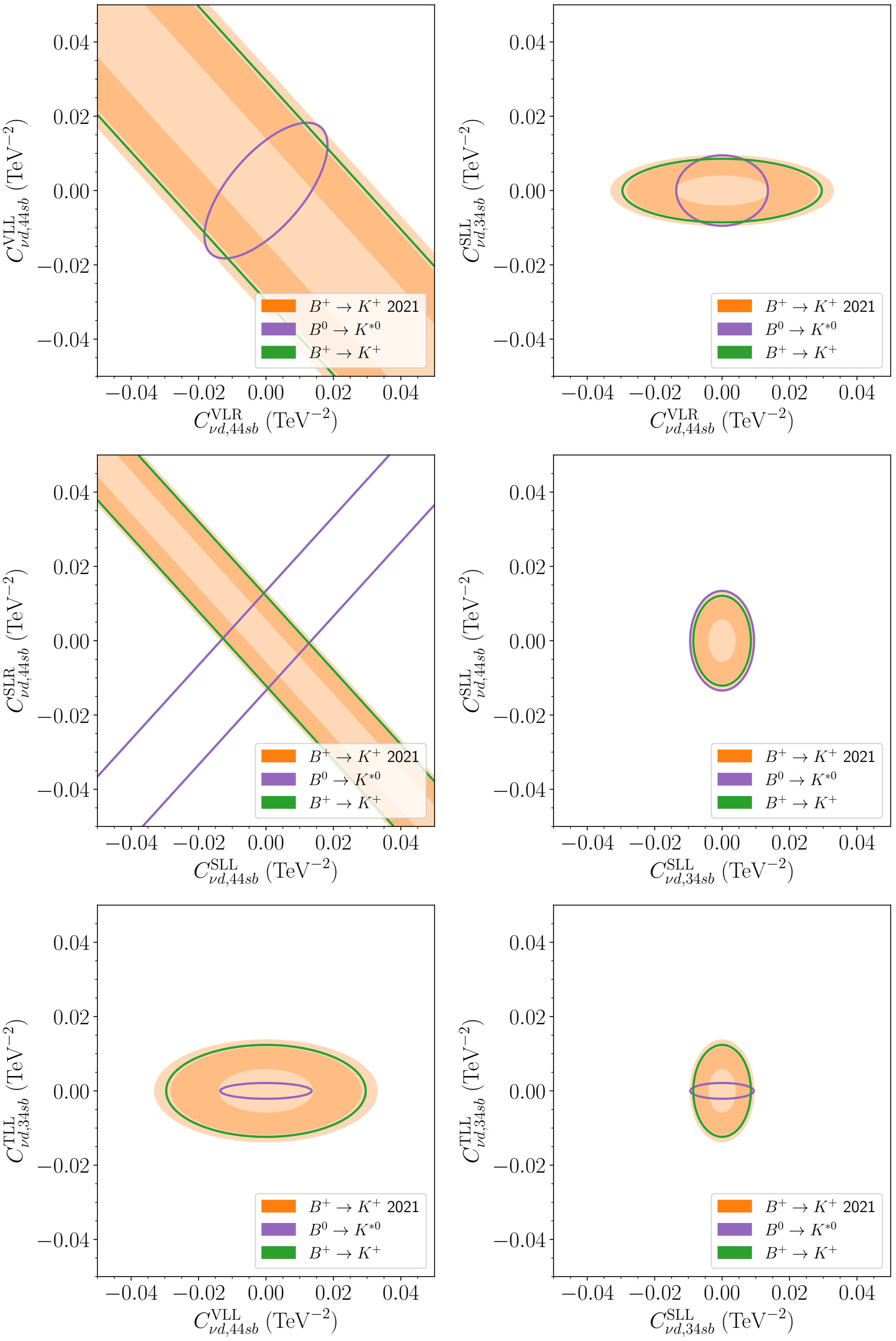

Figure 4.7: Parameter space which is compatible with the non-zero simple weighted average of $\text{Br}(B^+ \to K^+\nu\nu)$ [1, 8] at 1σ (2σ) [darker(lighter)-orange shaded region] and the current bounds on $B^+ \to K^+\nu\nu$ and $B^0 \to K^{*0}\nu\nu$.

The comparatively large vector Wilson coefficient reflects that $B \to K\nu\nu$ is generally less sensitive to the vector operator than the scalar operator. Besides, one has $\mathcal{O}^{\mathrm{TLL}}_{\nu d,34sb} = -\mathcal{O}^{\mathrm{TLL}}_{\nu d,43sb}$ and thus the combined contribution from the components of the tensor operator is also fairly large. The non-zero branching ratio $\mathrm{Br}(B^+ \to K^+\nu\nu)$ also directly implies $\mathrm{Br}(B^0 \to K^0\nu\nu) = (1.02 \pm 0.37) \times 10^{-5}$ which is perfectly compatible with the current bound $\mathrm{Br}(B^0 \to K^0\nu\nu) < 2.6 \times 10^{-5}$.

As a general result, one may assert that the non-zero weighted average can be most compellingly explained in terms of a contribution from scalar operators, since the relative uncertainties of the predicted branching ratios are at most roughly 13% at 1σ and thus fairly small. More specifically, the prediction for the neutral (charged) mode of $B \to K^*\nu\nu$ is roughly 20% (60%) smaller than (and hence perfectly compatible with) the current bound, but also still agrees with the SM prediction at 2σ. In particular, as the predictions are slightly larger than in the SM, this scenario will definitely be tested at Belle II. The neat agreement with the current bounds is reflected by the fact that if two operators contribute, the viable region in parameter space compatible with the average at 1σ in the plots in Figure 4.7 is connected only in the case of two non-interfering scalar operators.

An explanation via vector operators is less preferred due to some tension with $B^0 \to K^{*0}\nu\nu$ of which the 1σ region is already excluded. Still, the prediction for this channel is compatible with zero at 3σ. The latter statement also holds for $B^+ \to K^{*+}\nu\nu$, but its prediction respects the current bound at large parts of the 1σ range. Arguably, contributions to tensor operators are the least elegant way to account for the non-zero weighted average of $\mathrm{Br}(B^+ \to K^+\nu\nu)$. The implied predictions for both the neutral mode and the charged mode of $B \to K^*\nu\nu$ are already ruled out at much more than 1σ. Indeed, Figure 4.7 indicates that current bounds already constrain a possible contribution from tensor operators to be quite small, i.e. $|C^{\mathrm{TLL}}_{\nu d,34sb}| \lesssim 0.002\ \mathrm{TeV}^{-2}$, whereas $|C^{\mathrm{TLL}}_{\nu d,34sb}| \gtrsim 0.006\ \mathrm{TeV}^{-2}$ would be needed to explain the non-zero average at 1σ. Conversely, the uncertainties of the predictions are so large that they are compatible with zero at less than 2σ.

4.5 Conclusions

In this paper, we have studied how new physics contributing to $b \to s\nu\nu$ transitions is constrained by current bounds on the branching ratios of $B \to K\nu\nu$, $B \to K^*\nu\nu$, and $B \to X_s\nu\nu$, and what improvements can be expected from the projected measurement of these processes at Belle II. We have also taken into account the longitudinal polarisation fraction $F_L(B \to K^*\nu\nu)$. Throughout the analyses, we have assumed that the Belle-II results will confirm the SM expectations. Our investigation is based on the most general set of dimension-6 operators in low-energy effective theory (LEFT) which contribute to $b \to s\nu\nu$ [192, 298] including massive sterile neutrinos, except for the dimension-5 dipole operator the contribution of which can be expected to be very suppressed. We employ the form factors provided in [6] for $B \to K\nu\nu$ and the ones from [5] for the observables related to $B \to K^*\nu\nu$, both of which are based on a combined fit to LQCD and LCSR data. Finite-width effects are taken into account for the $B \to K^*$ form factors via increasing them by 10% following [39]. The implementation of the exclusive decays makes use of the general formalism developed in Ref. [302]. We also provide the leading-order expression for the inclusive decay mode which we computed with `FeynCalc` [317, 318].

We started our discussion with a consideration of the bounds in the case of new physics (dominantly) contributing to only one operator. We found that currently the vector operator is the least constrained one, whereas the most stringent bound holds for the tensor operator. The associated scale of new physics might reside at roughly 25 TeV in the latter case, which Belle II can be expected to refine to approximately 35 TeV. One should stress that the scalar and tensor operators exhibit symmetries under the exchange of the final-state neutrino flavours, and thus a contribution from a $\alpha\beta$ operator element with $\alpha \neq \beta$ always implies that the $\beta\alpha$ element also contributes with equal strength, which we do not compensate for in our basis.

The bulk of our paper is dedicated to the case of non-zero new-physics contributions to two different operators, as this allows the discussion of effects of interference between the operators, and complementarities between different observables to probe these contributions. We have also considered new-physics contributions to $\mathcal{O}^{\mathrm{VLL}}_{\nu d,\alpha\alpha sb}$ which is the only non-vanishing operator in the SM at leading-order. Since we assume that Belle II will not find significant deviations from the SM expectation, we exclude the possibility of efficient cancellations, and thus there is generally less parameter space available in this scenario. Only a simultaneous compensating contribution to $\mathcal{O}^{\mathrm{VLR}}_{\nu d,\alpha\alpha sb}$ could potentially make the experimental results appear consistent with the SM predictions.

Our results show that the combination of the processes $B \to K\nu\nu$ and $B \to K^*\nu\nu$ is generally the most powerful probe of new physics. Partly, this is due to the fact that $B \to K\nu\nu$ depends on the sum of left- and right-handed vector operators and scalar operators, respectively, while $B \to K\nu\nu$ is dominantly sensitive to the respective difference of these operators. Thus, these processes probe largely different regions in parameter space. Moreover, the experimental uncertainties for these processes are projected to be as small as ca. 10% with the 50 ab^{-1} data set. In the case of massive neutrinos, the bound imposed by $B \to K\nu\nu$ becomes completely superior in the case of large neutrino masses for all considered operators. Still, as indicated above, these observables individually are not safe from the possibility of cancellations among interfering contributions from different Wilson coefficients, in which case independent information from other processes is needed.

In particular, throughout our study a bound on the inclusive mode always translates into an unambiguous bound on each contributing operator. $B \to X_s\nu\nu$ is a suitable probe especially in the case of interfering vector operators, but it is also useful to constrain tensor operators for which it outperforms $B \to K\nu\nu$ for sterile-neutrino masses below $\lesssim 2.6$ GeV. Our conservative assumptions about the uncertainties associated with $B \to X_s\nu\nu$ could be nullified with a dedicated study of next-to-leading order contributions to the decay rate. Therefore, we wish to make a case for efforts to experimentally access the inclusive decay and to reduce its theory uncertainty.

Conversely, the longitudinal polarisation fraction F_L is very suitable to test the scenario of new physics yielding contributions to scalar operators. In the case of two massive neutrinos in the final state, it can even help distinguish whether the operators are of the same or opposite chirality. Here, it is perfectly competitive with the branching ratio of

$B \to K^*\nu\nu$. The latter observable is the most sensitive probe for tensor operators up to a sterile-neutrino mass of $\lesssim 4$ GeV and also competitive with $B \to K\nu\nu$ in the case of vector operators and small neutrino masses.

In summary, we have demonstrated that the search for rare process based on $b \to s$ quark transitions with missing energy in the final state at Belle II will considerably strengthen the current bounds on new physics contributing to these processes, and that the processes under consideration exhibit different and therefore complementary sensitivity to the different operators taken into account. Studies of non-leading contributions to the observables as well as the interpretation of the results in terms of SMEFT and their connection to other rare processes are left for future work.

4.6 Appendix: Form factors

We follow the parametrisation in [6]. For the $B \to P$ transition with $P = \pi,\ K,\ \bar{D}$, the form factors $f_0,\ f_+$ and f_T are defined as in

$$\begin{aligned}\langle P(k)|\bar{d}\gamma^\mu b|B(p)\rangle &= \left[(p+k)^\mu - \frac{m_B^2 - m_P^2}{q^2}q^\mu\right] f_+(q^2) + \frac{m_B^2 - m_P^2}{q^2}q^\mu f_0(q^2),\\ \langle P(k)|\bar{d}\sigma^{\mu\nu}q_\nu b|B(p)\rangle &= \frac{i f_T(q^2)}{m_B + m_P}\left(q^2(p+k)^\mu - (m_B^2 - m_P^2)q^\mu\right),\end{aligned} \tag{4.19}$$

where $q^\mu = p^\mu - k^\mu$, k and p are the 4-momenta of the P pseudoscalar meson and the B meson, respectively.

For the $B \to V$ decay with $V = \rho,\ K^*,\ \bar{D}^*$, the non-vanishing form factors $V,\ A_{0,1,2,3},\ T_{1,2,3}$

are

$$\begin{aligned}
\langle V(k,\eta)|\bar{d}\gamma^\mu b|B(p)\rangle &= \epsilon^{\mu\nu\rho\sigma}\eta^*_\nu p_\rho k_\sigma \frac{2V}{m_B+m_V}, \\
\langle V(k,\eta)|\bar{d}\gamma^\mu\gamma_5 b|B(p)\rangle &= i\eta^*_\nu \left[g^{\mu\nu}(m_B+m_V)A_1 - \frac{(p+k)^\mu q^\nu}{m_B+m_V}A_2 - q^\mu q^\nu \frac{2m_V}{q^2}(A_3-A_0)\right], \\
\langle V(k,\eta)|\bar{d}i\sigma^{\mu\nu}q_\nu b|B(p)\rangle &= \epsilon^{\mu\nu\rho\sigma}\eta^*_\nu p_\rho k_\sigma 2T_1, \\
\langle V(k,\eta)|\bar{d}i\sigma^{\mu\nu}\gamma_5 b|B(p)\rangle &= i\eta^*_\nu \Bigg[(g^{\mu\nu}(m_B^2-m_V^2) - (p+k)^\mu q^\nu)T_2 \\
&\quad + q^\nu\left(q^\mu - \frac{q^2}{m_B^2-m_V^2}(p+k)^\mu\right)T_3\Bigg],
\end{aligned} \tag{4.20}$$

where η is the polarisation vector of the vector meson. A_3 is a redundant quantity and can be expressed in terms of A_1 and A_2

$$A_3 \equiv \frac{m_B+m_V}{2m_V}A_1 - \frac{m_B-m_V}{2m_V}A_2. \tag{4.21}$$

In practice, it is common to replace A_2 and T_3 by

$$\begin{aligned}
A_{12} \equiv& \frac{(m_B+m_V)^2(m_B^2-m_V^2-q^2)A_1 - \lambda(q^2,m_B^2,m_V^2)A_2}{16m_B m_V^2(m_B+m_V)}, \\
T_{23} \equiv& \frac{(m_B^2-m_V^2)(m_B^2+3m_V^2-q^2)T_2 - \lambda(q^2,m_B^2,m_V^2)T_3}{8m_B m_V^2(m_B-m_V)}.
\end{aligned} \tag{4.22}$$

Furthermore, there are also three identities for the form factors at $q^2=0$:

$$\begin{aligned}
f_+(q^2=0) =& f_0(q^2=0), \\
A_0(q^2=0) =& A_3(q^2=0), \\
T_1(q^2=0) =& T_2(q^2=0).
\end{aligned} \tag{4.23}$$

Combining Eqs. (4.21), (4.22), and (4.23), one obtains

$$A_{12}(q^2=0) = \frac{m_B^2-m_V^2}{8m_B m_V}A_0(q^2=0). \tag{4.24}$$

4.7 Appendix: $S, P, V, A, \mathcal{T}$ basis

The LEFT operators can be related to the basis used in [302]. In order to take into account the Majorana nature of neutrinos we include an additional factor of 1/2 in the effective

Lagrangian. This ensures that the leptonic helicity amplitudes have the same form as in the case of Dirac fermions. The effective Lagrangian is thus given by

$$\mathcal{L} = \frac{1}{2} c_H \sum_i \sum_{\alpha,\beta} (C_{i,\alpha\beta} O_{i,\alpha\beta} + C'_{i,\alpha\beta} O'_{i,\alpha\beta}) \; . \tag{4.25}$$

where i runs over $S, P, V, A, \mathcal{T}$ and c_H determines the normalisation of the operators. In this work we choose $c_H = 1$.[9] The operators are given by

$$O_{S(P)\alpha\beta} = (\overline{s_L} b)(\overline{\nu_\alpha}(\gamma_5)\nu_\beta) \; , \quad O_{V(A)\alpha\beta} = (\overline{s_L}\gamma^\mu b)(\overline{\nu_\alpha}\gamma_\mu(\gamma_5)\nu_\beta) \; , \quad O_{\mathcal{T}\alpha\beta} = (\overline{s_L}\sigma^{\mu\nu} b)(\overline{\nu_\alpha}\sigma_{\mu\nu}\nu_\beta) \; . \tag{4.26}$$

The primed operators are obtained by replacing $s_L \to s_R$, i.e. $O' = O|_{s_L \to s_R}$ where $q_{L,R} \equiv P_{L,R} q$. The notation $O_{9(10)} \equiv O_{V(A)}$ is also commonly found in the literature. The operators have well-defined symmetry properties: the pseudo(scalar) operators are symmetric in the neutrino flavour indices and the (axial)vector and tensor operators are antisymmetric. We find for the Wilson coefficients using the $S, P, V, A, \mathcal{T}$ basis

$$\begin{aligned}
C_{V\alpha\beta} &= C^{\mathrm{VLL}}_{\nu d,[\alpha\beta]sb} \; , & C_{A\alpha\beta} &= -C^{\mathrm{VLL}}_{\nu d,(\alpha\beta)sb} \; , \\
C'_{V\alpha\beta} &= C^{VLR}_{\nu d,[\alpha\beta]sb} \; , & C'_{A\alpha\beta} &= -C^{VLR}_{\nu d,(\alpha\beta)sb} \; , \\
C_{S\alpha\beta} &= C^{\mathrm{SLR}}_{\nu d,(\alpha\beta)sb} + C^{\mathrm{SLL}*}_{\nu d,(\beta\alpha)bs} \; , & C_{P\alpha\beta} &= -C^{\mathrm{SLR}}_{\nu d,(\alpha\beta)sb} + C^{\mathrm{SLL}*}_{\nu d,(\beta\alpha)bs} \; , \\
C'_{S\alpha\beta} &= C^{\mathrm{SLL}}_{\nu d,(\alpha\beta)sb} + C^{\mathrm{SLR}*}_{\nu d,(\beta\alpha)bs} \; , & C'_{P\alpha\beta} &= -C^{\mathrm{SLL}}_{\nu d,(\alpha\beta)sb} + C^{\mathrm{SLR}*}_{\nu d,(\beta\alpha)bs} \; , \\
C_{\mathcal{T}\alpha\beta} &= 2C^{\mathrm{TLL}*}_{\nu d,[\beta\alpha]bs} \; , & C'_{\mathcal{T}\alpha\beta} &= 2C^{\mathrm{TLL}}_{\nu d,[\alpha\beta]sb} \; ,
\end{aligned} \tag{4.27}$$

where α, β denote the neutrino flavours. Parentheses $(\dots)$ indicate symmetrisation and square brackets $[\dots]$ indicate anti-symmetrisation of the neutrino flavour indices as in

$$M_{(ab)} \equiv \frac{1}{2}(M_{ab} + M_{ba}) \; , \qquad M_{[ab]} \equiv \frac{1}{2}(M_{ab} - M_{ba}) \; . \tag{4.28}$$

4.8 Appendix: $B \to K\nu_\alpha\nu_\beta$

For the convenience of the reader, we provide the expression for the coefficient $G^{(0)}$ of the Wigner-D function $D^0_{0,0}(\Omega) = 1$ for $\bar{B} \to \bar{K}\nu_\alpha\nu_\beta$ following [302]. Although the vector and

---

[9] Reference [302] uses $c_H = \frac{4G_F}{\sqrt{2}} \frac{\alpha}{4\pi} V^*_{ts} V_{tb}$. Note that we rewrote the effective Hamiltonian in terms of an effective Lagrangian and replaced ℓ in [302] by the neutrino fields ν.

tensor operator are antisymmetric in the neutrino flavour indices α, β, all combinations which enter the helicity amplitudes are symmetric under exchanging them. The CP-conjugate process $B \to K\nu_\alpha\nu_\beta$ is obtained via replacing $G^{(0)}$ by $\bar{G}^{(0)}$ where the Wilson coefficients in the helicity amplitudes are replaced by their complex conjugates. Note that this complex conjugation does not introduce additional minus signs into the coefficients of the Wigner-D functions for terms with antisymmetric Wilson coefficients. The CP conjugation also implies a redefinition of the angles, in particular $\theta_K \to \pi - \theta_K$, under which the relevant Wigner-D functions $D^0_{0,0}$ and $D^2_{0,0}$ are invariant though. According to [302],

$$\begin{aligned} N^{-1}G^{(0)}(q^2) = {} & \left(4\left(E_\alpha E_\beta + m_\alpha m_\beta\right) + \frac{\lambda_{\gamma^*}}{3q^2}\right)|h^V_{\alpha\beta}|^2 + \left(4\left(E_\alpha E_\beta - m_\alpha m_\beta\right) + \frac{\lambda_{\gamma^*}}{3q^2}\right)|h^A_{\alpha\beta}|^2 \\ & + \left(4\left(E_\alpha E_\beta - m_\alpha m_\beta\right) + \frac{\lambda_{\gamma^*}}{q^2}\right)|h^S_{\alpha\beta}|^2 + \left(4\left(E_\alpha E_\beta + m_\alpha m_\beta\right) + \frac{\lambda_{\gamma^*}}{q^2}\right)|h^P_{\alpha\beta}|^2 \\ & + 16\left(E_\alpha E_\beta + m_\alpha m_\beta - \frac{\lambda_{\gamma^*}}{12q^2}\right)|h^{T_t}_{\alpha\beta}|^2 + 8\left(E_\alpha E_\beta - m_\alpha m_\beta - \frac{\lambda_{\gamma^*}}{12q^2}\right)|h^T_{\alpha\beta}|^2 \\ & + 16\left(m_\alpha E_\beta + m_\beta E_\alpha\right)\,\mathrm{Im}\left[h^V_{\alpha\beta}h^{T_t*}_{\alpha\beta}\right] + 8\sqrt{2}\left(m_\alpha E_\beta - m_\beta E_\alpha\right)\,\mathrm{Im}\left[h^A_{\alpha\beta}h^{T*}_{\alpha\beta}\right], \end{aligned} \tag{4.29}$$

where the normalisation factor N, the energies $E_{\alpha,\beta}$ and the kinematic functions λ_{BK,γ^*} are defined as in

$$N = \frac{\sqrt{\lambda_{BK}\lambda_{\gamma^*}}}{(4\pi)^3 m_B^3 q^2(1+\delta_{\alpha\beta})}\ , \quad E_{\alpha,\beta} = \sqrt{m^2_{\alpha,\beta} + \frac{\lambda_{\gamma^*}}{4q^2}}\ , \quad \lambda_{BK} \equiv \lambda(m_B^2, m_K^2, q^2)\ , \quad \lambda_{\gamma^*} \equiv \lambda(q^2, m_\alpha^2, m_\beta^2) \tag{4.30}$$

and $\lambda(x,y,z) \equiv x^2 + y^2 + x^2 - 2xy - 2xz - 2yz$ denotes the Källén function. The symmetry factor for identical neutrinos in the final state is contained in N.

The helicity amplitudes are given by

$$h^V_{\alpha\beta} = \frac{\sqrt{\lambda_{BK}}}{2\sqrt{q^2}} \left(C_{V\alpha\beta} + C'_{V\alpha\beta}\right) f_+ \,, \tag{4.31}$$

$$h^A_{\alpha\beta} = \frac{\sqrt{\lambda_{BK}}}{2\sqrt{q^2}} \left(C_{A\alpha\beta} + C'_{A\alpha\beta}\right) f_+ \,, \tag{4.32}$$

$$h^S_{\alpha\beta} = \frac{m_B^2 - m_K^2}{2} \left(\frac{C_{S\alpha\beta} + C'_{S\alpha\beta}}{m_b - m_s} + \frac{m_\alpha - m_\beta}{q^2}(C_{V\alpha\beta} + C'_{V\alpha\beta})\right) f_0 \,, \tag{4.33}$$

$$h^P_{\alpha\beta} = \frac{m_B^2 - m_K^2}{2} \left(\frac{C_{P\alpha\beta} + C'_{P\alpha\beta}}{m_b - m_s} + \frac{m_\alpha + m_\beta}{q^2}(C_{A\alpha\beta} + C'_{A\alpha\beta})\right) f_0 \,, \tag{4.34}$$

$$h^T_{\alpha\beta} = -i\frac{\sqrt{\lambda_{BK}}}{\sqrt{2}(m_B + m_K)} \left(C_{\mathcal{T}\alpha\beta} - C'_{\mathcal{T}\alpha\beta}\right) f_T \,, \tag{4.35}$$

$$h^{T_t}_{\alpha\beta} = -i\frac{\sqrt{\lambda_{BK}}}{2(m_B + m_K)} \left(C_{\mathcal{T}\alpha\beta} + C'_{\mathcal{T}\alpha\beta}\right) f_T \tag{4.36}$$

in terms of the $S, P, V, A, \mathcal{T}$ basis. We provide the matching to the chiral LEFT basis in App. 4.7. For massless neutrinos, the expression reduces to

$$G^{(0)}(q^2) = \frac{\sqrt{\lambda_{BK}}q^2}{(4\pi)^3 m_B^3(1+\delta_{\alpha\beta})} \left(\frac{4}{3}|h^V_{\alpha\beta}|^2 + \frac{4}{3}|h^A_{\alpha\beta}|^2 + 2|h^S_{\alpha\beta}|^2 + 2|h^P_{\alpha\beta}|^2 + \frac{8}{3}|h^{T_t}_{\alpha\beta}|^2 + \frac{4}{3}|h^T_{\alpha\beta}|^2\right) . \tag{4.37}$$

4.9 Appendix: $B \to K^*\nu_\alpha\nu_\beta$

As the final-state neutrinos are not observed, we integrate over the neutrino solid angle. Thus there are only two relevant contributions which are described in terms of the coefficients of the Wigner-D functions $D^0_{0,0}(\Omega_K)$ and $D^2_{0,0}(\Omega_K)$ which depend on the solid angle Ω_K of the final-state K meson in the K^* rest frame. They are denoted by $G^{0,0}_0$ and $G^{2,0}_0$ for $\bar{B} \to \bar{K}^*\nu_\alpha\nu_\beta$ following [302]. The corresponding coefficients for the CP conjugate process $B \to K^*\nu_\alpha\nu_\beta$ are denoted by $\bar{G}^{0,0}_0$ and $\bar{G}^{2,0}_0$ and obtained from $G^{0,0}_0$ and $G^{2,0}_0$ by replacing all Wilson coefficients with their complex conjugates. The coefficient for the

Wigner-D function $D^0_{0,0}$ for $\bar{B} \to \bar{K}^* \nu_\alpha \nu_\beta$ is [302].

$$\begin{aligned}
N^{-1} G_0^{0,0} = {} & \frac{4}{9}\left(3E_\alpha E_\beta + \frac{\lambda_{\gamma^*}}{4q^2}\right) \sum_{a=0,\pm} \left(|H^V_{a\alpha\beta}|^2 + |H^A_{a\alpha\beta}|^2\right) + \frac{4m_\alpha m_\beta}{3} \sum_{a=0,\pm} \left(|H^V_{a\alpha\beta}|^2 - |H^A_{a\alpha\beta}|^2\right) \\
& + \frac{4}{3}\left(E_\alpha E_\beta - m_\alpha m_\beta + \frac{\lambda_{\gamma^*}}{4q^2}\right) |H^S_{\alpha\beta}|^2 + \frac{4}{3}\left(E_\alpha E_\beta + m_\alpha m_\beta + \frac{\lambda_{\gamma^*}}{4q^2}\right) |H^P_{\alpha\beta}|^2 \\
& + \frac{16}{9}\left(3(E_\alpha E_\beta + m_\alpha m_\beta) - \frac{\lambda_{\gamma^*}}{4q^2}\right) \sum_{a=0,\pm} |H^{T_t}_{a\alpha\beta}|^2 \\
& + \frac{8}{9}\left(3(E_\alpha E_\beta - m_\alpha m_\beta) - \frac{\lambda_{\gamma^*}}{4q^2}\right) \sum_{a=0,\pm} |H^{T}_{a\alpha\beta}|^2 \\
& + \frac{16}{3}(m_\alpha E_\beta + m_\beta E_\alpha)\, \mathrm{Im}\left[\sum_{a=0,\pm} H^V_{a\alpha\beta} H^{T_t *}_{a\alpha\beta}\right] \\
& + \frac{8\sqrt{2}}{3}(m_\alpha E_\beta - m_\beta E_\alpha)\, \mathrm{Im}\left[\sum_{a=0,\pm} H^V_{a\alpha\beta} H^{T *}_{a\alpha\beta}\right]
\end{aligned} \tag{4.38}$$

and the coefficient for the Wigner-D function $D^2_{0,0}$ is

$$\begin{aligned}
N^{-1} G_0^{2,0} = {} & -\frac{4}{9}\left(3E_\alpha E_\beta + \frac{\lambda_{\gamma^*}}{4q^2}\right) \sum_{b=V,A} \left(|H^b_{+\alpha\beta}|^2 + |H^b_{-\alpha\beta}|^2 - 2|H^b_{0\alpha\beta}|^2\right) \\
& - \frac{4m_\alpha m_\beta}{3}\left(|H^V_{+\alpha\beta}|^2 + |H^V_{-\alpha\beta}|^2 - 2|H^V_{0\alpha\beta}|^2 - (V \to A)\right) \\
& + \frac{8}{3}\left(E_\alpha E_\beta - m_\alpha m_\beta + \frac{\lambda_{\gamma^*}}{4q^2}\right) |H^S_{\alpha\beta}|^2 + \frac{8}{3}\left(E_\alpha E_\beta + m_\alpha m_\beta + \frac{\lambda_{\gamma^*}}{4q^2}\right) |H^P_{\alpha\beta}|^2 \\
& - \frac{16}{9}\left(3(E_\alpha E_\beta + m_\alpha m_\beta) - \frac{\lambda_{\gamma^*}}{4q^2}\right)\left(|H^{T_t}_{+\alpha\beta}|^2 + |H^{T_t}_{-\alpha\beta}|^2 - 2|H^{T_t}_{0\alpha\beta}|^2\right) \\
& - \frac{8}{9}\left(3(E_\alpha E_\beta - m_\alpha m_\beta) - \frac{\lambda_{\gamma^*}}{4q^2}\right)\left(|H^{T}_{+\alpha\beta}|^2 + |H^{T}_{-\alpha\beta}|^2 - 2|H^{T}_{0\alpha\beta}|^2\right) \\
& - \frac{16}{3}\left(m_\alpha E_\beta + m_\beta E_\alpha\right) \mathrm{Im}\left[H^V_{+\alpha\beta} H^{T_t *}_{+\alpha\beta} + H^V_{-\alpha\beta} H^{T_t *}_{-\alpha\beta} - 2H^V_{0\alpha\beta} H^{T_t *}_{0\alpha\beta}\right] \\
& - \frac{8\sqrt{2}}{3}\left(m_\alpha E_\beta - m_\beta E_\alpha\right) \mathrm{Im}\left[H^V_{+\alpha\beta} H^{T *}_{+\alpha\beta} + H^V_{-\alpha\beta} H^{T *}_{-\alpha\beta} - 2H^V_{0\alpha\beta} H^{T *}_{0\alpha\beta}\right] ,
\end{aligned} \tag{4.39}$$

where the normalisation factor N, the energies $E_{\alpha,\beta}$ and the kinematic functions λ_{BK^*,γ^*} are the same as in Eq. (4.30) with the kinematic function λ_{BK} replaced by $\lambda_{BK^*} \equiv$

$\lambda(m_B^2, m_{K^*}^2, q^2)$. The helicity amplitudes for $\bar{B} \to \bar{K}^*\nu_\alpha\nu_\beta$ are given by

$$\begin{aligned}
H^V_{0\alpha\beta} &= \frac{4im_B m_{K^*}}{\sqrt{q^2}} \left(C_{V\alpha\beta} - C'_{V\alpha\beta}\right) A_{12} \,, \\
H^A_{0\alpha\beta} &= \frac{4im_B m_{K^*}}{\sqrt{q^2}} \left(C_{A\alpha\beta} - C'_{A\alpha\beta}\right) A_{12} \,, \\
H^V_{\pm\alpha\beta} &= \frac{i}{2(m_B + m_{K^*})} \left[\pm \left(C_{V\alpha\beta} + C'_{V\alpha\beta}\right) \sqrt{\lambda_{BK^*}} V - (m_B + m_{K^*})^2 \left(C_{V\alpha\beta} - C'_{V\alpha\beta}\right) A_1\right] \,, \\
H^A_{\pm\alpha\beta} &= \frac{i}{2(m_B + m_{K^*})} \left[\pm \left(C_{A\alpha\beta} + C'_{A\alpha\beta}\right) \sqrt{\lambda_{BK^*}} V - (m_B + m_{K^*})^2 \left(C_{A\alpha\beta} - C'_{A\alpha\beta}\right) A_1\right] \,, \\
H^P_{\alpha\beta} &= \frac{i\sqrt{\lambda_{BK^*}}}{2} \left[\frac{C_{P\alpha\beta} - C'_{P\alpha\beta}}{m_b + m_s} + \frac{m_\alpha + m_\beta}{q^2} \left(C_{A\alpha\beta} - C'_{A\alpha\beta}\right)\right] A_0 \,, \\
H^S_{\alpha\beta} &= \frac{i\sqrt{\lambda_{BK^*}}}{2} \left[\frac{C_{S\alpha\beta} - C'_{S\alpha\beta}}{m_b + m_s} + \frac{m_\alpha - m_\beta}{q^2} \left(C_{V\alpha\beta} - C'_{V\alpha\beta}\right)\right] A_0 \,, \\
H^T_{0\alpha\beta} &= \frac{2\sqrt{2} m_B m_{K^*}}{m_B + m_{K^*}} \left(C_{\mathcal{T}\alpha\beta} + C'_{\mathcal{T}\alpha\beta}\right) T_{23} \,, \\
H^{T_t}_{0\alpha\beta} &= \frac{2 m_B m_{K^*}}{m_B + m_{K^*}} \left(C_{\mathcal{T}\alpha\beta} - C'_{\mathcal{T}\alpha\beta}\right) T_{23} \,, \\
H^T_{\pm\alpha\beta} &= \frac{1}{\sqrt{2q^2}} \left[\pm \left(C_{\mathcal{T}\alpha\beta} - C'_{\mathcal{T}\alpha\beta}\right) \sqrt{\lambda_{BK^*}} T_1 - \left(C_{\mathcal{T}\alpha\beta} + C'_{\mathcal{T}\alpha\beta}\right) (m_B^2 - m_{K^*}^2) T_2\right] \,, \\
H^{T_t}_{\pm\alpha\beta} &= \frac{1}{2\sqrt{q^2}} \left[\pm \left(C_{\mathcal{T}\alpha\beta} + C'_{\mathcal{T}\alpha\beta}\right) \sqrt{\lambda_{BK^*}} T_1 - \left(C_{\mathcal{T}\alpha\beta} - C'_{\mathcal{T}\alpha\beta}\right) (m_B^2 - m_{K^*}^2) T_2\right]
\end{aligned} \tag{4.40}$$

in terms of the $S, P, V, A, \mathcal{T}$ basis. The matching to the chiral LEFT basis is given in App. 4.7. For massless neutrinos, the normalisation factor reduces to

$$N = \frac{\sqrt{\lambda_{BK^*}}}{(4\pi)^3 m_B^3 (1 + \delta_{\alpha\beta})} \tag{4.41}$$

and the coefficients of the Wigner-D functions become

$$\begin{aligned}
G_0^{0,0} &= Nq^2 \left[\frac{4}{9} \sum_{a=0,\pm} (|H^V_{a\alpha\beta}|^2 + |H^A_{a\alpha\beta}|^2) + \frac{2}{3}|H^S_{\alpha\beta}|^2 + \frac{2}{3}|H^P_{\alpha\beta}|^2 + \frac{8}{9} \sum_{a=0,\pm} |H^{T_t}_{a\alpha\beta}|^2 + \frac{4}{9} \sum_{a=0,\pm} |H^T_{a\alpha\beta}|^2\right] \,, \\
G_0^{2,0} &= Nq^2 \left[-\frac{4}{9} \sum_{b=V,A} \left(|H^b_{+\alpha\beta}|^2 + |H^b_{-\alpha\beta}|^2 - 2|H^b_{0\alpha\beta}|^2\right) + \frac{4}{3}|H^S_{\alpha\beta}|^2 + \frac{4}{3}|H^P_{\alpha\beta}|^2\right. \\
&\quad \left. - \frac{8}{9} \left(|H^{T_t}_{+\alpha\beta}|^2 + |H^{T_t}_{-\alpha\beta}|^2 - 2|H^{T_t}_{0\alpha\beta}|^2\right) - \frac{4}{9} \left(|H^T_{+\alpha\beta}|^2 + |H^T_{-\alpha\beta}|^2 - 2|H^T_{0\alpha\beta}|^2\right)\right] .
\end{aligned} \tag{4.42}$$

For massless neutrinos, the binned longitudinal polarisation fraction F_L for the decay $B \to K^* \nu_\alpha \nu_\beta$ can be compactly written in terms of helicity amplitudes $\bar{H}$ as

$$\begin{aligned} F_L &= \frac{\left\langle \bar{G}_0^{0,0} + \bar{G}_0^{2,0} \right\rangle}{3 \left\langle \bar{G}_0^{0,0} \right\rangle} \\ &= \frac{4}{9} \frac{\left\langle N q^2 \left(|\bar{H}^V_{0\alpha\beta}|^2 + |\bar{H}^A_{0\alpha\beta}|^2 + \frac{3}{2} |\bar{H}^S_{\alpha\beta}|^2 + \frac{3}{2} |\bar{H}^P_{\alpha\beta}|^2 + 2 |\bar{H}^{T_t}_{0\alpha\beta}|^2 + |\bar{H}^T_{0\alpha\beta}|^2 \right) \right\rangle}{\left\langle \bar{G}_0^{0,0} \right\rangle} \,. \end{aligned} \tag{4.43}$$

The helicity amplitudes $\bar{H}$ are obtained from the corresponding helicity amplitude H by replacing all Wilson coefficients by the complex conjugates. The corresponding binned transverse polarisation fraction F_T is given by

$$F_T = 1 - F_L = \frac{4}{9} \frac{\left\langle N q^2 \sum_{a=\pm} \left(|\bar{H}^V_{a\alpha\beta}|^2 + |\bar{H}^A_{a\alpha\beta}|^2 + 2 |\bar{H}^{T_t}_{a\alpha\beta}|^2 + |\bar{H}^T_{a\alpha\beta}|^2 \right) \right\rangle}{\left\langle \bar{G}_0^{0,0} \right\rangle} \,. \tag{4.44}$$

4.10 Appendix: $B \to X_s \nu_\alpha \nu_\beta$

In the following, the different terms contributing to the inclusive differential decay rate which was computed via `FeynCalc` [317, 318] are given. The individual contributions from vector, scalar and tensor operators are given as in

$$
\begin{aligned}
\frac{d\Gamma^{\nu_\alpha\nu_\beta}_{\text{incl,V}}}{dq^2} &= \frac{q^2}{m_b}\Bigg(12\frac{m_s}{m_b}\Big[(m_\alpha^2 - 4m_\alpha m_\beta + m_\beta^2 - q^2)\Re(C^{\text{VLL}}_{\nu d,[\alpha\beta]sb}C^{\text{VLR}*}_{\nu d,[\alpha\beta]sb}) \\
&\quad + (m_\alpha^2 + 4m_\alpha m_\beta + m_\beta^2 - q^2)\Re(C^{\text{VLL}}_{\nu d,(\alpha\beta)sb}C^{\text{VLR}*}_{\nu d,(\alpha\beta)sb})\Big] \\
&\quad - \frac{1}{m_b^2}\Big[g(m_\alpha, m_\beta, m_s, \sqrt{q^2}, m_b)\frac{1}{q^4} - 6m_\alpha m_\beta(m_b^2 + m_s^2 - q^2)\Big] \\
&\quad \times \Big[\big|C^{\text{VLL}}_{\nu d,[\alpha\beta]sb}\big|^2 + \big|C^{\text{VLR}}_{\nu d,[\alpha\beta]sb}\big|^2\Big] \\
&\quad - \frac{1}{m_b^2}\Big[g(m_\alpha, m_\beta, m_s, \sqrt{q^2}, m_b)\frac{1}{q^4} + 6m_\alpha m_\beta(m_b^2 + m_s^2 - q^2)\Big] \\
&\quad \times \Big[\big|C^{\text{VLL}}_{\nu d,(\alpha\beta)sb}\big|^2 + \big|C^{\text{VLR}}_{\nu d,(\alpha\beta)sb}\big|^2\Big]\Bigg), \\
\frac{d\Gamma^{\nu_\alpha\nu_\beta}_{\text{incl,S}}}{dq^2} &= -3\frac{q^2}{m_b}\Bigg((m_\alpha^2 + m_\beta^2 - q^2) \\
&\quad \times \Big[\frac{1}{m_b^2}(m_b^2 + m_s^2 - q^2)\left(\left|C^{\text{SLL}}_{\nu d,\alpha\beta sb}\right|^2 + \left|C^{\text{SLR}}_{\nu d,\alpha\beta sb}\right|^2 + \left|C^{\text{SLL}}_{\nu d,\alpha\beta bs}\right|^2 + \left|C^{\text{SLR}}_{\nu d,\alpha\beta bs}\right|^2\right) \\
&\quad + 4\frac{m_s}{m_b}\Re(C^{\text{SLL}}_{\nu d,\alpha\beta sb}C^{\text{SLR}*}_{\nu d,\alpha\beta sb} + C^{\text{SLL}}_{\nu d,\alpha\beta bs}C^{\text{SLR}*}_{\nu d,\alpha\beta bs})\Big] \\
&\quad + 2m_\alpha m_\beta\Big[\frac{2}{m_b^2}(m_b^2 + m_s^2 - q^2)\text{Re}(C^{\text{SLL}}_{\nu d,\alpha\beta sb}C^{\text{SLL}}_{\nu d,\alpha\beta bs} + C^{\text{SLR}}_{\nu d,\alpha\beta sb}C^{\text{SLR}}_{\nu d,\alpha\beta bs}) \\
&\quad + 4\frac{m_s}{m_b}\Re(C^{\text{SLL}}_{\nu d,\alpha\beta sb}C^{\text{SLR}}_{\nu d,\alpha\beta bs} + C^{\text{SLR}}_{\nu d,\alpha\beta sb}C^{\text{SLL}}_{\nu d,\alpha\beta bs})\Big]\Bigg), \\
\frac{d\Gamma^{\nu_\alpha\nu_\beta}_{\text{incl,T}}}{dq^2} &= 16\frac{q^2}{m_b^3}\Bigg(\Big[3(m_\alpha^2 + m_\beta^2 - q^2)(m_b^2 + m_s^2 - q^2) - 2\,g(m_\alpha, m_\beta, m_s, \sqrt{q^2}, m_b)\frac{1}{q^4}\Big] \\
&\quad \times \left(\left|C^{\text{TLL}}_{\nu d,\alpha\beta sb}\right|^2 + \left|C^{\text{TLL}}_{\nu d,\alpha\beta bs}\right|^2\right) - 72m_\alpha m_\beta m_s m_b\text{Re}(C^{\text{TLL}}_{\nu d,\alpha\beta sb}C^{\text{TLL}}_{\nu d,\alpha\beta bs})\Bigg)\,.
\end{aligned}
\tag{4.45}
$$

Here, the function

$$
\begin{aligned}
g(x, y, s, w, m) &= \Big(2(x^4 + y^4) - w^4 - w^2(x^2 + y^2) - 4x^2y^2\Big)\lambda(m^2, s^2, w^2) \\
&\quad + 3w^2(x^4 + y^4 - 2x^2y^2 - w^4)(m^2 - w^2 + s^2)
\end{aligned}
\tag{4.46}
$$

was defined for convenience in order to shorten the expressions. The interference terms involving the vector operators and the scalar and tensor operators read

$$\begin{aligned}
\frac{d\Gamma^{\nu_\alpha\nu_\beta}_{\text{incl,VS}}}{dq^2} = & -\frac{3}{m_b^2}\Bigg((m_\alpha - m_\beta)\left((m_\alpha + m_\beta)^2 - q^2\right) \\
& \times \Big[\frac{m_s}{m_b}(m_b^2 - m_s^2 + q^2)\Re(C^{\text{VLL}}_{\nu d,[\alpha\beta]sb}(C^{\text{SLL}*}_{\nu d,\alpha\beta sb} + C^{\text{SLL}}_{\nu d,\alpha\beta bs}) + C^{\text{VLR}}_{\nu d,[\alpha\beta]sb}(C^{\text{SLR}*}_{\nu d,\alpha\beta sb} + C^{\text{SLR}}_{\nu d,\alpha\beta bs})) \\
& + (m_b^2 - m_s^2 - q^2)\Re(C^{\text{VLL}}_{\nu d,[\alpha\beta]sb}(C^{\text{SLR}*}_{\nu d,\alpha\beta sb} + C^{\text{SLR}}_{\nu d,\alpha\beta bs}) + C^{\text{VLR}}_{\nu d,[\alpha\beta]sb}(C^{\text{SLL}*}_{\nu d,\alpha\beta sb} + C^{\text{SLL}}_{\nu d,\alpha\beta bs}))\Big] \\
& + (m_\alpha + m_\beta)\left((m_\alpha - m_\beta)^2 - q^2\right) \\
& \times \Big[\frac{m_s}{m_b}(m_b^2 - m_s^2 + q^2)\Re(C^{\text{VLL}}_{\nu d,(\alpha\beta)sb}(C^{\text{SLL}*}_{\nu d,\alpha\beta sb} - C^{\text{SLL}}_{\nu d,\alpha\beta bs}) + C^{\text{VLR}}_{\nu d,(\alpha\beta)sb}(C^{\text{SLR}*}_{\nu d,\alpha\beta sb} - C^{\text{SLR}}_{\nu d,\alpha\beta bs})) \\
& + (m_b^2 - m_s^2 - q^2)\Re(C^{\text{VLL}}_{\nu d,(\alpha\beta)sb}(C^{\text{SLR}*}_{\nu d,\alpha\beta sb} - C^{\text{SLR}}_{\nu d,\alpha\beta bs}) + C^{\text{VLR}}_{\nu d,(\alpha\beta)sb}(C^{\text{SLL}*}_{\nu d,\alpha\beta sb} - C^{\text{SLL}}_{\nu d,\alpha\beta bs}))\Big]\Bigg)\,, \\
\frac{d\Gamma^{\nu_\alpha\nu_\beta}_{\text{incl,VT}}}{dq^2} = & \frac{36}{m_b^2}\Bigg((m_\alpha - m_\beta)\left((m_\alpha + m_\beta)^2 - q^2\right) \\
& \times \Big[\frac{m_s}{m_b}(m_b^2 - m_s^2 + q^2)\Re(C^{\text{VLL}}_{\nu d,(\alpha\beta)sb}C^{\text{TLL}*}_{\nu d,\alpha\beta sb} + C^{\text{VLR}}_{\nu d,(\alpha\beta)sb}C^{\text{TLL}}_{\nu d,\alpha\beta bs}) \\
& - (m_b^2 - m_s^2 - q^2)\Re(C^{\text{VLR}}_{\nu d,(\alpha\beta)sb}C^{\text{TLL}*}_{\nu d,\alpha\beta sb} + C^{\text{VLL}}_{\nu d,(\alpha\beta)sb}C^{\text{TLL}}_{\nu d,\alpha\beta bs})\Big] \\
& + (m_\alpha + m_\beta)\left((m_\alpha - m_\beta)^2 - q^2\right) \\
& \times \Big[\frac{m_s}{m_b}(m_b^2 - m_s^2 + q^2)\Re(C^{\text{VLL}}_{\nu d,[\alpha\beta]sb}C^{\text{TLL}*}_{\nu d,\alpha\beta sb} - C^{\text{VLR}}_{\nu d,[\alpha\beta]sb}C^{\text{TLL}}_{\nu d,\alpha\beta bs}) \\
& - (m_b^2 - m_s^2 - q^2)\Re(C^{\text{VLR}}_{\nu d,[\alpha\beta]sb}C^{\text{TLL}*}_{\nu d,\alpha\beta sb} - C^{\text{VLL}}_{\nu d,[\alpha\beta]sb}C^{\text{TLL}}_{\nu d,\alpha\beta bs})\Big]\Bigg)\,.
\end{aligned} \tag{4.47}$$

4.11 Appendix: Matching to SM Effective Field Theory with Sterile Neutrinos

For completeness we present the matching to SM effective field theory (SMEFT) with sterile neutrinos. The matching conditions have been obtained by translating the existing matching results in the literature [191, 192, 319] to the operator basis we are using. The relevant SMEFT operators are contained in the effective Lagrangians $\mathcal{L}_{6,7}$ for operators at dimension-6 and dimension-7, respectively [185, 191]

$$
\begin{aligned}
\mathcal{L}_6 \supset\; & C_H (H^\dagger H)^3 + C_{H\Box}(H^\dagger H)\Box(H^\dagger H) + C_{HD}(H^\dagger D^\mu H)^*(H^\dagger D_\mu H) \\
& + C_{HB} H^\dagger H B_{\mu\nu} B^{\mu\nu} + C_{HW} H^\dagger H W^I_{\mu\nu} W^{I\mu\nu} + C_{HWB} H^\dagger \tau^I H W^I_{\mu\nu} B^{\mu\nu} \\
& + C^{(1)}_{lq} (H^\dagger i \overset{\leftrightarrow}{D}_\mu H)(\bar{L}\gamma^\mu L) + C^{(3)}_{lq} (H^\dagger i \overset{\leftrightarrow}{D}{}^I_\mu H)(\bar{L}\tau^I \gamma^\mu L) + C_{ld}(\bar{L}\gamma_\mu L)(\bar{d}\gamma^\mu d) \\
& + C_{QN}(\bar{Q}\gamma_\mu Q)(\bar{N}\gamma^\mu N) + C_{dN}(\bar{d}\gamma_\mu d)(\bar{N}\gamma^\mu N) \\
& + C_{LNQd}(\bar{L}^\alpha N)\epsilon_{\alpha\beta}(\bar{Q}^\beta d) + C_{LdQN}(\bar{L}^\alpha d)\epsilon_{\alpha\beta}(\bar{Q}^\beta N) \\
\mathcal{L}_7 \supset\; & C_{\bar{d}LQLH1}\epsilon_{ij}\epsilon_{mn}(\bar{d}L^i)(\overline{Q^{cj}}L^m)H^n + C_{QNdH}(\bar{Q}N)(\overline{N^c}d)H + C_{dQNH}H^\dagger(\bar{d}Q)(\overline{N^c}N) \\
& + C_{QNLH1}\epsilon_{ij}(\bar{Q}\gamma_\mu Q)(\overline{N^c}\gamma^\mu L^i)H^j + C_{QNLH2}\epsilon_{ij}(\bar{Q}\gamma_\mu Q^i)(\overline{N^c}\gamma^\mu L^j)H \\
& + C_{dNLH}\epsilon_{ij}(\bar{d}\gamma_\mu d)(\overline{N^c}\gamma^\mu L^i)H^j
\end{aligned}
\tag{4.48}
$$

where N denotes right-handed neutrinos, i.e. right-handed SM singlet fermions, τ^I denotes the Pauli spin matrices and we suppressed flavour and colour indices. For the matching, we also require the modified Z-boson couplings [192]

$$
\mathcal{L} \supset -\bar{g}_Z Z_\mu \left[Z_{d_L}\bar{d}_L\gamma^\mu d_L + Z_{d_R}\bar{d}_R\gamma^\mu d_R + Z_\nu \bar{\nu}_K \gamma^\mu \nu_L + Z_N \bar{N}\gamma^\mu N + (Z_{\nu N}\overline{\nu^c}\gamma^\mu N + \text{h.c.}) \right] ,
\tag{4.49}
$$

where $\bar{g}_Z$ denotes the effective gauge coupling of the Z boson and depends on gauge couplings and the weak mixing angle $\bar{\theta}$

$$
\begin{aligned}
\bar{g}_Z &= \frac{\bar{e}}{\sin\bar{\theta}\cos\bar{\theta}}\left[1 + \frac{\bar{g}_1^2 + \bar{g}_2^2}{2\bar{g}_1\bar{g}_2} v_T^2 C_{HWB}\right] , & \bar{e} &= \bar{g}_2 \sin\bar{\theta} - \frac{1}{2}\cos\bar{\theta}\bar{g}_2 v_T^2 C_{HWB} , \\
\cos\bar{\theta} &= \frac{\bar{g}_2}{\sqrt{\bar{g}_1^2 + \bar{g}_2^2}}\left[1 - \frac{C_{HWB}v_T^2}{2}\frac{\bar{g}_1}{\bar{g}_2}\frac{\bar{g}_2^2 - \bar{g}_1^2}{\bar{g}_1^2 + \bar{g}_2^2}\right], & \bar{g}_1 &= g_1(1 + C_{HB}v_T^2) , \\
\sin\bar{\theta} &= \frac{\bar{g}_1}{\sqrt{\bar{g}_1^2 + \bar{g}_2^2}}\left[1 + \frac{C_{HWB}v_T^2}{2}\frac{\bar{g}_2}{\bar{g}_1}\frac{\bar{g}_2^2 - \bar{g}_1^2}{\bar{g}_1^2 + \bar{g}_2^2}\right], & \bar{g}_2 &= g_2(1 + C_{HW}v_T^2) .
\end{aligned}
\tag{4.50}
$$

The Z-boson couplings to the different fermion species are parameterised by

$$
\begin{aligned}
[Z_{d_L}]_{pr} &= \left(-\frac{1}{2} + \frac{1}{3}\sin^2\bar{\theta}\right)\delta_{pr} - \frac{v_T^2}{2}\left(C^{(1),pr}_{Hq} + C^{(3),pr}_{Hq}\right) , & [Z_{d_R}]_{pr} &= \frac{1}{3}\sin^2\bar{\theta}\delta_{pr} - \frac{v_T^2}{2}C^{pr}_{Hd} , \\
[Z_\nu]_{pr} &= \frac{1}{2}\delta_{pr} - \frac{v_T^2}{2}\left(C^{(1),pr}_{Hl} - C^{(3),pr}_{Hl}\right) , & [Z_N]_{pr} &= -\frac{v_T^2}{2}C^{pr}_{HN} , \\
[Z_{\nu N}]_{pr} &= \frac{v_T^3}{4\sqrt{2}}\left(C^{rp}_{NL1} + 2C^{rp}_{NL2}\right) .
\end{aligned}
\tag{4.51}
$$

Following [192], we write the renormalisable part of the SM Higgs potential as

$$V = \lambda \left(H^\dagger H - \frac{v^2}{2} \right)^2 \tag{4.52}$$

and the SM Higgs doublet H in unitary gauge as

$$H = \frac{1}{\sqrt{2}} \begin{pmatrix} 0 \\ [1 + c_{H,\text{kin}}]\, h + v_T \end{pmatrix} . \tag{4.53}$$

The Higgs field normalisation $1 + c_{H,\text{kin}}$ and the Higgs VEV v_T receive corrections from dimension-6 operators

$$c_{H,\text{kin}} \equiv \left(C_{H\Box} - \frac{1}{4} C_{HD} \right) v^2 , \qquad v_T \equiv \left(1 + \frac{3 C_H v^2}{8\lambda} \right) v . \tag{4.54}$$

After introducing and summarising the relevant SMEFT operators and expressions, it is straightforward to present the matching of the LEFT Wilson coefficients to SMEFT. We find for the LEFT Wilson coefficients with neutrino flavour indices $1 \leq \alpha, \beta \leq 3$

$$\begin{aligned}
C^{\text{VLL}}_{\nu d,\alpha\beta pr} &= C^{(1),\alpha\beta pr}_{lq} - C^{(3),\alpha\beta pr}_{lq} - \frac{\bar{g}_Z^2}{M_Z^2} [Z_{d_L}]_{pr} [Z_\nu]_{\alpha\beta}, & C^{\text{VLR}}_{\nu d,\alpha\beta pr} &= C^{\alpha\beta pr}_{ld} - \frac{\bar{g}_Z^2}{M_Z^2} [Z_{d_R}]_{pr} [Z_\nu]_{\alpha\beta}, \\
C^{\text{SLL}}_{\nu d,\alpha\beta pr} &= -\frac{v_T}{4\sqrt{2}} \left(C^{p\alpha r\beta}_{\bar{d}LQLH1} + C^{p\alpha r\beta}_{\bar{d}LQLH1} \right), & C^{\text{SLR}}_{\nu d,\alpha\beta pr} &= 0, \\
C^{\text{TLL}}_{\nu d,\alpha\beta pr} &= \frac{v_T}{16\sqrt{2}} \left(C^{p\alpha r\beta}_{\bar{d}LQLH1} - C^{p\beta r\alpha}_{\bar{d}LQLH1} \right) .
\end{aligned} \tag{4.55}$$

For Wilson coefficients pertaining only to sterile neutrinos with $\alpha, \beta \geq 4$, they are

$$\begin{aligned}
C^{\text{VLL}}_{\nu d,\alpha\beta pr} &= -C^{pr\beta\alpha}_{QN} + \frac{\bar{g}_Z^2}{M_Z^2} [Z_{d_L}]_{pr} [Z_N]_{\beta\alpha}, & C^{\text{VLR}}_{\nu d,\alpha\beta pr} &= -C^{pr\beta\alpha}_{dN} + \frac{\bar{g}_Z^2}{M_Z^2} [Z_{d_R}]_{pr} [Z_N]_{\beta\alpha}, \\
C^{\text{SLL}}_{\nu d,\alpha\beta pr} &= -\frac{v_T}{4\sqrt{2}} \left(C^{p\alpha\beta r}_{QNdH} + C^{p\beta\alpha r}_{QNdH} \right), & C^{\text{SLR}}_{\nu d,\alpha\beta pr} &= \frac{v_T}{\sqrt{2}} C^{pr\alpha\beta}_{dQNH}, \\
C^{\text{TLL}}_{\nu d,\alpha\beta pr} &= \frac{v_T}{16\sqrt{2}} \left(C^{p\alpha\beta r}_{QNdH} - C^{p\beta\alpha r}_{QNdH} \right) .
\end{aligned} \tag{4.56}$$

The different signs and orderings of neutrino flavour indices originate from the charge conjugation in $N \equiv \nu^c$ and the symmetry properties of the bilinears

$$\overline{\psi_i^c} \Gamma \psi^{cj} = \eta_\Gamma \overline{\psi^j} \Gamma \psi_i \qquad C^{-1} \Gamma C = \eta_\Gamma \Gamma^T \qquad \eta_\Gamma = \begin{cases} +1 & \text{for } \Gamma = 1, \gamma_5, \gamma^\mu \gamma_5 \\ -1 & \text{for } \Gamma = \gamma^\mu, \sigma^{\mu\nu}, \sigma^{\mu\nu}\gamma_5 \end{cases} . \tag{4.57}$$

Finally, SMEFT operators which contain both sterile and active neutrinos imply

$$\begin{aligned}
C^{\mathrm{VLL}}_{\nu d,\alpha\beta pr} &= \frac{v_T}{\sqrt{2}}\left(C^{pr\alpha\beta}_{QNLH1} - C^{pr\alpha\beta}_{QNLH2}\right) + \frac{\bar{g}_Z^2}{M_Z^2}[Z_{d_L}]_{pr}[Z_{\nu N}]_{\beta\alpha}, \\
C^{\mathrm{VLR}}_{\nu d,\alpha\beta pr} &= \frac{v_T}{\sqrt{2}}C^{pr\alpha\beta}_{dNLH} + \frac{\bar{g}_Z^2}{M_Z^2}[Z_{d_R}]_{pr}[Z_{\nu N}]_{\beta\alpha}, \\
C^{\mathrm{SLL}}_{\nu d,\alpha\beta pr} &= C^{\beta\alpha rp*}_{LNQd} - \frac{1}{2}C^{\beta pr\alpha*}_{LdQN}, \\
C^{\mathrm{SLR}}_{\nu d,\alpha\beta pr} &= 0, \\
C^{\mathrm{TLL}}_{\nu d,\alpha\beta pr} &= -\frac{1}{8}C^{\beta pr\alpha*}_{LdQN}
\end{aligned} \tag{4.58}$$

when $\alpha \geq 4$ and $1 \leq \beta \leq 3$ and

$$\begin{aligned}
C^{\mathrm{VLL}}_{\nu d,\alpha\beta pr} &= \frac{v_T}{\sqrt{2}}\left(C^{rp\beta\alpha*}_{QNLH1} - C^{rp\alpha\beta*}_{QNLH2}\right) + \frac{\bar{g}_Z^2}{M_Z^2}[Z_{d_L}]^*_{rp}[Z_{\nu N}]^*_{\alpha\beta}, \\
C^{\mathrm{VLR}}_{\nu d,\alpha\beta pr} &= \frac{v_T}{\sqrt{2}}C^{rp\beta\alpha*}_{dNLH} + \frac{\bar{g}_Z^2}{M_Z^2}[Z_{d_R}]^*_{rp}[Z_{\nu N}]^*_{\alpha\beta}, \\
C^{\mathrm{SLL}}_{\nu d,\alpha\beta pr} &= C^{\alpha\beta rp*}_{LNQd} - \frac{1}{2}C^{\alpha pr\beta*}_{LdQN}, \\
C^{\mathrm{SLR}}_{\nu d,\alpha\beta pr} &= 0, \\
C^{\mathrm{TLL}}_{\nu d,\alpha\beta pr} &= -\frac{1}{8}C^{\alpha pr\beta*}_{LdQN}
\end{aligned} \tag{4.59}$$

when $1 \leq \alpha \leq 3$ and $\beta \geq 4$.

Chapter 5

Flavour Anomalies Meet Flavour Symmetry

After having performed (partly) model-independent studies in this thesis so far, I lastly present an extensive investigation of a concrete NP model which provides a possible explanation for several currently observed flavour anomalies as well as for the charged fermion masses and quark mixing. The predicted interaction structure is constrained by the discrete symmetry $D_{17} \times Z_{17}$ which is broken at high energies by the VEVs of several spurion fields. I find that it is indeed possible to address the aforementioned anomalies in agreement with experimental constraints arising from various flavour observables. The presentation in this chapter draws from ref. [90].[1]

5.1 Introduction

The SM has been very successful in describing the gauge interactions involving fermions, the Higgs boson and gauge bosons. However, the observed values for the masses and

---

[1] I was primarily responsible for sections 4 and 5 as well as appendices C.3.2−C.3.6 and D therein, but also helped prepare the other sections and appendices. I acknowledge my co-authors Innes Bigaran, Claudia Hagedorn and Michael Schmidt and their contributions.

mixing among the fermions can only be accommodated with a judicious choice of free parameters, appearing in the Yukawa matrices, and cannot be predicted. In particular, it would be desirable to have a profound explanation at hand for the strong hierarchies among the charged fermion masses, and for the fact that the Cabibbo angle is the only sizeable quark mixing angle, while the lepton sector features two large mixing angles.

Given the success of symmetries in predicting the gauge interactions of the SM particles, it appears reasonable to also employ a symmetry G_f which acts on the flavour (or generation) space in order to explain the measured fermion masses and mixing. Abelian symmetries, such as a U(1) group [78], have been shown to be capable of accommodating the hierarchies among the charged fermion masses via an appropriate selection of charges for the different generations of SM fermion species. However, a non-abelian, discrete flavour symmetry group which can be broken non-trivially seems to be preferred in the light of the striking differences between quark and lepton mixing, as well as due to the capability of these groups to predict a certain mixing pattern, e.g. tri-bimaximal mixing among leptons [320–323]. See refs. [175–178] for reviews about applications in high-energy particle physics.

In recent years there have been several measurements of flavour-physics observables which deviate from their respective SM predictions and hint at a more non-trivial flavour structure. In particular, the ratios[2]

$$R(D^{(\star)}) = \frac{\Gamma(B \to D^{(\star)}\tau\nu)}{\Gamma(B \to D^{(\star)}\ell\nu)} \tag{5.1}$$

with $\ell = e, \mu$ which are sensitive probes of LFU have been measured at BaBar [128, 129], Belle [14, 125–127] and LHCb [15, 16, 124]. A combined fit yields larger values for $R(D^{(\star)})$ and exhibits a tension with the SM prediction at the $3.4\,\sigma$ level [10]. There is also a long-standing discrepancy between the measured value [18, 46] of the AMM of the muon, $a_\mu = (g-2)_\mu/2$, and its theoretical prediction [19, 324–358]. The combined fit to the experimental data shows a $4.2\,\sigma$ tension [18] in $\Delta a_\mu = a_\mu^{\mathrm{exp}} - a_\mu^{\mathrm{SM}}$.[3] The three anomalies are summarised in table 5.1.

In ref. [79] Bauer and Neubert have proposed a simultaneous explanation of the flavour

---

[2] For brevity, antiparticles are not indicated by overbars in schematic expressions in

Anomalies					
Observable	SM prediction		Experiment		Significance
$R(D)$	0.297 ± 0.008	[11–13]	$0.340 \pm 0.027 \pm 0.013$	[10]	$1.4\ \sigma$
$R(D^\star)$	0.245 ± 0.008	[11–13]	$0.295 \pm 0.010 \pm 0.010$	[10]	$2.9\ \sigma$
Δa_μ	0		$(2.51 \pm 0.59) \times 10^{-9}$	[18,19]	$4.2\ \sigma$

Table 5.1: **Overview of the three anomalies to be addressed in this chapter and their present significance.** The quoted experimental values for $R(D)$ and $R(D^\star)$ are adopted from the Heavy Flavour Averaging Group (HFLAV) fit *circa* 2021, and the combined significance of these two anomalies is $3.4\ \sigma$, with a correlation $\rho = -0.38$ [10].

anomalies via the scalar LQ ϕ transforming as $(3, 1, -\frac{1}{3})$ under the SM gauge group. The importance of LQ couplings to RH fermions has been emphasised in ref. [80] and it has been pointed out that ϕ alone cannot explain the discrepancies in $b \to s\mu\mu$ which requires the presence of additional particles; see e.g. refs. [359–371]. In the vast majority of these studies only the couplings which are needed to explain the flavour anomalies are assumed to be non-zero, without any explanation for their size or why the remaining couplings vanish.

In this chapter, I describe a model with a discrete flavour symmetry which explains the observed anomalies in $R(D^{(\star)})$ and in the AMM of the muon. This model is also capable of correctly describing the strong hierarchies among the charged fermion masses as well as quark mixing, while not accounting for neutrino masses and lepton mixing. Therefore, the three generations of SM fermions are (mostly) assigned to doublets and singlets of G_f, and a dihedral group is chosen for the flavour symmetry. The series of single-valued (double-valued) dihedral groups D_n (D'_n) groups feature one- and two-dimensional irreducible representations for $n \geq 3$ ($n \geq 2$); see e.g. refs. [372–375] for their application in the context of fermion mixing. The thorough analysis in this chapter shows that a model equipped with the flavour symmetry group $G_f = D_{17} \times Z_{17}$ can pass all requirements

---

this chapter unless required for clarity.

[3] There is an ongoing debate about the theoretical prediction of the HVP. While the current determination of the LO contribution is obtained from dispersion relations, c.f. ref. [19], recent lattice calculations [145–148] predict a value consistent with the experimental result for the AMM of the muon.

which for instance arise from the non-observation of cLFV decays such as $\tau \to \mu\gamma$. The residual symmetry Z_{17}^{diag} which furnishes a diagonal subgroup of G_f is preserved by the LQ couplings to the SM fermions at LO, and turns out crucial for appropriately suppressing the couplings to up quarks and electrons. The breaking of the flavour symmetry is achieved with the help of four spurions that acquire specific VEVs, given in terms of the expansion parameter $\lambda \approx 0.2$. For related studies on flavour symmetries in the context of explaining the anomalies observed in semi-leptonic B meson decays, see refs. [81–86].

The chapter is organised as follows. The model setup is introduced in section 5.2 wherein the choice of G_f, its residual symmetry and the assignment of transformation properties to the particles as well as the spurion fields are motivated. The explicit form of the mass matrices and the LQ couplings in the charged fermion mass basis is derived in section 5.3. Analytic expressions for the charged fermion masses and quark mixing are also given. Section 5.4 contains the phenomenological study which includes the analytic estimates and numerical results for primary and secondary observables. Conclusions are drawn in section 5.5, and further technical details are collected in the appendices 5.6 to 5.12.

5.2 Model Setup

The main motivation behind the model discussed in this chapter is to ameliorate the above-mentioned anomalies with a specific LQ coupling structure which is predicted by a (discrete) flavour symmetry. For that purpose, the scalar LQ S_1 [160], c.f. section 2.3.2, is added to the SM particle content, but I employ the notation $\phi \sim (3, 1, -\frac{1}{3})$ in this chapter which implies that the quantum numbers of ϕ coincide with those of $S_1^\dagger$. Sterile neutrinos are not included in the model, and baryon-number conservation is imposed in order to forbid the occurrence of diquark couplings. Furthermore, the structure of a type-II two-Higgs-doublet model [376, 377] is adopted, that is, the generation of up-type quark masses is achieved via the Higgs doublet H_u, whereas the masses of the down-type quarks and charged leptons arise from the presence of a second Higgs doublet H_d. In order to accommodate the hierarchy between the masses of the bottom quark (or the tau lepton) and the top quark, an adequate hierarchy among the VEVs of H_d and H_u must be chosen. This implies

$$\left\langle H_d^0 \right\rangle \equiv \frac{v_d}{\sqrt{2}} \sim 2.4\text{ GeV} \quad \text{and} \quad \left\langle H_u^0 \right\rangle \equiv \frac{v_u}{\sqrt{2}} \sim 174\text{ GeV} \tag{5.2}$$

and therefore $v_u^2 + v_d^2 = v^2 \sim (246\,\text{GeV})^2$. Consequently, the Yukawa sector of the SM is defined as in

$$\mathcal{L}_{\text{Yuk}} = -y_u^{ij}\,\overline{Q_{Li}}\,H_u\,u_{Rj} - y_d^{ij}\,\overline{Q_{Li}}\,H_d\,d_{Rj} - y_e^{ij}\,\overline{L_{Li}}\,H_d\,e_{Rj} + \text{h.c.} \tag{5.3}$$

which is consistent with eq. (2.14) up to the obvious difference due to the presence of H_u and H_d. I do not discuss the scalar potential of the model. The couplings of ϕ to the SM fermions are described as in

$$\mathcal{L}_{\text{LQ}}^{\text{int}} = \hat{x}_{ij}\,\overline{L_{Li}^c}\,\phi^\dagger\,Q_{Lj} + \hat{y}_{ij}\,\overline{e_{Ri}^c}\,\phi^\dagger\,u_{Rj} + \text{h.c.}\;. \tag{5.4}$$

Here, $\hat{x}_{ij}$ and $\hat{y}_{ij}$ are, in general, complex numbers which constitute the coupling matrices $\hat{\mathbf{x}}$ and $\hat{\mathbf{y}}$. The hats indicate the interaction basis of the SM fermions. Adopting the mass basis of the charged SM fermions yields

$$\mathcal{L}_{\text{LQ}}^{\text{mass}} = x_{ij}\,\overline{(\nu_L^{\text{m}})^c}_i\,\phi^\dagger\,d_{Lj}^{\text{m}} + y_{ij}\,\overline{(e_R^{\text{m}})^c}_i\,\phi^\dagger\,u_{Rj}^{\text{m}} - z_{ij}\,\overline{(e_L^{\text{m}})^c}_i\,\phi^\dagger\,u_{Lj}^{\text{m}} + \text{h.c.} \tag{5.5}$$

where the conventions are consistent with section 2.1.3. In a way similar to the interaction basis, x_{ij}, y_{ij} and z_{ij} are, in general, complex numbers which constitute the coupling matrices $\mathbf{x}$, $\mathbf{y}$ and $\mathbf{z}$. Note that

$$\mathbf{z} = \mathbf{x}\,V^\dagger \tag{5.6}$$

with the CKM matrix V. Neutrino masses are not accounted for in the model, and thus lepton mixing is unphysical as in the SM.

Regarding the interactions between ϕ and the different generations of SM fermions, a major guiding principle for the construction of the model is an (approximate) achievement of the texture

$$\mathbf{x} \sim \begin{pmatrix} 0 & 0 & 0 \\ 0 & \lambda^3 & \lambda \\ 0 & \lambda^2 & 1 \end{pmatrix} \quad \text{and} \quad \mathbf{y} \sim \begin{pmatrix} 0 & 0 & 0 \\ 0 & 0 & \lambda^3 \\ 0 & 1 & 0 \end{pmatrix}\,, \tag{5.7}$$

which was identified in ref. [80]. Here, $\lambda \approx 0.2$, and zeros denote entries which are generally further suppressed than $\lambda^4 \sim 10^{-3}$. All non-zero components are accompanied by complex order-one numbers. The above textures hold in a basis which (approximately) coincides with the mass basis of the down-type quarks and charged leptons, thus, the CKM matrix (largely) originates from the structure of the up-quark mass matrix. Furthermore, the unitary transformation associated with the RH up-type quarks is close to the unit matrix in flavour space.

In the model, the non-zero entries shown in the texture above are generated with the help of a single spurion field S. Protecting (most of) the zero entries in $\mathbf{y}$ is one motivation to introduce an external Z_N symmetry and assign different charges under it to the RH up quarks.

Furthermore, experimental constraints require that the first row and column of both LQ coupling matrices $\mathbf{x}$ and $\mathbf{y}$ are largely suppressed. In the model, this requirement is implemented with the help of a residual symmetry. I consider an extension of the SM gauge group by the group product

$$D_{17} \times Z_{17} \tag{5.8}$$

with the residual symmetry Z_{17}^{diag}, where Z_{17}^{diag} is the diagonal subgroup of a Z_{17} symmetry contained in D_{17} (and generated by the generator a of D_{17}; see appendix 5.6 for details) and the external Z_{17} symmetry. As long as Z_{17}^{diag} is intact, the vanishing elements in the texture in eq. (5.7) are protected from acquiring non-zero values. Conversely, the non-zero values therein should correspond to combinations of SM fermions and ϕ of which the added-up charge under the residual symmetry is zero. Besides, the first component of S which acquires a VEV must be uncharged under Z_{17}^{diag}. The charges of the fields contained in the model under the residual symmetry are listed in table 5.2.

Choosing a member of the series of dihedral groups D_n is furthermore motivated by the fact that they feature several one- and two-dimensional representations which allows for the assignments $\mathbf{1}+\mathbf{1}+\mathbf{1}$ and $\mathbf{2}+\mathbf{1}$ for the three fermion generations. Note that both the singlets and the doublets can be inequivalent, respectively. Assigning the third generation

Field	Z_{17}^{diag}	Field	Z_{17}^{diag}	Field	Z_{17}^{diag}	Field	Z_{17}^{diag}	Field	Z_{17}^{diag}
Q_{L1}	3	d_{R1}	5	e_{R1}	5	S_1	0	W_1	14
Q_{L2}	16	d_{R2}	14	e_{R2}	16	S_2	15	W_2	10
Q_{L3}	16	d_{R3}	7	e_{R3}	9	T_1	10		
u_{R1}	13	L_{L1}	3	H_u	15	T_2	6		
u_{R2}	8	L_{L2}	1	H_d	9	U_1	10		
u_{R3}	1	L_{L3}	1	ϕ	0	U_2	6		

Table 5.2: **Charges under the residual symmetry $\boldsymbol{Z_{17}^{\text{diag}}}$.** I list the charges of the different fermions, scalars and spurion fields under the residual symmetry Z_{17}^{diag}, preserved by the LO structure of the LQ couplings $\mathbf{x}$ and $\mathbf{y}$; see eq. (5.7). This residual symmetry Z_{17}^{diag} is the diagonal subgroup of the Z_{17} symmetry contained in D_{17} and generated by the generator a, compare appendix 5.6, and the external Z_{17} symmetry.

to a singlet is a reasonable choice in particular regarding the quark sector, since mixing between the third quark generation and the first two ones is small. Indeed, the assignment $\mathbf{2}+\mathbf{1}$ is used for LH quarks as well as LH and RH leptons; see table 5.3. Conversely, the assignment $\mathbf{1}+\mathbf{1}+\mathbf{1}$ is used for RH up-type quarks as it is helpful regarding the pronounced hierarchy among the masses of the up-type quarks, and the desired structure of the interactions between RH up-type quarks and RH charged leptons.

Further spurion fields T, U, W are introduced in order to account for the charged fermion masses and quark mixing in the SM. These spurions acquire VEVs which generally break the residual flavour symmetry. The spurion T generates the masses of the muon and the strange quark, U gives rise to the masses of the electron and the down quark, and W generates the charm-quark mass and the Cabibbo angle. A specific combination of T and U together also give rise to the up-quark mass, whereas an operator involving $(S^\dagger)^2$ further generates the smaller quark mixing angles; see eqs. (5.117), (5.119) and (5.121). The VEVs of the spurions are given by

$$\langle S\rangle = \begin{pmatrix} \lambda \\ 0 \end{pmatrix} \,, \qquad \langle T\rangle = \begin{pmatrix} \lambda^2 \\ 0 \end{pmatrix} \,, \qquad \langle U\rangle = \begin{pmatrix} 0 \\ \lambda^4 \end{pmatrix} \,, \qquad \langle W\rangle = \begin{pmatrix} \lambda^5 \\ \lambda^4 \end{pmatrix} \,. \tag{5.9}$$

Since the potential of these spurions is not adressed and thus neither potential mechanisms to achieve the alignment of their VEVs, the latter is assumed to be exact in the following.

Field	SU(3)	SU(2)	U(1)	D_{17}	Z_{17}
$Q_L = \begin{pmatrix} Q_{L1} \\ Q_{L2} \end{pmatrix}$	3	2	$\frac{1}{6}$	$\mathbf{2_2}$	1
Q_{L3}	3	2	$\frac{1}{6}$	$\mathbf{1_1}$	16
u_{R1}	3	1	$\frac{2}{3}$	$\mathbf{1_2}$	13
u_{R2}	3	1	$\frac{2}{3}$	$\mathbf{1_1}$	8
u_{R3}	3	1	$\frac{2}{3}$	$\mathbf{1_1}$	1
$d_R = \begin{pmatrix} d_{R1} \\ d_{R2} \end{pmatrix}$	3	1	$-\frac{1}{3}$	$\mathbf{2_4}$	1
d_{R3}	3	1	$-\frac{1}{3}$	$\mathbf{1_1}$	7
$L_L = \begin{pmatrix} L_{L1} \\ L_{L2} \end{pmatrix}$	1	2	$-\frac{1}{2}$	$\mathbf{2_1}$	2
L_{L3}	1	2	$-\frac{1}{2}$	$\mathbf{1_1}$	1
$e_R = \begin{pmatrix} e_{R1} \\ e_{R2} \end{pmatrix}$	1	1	-1	$\mathbf{2_3}$	2
e_{R3}	1	1	-1	$\mathbf{1_1}$	9
H_u	1	2	$-\frac{1}{2}$	$\mathbf{1_1}$	15
H_d	1	2	$\frac{1}{2}$	$\mathbf{1_1}$	9
ϕ	3	1	$-\frac{1}{3}$	$\mathbf{1_1}$	0
$S = \begin{pmatrix} S_1 \\ S_2 \end{pmatrix}$	1	1	0	$\mathbf{2_1}$	16
$T = \begin{pmatrix} T_1 \\ T_2 \end{pmatrix}$	1	1	0	$\mathbf{2_2}$	8
$U = \begin{pmatrix} U_1 \\ U_2 \end{pmatrix}$	1	1	0	$\mathbf{2_2}$	8
$W = \begin{pmatrix} W_1 \\ W_2 \end{pmatrix}$	1	1	0	$\mathbf{2_2}$	12

Table 5.3: **Particle content of the model**. The fermions, scalar fields and spurions (flavour-symmetry breaking fields) and their transformation properties under the SM gauge group SU(3) × SU(2) × U(1) as well as the flavour symmetry $G_f = D_{17} \times Z_{17}$ are given. Particles in an irreducible two-dimensional representation of D_{17} are evidenced in terms of two-component vectors.

5.3 Mass Matrices and Leptoquark Couplings

In this section, the form of the charged fermion mass matrices M_u, M_d and M_e, analytic formulae for charged fermion masses, the unitary matrices L_u, R_u, L_d, R_d, L_e and R_e relating the interaction basis and mass basis of the SM fermions, and the form of the LQ couplings $\mathbf{x}$, $\mathbf{y}$ and $\mathbf{z}$ given in eq. (5.5) are presented, given the transformation properties of the particles contained in the model; see table 5.3. I take into account all operators which are invariant under the flavour symmetry and yield a contribution up to and including order λ^{12} in the symmetry-breaking parameter, given the VEVs of the spurion fields as indicated in eq. (5.9). The relevant underlying Lagrangians including the operators as well as the resulting LQ couplings $\hat{\mathbf{x}}$ and $\hat{\mathbf{y}}$ in the interaction basis are listed in appendix 5.7.

The matrices M_u, M_d, M_e, $\mathbf{x}$, $\mathbf{y}$ and $\mathbf{z}$ are given in an effective parametrisation. The relations between these parameters and the coefficients of the contributing operators can be found in appendix 5.9. The parameters are implicitly assumed to be real for the analytic derivations discussed in this section, but they are taken to be complex-valued in the phenomenological studies presented further below.

I focus on the scenario of a slight modification of the up-quark mass matrix M_u for the model under consideration, dubbed ‘scenario B’, in comparison with ‘scenario A’ without any modification. The motivation to introduce scenario B is the observation that the CKM mixing matrix V as obtained in scenario A cannot be in full agreement with experimental data; see section 5.3.1 below for more information. Therefore, the presentation of the relevant results for scenario A is relegated to appendix 5.8. Still, the form of the LQ coupling matrices $\mathbf{x}$, $\mathbf{y}$ and $\mathbf{z}$ is computed in both scenarios.

5.3.1 Quark Sector

Herein I discuss the results for the up-type quark mass matrix M_u and the down-type quark mass matrix M_d as well as the CKM mixing matrix V in scenario B.

5.3.1.1 Up-Quark Sector

The form of the up-type quark mass matrix M_u as predicted in scenario A is given in eq. (5.127) in the appendix, and the unitary matrices L_u and R_u which achieve the diagonalisation of M_u are given in eqs. (5.128) and (5.129). Therefore, one can already infer that the CKM-matrix element

$$V_{td} = (L_u^*)_{13}(L_d)_{11} + (L_u^*)_{23}(L_d)_{21} + (L_u^*)_{33}(L_d)_{31} \tag{5.10}$$

is likely to very suppressed, since L_d is close to the identity matrix in flavour space and thus $(L_d)_{21}$ and $(L_d)_{31}$ will be very small, and in addition $(L_u)_{13} \sim \lambda^8$. Consequently, the Jarlskog invariant J_{CP} can also be expected to be very small, cf. eq. (2.29). Besides, the CKM-matrix elements V_{us}, V_{ub} and V_{cb} will turn out to be too strongly correlated as per the tight relation between the elements $(L_u)_{21}$, $(L_u)_{31}$ and $(L_u)_{32}$.

A simple way to resolve these issues is an enhancement of the element $(M_u)_{13}$ in the up-type quark mass matrix, that is

$$M_u = \begin{pmatrix} f_{11}\,\lambda^8 & f_{12}\,\lambda^5 & \tilde{f}_{13}\,\lambda^3 \\ f_{21}\,\lambda^{10} & f_{22}\,\lambda^4 & f_{23}\,\lambda^2 \\ f_{31}\,\lambda^{12} & f_{32}\,\lambda^4 & f_{33} \end{pmatrix} \left\langle H_u^0 \right\rangle \tag{5.11}$$

where $\tilde{f}_{13}$ and the f_{ij} are generally independent, complex order-one numbers, apart from f_{12} and f_{22} which satisfy

$$f_{12} - f_{22} \sim c\,\lambda^2 \tag{5.12}$$

with c complex.[4] This relation is sourced by the operators with coefficients α_5^u and α_6^u in eq. (5.118); see also eq. (5.140) in appendix 5.9. Therein, the definition of the other parameters f_{ij} in terms of the coefficients α_i^u are given therein as well.

A further contribution added *ad hoc* to the element $(M_u)_{13}$ is not explained by an ap-

---

[4] For the sake of clarity, one could instead express the element $(M_u)_{12}$ as $(f_{22} + \tilde{f}_{12}\lambda^2)\,\lambda^5\,\langle H_u^0\rangle$, where $\tilde{f}_{12}$ is a complex order-one number.

propriate operator in the context of this model.[5] Thus, the Lagrangians presented in section 5.7 are valid both for scenario A and scenario B. Still, as it will become clear from the analytic estimates for the primary observables discussed later on in this chapter, the enhancement of $(M_u)_{13}$ does not appreciably affect the phenomenology induced by ϕ.

The effective parametrisation of M_u in scenario B implies the following LO results for the up-type quark masses:

$$\begin{aligned} m_u &= \left| f_{11}\,\lambda^8 + \mathcal{O}(\lambda^{10}) \right| \left\langle H_u^0 \right\rangle \,, \\ m_c &= \left| f_{22}\,\lambda^4 + \left(\frac{f_{12}^2}{2\,f_{22}} - \frac{f_{23} f_{32}}{f_{33}} \right) \lambda^6 + \mathcal{O}(\lambda^8) \right| \left\langle H_u^0 \right\rangle \,, \\ m_t &= \left| f_{33} + \frac{f_{23}^2}{2\,f_{33}}\,\lambda^4 + \mathcal{O}(\lambda^6) \right| \left\langle H_u^0 \right\rangle \,. \end{aligned} \tag{5.13}$$

As expected from the construction of the model, the dominant contributions to the three up-type quark masses originate from the first, second and fourth operator in eq. (5.117), respectively. Also, note that the enhancement of $(M_u)_{13}$ only causes further subleading contributions to m_t to appear at order λ^6 instead of λ^8 as in scenario A.

The unitary matrices L_u and R_u which diagonalise M_u read

$$L_u = \begin{pmatrix} 1 - \frac{f_{12}^2}{2\,f_{22}^2}\,\lambda^2 + \mathcal{O}(\lambda^4) & \frac{f_{12}}{f_{22}}\,\lambda + \mathcal{O}(\lambda^3) & \frac{\tilde{f}_{13}}{f_{33}}\,\lambda^3 + \mathcal{O}(\lambda^7) \\ -\frac{f_{12}}{f_{22}}\,\lambda + \mathcal{O}(\lambda^3) & 1 - \frac{f_{12}^2}{2\,f_{22}^2}\,\lambda^2 + \mathcal{O}(\lambda^4) & \frac{f_{23}}{f_{33}}\,\lambda^2 + \mathcal{O}(\lambda^6) \\ \left(\frac{f_{12} f_{23}}{f_{22} f_{33}} - \frac{\tilde{f}_{13}}{f_{33}} \right) \lambda^3 + \mathcal{O}(\lambda^5) & -\frac{f_{23}}{f_{33}}\,\lambda^2 + \mathcal{O}(\lambda^4) & 1 - \frac{f_{23}^2}{2\,f_{33}^2}\,\lambda^4 + \mathcal{O}(\lambda^6) \end{pmatrix} \tag{5.14}$$

---

[5] The field combinations $H_u\, u_{R3}$ and $H_d\, d_{R3}$ transform in the same way in order to generate the LO contributions to the top- and bottom-quark mass, respectively, when paired with $\overline{Q_{L3}}$. For instance, this means that the invariance of $\overline{Q_L}\, H_u\, u_{R3}\, (S^\dagger)^2$ which sources the LO contribution to the mixing angle θ_{23} also implies the invariance of $\overline{Q_L}\, H_d\, d_{R3}\, (S^\dagger)^2$. Importantly, if an element $(M_u)_{13} \sim \lambda^3 \, \langle H_u^0 \rangle$ was generated via an operator, I would immediately also obtain $(M_d)_{13} \sim \lambda^3 \, \langle H_d^0 \rangle$ and thus enhance $(L_d)_{31}$ and consequently the elements in the first column of the LQ coupling $\mathbf{x}$ in the charged fermion mass basis. Therefore, I refrain from inducing $(M_u)_{13}$ via an operator which explicitly breaks the flavour symmetry. On the contrary, generating $(M_u)_{13} \sim \lambda^3 \, \langle H_u^0 \rangle$ in a manner which is consistent with the flavour symmetry likely necessitates a modification of the transformation properties of (some of) the SM fermions under G_f, and/or of G_f itself. An exploration of this option is beyond the scope of this thesis.

and

$$R_u = \begin{pmatrix} 1+\mathcal{O}(\lambda^{10}) & \frac{f_{11}f_{12}}{f_{22}^2}\,\lambda^5+\mathcal{O}(\lambda^6) & \frac{f_{11}\tilde{f}_{13}}{f_{33}^2}\,\lambda^{11}+\mathcal{O}(\lambda^{12}) \\ -\frac{f_{11}f_{12}}{f_{22}^2}\,\lambda^5+\mathcal{O}(\lambda^6) & 1+\mathcal{O}(\lambda^8) & \frac{f_{32}}{f_{33}}\,\lambda^4+\mathcal{O}(\lambda^6) \\ \frac{f_{11}f_{12}f_{32}}{f_{22}^2 f_{33}}\,\lambda^9+\mathcal{O}(\lambda^{10}) & -\frac{f_{32}}{f_{33}}\,\lambda^4+\mathcal{O}(\lambda^6) & 1+\mathcal{O}(\lambda^8) \end{pmatrix} . \tag{5.15}$$

I note that L_u is the primary source of the CKM mixing matrix, whereas R_u is close to the identity matrix, which is thus in good agreement with the basis in which the textures of the LQ couplings $\mathbf{x}$ and $\mathbf{y}$ are given in eq. (5.7). As expected, one now has $(L_u)_{13} \sim \lambda^3$, and the tight relation between the elements $(L_u)_{21}$, $(L_u)_{31}$ and $(L_u)_{32}$ observed for scenario A, see section 5.8.1, is relaxed. The largest deviation of R_u from the identity matrix is of order λ^4, due to the operator with the coefficient α_7^u which appears automatically upon fixing the LO operators in the up-type quark sector; see section 5.7.1. Apart from $(R_u)_{13} \sim \lambda^{11}$ herein, the matrix R_u is identical in scenario A and scenario B.

5.3.1.2 Down-Quark Sector

The effective parametrisation of the down-type quark mass matrix, including all contributions up to and including order λ^{12}, reads

$$M_d = \begin{pmatrix} d_{11}\,\lambda^4 & d_{12}\,\lambda^8 & d_{13}\,\lambda^8 \\ d_{21}\,\lambda^{10} & d_{22}\,\lambda^2 & d_{23}\,\lambda^2 \\ d_{31}\,\lambda^{12} & d_{32}\,\lambda^4 & d_{33} \end{pmatrix} \left\langle H_d^0 \right\rangle \tag{5.16}$$

with d_{ij} being, in general, independent complex order-one numbers, related to the coefficients α_i^d as shown in eq. (5.141) in appendix 5.9. Furthermore, the LO results for the down-type quark masses are given as in

$$\begin{aligned} m_d &= \left| d_{11}\,\lambda^4 + \mathcal{O}(\lambda^{12}) \right| \left\langle H_d^0 \right\rangle , \\ m_s &= \left| d_{22}\,\lambda^2 - \frac{d_{23}(d_{22}d_{23}+2\,d_{32}d_{33})}{2\,d_{33}^2}\,\lambda^6 + \mathcal{O}(\lambda^{10}) \right| \left\langle H_d^0 \right\rangle , \\ m_b &= \left| d_{33} + \frac{d_{23}^2}{2\,d_{33}}\,\lambda^4 + \mathcal{O}(\lambda^8) \right| \left\langle H_d^0 \right\rangle , \end{aligned} \tag{5.17}$$

with the dominant contributions arising from the three operators in eq. (5.119), as expected from the construction of the model.

The unitary matrices L_d and R_d read

$$L_d = \begin{pmatrix} 1 - \frac{d_{12}^2}{2\,d_{22}^2}\,\lambda^{12} + \mathfrak{o}(\lambda^{12}) & \frac{d_{12}}{d_{22}}\,\lambda^6 + \mathcal{O}(\lambda^{10}) & \frac{d_{13}}{d_{33}}\,\lambda^8 + \mathcal{O}(\lambda^{12}) \\ -\frac{d_{12}}{d_{22}}\,\lambda^6 + \mathcal{O}(\lambda^{10}) & 1 - \frac{d_{23}^2}{2\,d_{33}^2}\,\lambda^4 + \mathcal{O}(\lambda^8) & \frac{d_{23}}{d_{33}}\,\lambda^2 + \mathcal{O}(\lambda^6) \\ L_{d,31}\,\lambda^8 + \mathcal{O}(\lambda^{12}) & -\frac{d_{23}}{d_{33}}\,\lambda^2 + \mathcal{O}(\lambda^6) & 1 - \frac{d_{23}^2}{2\,d_{33}^2}\,\lambda^4 + \mathcal{O}(\lambda^8) \end{pmatrix} \tag{5.18}$$

with

$$L_{d,31} = \frac{d_{12}d_{23} - d_{13}d_{22}}{d_{22}d_{33}} \tag{5.19}$$

and

$$R_d = \begin{pmatrix} 1 + \mathfrak{o}(\lambda^{12}) & R_{d,12}\,\lambda^8 + \mathcal{O}(\lambda^{12}) & R_{d,13}\,\lambda^{12} + \mathfrak{o}(\lambda^{12}) \\ -R_{d,12}\,\lambda^8 - \mathcal{O}(\lambda^{12}) & 1 + \mathcal{O}(\lambda^8) & \frac{(d_{22}d_{23}+d_{32}d_{33})}{d_{33}^2}\,\lambda^4 + \mathcal{O}(\lambda^8) \\ \mathcal{O}(\lambda^{12}) & -\frac{(d_{22}d_{23}+d_{32}d_{33})}{d_{33}^2}\,\lambda^4 + \mathcal{O}(\lambda^8) & 1 + \mathcal{O}(\lambda^8) \end{pmatrix} \tag{5.20}$$

with

$$R_{d,12} = \frac{d_{11}d_{12} + d_{21}d_{22}}{d_{22}^2} \qquad \text{and} \qquad R_{d,13} = \frac{d_{11}d_{13} + d_{21}d_{23} + d_{31}d_{33}}{d_{33}^2}\;. \tag{5.21}$$

Both L_d and R_d are close to the identity matrix, except for the (23)-block in L_d where a rotation of order λ^2 is present which is a consequence of the operator $\overline{Q_L}\,H_d\,d_{R3}\,(S^\dagger)^2$ being invariant. This implies a contribution to the quark mixing angle θ_{23} of the same order in λ as the contribution arising from the up-quark sector; see the (23)-block of L_u in eq. (5.14) and eq. (5.128) as well as the CKM mixing matrix in eq. (5.130) (scenario A) and eq. (5.22) (scenario B). Furthermore, it induces contributions to the elements x_{22} and x_{32} of the LQ coupling $\mathbf{x}$ in the charged fermion mass basis which are of the same order as the elements $\hat{x}_{22}$ and $\hat{x}_{32}$ of the LQ coupling $\hat{\mathbf{x}}$ in the interaction basis; see eq. (5.29) and eq. (5.145) in appendix 5.9.

5.3.1.3 Quark Mixing

I obtain the CKM mixing matrix

$$V = L_u^\dagger\, L_d = \begin{pmatrix} 1-\frac{f_{12}^2}{2\,f_{22}^2}\,\lambda^2+\mathcal{O}(\lambda^4) & -\frac{f_{12}}{f_{22}}\,\lambda+\mathcal{O}(\lambda^3) & \left(\frac{f_{12}}{f_{22}}V_{32}-\frac{\tilde{f}_{13}}{f_{33}}\right)\lambda^3+\mathcal{O}(\lambda^5) \\ \frac{f_{12}}{f_{22}}\,\lambda+\mathcal{O}(\lambda^3) & 1-\frac{f_{12}^2}{2\,f_{22}^2}\,\lambda^2+\mathcal{O}(\lambda^4) & -V_{32}\,\lambda^2+\mathcal{O}(\lambda^4) \\ \frac{\tilde{f}_{13}}{f_{33}}\,\lambda^3+\mathcal{O}(\lambda^7) & V_{32}\,\lambda^2+\mathcal{O}(\lambda^6) & 1-\frac{1}{2}(V_{32})^2\,\lambda^4+\mathcal{O}(\lambda^6) \end{pmatrix} \tag{5.22}$$

with

$$V_{32} \equiv \frac{f_{23}}{f_{33}} - \frac{d_{23}}{d_{33}} \ . \tag{5.23}$$

Clearly, this mixing matrix predicted in scenario B features the required modifications: the element $V_{td} \sim \lambda^3$, the Jarlskog invariant $J_{\mathrm{CP}} = \mathrm{Im}(V_{ud}V_{tb}V_{ub}^*V_{td}^*) \sim \lambda^6$ and a not-too-tight relation between V_{us}, V_{ub} and V_{cb}. Indeed, the results of a chi-squared fit show that scenario B can be brought into excellent agreement with experimental data on quark-mixing parameters [29] and the charged fermion masses at the scale $\mu = 1\,\mathrm{TeV}$ [378].

5.3.2 Charged Lepton Sector

For the charged lepton mass matrix M_e I find the effective parametrisation

$$M_e = \begin{pmatrix} e_{11}\,\lambda^4 & e_{12}\,\lambda^{12} & \mathfrak{o}(\lambda^{12}) \\ e_{21}\,\lambda^8 & e_{22}\,\lambda^2 & e_{23}\,\lambda \\ e_{31}\,\lambda^9 & e_{32}\,\lambda^3 & e_{33} \end{pmatrix} \left\langle H_d^0 \right\rangle \tag{5.24}$$

with e_{ij} being complex order-one numbers that are related to the coefficients α_i^e as indicated in eq. (5.142) in appendix 5.9. The element $(M_e)_{13}$ is generated only at an order higher than λ^{12}.

This implies the following LO results for the charged lepton masses

$$\begin{aligned} m_e &= \left| e_{11}\,\lambda^4 + \mathfrak{o}(\lambda^{12}) \right| \left\langle H_d^0 \right\rangle , \\ m_\mu &= \left| e_{22}\,\lambda^2 - \frac{e_{23}(e_{22}e_{23}+2\,e_{32}e_{33})}{2\,e_{33}^2}\,\lambda^4 + \mathcal{O}(\lambda^6) \right| \left\langle H_d^0 \right\rangle , \\ m_\tau &= \left| e_{33} + \frac{e_{23}^2}{2\,e_{33}}\,\lambda^2 + \mathcal{O}(\lambda^4) \right| \left\langle H_d^0 \right\rangle . \end{aligned} \tag{5.25}$$

As expected, the respective dominant contributions arise from the three operators in eq. (5.121).

The unitary matrices L_e and R_e read

$$L_e = \begin{pmatrix} 1+\mathfrak{o}(\lambda^{12}) & \frac{e_{11}e_{21}}{e_{22}^2}\,\lambda^8+\mathcal{O}(\lambda^{10}) & \mathfrak{o}(\lambda^{12}) \\ -\frac{e_{11}e_{21}}{e_{22}^2}\,\lambda^8+\mathcal{O}(\lambda^{10}) & 1-\frac{e_{23}^2}{2\,e_{33}^2}\,\lambda^2+\mathcal{O}(\lambda^4) & \frac{e_{23}}{e_{33}}\,\lambda+\mathcal{O}(\lambda^3) \\ \frac{e_{11}e_{21}e_{23}}{e_{22}^2e_{33}}\,\lambda^9+\mathcal{O}(\lambda^{11}) & -\frac{e_{23}}{e_{33}}\,\lambda+\mathcal{O}(\lambda^3) & 1-\frac{e_{23}^2}{2\,e_{33}^2}\,\lambda^2+\mathcal{O}(\lambda^4) \end{pmatrix} \tag{5.26}$$

and

$$R_e = \begin{pmatrix} 1-\frac{e_{21}^2}{2\,e_{22}^2}\,\lambda^{12}+\mathfrak{o}(\lambda^{12}) & \frac{e_{21}}{e_{22}}\,\lambda^6+\mathcal{O}(\lambda^8) & \frac{(e_{21}e_{23}+e_{31}e_{33})}{e_{33}^2}\,\lambda^9+\mathcal{O}(\lambda^{11}) \\ -\frac{e_{21}}{e_{22}}\,\lambda^6+\mathcal{O}(\lambda^8) & 1-\frac{1}{2}(R_{e,23})^2\lambda^6+\mathcal{O}(\lambda^8) & R_{e,23}\,\lambda^3+\mathcal{O}(\lambda^5) \\ R_{e,31}\,\lambda^9+\mathcal{O}(\lambda^{11}) & -R_{e,23}\,\lambda^3+\mathcal{O}(\lambda^5) & 1-\frac{1}{2}(R_{e,23})^2\,\lambda^6+\mathcal{O}(\lambda^8) \end{pmatrix} . \tag{5.27}$$

with

$$R_{e,23} \equiv \frac{e_{22}e_{23}+e_{32}e_{33}}{e_{33}^2} \qquad \text{and} \qquad R_{e,31} \equiv \frac{1}{e_{33}}\left(\frac{e_{21}e_{32}}{e_{22}} - e_{31}\right) . \tag{5.28}$$

I reiterate that since neutrinos are massless in this model, lepton mixing is unphysical and thus the neutrinos transform with L_e.

In both L_e and R_e, the (23)-block deviates from being close to the identity matrix. The element $(L_e)_{23} \sim \lambda$ is mainly due to the operator $\overline{L_L}\,H_d\,e_{R3}\,S^\dagger$ which arises because $\overline{L_{L3}}\,H_d\,e_{R3}$ is induced at tree level, L_{L2} and L_{L3} carry the same charge under Z_{17}^{diag}, and L_L and S both transform under $\mathbf{2_1}$ and thus the product contains the combination $L_{L2}\,S_1$. Similarly, the operator $\overline{L_{L3}}\,H_d\,e_R\,S\,T$ which sources the element $(R_e)_{23} \sim \lambda^3$ is automatically induced upon fixing the field content of the operators arising at tree level in the model.

5.3.3 Leptoquark Couplings

Herein I discuss the form of the LQ couplings $\mathbf{x}$, $\mathbf{y}$ and $\mathbf{z}$, defined in (5.5) and given in the charged fermion mass basis, in scenario B. The LQ couplings $\hat{\mathbf{x}}$, $\hat{\mathbf{y}}$ in the interaction basis, as well as $\mathbf{x}$, $\mathbf{y}$ and $\mathbf{z}$ in scenario A are given in section 5.8.3.

5.3.3.1 Couplings in Charged Fermion Mass Basis

I use the matrices L_d and L_e defined in eqs. (5.18) and (5.26) as well as the LQ coupling $\hat{\mathbf{x}}$ in eq. (5.135) to obtain

$$\mathbf{x} = L_e^T \, \hat{\mathbf{x}} \, L_d = \begin{pmatrix} a_{11}\,\lambda^9 & a_{12}\,\lambda^{11} & a_{13}\,\lambda^9 \\ a_{21}\,\lambda^8 & a_{22}\,\lambda^3 & a_{23}\,\lambda \\ a_{31}\,\lambda^8 & a_{32}\,\lambda^2 & a_{33} \end{pmatrix} , \tag{5.29}$$

where the effective parameters a_{ij} are related to the coefficients $\hat{a}_{ij}$, d_{ij} and e_{ij} contained in the matrices $\hat{\mathbf{x}}$ in eq. (5.135), M_d in eq. (5.16) and M_e in eq. (5.24), respectively. The explicit form of these relations is given in eq. (5.145) in appendix 5.9. In general, the a_{ij} can also be expected to be complex order-one numbers.

Comparing the form of the LQ coupling $\mathbf{x}$ in eq. (5.29) to the texture of $\mathbf{x}$ in eq. (5.7), one finds that all of the elements x_{33}, x_{23}, x_{32} and x_{22} are generated at the correct order in λ, respectively, whereas the remaining elements in the first row and/or column are strongly suppressed. Note that in the case of x_{22} and x_{23}, the LO contributions are not only sourced by the respective elements $\hat{x}_{22}$ and $\hat{x}_{23}$ in the interaction basis, but also by the order-λ rotation in the (23)-block of L_e; see eq. (5.145) in appendix 5.9.

Furthermore, applying the matrices L_u and L_e, see eqs. (5.14) and (5.26), to the LQ coupling $\hat{\mathbf{x}}$ in eq. (5.135), I find

$$\mathbf{z} = L_e^T \, \hat{\mathbf{x}} \, L_u = \begin{pmatrix} c_{11}\,\lambda^9 & c_{12}\,\lambda^{10} & c_{13}\,\lambda^9 \\ c_{21}\,\lambda^4 & c_{22}\,\lambda^3 & c_{23}\,\lambda \\ c_{31}\,\lambda^3 & c_{32}\,\lambda^2 & c_{33} \end{pmatrix} . \tag{5.30}$$

While the orders of magnitude in λ at which the different elements of $\mathbf{z}$ are induced are identical in scenario A and scenario B, the relations between the effective parameters c_{ij} and the coefficients $\hat{a}_{ij}$, e_{ij}, f_{ij} and $\tilde{f}_{13}$ are slightly different. Comparing to eq. (5.146) in appendix 5.9, I now have

$$\begin{aligned} c_{21} &= -\frac{f_{12}}{e_{33} f_{22} f_{33}} \left(\hat{a}_{33} e_{23} f_{23} - \hat{a}_{23} e_{33} f_{23} - \hat{a}_{32} e_{23} f_{33} + \hat{a}_{22} e_{33} f_{33} \right) \\ &\quad - \frac{\tilde{f}_{13}}{f_{33}} \left(\hat{a}_{23} - \frac{\hat{a}_{33} e_{23}}{e_{33}} \right) + \mathcal{O}(\lambda^2) \, , \\ c_{31} &= \frac{f_{12} (\hat{a}_{33} f_{23} - \hat{a}_{32} f_{33})}{f_{22} f_{33}} - \frac{\tilde{f}_{13}}{f_{33}} \hat{a}_{33} + \mathcal{O}(\lambda^2) \, . \end{aligned} \tag{5.31}$$

From the unitary matrices R_u and R_e in eqs. (5.15) and (5.27) as well as $\hat{\mathbf{y}}$ in eq. (5.136), I obtain the form of the LQ coupling $\mathbf{y}$ in the charged fermion mass basis as in

$$\mathbf{y} = R_e^T \, \hat{\mathbf{y}} \, R_u = \begin{pmatrix} b_{11} \, \lambda^9 & b_{12} \, \lambda^9 & b_{13} \, \lambda^9 \\ b_{21} \, \lambda^8 & b_{22} \, \lambda^3 & b_{23} \, \lambda^3 \\ b_{31} \, \lambda^5 & b_{32} & b_{33} \, \lambda^4 \end{pmatrix} . \tag{5.32}$$

The effective parameters b_{ij} are related to the coefficients $\hat{b}_{ij}$, e_{ij} and f_{ij}, with the exact form of these relations given in eq. (5.147) in appendix 5.9.

Comparing this form of the LQ coupling $\mathbf{y}$ with the texture in eq. (5.7), one sees that the elements $y_{22} \sim \lambda^3$, $y_{33} \sim \lambda^4$ and $y_{31} \sim \lambda^5$ turn out to be larger than anticipated in the charged fermion mass basis, which is mainly due to $(R_u)_{23} \sim \lambda^4$ and $(R_u)_{12} \sim \lambda^5$; see eq. (5.15). Still, as will be clear from section 5.4, none of these couplings plays a major role for the currently viable parameter space of the model. The LO contribution to the element y_{22} is not only sourced by the interaction-basis element $\hat{y}_{22}$, but also by the order-λ^3 rotation in R_e; see eq. (5.147) in appendix 5.9. Moreover, the LQ couplings y_{1j} involving the electron are very small. Note that the enhancement of the element $(M_u)_{13}$ of the up-quark mass matrix in scenario B only leaves a slight imprint on the form of $\mathbf{y}$, with the largest contribution appearing at order λ^7 in y_{31}.

5.4 Phenomenological Study

In this section, I will mainly discuss the strategy and results of an analytic and numerical study of the *primary observables* which will be defined in section 5.4.1.1 just below. Ref. [90] also contains an extensive discussion of a second study which is referred to as *comprehensive* since it also takes into account observables which are currently not competitive, and includes a fit to charged fermion masses and quark mixing. The strategy employed for the comprehensive scan will also be sketched herein, and the findings for the primary and secondary observables will be presented where appropriate.

5.4.1 Employed Strategy and Parametrisations

5.4.1.1 Primary Scan

Besides $R(D)$, $R(D^\star)$ and Δa_μ of which I aim to explain the anomalous experimental data, the *primary observables* comprise those for which the model contributions may be in conflict with current experimental bounds in some regions of parameter space, or can be probed in near-future experiments. A brief discussion of the results for *secondary observables* is also provided in section 5.4.12. These are not currently competitive in shaping or probing the parameter space of the model, but promise to do so in the near- or mid-term future. Where results are expressed in terms of LEFT, see also section 2.4.3, the Jenkins-Manohar-Stoffer (JMS) basis [192] is chosen.

Note that in the primary scan, I do not explicitly refer to the interaction basis of the SM fermions as the underlying structure which has been utilised for the construction of the model, but instead treat (most of) the effective parameters in the LQ coupling matrices $\mathbf{x}$, $\mathbf{y}$ and $\mathbf{z}$ as unrelated order-one coefficients for simplicity. Indeed, the magnitudes of the effective parameters a_{ij}, b_{ij} and c^B_{ij} (except for b_{32} and c^B_{12}), the latter to be defined momentarily, are independently varied in the range

$$\left[\lambda, \frac{1}{\lambda}\right] \approx [0.23, 4.42] \tag{5.33}$$

in order not to jeopardise the expansion in λ, and their phases within

$$[0, 2\pi) \, . \tag{5.34}$$

A narrower range is chosen for the magnitude of the effective parameter b_{32} for $\hat{m}_\phi = 2$, in order to respect a constraint arising from searches for high-p_T $\tau\bar{\tau}$ pairs at colliders; see table 5.4 and section 5.4.10 for details.

As a further simplification, I assume that the phenomenology of the scalar sector of the model is dominated by effects induced by ϕ, and only the lightest Higgs is SM-like with all other scalar states being effectively decoupled.[6]

In order to better reflect the fact that the coupling matrix $\mathbf{z}$ is directly linked to $\mathbf{x}$ via the CKM matrix as per eq. (5.6), instead of the form given in eq. (5.30) I employ the parametrisation

$$\mathbf{z} = \begin{pmatrix} (a_{11} - \frac{(c^B_{12})^2}{2\,a_{11}}\,\lambda^2 + c^B_{11}\,\lambda^3)\,\lambda^9 & c^B_{12}\,\lambda^{10} & (a_{13} + c^B_{13}\,\lambda^3)\,\lambda^9 \\ c_{21}\,\lambda^4 & (a_{22} + a_{23}\,\tilde{c} + c^B_{22}\,\lambda^2)\,\lambda^3 & (a_{23} + c^B_{23}\,\lambda^4)\,\lambda \\ c_{31}\,\lambda^3 & (a_{32} + a_{33}\,\tilde{c} + c^B_{32}\,\lambda^2)\,\lambda^2 & a_{33} + c^B_{33}\,\lambda^4 \end{pmatrix} \tag{5.35}$$

where

$$\begin{aligned} c_{21} &\equiv -\frac{c^B_{12}}{a_{11}}\,(a_{22} + a_{23}\,\tilde{c}) - a_{23}\,\bar{c} + c^B_{21}\,\lambda\;, \\ c_{31} &\equiv -\frac{c^B_{12}}{a_{11}}\,(a_{32} + a_{33}\,\tilde{c}) - a_{33}\,\bar{c} + c^B_{31}\,\lambda\;. \end{aligned} \tag{5.36}$$

This reflects scenario B which I will exclusively focus on due to its capability to correctly account for experimental data on quark mixing, as emphasised in section 5.3.1.3.[7] Furthermore, I define[8]

$$c^B_{12} = \frac{\hat{a}_{11} f_{12}}{f_{22}} + \mathcal{O}(\lambda)\;\;,\;\; \tilde{c} = \frac{d_{23}}{d_{33}} - \frac{f_{23}}{f_{33}} \;\text{ and }\; \bar{c} = \frac{\tilde{f}_{13}}{f_{33}} \tag{5.37}$$

and the remaining effective parameters c^B_{ij} are taken to be complex order-one numbers, thereby reflecting rather involved combinations of the $\hat{a}_{ij}$, $\hat{b}_{ij}$, f_{ij}, d_{ij} and e_{ij}. Together with

$$a_{11} = \hat{a}_{11} + \mathcal{O}(\lambda^3)\;, \tag{5.38}$$

---

[6] This can be justified for instance in the scenario of inducing one of the Higgs VEVs [379]. A dynamical mechanism to achieve this might require a further extension of the scalar field content of the model, and a soft breaking of the imposed symmetry. The pertinent discussion is well beyond the scope of this thesis.

[7] Note that c_{21} and c_{31} are the only two effective LQ coupling parameters of which the form differs in scenario A and scenario B. Still, neither of them plays a major role for the primary observables. c_{21} enters a subleading contribution to $\mu - e$ conversion in nuclei, as can be seen in section 5.4.6 and table 5.5. c_{31} is relevant for the leptonic decay $B \to \tau\nu$ which constitutes a secondary observable and will be commented on in section 5.4.12.4.

[8] The parameter $\tilde{c}$ is formally equivalent to $-V_{32}$ defined in eq. (5.23).

this implies

$$|V_{us}| \approx \left|\frac{c_{12}^B}{a_{11}}\right| \lambda \; , \quad |V_{cb}| \approx |\tilde{c}|\lambda^2 \quad \text{and} \quad |V_{td}| \approx |\bar{c}|\lambda^3 \tag{5.39}$$

to LO in λ. Regarding the respective powers of λ, this is consistent with experimental data on quark mixing, see eq. (2.27), thus I further decompose

$$c_{12}^B = a_{11}\, \alpha\, e^{i\,\omega_1} \; , \quad \tilde{c} = \beta\, e^{i\,\omega_2} \; , \quad \bar{c} = \gamma\, e^{i\,\omega_3} \tag{5.40}$$

where the parameters α, β and γ are varied in the range

$$[0.5, 1.5] \tag{5.41}$$

and the phases ω_i, $i = 1, 2, 3$ in

$$[0, 2\pi) \; . \tag{5.42}$$

This does not reflect any information on CP violation.

Both the primary scan and the comprehensive scan are performed for each of the following three LQ ϕ masses

$$\hat{m}_\phi \equiv \frac{m_\phi}{\text{TeV}} = 2\,, 4 \text{ and } 6 \; . \tag{5.43}$$

From the LQ coupling matrices in eqs. (5.29), (5.30) and (5.32), one may infer that ϕ will dominantly decay into one of the three pairs $\nu_{L\tau} b$, τc or τt of final-state particles. For BR$(\phi \to \nu_{L\tau} b) \sim$ BR$(\phi \to \tau t)$, that is, for the two BRs taking similar values which is the case in the model since the relevant couplings are related via quark mixing, the lower bound $\hat{m}_\phi \gtrsim 1.2$ at 95 CL has been established at ATLAS [380]. Decays with muons or electrons in the final state are further suppressed by at least λ^2. Still, the above choice of benchmark masses is also consistent with the most stringent limits on LQs solely coupling to muons (electrons), for which $\hat{m}_\phi > 1.7\,(1.8)$. This bound is robust regarding different flavours of the coupled quark [381]; one may also consult ref. [382]. For the mass $\hat{m}_\phi = 2(4)[6]$, a sample of $4(3)[2] \times 10^6$ points has been generated in the primary scan.

For each observable discussed in this section, an analytic estimate is derived which evidences the respective dominant contribution and involved LQ couplings in the charged fermion mass basis. Note, though, that for the numerical study, including the displayed plots which illustrate the results, the complete analytic expressions are employed. They are given in the remainder of this section as well as in sections 5.10, 5.11 and 5.12, and used to calculate the contributions to the primary observables. In line with the considerations in section 2.4.3, RG running under QED is typically neglected, that is, the relevant leptonic observables are directly evaluated at the scale $\mu = m_\phi$. On the contrary, RG running under QCD between the scales $\mu = m_\phi$ and $\mu = \mu_B \equiv 4.8$ GeV is taken into account for $R(D)$, $R(D^\star)$ and τ_{Bc}^{SM}; see eq. (5.47). For the observables $\text{BR}(\tau \to \mu\gamma)$, $\text{BR}(\mu \to e\gamma)$, $\text{BR}(\tau \to 3\mu)$, $\text{BR}(\tau \to \mu e\bar{e})$, $\text{BR}(\mu \to 3e)$, $R^\nu_{K^{(\star)}}$, τ_{Bc}^{SM} and $g_{\tau_A}/g_A^{\text{SM}}$, the current experimental bounds are imposed; see table 5.4. A concise discussion of contributions to the scalar charged-current WC $C^{SRR}_{\nu edu,3332}$ is provided in section 5.4.11.

Regarding the sample points displayed in the scatter plots which reflect the findings of the primary scan, the following conventions hold:

- A round light-coloured sample point indicates that at least one of the imposed experimental bounds is violated.
- A sample point with the shape of a star (plus sign) [cross] indicates that all imposed experimental bounds are respected in the case of $\hat{m}_\phi = 2(4)[6]$.
- Different colours are used to distinguish the different masses $\hat{m}_\phi = 2, 4, 6$.

I employ solid lines for bounds arising from existing experimental data, and dashed lines signify prospective bounds or future sensitivities. In the former case, regions in parameter space for which agreement with existing data is established at difference CLs may be highlighted with grey shadings. Lastly, I mark the employed SM predictions for the observables $R(D)$ and $R(D^\star)$ at $1\,\sigma$ with a black cross in figure 5.2, and green-shaded bands in the respective top panel of figures 5.5, 5.6, 5.15 and 5.18.

5.4.1.2 Comprehensive Scan

In the comprehensive scan, 1.5×10^5 sample points were generated for each LQ mass.[9] The effective parameters f_{ij}, d_{ij} and e_{ij} were fixed in a chi-squared fit to the (running) charged fermion masses at the scale $\mu = 1\,\mathrm{TeV}$ [378] and to quark mixing [29]. In order to achieve this, the VEV of H_d was varied in the range $\langle H_d^0 \rangle/\mathrm{GeV} \in [1.22, 4.86]$ in accordance with eq. (5.2). Note that in the comprehensive scan it is also assumed that besides the LQ ϕ only one SM-like Higgs is present in the scalar sector, which can be easily accounted for by appropriately rescaling the effective parameters d_{ij} and e_{ij}. Since the unitary matrices L_d, R_d, L_e and R_e only depend on ratios of these, they are unaffected by this rescaling and thus the LQ coupling matrices $\mathbf{x}$, $\mathbf{y}$ and $\mathbf{z}$ also remain unaltered.

A further motivation to conduct a second numerical study is the possibility to efficiently target regions in the high-dimensional parameter space of the model which were identified in the primary scan as compatible with an explanation of the flavour anomalies, and as consistent with current experimental bounds. This is achieved via a suitable biasing of the most relevant effective parameters, as is explained in sections 5.4.3.2 and 5.4.4.

Furthermore, since the comprehensive scan is based on a variation of the effective parameters in the LQ coupling matrices $\hat{\mathbf{x}}$ and $\hat{\mathbf{y}}$, it properly accounts for effects which originate from the unitary transformations relating the interaction basis and the charged fermion mass basis. This in general implies additional contributions to the effective LQ parameters in the coupling matrices $\mathbf{x}$, $\mathbf{y}$ and $\mathbf{z}$, which may push them outside the range $[\lambda, 1/\lambda]$ and thus leave an imprint on the phenomenology in some instances as discussed below. For simplicity, the relations between effective parameters given in appendix 5.9 which hold at LO in λ are employed to translate between the interaction basis and the charged fermion mass basis. As these generally involve both the SM Yukawa parameters f_{ij}, d_{ij} and e_{ij}

---

[9] As already mentioned in the beginning of section 5.4, I will discuss the findings of the comprehensive scan and include the pertinent plots where appropriate in the following. Note that the comprehensive scan as well as the discussion of the results as presented in ref. [90] are primarily an achievement by my co-author Innes Bigaran. If no explicit reference is made to the comprehensive scan in the main text herein, it is understood that the results agree with those from the primary scan.

as well as the LQ parameters $\hat{a}_{ij}$ and $\hat{b}_{ij}$, the ranges which the effective LQ parameters fall into may be sensitive both to the fit to charged fermion masses and quark mixing and to the biases. In the comprehensive scan, the observables $R(D)$, $R(D^\star)$ and $R^{\nu}_{K^\star}$ are calculated via the WCs defined in eqs. (5.45) and (5.69) further below in this section, the `Wilson` package [383] and `flavio` [11,12]. Δa_μ, $\mathrm{BR}(\tau \to \mu\gamma)$, $\mathrm{BR}(\mu \to e\gamma)$ and $\mathrm{CR}(\mu - e;$ Al) are computed with the help of `SARAH` [384, 385] and `SPheno` [385]. Trilepton decays and $g_{\tau_A}/g_A^{\mathrm{SM}}$ are calculated in the same way as in the primary scan.

The conventions for the plots which illustrate the results from the comprehensive scan are not identical to those for the primary scan. Firstly, the displayed coloured points pass all considered constraints. Red stars are employed for $\hat{m}_\phi = 2$, yellow plus signs for $\hat{m}_\phi = 4$ and blue crosses for $\hat{m}_\phi = 6$, as displayed in the plot legends. Dotted black lines indicate the central values for SM predictions. If relevant for the observable under consideration, a red-brown shaded region indicates the prospective reach as labelled, with the best-fit value denoted with a solid red-brown line. Where a parameter (or combination of parameters) is shown on an axis, a grey-shaded band signifies the region of parameter space probed in the primary scan. The overlaid white crosses (labelled 'Anomalies' in the legends) mark sample points that can simultaneously address the anomalies in $R(D)$, $R(D^\star)$ and Δa_μ within the respective $3\,\sigma$ regions about their present best-fit values. Slightly different conventions are employed in figure 5.7; see the caption therein for further information. Lastly, in agreement with the conventions for the primary scan, solid black lines indicate current experimental bounds, dashed black lines stand for prospective bounds, and grey-shaded areas indicate the regions about the present experimental best-fit values pertaining to different CLs where a physical observable is shown on an axis.

5.4.2 $R(D)$ and $R(D^\star)$

I begin the discussion of the phenomenology of the model under consideration with the LFU ratios $R(D)$ and $R(D^\star)$. They are mediated via semi-leptonic charged current tran-

LIST OF PRIMARY OBSERVABLES					
Observable	Experiment				
	Current constraint/measurement			Future reach	
$R(D)$	$0.339 \pm 0.026 \pm 0.014$	at $1\,\sigma$ level	[10]	$\pm 0.016\,(0.008)$ for $5\,(50)\,\mathrm{ab}^{-1}$	[17]
$R(D^\star)$	$0.295 \pm 0.010 \pm 0.010$	at $1\,\sigma$ level	[10]	$\pm 0.009\,(0.0045)$ for $5\,(50)\,\mathrm{ab}^{-1}$	[17]
Δa_μ	$(2.51 \pm 0.59) \times 10^{-9}$	at $1\,\sigma$ level	[18,19]	$\pm 0.4 \times 10^{-9}$	[20]
$\mathrm{BR}(\tau \to \mu\gamma)$	4.2×10^{-8}	at 90% C.L.	[21]	6.9×10^{-9}	[386]
$\mathrm{BR}(\mu \to e\gamma)$	4.2×10^{-13}	at 90% C.L.	[22]	6×10^{-14}	[23]
$\mathrm{BR}(\tau \to 3\,\mu)$	2.1×10^{-8}	at 90% C.L.	[28]	3.6×10^{-10}	[386]
$\mathrm{BR}(\tau \to \mu e\bar{e})$	1.8×10^{-8}	at 90% C.L.	[28]	2.9×10^{-10}	[386]
$\mathrm{BR}(\mu \to 3\,e)$	1.0×10^{-12}	at 90% C.L.	[242]	$20\,(1) \times 10^{-16}$	[27]
$\mathrm{CR}(\mu - e;\,\mathrm{Al})$				$2.6\,(2.9) \times 10^{-17}$	[25,26]
$R^\nu_{K^\star}$	2.7	at 90% C.L.	[24]	$1.0 \pm 0.25\,(0.1)$ for $5\,(50)\,\mathrm{ab}^{-1}$	[7]
$g_{\tau_A}/g_A^{\mathrm{SM}}$	1.00154 ± 0.00128	at $1\,\sigma$ level	[30,31]	$\pm 7.5\,(0.75) \times 10^{-5}$	[31–33]
$\tau_{B_c}^{\mathrm{SM}}$	$0.52^{+0.18}_{-0.12}$ ps	at $1\,\sigma$ level	[387]		
$c\bar{c} \to \tau\bar{\tau}$	$\lvert b_{32}\rvert < 2.6$ $(\hat{m}_\phi = 2)$		[161,388]		

Table 5.4: **List of primary observables**. Herein I list the observables of which the anomalous data ought to be explained, as well as the ones which dominantly constrain this model, together with the respective current measurement/constraint and future reach. The values for $R(D)$ and $R(D^\star)$ reflect the 2021 averages from the HFLAV collaboration. The future reach for $\mathrm{BR}(\mu \to 3e)$ outside (inside) the parentheses refers to Phase 1 (2) of the Mu3E experiment. For $\mathrm{CR}(\mu \to e;\,\mathrm{Al})$, the first (second) value indicates the future reach of COMET (Mu2E). The future reach for $R^\nu_{K^\star}$ holds under the assumption that the result of the measurement will agree with the SM expectation [7]. Regarding the projections for g_{τ_A}, it is assumed that the experimental uncertainty will be reduced by the same factor as $\sin^2\theta_{\mathrm{eff}}$ as in ref. [31]; the unbracketed projection refers to the International Linear Collider (ILC) [32], whereas the bracketed value is for the Future Circular Collider (FCC) [33]. The current experimental constraint on the B_c lifetime is $\tau_{B_c}^{\mathrm{exp}} = (0.510 \pm 0.009)$ ps [10,29]. Note that the constraint arising from high-p_T $\tau\bar{\tau}$ searches differs from the other constraints in that it is directly imposed in the primary scan via an adequate restriction of the range for $\lvert b_{32}\rvert$ as indicated.

sitions, for which the effective Lagrangian reads

$$\begin{aligned}\mathcal{L} \supset\ & C^{VLL}_{\nu edu,ijkl}\big(\bar{\nu}_i\gamma^\mu P_L e_j\big)\big(\bar{d}_k\gamma_\mu P_L u_l\big) + C^{VLR}_{\nu edu,ijkl}\big(\bar{\nu}_i\gamma^\mu P_L e_j\big)\big(\bar{d}_k\gamma_\mu P_R u_l\big) \\ & + C^{SRL}_{\nu edu,ijkl}\big(\bar{\nu}_i P_R e_j\big)\big(\bar{d}_k P_L u_l\big) + C^{SRR}_{\nu edu,ijkl}\big(\bar{\nu}_i P_R e_j\big)\big(\bar{d}_k P_R u_l\big) \\ & + C^{TRR}_{\nu edu,ijkl}\big(\bar{\nu}_i\sigma^{\mu\nu} P_R e_j\big)\big(\bar{d}_k\sigma_{\mu\nu} P_R u_l\big) + \text{h.c.}\,.\end{aligned} \tag{5.44}$$

Integrating out ϕ, I find the following contributions via tree-level matching:

$$C^{VLL}_{\nu edu,ijkl} = -\frac{x^*_{ik} z_{jl}}{2m_\phi^2}\,, \qquad C^{SRR}_{\nu edu,ijkl} = -\frac{x^*_{ik} y_{jl}}{2m_\phi^2}\,, \qquad C^{TRR}_{\nu edu,ijkl} = \frac{1}{4}\frac{x^*_{ik} y_{jl}}{2m_\phi^2}\,. \tag{5.45}$$

Observable	Effective parameters
$R(D)$	a_{33}, b_{32}, (a_{23})
$R(D^\star)$	a_{33}, b_{32}, (a_{23})
Δa_μ	b_{23}, c_{23}
$\mathrm{BR}(\tau \to \mu\gamma)$	b_{23}, c_{33}
$\mathrm{BR}(\mu \to e\gamma)$	b_{13}, c_{23}
$\mathrm{BR}(\tau \to 3\,\mu)$	b_{23}, c_{33}, (c_{23})
$\mathrm{BR}(\tau \to \mu e\bar{e})$	b_{23}, c_{33}, (c_{23})

Observable	Effective parameters
$\mathrm{BR}(\mu \to 3\,e)$	b_{13}, c_{23}
$\mathrm{CR}(\mu \to e;\,\mathrm{Al})$	b_{13}, c_{23}, $(b_{11}$, b_{23}, c_{13}, $c_{21})$
$R^\nu_{K^\star}$	a_{32}, a_{33}, $(a_{22}$, $a_{23})$
$g_{\tau_A}/g_A^{\mathrm{SM}}$	c_{33}
$\tau^{\mathrm{SM}}_{B_c}$	a_{33}, b_{32}, (a_{23})
$c\bar{c} \to \tau\bar{\tau}$	b_{32}
$bc \to \tau\nu$	a_{33}, b_{32}, (c_{32})

Table 5.5: **List of primary observables with the relevant effective parameters**. I list the primary observables together with the effective parameters related to the LQ couplings in the charged fermion mass basis which capture the most relevant contributions, respectively, in line with the analytic estimates performed in this section. The parameters listed in round brackets refer to contributions which are subdominant.

On the contrary, $C^{VLR}_{\nu edu,ijkl}$ and $C^{SRL}_{\nu edu,ijkl}$ are only sourced at loop level and thus disregarded. The underlying quark-level transition for $R(D)$ and $R(D^\star)$ is given by $b \to c$, thus I specify $k = 3$ and $l = 2$ henceforth. According to eq. (5.45), one has

$$C^{SRR}_{\nu edu,ij32}(m_\phi) = -4\,C^{TRR}_{\nu edu,ij32}(m_\phi) \tag{5.46}$$

at the matching scale $\mu = m_\phi$. Since it is common to define the observables $R(D)$ and $R(D^\star)$ at a scale close to the mass of the bottom quark, I account for the effects of RG running as follows, extracted from the package `Wilson` [383]:

$$\frac{C^{VLL}_{\nu edu,\beta\alpha32}(\mu_B)}{C^{VLL}_{\nu edu,\beta\alpha32}(m_\phi)} \approx \left\{\begin{matrix} 1.016, & \hat{m}_\phi = 2 \\ 1.018, & \hat{m}_\phi = 4 \\ 1.019, & \hat{m}_\phi = 6 \end{matrix}\right\}, \quad \frac{C^{SRR}_{\nu edu,\beta\alpha32}(\mu_B)}{C^{SRR}_{\nu edu,\beta\alpha32}(m_\phi)} \approx \left\{\begin{matrix} 1.675, & \hat{m}_\phi = 2 \\ 1.736, & \hat{m}_\phi = 4 \\ 1.770, & \hat{m}_\phi = 6 \end{matrix}\right\},$$
$$\frac{C^{TRR}_{\nu edu,\beta\alpha32}(\mu_B)}{C^{TRR}_{\nu edu,\beta\alpha32}(m_\phi)} \approx \left\{\begin{matrix} 0.860, & \hat{m}_\phi = 2 \\ 0.852, & \hat{m}_\phi = 4 \\ 0.848, & \hat{m}_\phi = 6 \end{matrix}\right\}. \tag{5.47}$$

Here, I have chosen the scale

$$\mu = \mu_B \equiv 4.8\ \mathrm{GeV}\ . \tag{5.48}$$

Note in particular that RG running implies

$$C^{SRR}_{\nu edu,ij32}(\mu_B) \approx -8\,C^{TRR}_{\nu edu,ij32}(\mu_B)\ . \tag{5.49}$$

The formulae used for the computation of $R(D)$ and $R(D^\star)$ in the primary scan are derived from requiring that the results agree with the output of the package `flavio` [11,12], v2.3.[10] Thus, the SM predictions $R(D)_{\text{SM}} = 0.297 \pm 0.008$ and $R(D^\star)_{\text{SM}} = 0.245 \pm 0.008$ obtained from `flavio` are employed as well. Their discrepancy with current data has a significance of roughly $3\,\sigma$, as can be seen in table 5.1.[11]

As the model predicts the main contributions to $R(D)$ and $R(D^\star)$ to be induced in the tau-lepton channel, I focus on $j = 3$ henceforth. Moreover, the dominant correction will arise from the large coupling $x_{33} \sim 1$ which involves a tau neutrino ν_τ. In this case, interference with the SM contribution occurs, as the flavours of the final-state leptons match. Since the coupling $x_{23} \sim \lambda$ is also fairly large, neglecting the lepton-flavour violating (LFV) channel with a muon neutrino ν_μ is generally not justified. Contrariwise, the residual symmetry Z_{17}^{diag} successfully protects the couplings to electron neutrinos ν_e, resulting in $x_{11} \sim \lambda^9$, $x_{13} \sim \lambda^9$ and $x_{12} \sim \lambda^{11}$, respectively, which implies that this channel can never have a sizeable impact. Eventually, I find the approximate expressions

$$\begin{aligned}
\frac{R(D)}{R(D)_{\text{SM}}} &\approx 1 - 1.17\ \text{Re}\left(\hat{C}^{SRR}_{\nu edu,3332}(\mu_B)\right) + 0.72\ \text{Re}\left(\hat{C}^{TRR}_{\nu edu,3332}(\mu_B)\right) \\
&\quad + 0.63\left(\left|\hat{C}^{SRR}_{\nu edu,3332}(\mu_B)\right|^2 + \left|\hat{C}^{SRR}_{\nu edu,2332}(\mu_B)\right|^2\right) \\
&\quad + 0.37\left(\left|\hat{C}^{TRR}_{\nu edu,3332}(\mu_B)\right|^2 + \left|\hat{C}^{TRR}_{\nu edu,2332}(\mu_B)\right|^2\right) \\
&\approx 1 + 1.07\ \frac{|a_{33}b_{32}|}{\hat{m}_\phi^2}\cos\left(\text{Arg}(a_{33}) - \text{Arg}(b_{32})\right) \\
&\quad + 0.46\ \frac{|a_{33}b_{32}|^2}{\hat{m}_\phi^4} + 0.02\ \frac{|a_{23}b_{32}|^2}{\hat{m}_\phi^4}
\end{aligned} \tag{5.50}$$

---

[10] As the formulae are lengthy, they are relegated to appendix 5.10.

[11] $R(D)$ and $R(D^\star)$ are implemented in `flavio` via the helicity formalism [302]. Regarding the employed form factors, ref. [13] which makes use of HQET, see section 2.4.4, has been used since v2.0.

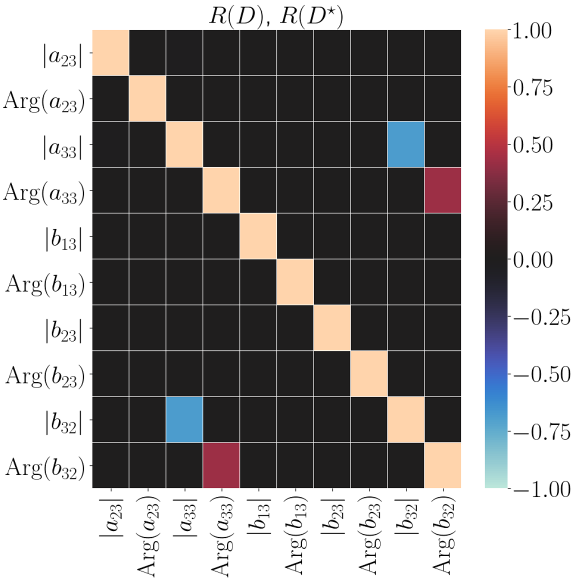

Figure 5.1: **Correlation plot for $\hat{m}_\phi = 4$ based on the sample points which explain $R(D^{(\star)})$ at $2\,\sigma$ or $1\,\sigma$ in the primary scan.** The plot visualises Spearman's rank correlation coefficient calculated via the library `seaborn` [9]. A negative (positive) correlation among, say, two coefficient magnitudes indicates that if one of them increases, the other tends to decrease (also increase). Note that sample points not respecting the experimental bounds are taken into account here as well.

and

$$\begin{aligned}\frac{R(D^\star)}{R(D^\star)_{\mathrm{SM}}} &\approx 1 + 0.10\ \mathrm{Re}\left(\hat{C}^{SRR}_{\nu edu,3332}(\mu_B)\right) + 4.21\ \mathrm{Re}\left(\hat{C}^{TRR}_{\nu edu,3332}(\mu_B)\right)\\ &\quad + 0.03\ \left(\left|\hat{C}^{SRR}_{\nu edu,3332}(\mu_B)\right|^2 + \left|\hat{C}^{SRR}_{\nu edu,2332}(\mu_B)\right|^2\right)\\ &\quad + 8.60\left(\left|\hat{C}^{TRR}_{\nu edu,3332}(\mu_B)\right|^2 + \left|\hat{C}^{TRR}_{\nu edu,2332}(\mu_B)\right|^2\right)\\ &\approx 1 + 0.36\ \frac{|a_{33}b_{32}|}{\hat{m}_\phi^2}\cos\left(\mathrm{Arg}(a_{33}) - \mathrm{Arg}(b_{32})\right)\\ &\quad + 0.12\ \frac{|a_{33}b_{32}|^2}{\hat{m}_\phi^4} + 0.01\ \frac{|a_{23}b_{32}|^2}{\hat{m}_\phi^4}\ .\end{aligned} \tag{5.51}$$

Here, the dominant LFV contributions are captured via the WCs with the flavour-index combination 2332, and the parameter product $a_{23}b_{32}$ in the respective last line. Furthermore, for the sake of convenience, dimensionless WCs

$$\hat{C} \equiv C \cdot \mathrm{TeV}^2 \tag{5.52}$$

were introduced. Note that ϕ dominantly sources $R(D)$ via the scalar operator, and $R(D^\star)$ via the tensor operator. On the contrary, the hierarchy $z_{32}/y_{32} \sim \lambda^2$ implies that corrections mediated by vector operators are further suppressed and can hence be neglected.

The estimates in eqs. (5.50) and (5.51) suggest that the contributions to both $R(D)$ and

$R(D^\star)$ are largely controlled by the product $|a_{33}b_{32}|$ which has to fall in an appropriate range to explain the anomaly. Furthermore, whether an enhancement or a suppression of $R(D)$ and $R(D^\star)$ is obtained may be suspected to largely depend on the cosines associated with the real parts of the NP WCs which interfere with the SM contributions. Seeing as the best-fit values are larger than the SM predictions in either case, one expects that the cosines should take values close to $+1$ for that purpose, which would imply that the arguments of the complex coefficients a_{33} and b_{32} should approximately coincide, hence be positively correlated.

These considerations are substantiated via selecting only the points from the entire generated sample for which the anomaly in $R(D)$ and $R(D^\star)$ is explained at a certain CL, and then determining Spearman's rank correlation coefficient for all pairwise combinations of the LQ coupling parameters. For that purpose, the library `seaborn` [9] has been used, and the results are shown in the correlation plot in figure 5.1.

Besides the coefficients a_{33} and b_{32} which play a major role for $R(D)$ and $R(D^\star)$, the coefficients a_{23}, b_{13} and b_{23} are included as well for the sake of comparison due to their relevance for contributions to the AMM of the muon and radiative cLFV lepton decays; see section 5.4.3. The case $\hat{m}_\phi = 4$ and an (inclusive) CL of $2\,\sigma$ are chosen as an illustrative example, the results are not appreciably different for the other considered masses and CLs. Note that the sample points taken into account in figure 5.1 comprise all those which explain $R(D)$ and $R(D^\star)$, regardless of whether they also respect the imposed experimental bounds or not, thereby making up roughly 10% of the entire sample for $\hat{m}_\phi = 4$. A blueish (reddish) colour illustrates a negative (positive) correlation, whereas black indicates the absence of any appreciable correlation. One can see that the contribution linear in $|a_{33}b_{32}|$ is required to be positive for an explanation of $R(D)$ and $R(D^\star)$, that is, the contribution quadratic in $|a_{33}b_{32}|$ is generically too small to yield a dominant effect.

The results from the primary scan in the $R(D) - R(D^\star)$ plane are displayed in the left plot of figure 5.2. The distinctive linear relation

$$R(D^\star) \approx 0.30\,R(D) + 0.15 \tag{5.53}$$

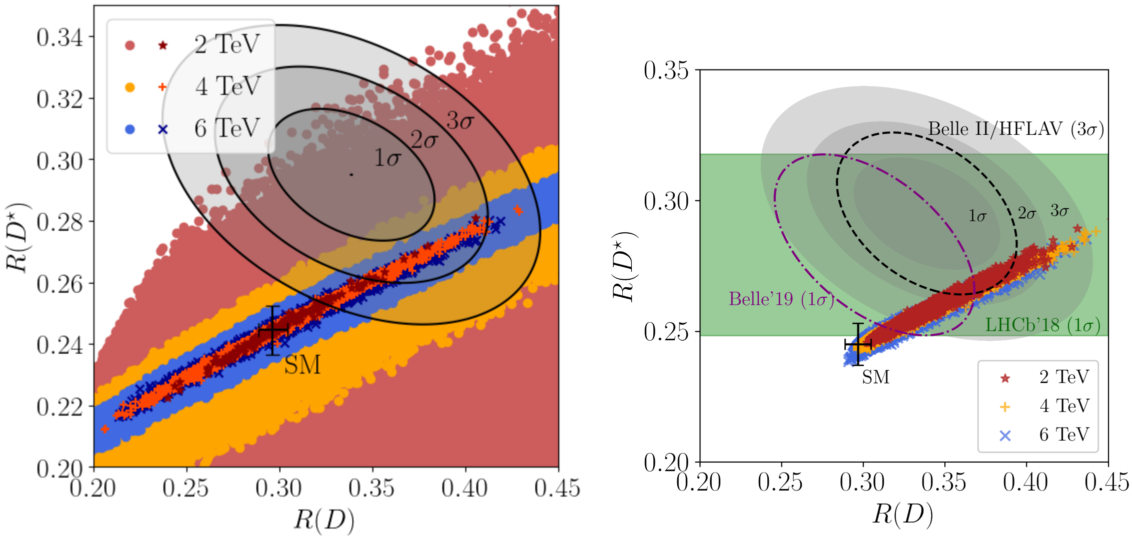

Figure 5.2: **Model predictions for $R(D)$ and $R(D^\star)$. Left:** Results from primary scan. The regions marked by solid lines are compatible with the current experimental world averages for $R(D^{(\star)})$ [10] at the indicated CL; see table 5.4. I use the values output by `flavio`, v2.3 for the SM predictions for $R(D^{(\star)})$ at $1\,\sigma$ [11–13] indicated by the black cross, see section 5.10. The round points (geometric shapes) indicate that current experimental bounds are violated (respected); see also the main text of section 5.4.1.1. **Right:** Results from comprehensive scan. The shown sample points respect the experimental bounds from primary constraints; see also section 5.4.1.2. The dot-dashed purple ellipse shows the $1\,\sigma$ contour about the most recent results for $R(D)$ and $R(D^\star)$ from Belle [14], and the green band indicates the $1\,\sigma$ region about the most recent result for $R(D^\star)$ from LHCb [15, 16]. The black dashed ellipse shows the prospective reach at Belle II [17] at the level of $3\,\sigma$ for 5 ab^{-1} of data under the assumption of the best-fit value and correlation coefficient from the HFLAV collaboration as of 2021 [10].

holds after the experimental bounds are imposed, implying that ϕ can accommodate the anomalous data in $R(D)$ and $R(D^\star)$ at the level of $2\,\sigma$, regardless of which benchmark mass is considered. This is confirmed by the findings of the comprehensive scan, see the right plot in figure 5.2. Moreover, if the best-fit value and the correlation coefficient reported by HFLAV remain unchanged, but the uncertainties for $R(D)$ and $R(D^\star)$ shrink as projected by the Belle-II collaboration, see table 5.4, an accommodation of the anomaly within the model would still be possible at $3\,\sigma$ for all LQ masses.

5.4.3 Radiative Lepton Transitions

In order to describe radiative transitions of charged leptons, I make use of the contribution from the dipole operator which enters the relevant leptonic effective Lagrangian

$$\mathcal{L} \supset C_{e\gamma}^{ij} (\overline{e}_i \sigma^{\mu\nu} P_R e_j) F_{\mu\nu} + \text{h.c.} \,. \tag{5.54}$$

Herein, I define the covariant derivative for QED as in $D_\mu = \partial_\mu + iQeA_\mu$ which agrees with ref. [192]. Note that as per $\psi = (P_L + P_R)\psi$ with the projection operators introduced in eq. (2.8), the transitions described by eq. (5.54) necessarily involve a chirality flip.

Evaluating the one-loop amplitudes of the contributions mediated by ϕ and matching the results onto LEFT with the help of `FeynRules` [389], `FeynArts` [390], `FormCalc` [391,392], `Package-X` [393], and `ANT` [394] yields

$$\begin{aligned} C_{e\gamma}^{ij} = -\frac{e}{32\pi^2 m_\phi^2} \sum_m \Bigg(&\Big(m_{e_i} y_{im}^* y_{jm} + m_{e_j} z_{im}^* z_{jm} \Big) \left[f_S(t_{u_m}) - 3 f_F(t_{u_m}) \right] \\ &- m_{u_m} z_{im}^* y_{jm} \left[g_S(t_{u_m}) - 3 g_F(t_{u_m}) \right] \Bigg) \end{aligned} \tag{5.55}$$

with the unit electric charge $e = |e|$ and the abbreviation

$$t_X \equiv \frac{m_X^2}{m_\phi^2} \,. \tag{5.56}$$

Moreover, the loop functions

$$\begin{aligned} f_S(x) &= \frac{x+1}{4(x-1)^2} - \frac{x \ln x}{2(x-1)^3} \,, \quad & f_F(x) &= \frac{x^2 - 5x - 2}{12(x-1)^3} + \frac{x \ln x}{2(x-1)^4} \,, \\ g_S(x) &= \frac{1}{x-1} - \frac{\ln x}{(x-1)^2} \,, & g_F(x) &= \frac{x-3}{2(x-1)^2} + \frac{\ln x}{(x-1)^3} \end{aligned} \tag{5.57}$$

enter. Expanding them in small arguments, I approximately find

$$C_{e\gamma}^{ij} \approx \frac{e}{128\pi^2 m_\phi^2} \sum_m \Big(m_{e_i} y_{im}^* y_{jm} + m_{e_j} z_{im}^* z_{jm} + 2 m_{u_m} z_{im}^* y_{jm} (7 + 4 \ln t_{u_m}) \Big) \,. \tag{5.58}$$

This result neatly illustrates that the chirality flip occurs due to a mass insertion either on an external lepton line (first two terms), or the internal up-quark line (right-hand term). Thus, the latter contribution will be the dominant one for $m = 3$ due to the large mass of the top quark. Generally, the finite contributions to the AMM arise from the photon coupling to either the internal LQ propagator or the internal up-type quark propagator.

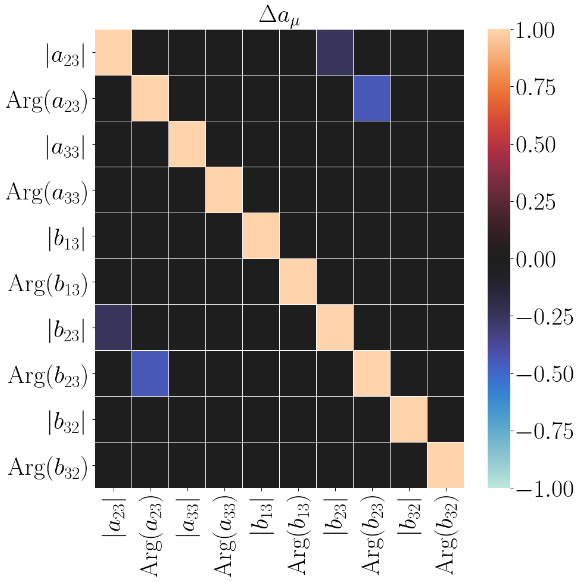

Figure 5.3: **Correlation plot for $\hat{m}_\phi = 4$ based on the sample points which explain Δa_μ at $2\,\sigma$ or $1\,\sigma$ in the primary scan.** The plot visualises Spearman's rank correlation coefficient calculated via the library `seaborn` [9]. A negative (positive) correlation among, say, two coefficient magnitudes indicates that if one of them increases, the other tends to decrease (also increase). Note that sample points not respecting the experimental bounds are taken into account here as well.

5.4.3.1 Anomalous Magnetic Moment of the Muon

Turning now to the AMM of the muon and using eqs. (2.51) and (5.54), I find

$$\begin{aligned}\Delta a_\mu &= \frac{4m_\mu}{e}\,\mathrm{Re}(C^{22}_{e\gamma}) \approx \frac{m_\mu m_t}{16\pi^2 m_\phi^2}(7+4\ln t_t)\,\mathrm{Re}(z^*_{23}y_{23}) \\ &\approx -\frac{5}{\hat{m}_\phi^2}\mathrm{Re}(b_{23}c^*_{23})\times 10^{-9} = -\frac{5}{\hat{m}_\phi^2}|b_{23}c_{23}|\cos\left(\mathrm{Arg}(b_{23})-\mathrm{Arg}(c_{23})\right)\times 10^{-9}\ .\end{aligned} \tag{5.59}$$

After the announcement of the Run-1 results from the $g-2$ experiment at Fermilab [18], the combined significance of the experimental anomaly in the AMM of the muon now stands at $4.2\,\sigma$; see also section 2.2.2. The result $\Delta a_\mu \sim 10^{-9}$ obtained from the estimate above suggests that the model under consideration can ameliorate this anomalous data, see also table 5.4, which I will elaborate on in the following.

Firstly, a positive contribution to Δa_μ is required, which implies that the cosine in eq.(5.59) must cancel the negative sign in front. Therefore, the difference of the arguments of the coefficients[12] $c_{23} \approx a_{23}$ and b_{23} needs to be in a vicinity of π, signaling the requirement of

---

[12] As can be seen in eq. (5.35), the effective parameters c_{23} and a_{23} as well as c_{33} and a_{33} agree up to $\mathcal{O}(\lambda^4)$, respectively, and since c_{23} and c_{33} are not varied as fundamental parameters in the primary scan, the implications for these coefficients will be mainly discussed in terms of a_{23} and a_{33}.

a negative correlation between $\mathrm{Arg}(c_{23}) \approx \mathrm{Arg}(a_{23})$ and $\mathrm{Arg}(b_{23})$. This is confirmed via the correlation plot in figure 5.3 which indicates a (moderate) negative correlation, both in the case of $|a_{23}|$ and $|b_{23}|$ as well as for the phase differences. The points constituting the plot may or may not respect the imposed experimental bounds and comprise roughly 15% of the entire sample for the mass $\hat{m}_\phi = 4$ used as a benchmark here.

Note that the negative correlation of the magnitudes is less pronounced than in the case of $|a_{33}|$ and $|b_{32}|$ if the anomaly in $R(D)$ and $R(D^\star)$ ought to be explained. I interpret this as being due to the fact that the product $|a_{33}b_{32}|$ more directly determines the result for $R(D^{(\star)})$, since there is not only the contribution arising from interference with the SM, but also the (smaller) contribution proportional to $|a_{33}b_{32}|^2$ which is unaffected by $\mathrm{Arg}(a_{33}) - \mathrm{Arg}(b_{32})$, as can be seen in eqs. (5.50) and (5.51). On the contrary, say, a too large value $|a_{23}b_{23}|$ can always directly get compensated by $\mathrm{Arg}(a_{23}) - \mathrm{Arg}(b_{23})$; thus the result for Δa_μ exhibits a more similar sensitivity to the magnitudes and the phase difference of a_{23} and b_{23}.

The primary scan shows that a priori, a result up to $\Delta a_\mu \approx 3 \cdot 10^{-9}$ or larger is possible, depending on the LQ mass, in line with the estimate in eq. (5.59) in the case of large LQ couplings. Still, after imposing the experimental bounds, $\Delta a_\mu \sim 10^{-9}$ is not a generic result, but instead I found a further suppression by one or two orders of magnitude for about 90% of the viable sample points with positive Δa_μ generated in the primary scan, irrespective of the LQ mass. Imposing the experimental bounds does not result in a preference for either sign of Δa_μ, as is expected since none of the primary observables exhibit a particular sensitivity to the phase of b_{23} or a_{23}. Still, the results hint towards the possibility of explaining Δa_μ at $2\,\sigma$ or better in the model. See section 5.4.4 for the pertinent plots and further discussions.

Regarding the case of other charged leptons, I note that the model under consideration can generate contributions $|\Delta a_e| \sim 10^{-21}$ and $|\Delta a_\tau| \sim 10^{-7}$ as is found in the comprehensive scan, which are however well below the respective present and future experimental reaches [395–398]. The EDM of the muon will be briefly discussed in section 5.4.12.1.

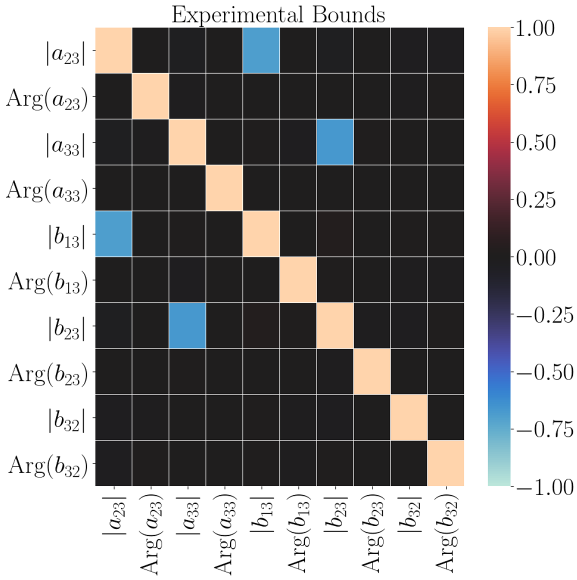

Figure 5.4: **Correlation plot for $\hat{m}_\phi = 4$ based on the sample points which respect all imposed experimental constraints in the primary scan.** The plot visualises Spearman's rank correlation coefficient calculated via the library `seaborn` [9]. A negative (positive) correlation among, say, two coefficient magnitudes indicates that if one of them increases, the other tends to decrease (also increase). The LO contributions to $\mathrm{BR}(\tau \to \mu\gamma)$ and $\mathrm{BR}(\mu \to e\gamma)$ are proportional to $|a_{33}b_{23}|^2$ and $|a_{23}b_{13}|^2$, respectively.

5.4.3.2 Radiative Charged Lepton Flavour Violating Decays

Contributions to the dipole operator generally also imply the occurrence of radiative cLFV decays, of which the BRs read

$$\mathrm{BR}(e_i \to e_j\gamma) = \frac{m_{e_i}^3}{4\pi\Gamma_{e_i}}\left(|C_{e\gamma}^{ij}|^2 + |C_{e\gamma}^{ji}|^2\right) . \tag{5.60}$$

Here, the full decay width of the charged lepton e_i is signified by Γ_{e_i}. Again focussing on the dominant contribution with a top-quark mass insertion in the loop, I approximately find

$$\mathrm{BR}(e_i \to e_j\gamma) \approx \frac{e^2 m_t^2 m_{e_i}^3}{128^2\pi^5\Gamma_{e_i} m_\phi^4}|7 + 4\ln t_t|^2\left(|z_{i3}y_{j3}|^2 + |z_{j3}y_{i3}|^2\right) . \tag{5.61}$$

Further specifying the flavour channels $\mu \to e$ and $\tau \to \mu$, one obtains

$$\mathrm{BR}(\mu \to e\gamma) \approx \frac{e^2 m_t^2 m_\mu^3}{128^2\pi^5\Gamma_\mu m_\phi^4}|7 + 4\ln t_t|^2|z_{23}y_{13}|^2 \approx \frac{8}{\hat{m}_\phi^4}|c_{23}b_{13}|^2 \times 10^{-11} \tag{5.62}$$

and

$$\mathrm{BR}(\tau \to \mu\gamma) \approx \frac{e^2 m_t^2 m_\tau^3}{128^2\pi^5\Gamma_\tau m_\phi^4}|7 + 4\ln t_t|^2|z_{33}y_{23}|^2 \approx \frac{3}{\hat{m}_\phi^4}|c_{33}b_{23}|^2 \times 10^{-6} . \tag{5.63}$$

In fact, the viable parameter space for the model is predominantly shaped by the established experimental limits on these two BRs. This is further evidenced by the correlation plot in figure 5.4 showing the coefficients of the LQ couplings which display non-zero correlations when all the experimental bounds considered in the primary scan are imposed. Note that for the selected benchmark mass $\hat{m}_\phi = 4$ this is the case for only 0.35% of the generated sample points.

Therefore, imposing an adequate negative correlation between the magnitudes $|a_{23}|$ and $|b_{13}|$ as well as $|a_{33}|$ and $|b_{23}|$, respectively, is sufficient in the primary scan to render a sample point compatible with every experimental constraint taken into account. In other words, one in principle only needs to sufficiently constrain the products $|b_{13}a_{23}|$ and $|b_{23}a_{33}|$, which is in excellent agreement with eqs. (5.62) and (5.63) above. Thus, if a bound on another observable is violated, this generally implies in the primary scan that either $\mathrm{BR}(\tau \to \mu\gamma)$ or $\mathrm{BR}(\mu \to e\gamma)$, or both of them, is too large as well. Still, this observation needs to be revised in particular in the light of the results from the comprehensive scan for the observable $R^{\nu}_{K^{(\star)}}$, which is the subject of section 5.4.5.

Combining the estimates for Δa_μ and $\mathrm{BR}(\mu \to e\gamma)$, I approximately find

$$|\Delta a_\mu| \lesssim \frac{5}{\hat{m}_\phi^2}|b_{23}c_{23}| \times 10^{-9} < 5\sqrt{\mathrm{BR}(\mu \to e\gamma)_{\mathrm{exp}}}\,\frac{|b_{23}|}{|b_{13}|} \times 10^{-9} \lesssim \frac{1.6}{|b_{13}|} \times 10^{-9}\,. \tag{5.64}$$

Note that the smallness of the coupling $|y_{13}| \sim |b_{13}|\lambda^9$ due to the residual symmetry Z_{17}^{diag} implies that $\mathrm{BR}(\mu \to e\gamma)$ does not provide a more stringent constraint than $\mathrm{BR}(\tau \to \mu\gamma)$, although the experimental bound on the former is five orders of magnitude stronger than the one on the latter. As is found in the primary scan, one generally generates large contributions $\mathrm{BR}(\tau \to \mu\gamma) \gtrsim \mathcal{O}(10^{-9})$, depending on the LQ mass. Still, the experimental bound on $\mathrm{BR}(\mu \to e\gamma)$ is easily saturated as well. See the pertinent plots and further discussions in section 5.4.4 below. On the contrary, the hierarchy $y_{13}/y_{23} \sim \lambda^6$ also implies that the experimental bound on $\mathrm{BR}(\tau \to e\gamma)$ does not give rise to a relevant constraint for the model, despite it being similarly stringent as the one on $\mathrm{BR}(\tau \to \mu\gamma)$.

In the comprehensive scan, the competitiveness of the processes $\tau \to \mu\gamma$ and $\mu \to e\gamma$ in shaping the parameter space is incorporated via a suitable biasing of the involved effective parameters, as derived from the results of the primary scan. Explicitly, I require

$$|b_{23}| \lesssim \frac{1}{|a_{33}|} \left\{ \begin{array}{ll} 0.16, & \hat{m}_\phi = 2 \\ 0.45, & \hat{m}_\phi = 4 \\ 0.86, & \hat{m}_\phi = 6 \end{array} \right\} \tag{5.65}$$

and

$$|b_{13}| \lesssim \frac{1}{|a_{23}|} \left\{ \begin{array}{ll} 0.41, & \hat{m}_\phi = 2 \\ 1.16, & \hat{m}_\phi = 4 \\ 2.22, & \hat{m}_\phi = 6 \end{array} \right\} . \tag{5.66}$$

Thus, the parameters $|b_{13}|$ and $|a_{23}|$ as well as $|b_{23}|$ and $|a_{33}|$ are correlated in the comprehensive scan not only due to the imposed experimental bounds on $\mathrm{BR}(\tau \to \mu\gamma)$ and $\mathrm{BR}(\mu \to e\gamma)$, but also *a priori* due to the biases enforced as per eqs. (5.65) and (5.66). Note that the ranges for $|a_{23}|$ and $|a_{33}|$ employed in the comprehensive scan also arise from a biasing procedure; see the following section 5.4.4 for more details.

On a slightly different note, I emphasise that ϕ also induces a correction to the charged lepton masses in a manner similar to the radiative transitions discussed in this section. Still, in the case of the electron and the tau lepton, the contributions are very small compared to the respective measured masses. On the contrary, the muon mass can receive $\mathcal{O}(m_\mu)$ corrections which may however be absorbed via a redefinition of the effective parameter e_{22}.[13]

5.4.4 Simultaneous Explanation of All Anomalies

From $\Delta a_\mu \propto |b_{23} c_{23}|$, cf. eq. (5.59), and $R(D^{(\star)})$ being mainly controlled by $|a_{33} b_{32}|$ as can be seen in eqs. (5.50) and (5.51), one may conclude that a priori these observables are not (strongly) correlated in the model. Still, $\mathrm{BR}(\tau \to \mu\gamma)$ is intertwined with $R(D)$ and $R(D^\star)$ via $|c_{33}| \approx |a_{33}|$, and with Δa_μ via $|b_{23}|$, whereas the latter also largely depends on $|c_{23}| \approx |a_{23}|$ which is constrained via $\mathrm{BR}(\mu \to e\gamma)$; see sections 5.4.2 and 5.4.3. Thus,

---

[13] See for instance refs. [399, 400] for a different approach in which a constraint related to these corrections is imposed.

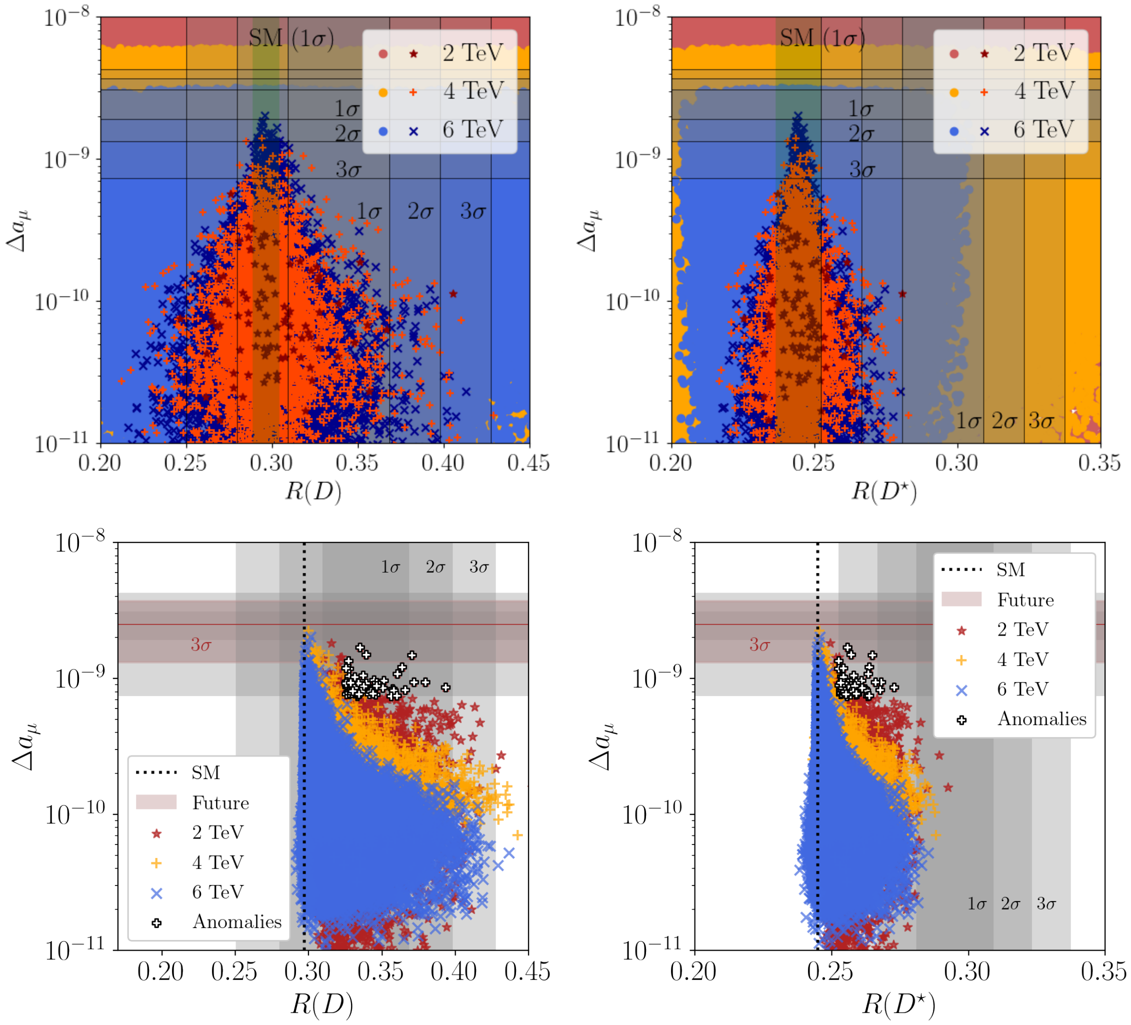

Figure 5.5: **Model predictions for $R(D)$, $R(D^\star)$ and Δa_μ. Upper panel:** Results from primary scan. The regions marked by solid lines are compatible with the current experimental world averages for $R(D^{(\star)})$ [10] and Δa_μ [18, 19], respectively, at the indicated CL; see table 5.4. The SM predictions for $R(D^{(\star)})$ at $1\,\sigma$ [11–13] are indicated by the green-shaded bands. The round points (geometric shapes) indicate that current experimental bounds are violated (respected); see also the main text of section 5.4.1.1. **Lower panel:** Results from comprehensive scan. The shown sample points respect the experimental bounds from primary constraints; see also section 5.4.1.2. The red-brown band indicates the projected sensitivity of the Muon g−2 experiment [20] at the level of $3\,\sigma$. This (roughly) overlays the present $2\,\sigma$ region under the assumption that the current experimental best-fit value persists (red-brown solid line).

enforcing the bounds on these two BRs results in a distinct correlation between Δa_μ and $R(D^{(\star)})$.

The capability of the model to explain the anomalies in $R(D)$, $R(D^\star)$ and Δa_μ is illustrated in figure 5.5. Therein, the effect of imposing the bound on $\mathrm{BR}(\tau \to \mu\gamma)$ helps understand the shape of the viable parameter space. As indicated in section 5.4.2, the difference of $R(D)/R(D)_{\mathrm{SM}}$ and $R(D^\star)/R(D^\star)_{\mathrm{SM}}$ from 1 can be approximated as a quadratic function in $|a_{33}|$, respectively; see eqs. (5.50) and (5.51). Together with $\Delta a_\mu \propto |b_{23}|$, see eq. (5.59), and the experimental limit on $\mathrm{BR}(\tau \to \mu\gamma)$ constraining the product $|b_{23}c_{33}| \approx |b_{23}a_{33}|$ according to eq. (5.63), this bounds $R(D)/R(D)_{\mathrm{SM}}$ and $R(D^\star)/R(D^\star)_{\mathrm{SM}}$ from above as a function of Δa_μ.

Consequently, both $R(D)$ and $R(D^\star)$ can individually be explained at least at $2\,\sigma$ for all considered LQ masses in agreement with the current experimental bound on $\mathrm{BR}(\tau \to \mu\gamma)$; see figure 5.6. Still, the model contribution to $R(D^\star)$ will always be smaller than the experimental best-fit value. Note, though, that even in the case of a non-observation of $\tau \to \mu\gamma$ at Belle II [7], an explanation of $R(D)$ within $1\,\sigma$ would still be possible, whereas an accommodation of the anomaly in $R(D^\star)$ would be disfavoured in that case.

The upcoming searches for $\tau \to \mu\gamma$ and $\mu \to e\gamma$ [23] will both probe large parts of the currently viable parameter space. $\tau \to \mu\gamma$ can be expected to provide a particularly efficient test of the model in the case of $\hat{m}_\phi = 2$. The bottom-left plot in figure 5.6 also indicates that current data on $\tau \to \mu\gamma$ implies the upper limit $\Delta a_\mu \lesssim 3 \times 10^{-9}$ in the model which can readily be recovered from combining the estimates in eq. (5.59) and (5.63) with the current experimental bound $\mathrm{BR}(\tau \to \mu\gamma)_{\mathrm{exp}} < 4.2 \times 10^{-8}$ [21] for the magnitudes of the involved effective LQ parameters not much larger than, say, 2. In addition, both the future search for $\tau \to \mu\gamma$ at Belle II and the one for $\mu \to e\gamma$ at MEG II will test the capability of the model to explain Δa_μ and potentially render this option at least unlikely.

Using `flavio` [11–13], one finds that the SM prediction $R(D)_{\mathrm{SM}} = 0.297 \pm 0.008$ is compatible with the current experimental world average at $2\,\sigma$, that is, the anomaly is primarily constituted by the discrepancy between $R(D^\star)_{\mathrm{SM}} = 0.245 \pm 0.008$ and the corresponding experimental value [10] which overlap only at $3\,\sigma$.[14] Thus, a combined explanation of the anomalies in $R(D)$, $R(D^\star)$ and Δa_μ at a CL of $3\,\sigma$ or better is very challenging to achieve

---

[14] Since the values for $R(D)_{\mathrm{SM}}$ and $R(D^\star)_{\mathrm{SM}}$ output by `flavio` differ from those quoted in ref. [10], the significances are not in exact correspondence with the ones in Table 5.1.

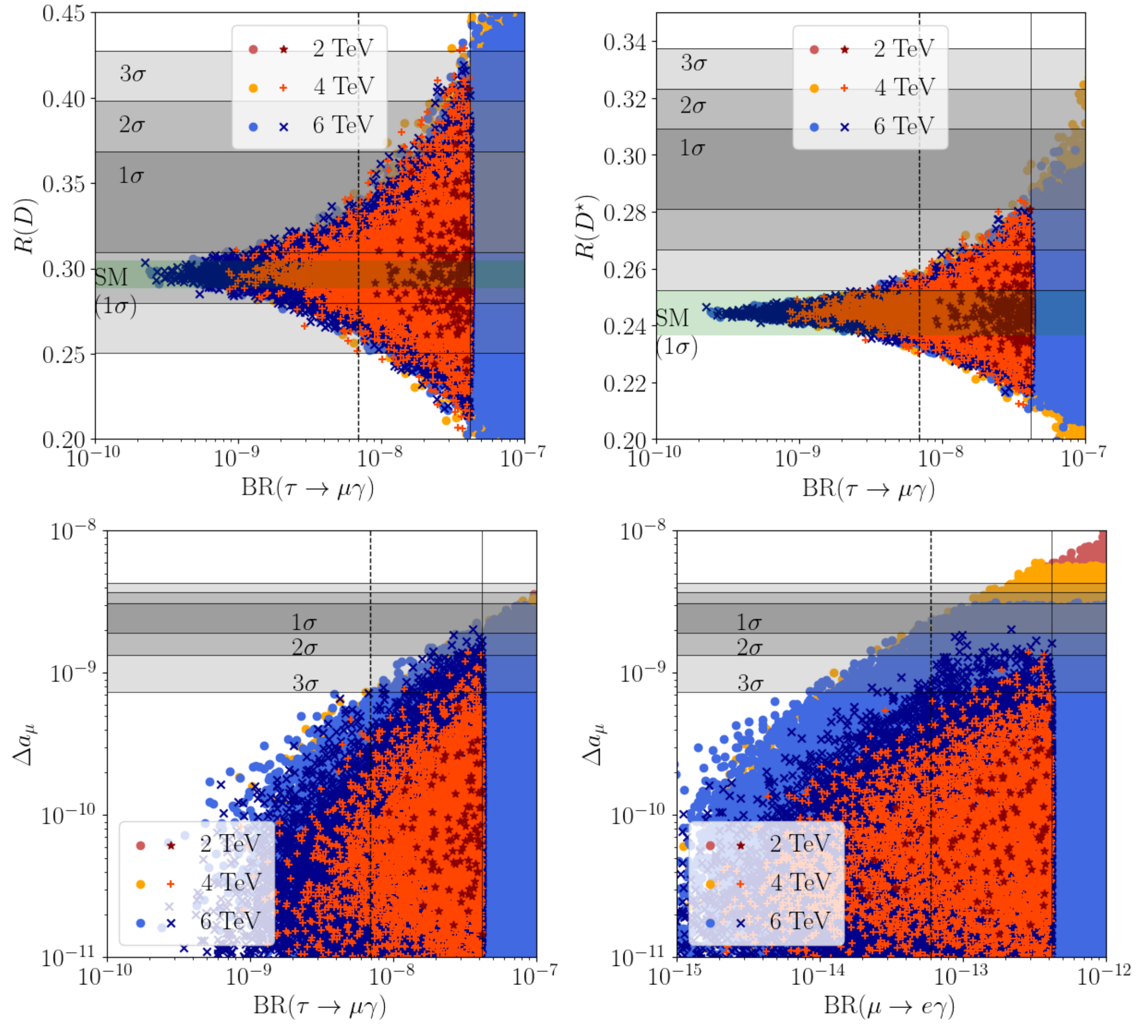

Figure 5.6: **Constraining power and future reach of $\tau \to \mu\gamma$ and $\mu \to e\gamma$ as found in the primary scan.** The vertical solid (dashed) lines indicate the current bound on (future sensitivity of) $\mathrm{BR}(\tau \to \mu\gamma)$ [7, 21] in the upper panel and the bottom-left plot, and the current bound on (future sensitivity of) $\mathrm{BR}(\mu \to e\gamma)$ [22, 23] in the bottom-right plot; see table 5.4. The round points (geometric shapes) indicate that current experimental bounds are violated (respected); see also the main text of section 5.4.1.1.

in the primary scan in particular due to the correlation between the latter two observables.

This situation is remedied in the comprehensive scan with the help of an adequate biasing of the effective parameters a_{33}, b_{32}, a_{23} and b_{23} as laid out in table 5.6. The shown ranges reflect the sample points generated in the primary scan for which all considered experimental bounds are respected and at least one of the anomalies in $R(D^{(\star)})$ or Δa_μ are

$\hat{m}_\phi$	$\lvert a_{33}\rvert$	$\lvert b_{32}\rvert$	$\cos[\Delta(a_{33}, b_{32})]$	$\lvert a_{23}\rvert$	$\cos[\Delta(a_{23}, b_{23})]$
2	$[0.2, 0.7]$	$[1.1, 2.6]$	$[0.4, 1.0]$	–	–
4	$[0.2, 1.9]$	$[1.0, 4.5]$	$[0.1, 1.0]$	$[1.6, 4.4]$	$[-1.0, -0.5]$
6	$[0.2, 3.6]$	$[0.8, 4.5]$	$[0.0, 1.0]$	$[1.4, 4.4]$	$[-1.0, -0.3]$

Table 5.6: **Inputs for biasing in the comprehensive scan, derived from the samples generated in the primary scan**. I define $\Delta(r_{ij}, s_{kl}) \equiv \mathrm{Arg}(r_{ij}) - \mathrm{Arg}(s_{kl})$. Every sample point found in the primary scan which respects all experimental bounds and explains $R(D^{(\star)})$ or Δa_μ (or both) at $3\,\sigma$ falls into the displayed ranges. The interval bounds are rounded to one decimal place. Since no sample points which explain Δa_μ at $3\,\sigma$ were found for $\hat{m}_\phi = 2$ in the primary scan, the default ranges $[\lambda, 1/\lambda]$ and $[-1.0, 0.0]$ are adopted for $|a_{23}|$ and $\cos[\Delta(a_{23}, b_{23})]$, respectively, in the comprehensive scan. Note that the inequalities in eq. (5.65) and (5.66) are imposed as well, as is explained in the main text.

explained at $3\,\sigma$. In the case of $|a_{33}|$, the union of the ranges separately extracted from the sample points explaining $R(D^{(\star)})$ at $3\,\sigma$ and those explaining Δa_μ at $3\,\sigma$ is displayed. Still, an efficient accommodation of the constraints arising from $\mathrm{BR}(\tau \to \mu\gamma)$ and $\mathrm{BR}(\mu \to e\gamma)$ requires further imposing the inequalities in eqs. (5.65) and (5.66). Note that the bound on $\mathrm{BR}(\tau \to \mu\gamma)$ controls whether a sample point will explain $R(D^{(\star)})$, for which $|a_{33}|$ needs to be rather large, or Δa_μ, for which $|b_{23}|$ must be rather large.

As they are extracted from the primary scan, the biases are expressed in the charged fermion mass basis. Still, the given ranges are utilised to sample $\hat{a}_{33}$, $\hat{b}_{32}$ and $\hat{b}_{23}$ in the interaction basis, since these coefficients constitute the only contribution to the respective parameters in the charged fermion mass basis at LO in λ; see eqs. (5.145) and (5.147). Nonetheless, since the complete relations between the LQ coupling parameters in the interaction basis and the mass basis are used, the ranges of the resulting coefficients in the latter may not strictly adhere to the ranges laid out in table 5.6 in the sampling for the comprehensive scan.

Note that sample points with $|a_{23}|$ being as large as $1/\lambda$ which respect all imposed constraints are found in the comprehensive scan for all considered LQ masses, and thus eq. (5.66) implies that $|b_{13}|$ may be pushed outside the default range $[\lambda, 1/\lambda]$.[15] The

---

[15] On the contrary, the biases for $|a_{33}|$ are compatible with maintaining the range $[\lambda, 1/\lambda]$ for $|b_{23}|$ to a good degree. This is in agreement with the model since $|b_{23}| = |\hat{b}_{23}|$ at LO

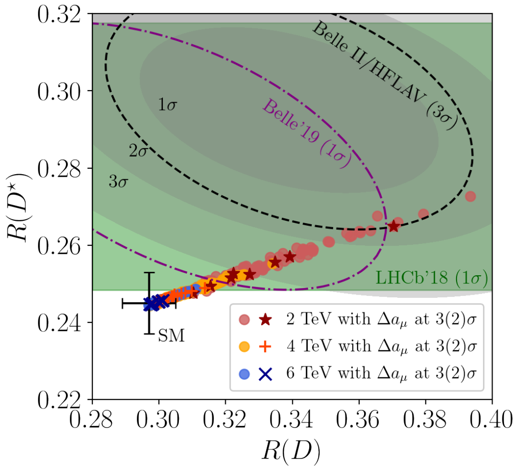

Figure 5.7: **Illustration of the capability of the model to simultaneously explain the anomalies in $R(D)$, $R(D^\star)$ and Δa_μ in the comprehensive scan.** The sample points shown as light-coloured dot points (dark-coloured points with specific shapes) respect the experimental bounds from primary constraints and explain Δa_μ within the $3\,\sigma$ ($2\,\sigma$) range about the present best-fit value. Apart from that, the plot is to be read in the same way as the right plot in figure 5.2.

model can accommodate this in a somewhat accidental manner, since the effective parameter b_{13} picks up an additional contribution from the adoption of the charged fermion mass basis, that is,[16]

$$b_{13} = \hat{b}_{13} - \hat{b}_{23}\frac{e_{21}}{e_{22}} + \mathcal{O}(\lambda^2)\,. \tag{5.67}$$

Indeed, values as small as $|b_{13}| \approx 0.004 \sim \lambda^4$ are obtained in the comprehensive scan. Importantly, as per eq. (5.64), this implies that larger results for Δa_μ are attainable than suggested by the primary scan where $|b_{13}| > \lambda$ was enforced.

Overall, I observe that the biases imposed in the comprehensive scan help establish the fact that the model under consideration respects all primary constraints and can explain the anomalous data in $R(D)$, $R(D^\star)$ and Δa_μ at the level of $3\,\sigma$ for $\hat{m}_\phi = 2$ and 4. Furthermore, even a sample point for which all anomalies are simultaneously explained at $2\,\sigma$ was identified in the case of $\hat{m}_\phi = 2$; see figure 5.7.

Apart from the conventions employed for figure 5.7 as is explained in the caption therein

---

in λ; see eq. (5.147).

[16] The parameter e_{22} is directly determined from the fact that it constitutes the LO contribution to the muon mass in the model. Still, since lepton mixing is unphysical, the parameter e_{21} is only indirectly constrained from the diagonalisation of the charged lepton mass matrix in eq. (5.24). Indeed, the fit to charged fermion masses and quark mixing seems to prefer the ratio $|e_{21}/e_{22}|$ to take values roughly between 1 and 4.5 and thus cannot bar cancellations among both LO contributions to b_{13}.

as well as in section 5.4.1.2, a simultaneous explanation of the anomalies at $3\,\sigma$ or better is achieved in the comprehensive scan only for the white crosses displayed in the plots. In fact, *all* of these have $|b_{13}| < \lambda$. If solely Δa_μ is considered, an accommodation of the anomaly requires $|b_{13}| < \lambda$ only for $\hat{m}_\phi = 2$, whereas $|b_{13}|$ can be larger for $\hat{m}_\phi = 4, 6$. This is the only instance in which experimental data favours the LO contribution to a LQ coupling to be suppressed by more powers of λ than anticipated in the construction of the model.

Lastly, I remark that in the comprehensive scan, a simultaneous explanation of the anomalies together typically, albeit not necessarily implied a signal in $\tau \to \mu\gamma$ at Belle II and/or in $\mu \to e\gamma$ at MEG II.

5.4.5 $R^\nu_{K^{(*)}}$

The effective Lagrangian for neutral-current semi-leptonic $b \to s\nu\bar{\nu}$ transitions reads

$$\mathcal{L} \supset C^{VLL}_{\nu q,ij23}(\bar{\nu}_i\gamma^\mu P_L\nu_j)(\bar{s}\gamma_\mu P_L b) + C^{VLR}_{\nu q,ij23}(\bar{\nu}_i\gamma^\mu P_L\nu_j)(\bar{s}\gamma_\mu P_R b) + \text{h.c.}\,. \tag{5.68}$$

In the SM, contributions to $C^{VLL}_{\nu q,ij23}$ are generated at the level of one loop through penguin and box diagrams, whereas $C^{VLR}_{\nu q,ij23}$ is sourced only at higher order. In addition, ϕ induces tree-level corrections to $C^{VLL}_{\nu q,ij23}$, but not to $C^{VLR}_{\nu q,ij23}$, so I henceforth disregard the influence of the latter. Tree-level matching yields

$$C^{VLL}_{\nu d,ij23} = \frac{x_{j3}x^*_{i2}}{2m^2_\phi}\,. \tag{5.69}$$

Unlike in the SM, the flavours of the neutrino and antineutrino in the final state do not have to match in the model under consideration. The BR for the decay $B \to K^{(\star)}\nu\bar{\nu}$ is normalised with respect to the SM prediction in the ratio $R^\nu_{K^{(\star)}}$. In accordance with ref. [76], I write

$$R^\nu_{K^{(\star)}} = \frac{1}{3}\sum_{\alpha,\beta=1}^{3}\left|\delta_{\alpha\beta} + \frac{C^{VLL}_{\nu d,\alpha\beta 23}}{C^{VLL}_{\nu d,23,\text{SM}}}\right|^2\,. \tag{5.70}$$

Here, the value $C^{VLL}_{\nu d,23,\text{SM}} \approx (1.01 - 0.02i)\frac{10^{-2}}{\text{TeV}^2}$ is used which is output by `flavio`, v2.3, see also ref. [303], at the scale $\mu = \mu_B$ and re-expressed in the JMS basis. The absence of sizeable contributions to RH vector currents furthermore implies $R^{\nu}_{K} \approx R^{\nu}_{K^{\star}}$, therefore I only employ the current bound $R^{\nu}_{K^{\star}} < 2.7$ at 90% CL [24] in the following as it is the more stringent one.

If the flavours of the neutrino and antineutrino in the final state coincide, interference with the SM contribution occurs. The interaction structure of the model implies that one obtains the largest NP contribution for a tau neutrino-antineutrino pair $\nu_\tau\overline{\nu}_\tau$ (top line below), whereas the case of a muon neutrino-antineutrino pair $\nu_\mu\overline{\nu}_\mu$ (middle line below) will also prove non-negligible. Lastly, I also provide the LO LFV combinations $\nu_\tau\overline{\nu}_\mu$ and $\nu_\mu\overline{\nu}_\tau$ (bottom line below), respectively:

$$\begin{aligned} R^{\nu}_{K^{(\star)}} \approx{}& 1 + 1.69\frac{|a_{33}a_{32}|}{\hat{m}_\phi^2}\cos\left(\mathrm{Arg}(a_{33}) - \mathrm{Arg}(a_{32})\right) + 2.15\frac{|a_{33}a_{32}|^2}{\hat{m}_\phi^4} \\ &+ 0.09\frac{|a_{23}a_{22}|}{\hat{m}_\phi^2}\cos\left(\mathrm{Arg}(a_{23}) - \mathrm{Arg}(a_{22})\right) + 0.01\frac{|a_{23}a_{22}|^2}{\hat{m}_\phi^4} \\ &+ 0.11\left(\frac{|a_{23}a_{32}|^2}{\hat{m}_\phi^4} + \frac{|a_{33}a_{22}|^2}{\hat{m}_\phi^4}\right) . \end{aligned} \tag{5.71}$$

Consequently, one may approximate $R^{\nu}_{K^{(\star)}}$ as a quadratic function in $|a_{33}|$ to LO, in a vein similar to $R(D)/R(D)_{\mathrm{SM}}$ and $R(D^\star)/R(D^\star)_{\mathrm{SM}}$ in eqs. (5.50) and (5.51), respectively. In this way, the constraint on $\mathrm{BR}(\tau \to \mu\gamma) \propto |a_{33}b_{23}|^2$ correlates $R^{\nu}_{K^{(\star)}}$ with $\Delta a_\mu \propto |b_{23}|$, and the LO contribution is expected to effectively compete with an explanation of the anomaly in Δa_μ. This is confirmed by the results of the primary scan, and further substantiated by the comprehensive scan for the larger benchmark masses $\hat{m}_\phi = 4, 6$, as can be seen in figure 5.8. The correlation is less strict for $\hat{m}_\phi = 2$ where subleading contributions, including LFV ones, become more relevant. In order to saturate the current bound, $|a_{33}|$ needs to be (almost) as large as allowed by the biasing for $\hat{m}_\phi = 4, 6$, whereas it can be smaller for $\hat{m}_\phi = 2$; see table 5.6 and the bottom-left plot in figure 5.9.

There are two effective LQ coupling parameters which receive an additional contribution from the adoption of the charged fermion mass basis, respectively, and play a major role in shaping the results for $R^{\nu}_{K^{(\star)}}$ in the comprehensive scan. Firstly, the coupling of a tau neutrino ν_τ to a strange quark s is given by $x_{32} = a_{32}\lambda^2$ where

$$a_{32} = \hat{a}_{32} - \hat{a}_{33}\frac{d_{23}}{d_{33}} + \mathcal{O}(\lambda^2) \tag{5.72}$$

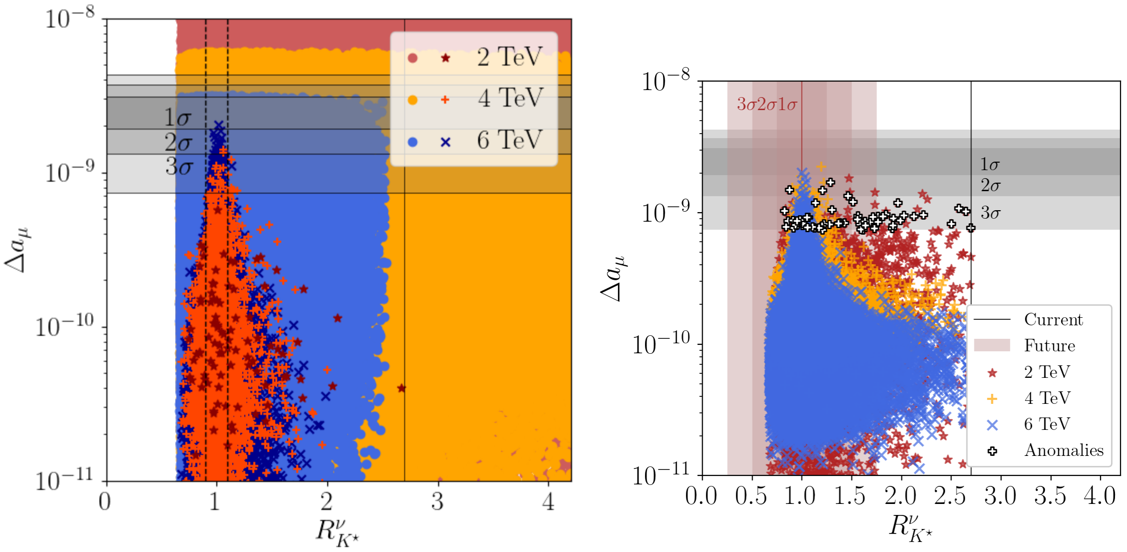

Figure 5.8: **Constraining power and future reach of $R^\nu_{K^\star}$. Left:** Results from primary scan. The vertical solid line indicates (dashed lines indicate) the region compatible with the current experimental bound on (future reach of) $R^\nu_{K^\star}$ [7, 24]; see also table 5.4. For the future reach, a SM-like result and an uncertainty of 10% is assumed. The round points (geometric shapes) indicate that current experimental bounds are violated (respected); see also the main text of section 5.4.1.1. **Right:** Results from comprehensive scan. The shown sample points respect the experimental bounds from primary constraints; see also section 5.4.1.2. The red-brown shaded regions indicate the projected reach for $R^\nu_{K^\star}$ at Belle II for 5 ab^{-1} of data, again under the assumption that the best-fit value is SM-like.

and secondly, the coupling of a muon neutrino ν_μ to a strange quark s is given by $x_{22} = a_{22}\lambda^3$ where

$$a_{22} = \hat{a}_{22} - \left(\hat{a}_{23} - \hat{a}_{23}\frac{e_{23}}{e_{33}}\right)\frac{d_{23}}{d_{33}} - \hat{a}_{32}\frac{e_{23}}{e_{33}} + \mathcal{O}(\lambda^2)\,. \tag{5.73}$$

Indeed, $\mathcal{O}(10)$ results are possible in the comprehensive scan for both $|a_{22}|$ and $|a_{32}|$, which again cannot be fully accounted for in the primary scan due to the imposed range $[\lambda, 1/\lambda]$; see the top panel in figure 5.9.

Since larger values can be generated for $|a_{32}|$, the LO contribution to $R^\nu_{K^{(\star)}}$ from ϕ which is proportional to $|a_{33}a_{32}|$ and interferes with the SM may be further enhanced. The fact that sample points which respect all experimental constraints and for which $|a_{23}|$ can be as large as $1/\lambda$ can be accessed in the comprehensive scan implies that substantial contributions to $R^\nu_{K^\star}$ via the LFV channel with the combination $\nu_\tau\bar{\nu}_\mu$ which is governed by $|a_{23}a_{32}|$ are attainable. The same holds for the contribution involving the combination

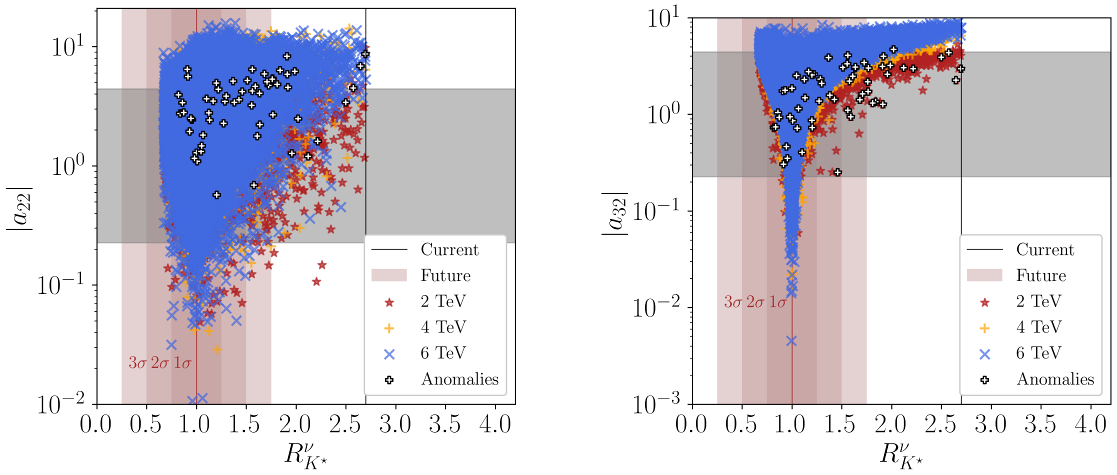

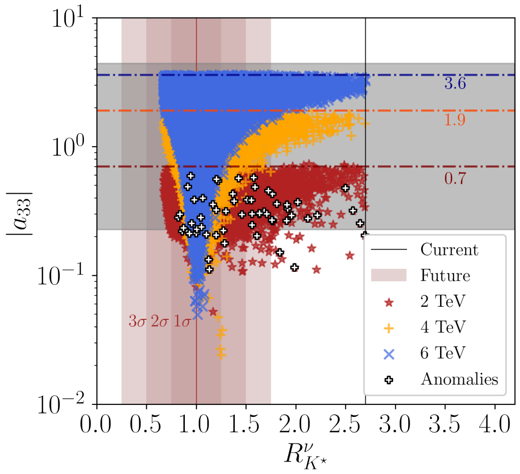

Figure 5.9: **Results for $R^{\nu}_{K^{(\star)}}$ as a function of the magnitudes of several effective parameters in the comprehensive scan.** The shown sample points respect the experimental bounds from primary constraints; see also section 5.4.1.2. The red-brown shaded regions indicate the projected reach for $R^{\nu}_{K^{\star}}$ at Belle II for 5 ab^{-1} of data under the assumption that the best-fit value is SM-like. For the bottom-left plot, the dot-dashed lines correspond to the respective upper limit on $|a_{33}|$ for each LQ mass as given in table 5.6, in dark red (orange) [dark blue] for $\hat{m}_{\phi} = 2(4)[6]$.

$\nu_{\mu}\overline{\nu}_{\mu}$ driven by $|a_{23}a_{22}|$ which interferes with the SM. Note that since the biases on $|a_{33}|$ force this parameter to be smaller than $1/\lambda$, a similarly large contribution to the final-state combination $\nu_{\mu}\overline{\nu}_{\tau}$ governed by $|a_{33}a_{22}|$ is not expected.

Still, despite the imposed (moderate) suppression of $|a_{33}|$, large attainable magnitudes of a_{22} and a_{32} result in the fact that the model can generate contributions which exceed the current experimental bound on $R^{\nu}_{K^{\star}}$. This is in stark contrast with the primary scan where the restriction to the range $[\lambda, 1/\lambda]$ in particular implied that this bound could *a priori* not be reached for $\hat{m}_{\phi} = 6$, irrespective of whether other experimental constraints are imposed or not. Notwithstanding, the comprehensive scan demonstrates that $R^{\nu}_{K^{(\star)}}$ genuinely takes part in shaping the viable model parameter space for all LQ masses, which is not obvious from the results of the primary scan either.

Overall, this suggests that if the expected measurement of $B \to K^{(\star)}$ + invisible at Belle II [7] does not reveal a substantial deviation from the SM expectation, the model would be in the best position to explain the anomaly in Δa_μ. Still, even if there was a large excess in $R^\nu_{K^{(\star)}}$, the anomalous data in Δa_μ could still be accounted for if the LQ is sufficiently light, that is, for $\hat{m}_\phi = 2$.

5.4.6 $\mu - e$ Conversion in Aluminium

For the description of $\mu - e$ conversion in nuclei one needs the effective Lagrangian for neutral-current semi-leptonic interactions

$$\begin{aligned}\mathcal{L} \supset\ & C^{VLL}_{eq,ijkl}(\overline{e}_i\gamma^\mu P_L e_j)(\overline{q}_k\gamma_\mu P_L q_l) + C^{VRR}_{eq,ijkl}(\overline{e}_i\gamma^\mu P_R e_j)(\overline{q}_k\gamma_\mu P_R q_l)\\ &+ C^{VLR}_{eq,ijkl}(\overline{e}_i\gamma^\mu P_L e_j)(\overline{q}_k\gamma_\mu P_R q_l) + C^{VLR}_{qe,ijkl}(\overline{q}_i\gamma_\mu P_L q_j)(\overline{e}_k\gamma^\mu P_R e_l)\\ &+ \Big[C^{SRR}_{eq,ijkl}(\overline{e}_i P_R e_j)(\overline{q}_k P_R q_l) + C^{SRL}_{eq,ijkl}(\overline{e}_i P_R e_j)(\overline{q}_k P_L q_l)\\ &+ C^{TRR}_{eq,ijkl}(\overline{e}_i\sigma^{\mu\nu} P_R e_j)(\overline{q}_k\sigma_{\mu\nu} P_R q_l) + \text{h.c.}\Big]\,.\end{aligned} \tag{5.74}$$

Integrating out ϕ, one obtains

$$C^{VLL}_{eu,ijkl} = \frac{z_{jl}z^*_{ik}}{2m^2_\phi}\,,\quad C^{VRR}_{eu,ijkl} = \frac{y_{ik}y^*_{jl}}{2m^2_\phi}\,,\quad C^{SRR}_{eu,ijkl} = \frac{z^*_{ik}y_{jl}}{2m^2_\phi}\,,\quad C^{TRR}_{eu,ijkl} = -\frac{1}{4}\frac{z^*_{ik}y_{jl}}{2m^2_\phi} \tag{5.75}$$

via tree-level matching. The full expression for the conversion rate reads [277]

$$\begin{aligned}\omega_{\text{conv}} =\ & \left|-\frac{C_{e\gamma,12}}{2m_\mu}D + \tilde{g}^{(p)}_{LS}S^{(p)} + \tilde{g}^{(p)}_{LV}V^{(p)} + (p\to n)\right|^2\\ &+ \left|-\frac{C^*_{e\gamma,21}}{2m_\mu}D + \tilde{g}^{(p)}_{RS}S^{(p)} + \tilde{g}^{(p)}_{RV}V^{(p)} + (p\to n)\right|^2\end{aligned} \tag{5.76}$$

with the effective coupling constants $g^{(N)}_X$ for $N \in (p, n)$ and $X \in (LS, LV, RS, RV)$ given in appendix 5.12 and the nuclear overlap integrals D, $S^{(N)}$ and $V^{(N)}$ taken from ref. [277]. In the model under consideration, the dominant contributions are again due to the dipole operator which is induced at the level of one loop. Tree-level contributions from scalar operators have a subdominant effect, while the remaining contributions can be neglected:

$$\begin{aligned}\omega_{\text{conv}} &\approx \left|-\frac{C^{12}_{e\gamma}}{2m_\mu}D\right|^2 + \left|-\frac{C^{21*}_{e\gamma}}{2m_\mu}D + \tilde{g}^{(p)}_{RS}S^{(p)} + \tilde{g}^{(n)}_{RS}S^{(n)}\right|^2 \\ &\approx \frac{D^2}{4m_\mu^2}\frac{e^2\,m_t^2}{64^2\pi^4 m_\phi^4}(7+4\ln t_t)^2|z_{13}y_{23}|^2 \\ &\quad + \Bigg| - \frac{D}{2m_\mu}\frac{e\,m_t}{64\pi^2 m_\phi^2}(7+4\ln t_t)z_{23}y^*_{13} \\ &\qquad + \left(G^{u,p}_S S^{(p)} + G^{u,n}_S S^{(n)}\right)\frac{z_{21}y^*_{11}}{2m_\phi^2}\Bigg|^2\end{aligned} \tag{5.77}$$

Numerically, one has $G^{u,p}_S = 5.1$, $G^{u,n}_S = 4.3$ [401] and $D = 0.0362m_\mu^{5/2}$, $S^{(p)} = 0.0155m_\mu^{5/2}$ and $S^{(n)} = 0.0167m_\mu^{5/2}$ for aluminium [277]. Furthermore, the muon capture rate in aluminium is given by $\omega_{\text{capt}} = 0.7054 \times 10^6\,\text{s}^{-1}$ [277]. After normalising the conversion rate to the capture rate in the conversion ratio (CR) given by $\omega_{\text{conv}}/\omega_{\text{capt}}$ which is the quantity typically reported by experimental collaborations, I approximately find

$$\text{CR}(\mu\to e;\text{Al}) \approx 2.243\left(0.003\frac{|c_{13}b_{23}|^2}{\hat{m}_\phi^4} + \left|\frac{c_{23}b^*_{13}}{\hat{m}_\phi^2} + 0.003\frac{c_{21}b^*_{11}}{\hat{m}_\phi^2}\right|^2\right) \times 10^{-13}\,. \tag{5.78}$$

The dominant contribution from the dipole-operator WC $C^{21}_{e\gamma} \propto c^*_{23}b_{13}$ is constrained by the non-observation of $\mu \to e\gamma$. Neglecting all other contributions, I find

$$\text{CR}(\mu\to e;\text{Al}) \approx \underbrace{\pi\frac{\Gamma_\mu D^2}{\omega_{\text{capt}}m_\mu^5}}_{\approx 0.0027}\,\text{BR}(\mu\to e\gamma) \tag{5.79}$$

and thus a very stringent correlation between the two rates. In this case, the plots in the top panel in figure 5.10 would simply feature a straight line in the centre of the coloured region, respectively. Subdominant contributions, mostly due to scalar operators as elaborated on above, can result in a deviation from the photon-penguin approximation by a factor 2 or 3, while further outliers are incompatible with the considered constraints. Still, the future search for $\mu - e$ conversion in aluminium can be expected to complement the one for $\mu \to 3\,e$, as can be directly compared in the top-right plot in figure 5.10. COMET [25] and Mu2e [26] are projected to efficiently probe the scenario of the model explaining Δa_μ, see the bottom-left plot in figure 5.10, and to generally provide an excellent test for the cLFV $\mu \to e$ transition, superseding the currently more stringent bound on

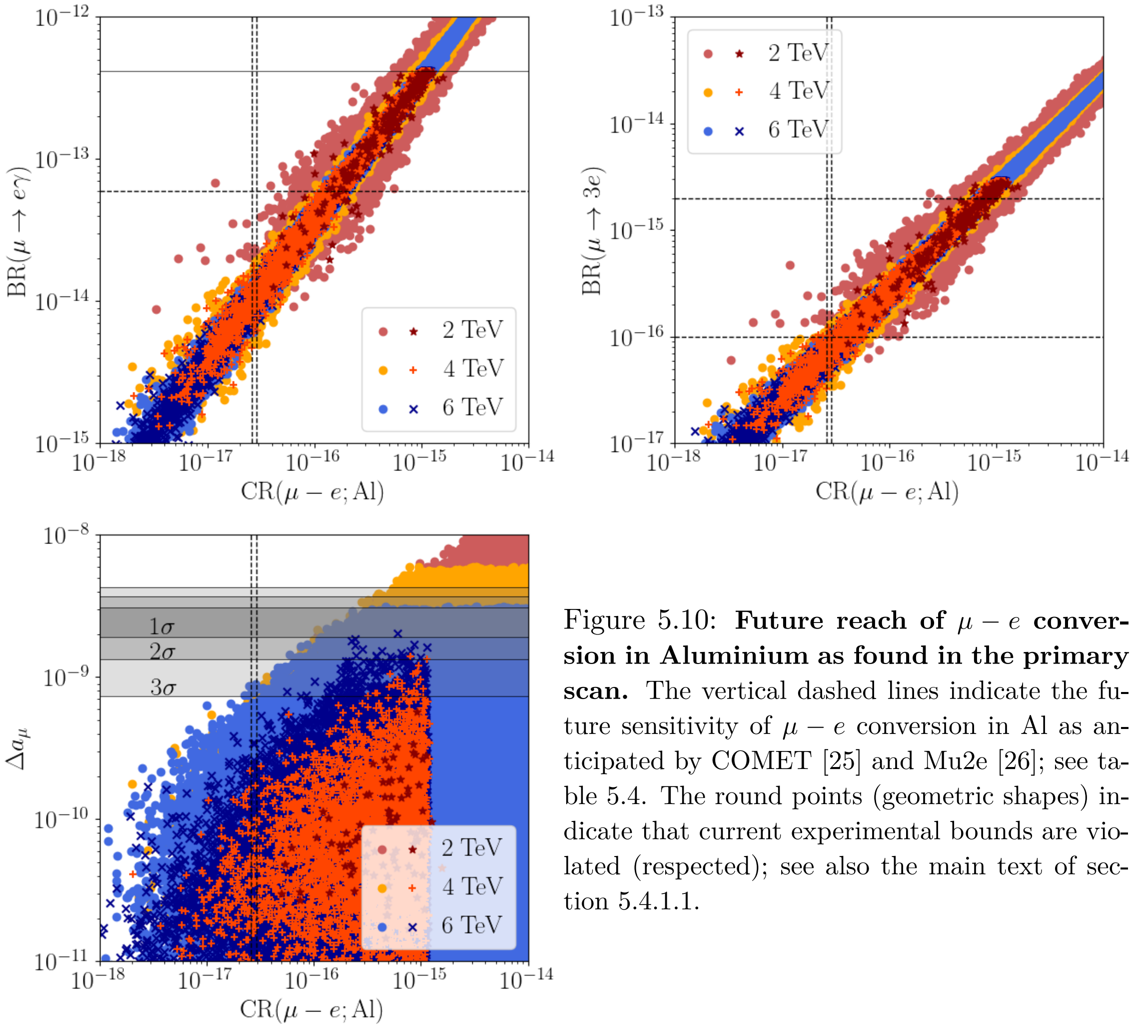

Figure 5.10: **Future reach of $\mu - e$ conversion in Aluminium as found in the primary scan.** The vertical dashed lines indicate the future sensitivity of $\mu - e$ conversion in Al as anticipated by COMET [25] and Mu2e [26]; see table 5.4. The round points (geometric shapes) indicate that current experimental bounds are violated (respected); see also the main text of section 5.4.1.1.

$\mathrm{BR}(\mu \to e\gamma)$.[17] Indeed, *all* the sample points found in the comprehensive scan which simultaneously explain the anomalies in $R(D)$, $R(D^\star)$ and Δa_μ fall above the projected sensitivity of either experiment; see the bottom plot in figure 5.14 further below.

---

[17] One might note that, relatively independently of the target nucleus, the model can generate $\mathcal{O}(10^{-13})$ contributions to the respective $\mu - e$ CRs for $\hat{m}_\phi = 4$ and 6, and $\mathcal{O}(10^{-12})$ contributions for $\hat{m}_\phi = 2$, which are however ruled out due to the stringent bound on and the strong correlation with $\mathrm{BR}(\mu \to e\gamma)$ in this regime. Thus, the current experimental bounds $\mathrm{CR}(\mu \to e;\ \mathrm{Ti[Au]\{Pb\}})_{\mathrm{exp}} < 0.061[0.070]\{4.6\} \times 10^{-11}$ [402–404] do not impose relevant constraints on the model. In addition, the reach of future searches for $\mu - e$ conversion in aluminium [25, 26] is projected to be three to four orders of magnitude better than for carbon targets [405].

5.4.7 Trilepton Decays

In order to describe decays with one lepton in the initial state and three leptons in the final state, one needs the relevant effective Lagrangian

$$\begin{aligned}\mathcal{L} \supset\, & C^{VLL}_{ee,ijkl}(\bar{e}_i\gamma^\mu P_L e_j)(\bar{e}_k\gamma_\mu P_L e_l) + C^{VRR}_{ee,ijkl}(\bar{e}_i\gamma^\mu P_R e_j)(\bar{e}_k\gamma_\mu P_R e_l) \\ & + C^{VLR}_{ee,ijkl}(\bar{e}_i\gamma^\mu P_L e_j)(\bar{e}_k\gamma_\mu P_R e_l) + \left[C^{SRR}_{ee,ijkl}(\bar{e}_i P_R e_j)(\bar{e}_k P_R e_l) + \text{h.c.}\right] \,.\end{aligned} \tag{5.80}$$

Note that not all of the WCs contained in the sums above are independent. In the following, I will consider two different cases. If the flavours of all the final-state leptons match, the BR reads [406]

$$\begin{aligned}\text{BR}(e_i \to e_j e_j \bar{e}_j) = \frac{m_{e_i}^5}{3(16\pi)^3\Gamma_{e_i}} \Bigg[& 64\left|C^{VLL}_{ee,jijj}\right|^2 + 64\left|C^{VRR}_{ee,jijj}\right|^2 + 8\left|C^{VLR}_{ee,jijj}\right|^2 + 8\left|C^{VLR}_{ee,jjji}\right|^2 \\ & + \frac{256e^2}{m_{e_i}^2}\left(\ln\frac{m_{e_i}^2}{m_{e_j}^2} - \frac{11}{4}\right)\left(|C^{ji}_{e\gamma}|^2 + |C^{ij}_{e\gamma}|^2\right) \\ & - \frac{64e}{m_{e_i}}\text{Re}\left[\left(4C^{VLL}_{ee,jijj} + C^{VLR}_{ee,jijj}\right)C^{ji*}_{e\gamma} + \left(4C^{VRR}_{ee,jijj} + C^{VLR}_{ee,jjji}\right)C^{ij}_{e\gamma}\right]\Bigg] \,.\end{aligned} \tag{5.81}$$

If there is a lepton-antilepton pair in the final state of which the flavour is different from the one of the third lepton, the BR reads

$$\begin{aligned}\text{BR}(e_i \to e_j e_k \bar{e}_k) = \frac{m_{e_i}^5}{3(16\pi)^3\Gamma_{e_i}} \Bigg[& 128\left|C^{VLL}_{ee,jikk}\right|^2 + 128\left|C^{VRR}_{ee,jikk}\right|^2 + 8\left|C^{VLR}_{ee,jikk}\right|^2 + 8\left|C^{VLR}_{ee,kkji}\right|^2 \\ & + \frac{256e^2}{m_{e_i}^2}\left(\ln\frac{m_{e_i}^2}{m_{e_j}^2} - 3\right)\left(|C^{ji}_{e\gamma}|^2 + |C^{ij}_{e\gamma}|^2\right) \\ & - \frac{64e}{m_{e_i}}\text{Re}\left[\left(4C^{VLL}_{ee,jikk} + C^{VLR}_{ee,jikk}\right)C^{ji*}_{e\gamma} + \left(4C^{VRR}_{ee,jikk} + C^{VLR}_{ee,kkji}\right)C^{ij}_{e\gamma}\right]\Bigg] \,.\end{aligned} \tag{5.82}$$

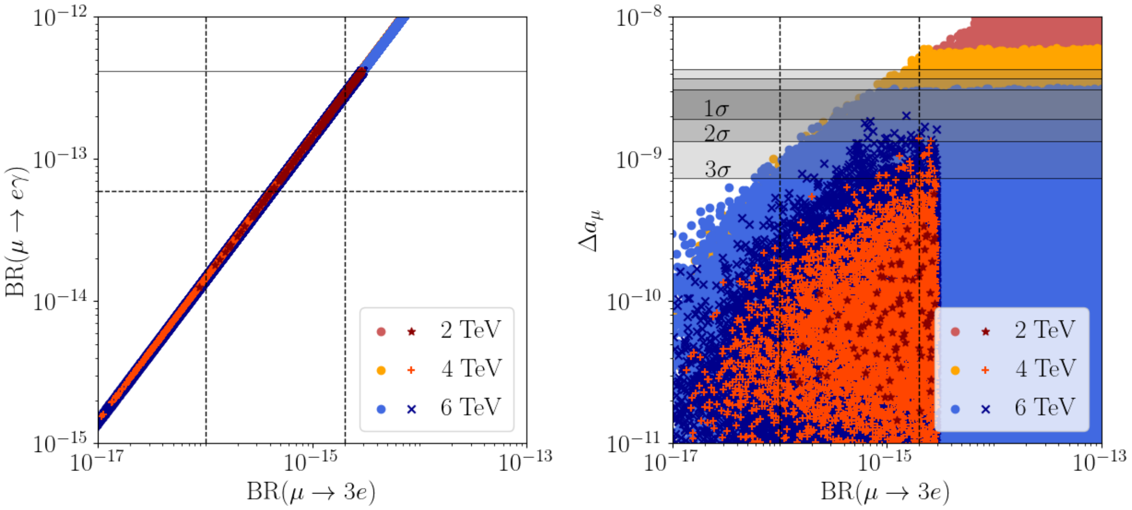

Figure 5.11: **Constraining power and future reach of $\mu \to 3e$ as found in the primary scan.** The vertical dashed lines indicate the respective projected reach of the phase-1 and phase-2 runs of the future search for $\mu \to 3e$ [27]; see table 5.4. The round points (geometric shapes) indicate that current experimental bounds are violated (respected); see also the main text of section 5.4.1.1.

5.4.7.1 $\mu \to 3e$

In the model under consideration, the decay mode $\mu \to 3e$ is entirely dominated by contributions to the dipole operator. Indeed, one finds

$$\begin{aligned} \mathrm{BR}(\mu \to 3e) &\approx \frac{e^2 m_\mu^3}{48\pi^3 \Gamma_\mu} \left(\ln \frac{m_\mu^2}{m_e^2} - \frac{11}{4} \right) \left| C_{e\gamma}^{21} \right|^2 \\ &\approx \frac{e^2}{12\pi^2} \frac{e^2 m_t^2 m_\mu^3}{128^2 \pi^5 \Gamma_\mu m_\phi^4} \left(\ln \frac{m_\mu^2}{m_e^2} - \frac{11}{4} \right) \left| z_{23} y_{13} \right|^2 \\ &\approx \frac{6}{\hat{m}_\phi^4} |c_{23} b_{13}|^2 \times 10^{-13} \, . \end{aligned} \tag{5.83}$$

Furthermore, this implies that the BR is strictly correlated with the one for $\mu \to e\gamma$, and a comparison with eq. (5.62) yields

$$\mathrm{BR}(\mu \to 3e) \approx \underbrace{\frac{e^2}{12\pi^2} \left(\ln \frac{m_\mu^2}{m_e^2} - \frac{11}{4} \right)}_{\approx 0.0069} \mathrm{BR}(\mu \to e\gamma) \, . \tag{5.84}$$

These expectations are confirmed by the results from the primary scan, as can be seen in the left plot in figure 5.11, and from the comprehensive scan. In addition, the right plot illustrates that the future search for $\mu \to 3e$ at Mu3e [27] can be expected to probe a substantial portion of the parameter space which is currently viable, and might challenge the scenario of the model explaining Δa_μ.

5.4.7.2 $\tau \to 3\mu$

Unlike $\mu \to 3e$, the decay channel $\tau \to 3\mu$ is not only sensitive to the dipole operator, but contributions from Z-penguin diagrams with two top-quark mass insertions can also be important. I find

$$\begin{aligned}
\mathrm{BR}(\tau \to 3\mu) &\approx \frac{m_\tau^5}{3(16\pi)^3\Gamma_\tau}\Bigg[64\left|C^{VLL}_{ee,2322}\right|^2 + 8\left|C^{VLR}_{ee,2322}\right|^2 \\
&\qquad + \frac{256e^2}{m_\tau^2}\left(\ln\frac{m_\tau^2}{m_\mu^2} - \frac{11}{4}\right)\left|C^{21}_{e\gamma}\right|^2\Bigg] \\
&\approx \frac{1}{64\pi^4}\frac{m_t^2 m_\tau^3}{3(16\pi)^3\Gamma_\tau}\Bigg[4\,e^4(7+4\ln t_t)^2\left(\ln\frac{m_\tau^2}{m_\mu^2} - \frac{11}{4}\right)\frac{|y_{23}z_{33}|^2}{m_\phi^4} \\
&\qquad + 72\,G_F^2 m_t^2 m_\tau^2(1+\ln t_t)^2\big((1-2s_W^2)^2 + 2s_W^4\big)\frac{|z_{23}z_{33}|^2}{m_\phi^4}\Bigg] \\
&\approx 1.46\times 10^{-7}\frac{|b_{23}c_{33}|^2 + 0.07|c_{23}c_{33}|^2}{\hat{m}_\phi^4}\,.
\end{aligned} \tag{5.85}$$

Instead, in the limit of exact photon-penguin dominance one finds [273, 274]

$$\mathrm{BR}(\tau \to 3\mu) \approx \underbrace{\frac{e^2}{12\pi^2}\left(\ln\left(\frac{m_\tau^2}{m_\mu^2}\right) - \frac{11}{4}\right)}_{\approx 0.0025}\mathrm{BR}(\tau \to \mu\gamma) \tag{5.86}$$

which would imply that an observation of $\tau \to 3\mu$ at Belle II is not possible due to the experimental constraint on $\mathrm{BR}(\tau \to \mu\gamma)$. This case corresponds to the upper edge of the coloured region in the left plot of figure 5.12. Still, with the presence of Z-penguin contributions taken into account, the search for $\tau \to 3\mu$ at Belle II [7] will be sensitive to a portion of the parameter space which is currently viable. As can be seen in the right plot in figure 5.12, this is also the case for $\hat{m}_\phi = 2$.

The hierarchy $|c_{23}| \approx |a_{23}| \gg |b_{23}|$ required for large Z-penguin contributions tends to suppress the product of the two coupling magnitudes and thus the result for Δa_μ, the latter

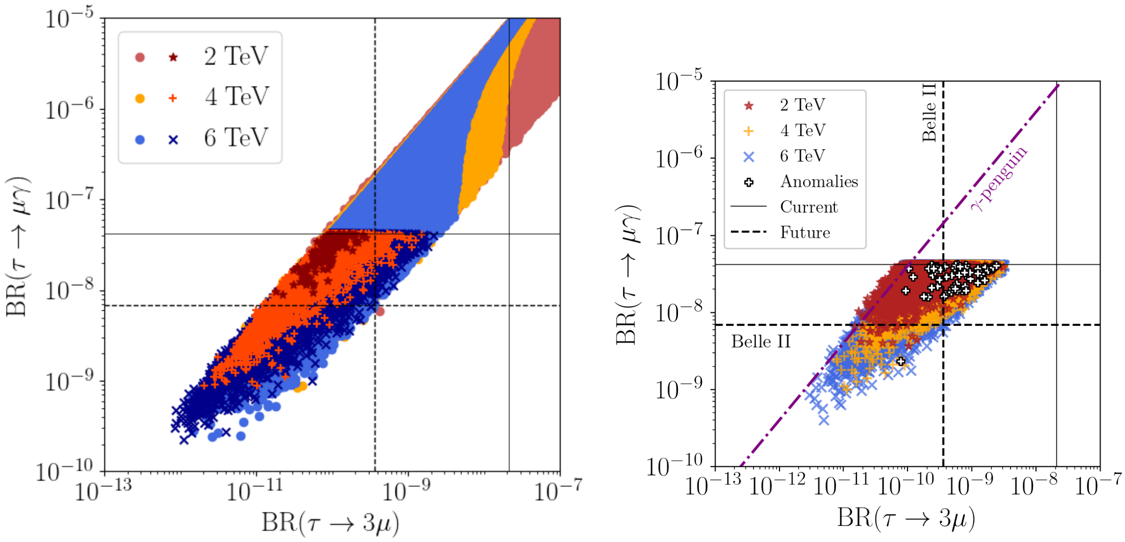

Figure 5.12: **Constraining power and future reach of $\tau \to 3\mu$ in relation with $\tau \to \mu\gamma$.** **Left:** Results from primary scan. The vertical solid (dashed) lines indicate the current bound on (future sensitivity of) $\tau \to 3\mu$ [7, 28]; see table 5.4. The round points (geometric shapes) indicate that current experimental bounds are violated (respected); see also the main text of section 5.4.1.1. **Right:** Results from comprehensive scan. The shown sample points respect the experimental bounds from primary constraints; see also section 5.4.1.2. The purple dot-dashed line (labelled "γ-penguin") illustrates the approximate correlation between $\tau \to 3\mu$ and $\tau \to \mu\gamma$ in the limit of photon-penguin dominance as given in eq. (5.86).

particularly efficiently in the case of $\hat{m}_\phi = 6$; see eqs. (5.59) and (5.85). As a consequence, observing $\tau \to 3\mu$ at Belle II would indicate that an explanation of $\Delta a_\mu \propto |b_{23}|$ is very unlikely for $\hat{m}_\phi = 6$ and, due to the increased sensitivity to the constraint on BR($\tau \to \mu\gamma$), also for $\hat{m}_\phi = 4$; see figure 5.13. For these two masses, conversely, the largest contributions to Δa_μ are generated if BR($\tau \to 3\mu$) remains below the prospected sensitivity. In turn, for $\hat{m}_\phi = 2$, the ratio $|b_{23}/c_{23}|$ being small in the regime of large Z-penguin contributions does not efficiently suppress the results for Δa_μ.

The inequality in eq. (5.65) imposed in the comprehensive scan implies that the photon-penguin contributions to $\tau \to 3\mu$ are generally smaller than in the primary scan. Indeed, since a simultaneous explanation of the anomalies in $R(D)$, $R(D^\star)$ and Δa_μ hinges on an efficient accommodation of the experimental bound on BR($\tau \to \mu\gamma$), it is often accompanied by a signal in $\tau \to 3\mu$ at Belle II as is visible in the plots illustrating the results from the comprehensive scan.

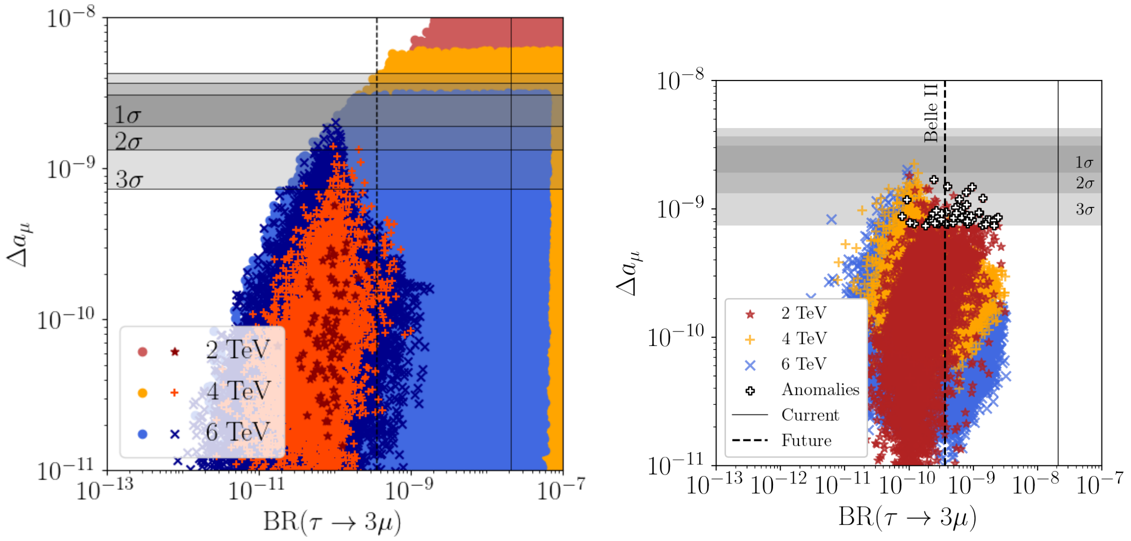

Figure 5.13: **Constraining power and future reach of $\tau \to 3\mu$ in relation with Δa_μ. Left:** Results from primary scan. The vertical solid (dashed) lines indicate the current bound on (future sensitivity of) $\tau \to 3\mu$ [7, 28]; see table 5.4. The round points (geometric shapes) indicate that current experimental bounds are violated (respected); see also the main text of section 5.4.1.1. **Right:** Results from comprehensive scan. The shown sample points respect the experimental bounds from primary constraints; see also section 5.4.1.2.

In the model, an observation of $\tau \to 3\mu$ effectively enforces an observation of $\tau \to \mu\gamma$, but the reverse case is not true in general. Furthermore, the plots in the top panel of figure 5.14 seem to suggest that a result $\mathrm{BR}(\tau \to 3\mu) \gtrsim \mathcal{O}(10^{-10})$ becomes increasingly disfavoured if the contributions to cLFV $\mu \to e$ transitions shrink. Since by construction $|b_{13}| > \lambda$ in the primary scan, this shrinkage mainly relies on a small $|c_{23}| \approx |a_{23}|$, see eqs. (5.62), (5.78) and (5.83), and so the Z-penguin contributions to $\tau \to 3\mu$ become more suppressed. Hence, $\mathrm{BR}(\tau \to 3\mu)$ is more tightly correlated with $\mathrm{BR}(\tau \to \mu\gamma)$ in this case, and it is more difficult to respect the stringent experimental bound on the latter. In turn, if $\tau \to 3\mu$ is observable at Belle II, $|c_{23}| \approx |a_{23}|$ must be rather large and therefore one generates an enhancement of $\mathrm{BR}(\mu \to e\gamma)$ and $\mathrm{CR}(\mu - e; \mathrm{Al})$. Still, since $|b_{13}| \ll \lambda$ is possible in the comprehensive scan, the rates for cLFV $\mu \to e$ processes can get efficiently suppressed without a direct impact on the Z-penguin contributions. Indeed, the distinct slope of the right edge of the coloured region in the top plots in figure (5.14) has almost entirely disappeared in the bottom-left plot therein. This indicates that there is no pronounced correlation between $\mathrm{BR}(\tau \to 3\mu)$ and cLFV $\mu \to e$ transitions in the comprehensive scan.

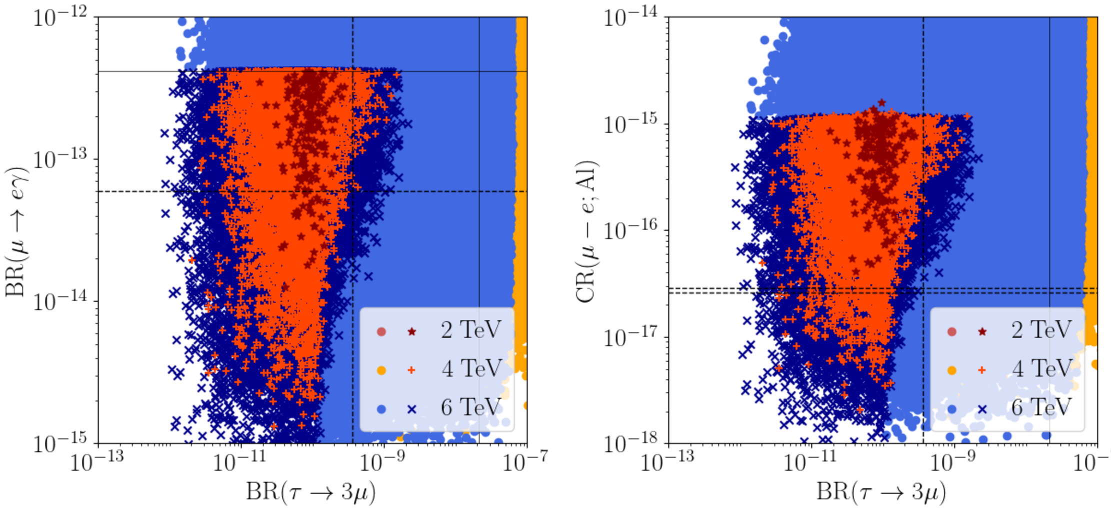

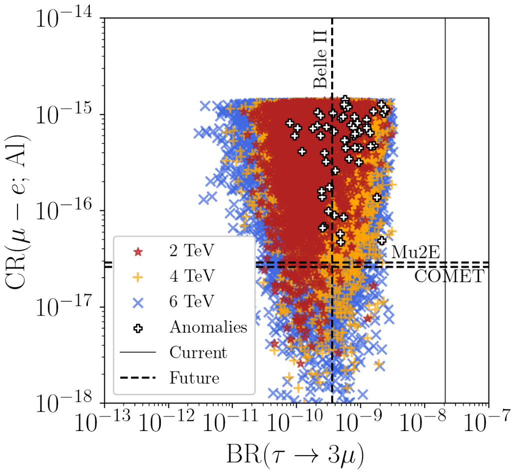

Figure 5.14: **Constraining power and future reach of $\tau \to 3\mu$ in relation with $\mu \to e$ transitions. Top panel:** Results from primary scan. The vertical solid (dashed) lines indicate the current bound on (future sensitivity of) $\tau \to 3\mu$ [7, 28]; see table 5.4. The round points (geometric shapes) indicate that current experimental bounds are violated (respected); see also the main text of section 5.4.1.1. **Bottom-left plot:** Results from comprehensive scan. The shown sample points respect the experimental bounds from primary constraints; see also section 5.4.1.2.

The discussion above generally also holds for the decay channel $\tau \to \mu e\bar{e}$, for which an estimate yields

$$\begin{aligned}
\mathrm{BR}(\tau \to \mu e\bar{e}) &\approx \frac{m_\tau^5}{3(16\pi)^3\Gamma_\tau}\Bigg[128\left|C^{VLL}_{ee,2311}\right|^2 + 8\left|C^{VLR}_{ee,2311}\right|^2 \\
&\qquad + \frac{256e^2}{m_\tau^2}\left(\ln\frac{m_\tau^2}{m_\mu^2} - 3\right)\left|C^{21}_{e\gamma}\right|^2\Bigg] \\
&\approx \frac{1}{64\pi^4}\frac{m_t^2 m_\tau^3}{3(16\pi)^3\Gamma_\tau}\Bigg[4\,e^4(7+4\ln t_t)^2\left(\ln\frac{m_\tau^2}{m_\mu^2} - \frac{11}{4}\right)\frac{|y_{23}z_{33}|^2}{m_\phi^4} \\
&\qquad + 72\,G_F^2 m_t^2 m_\tau^2(1+\ln t_t)^2\left(\frac{1}{2}(1-2s_W^2)^2 + 2s_W^4\right)\frac{|z_{23}z_{33}|^2}{m_\phi^4}\Bigg] \\
&\approx 1.34\times 10^{-7}\frac{|b_{23}c_{33}|^2 + 0.05|c_{23}c_{33}|^2}{\hat{m}_\phi^4}\,.
\end{aligned} \tag{5.87}$$

In the limit of exact photon-penguin dominance, one finds

$$\mathrm{BR}(\tau \to \mu e\bar{e}) \approx \underbrace{\frac{e^2}{12\pi^2}\left(\ln\left(\frac{m_\tau^2}{m_\mu^2}\right) - 3\right)}_{\approx 0.0023} \mathrm{BR}(\tau \to \mu\gamma) \tag{5.88}$$

as well as

$$\frac{\mathrm{BR}(\tau \to 3\mu)}{\mathrm{BR}(\tau \to \mu e\bar{e})} \approx \frac{2\ln(m_\tau/m_\mu) - 11/4}{2\ln(m_\tau/m_\mu) - 3} \approx 1.09\ . \tag{5.89}$$

More generally, the obtained BRs for $\tau \to 3\mu$ and $\tau \to \mu e\bar{e}$ are almost coincident in the primary scan, whereas larger deviations appear in the comprehensive scan. This is mainly due to the possibility of generating effective coupling parameters with magnitudes (much) larger than $1/\lambda$ in the latter, which can result in contributions from box diagrams becoming more relevant.

Similar to the role of $\tau \to e\gamma$ among the radiative cLFV decays, trilepton decays with other flavour combinations in the final state do not give rise to relevant constraints on the model, neither regarding current data nor in the light of near-future searches.

5.4.8 $B_c \to \tau\,\nu$

In the model, ϕ contributes to the leptonic decay channel $B_c \to \tau\nu$ and therefore modifies the lifetime of the B_c meson, as was originally elaborated on in ref. [131]. In line with this approach, I employ a constraint on the SM contribution to the lifetime. A pseudoscalar meson B_k constituted by a bottom quark b and an up-type quark u_k decays into a tau lepton and a neutrino with a rate [29, 407]

$$\begin{aligned}\Gamma_{B_k\to\tau\nu} = \frac{G_F^2}{8\pi} m_{B_k} f_{B_k}^2 |V_{u_k b}|^2 m_\tau^2 \left(1 - \frac{m_\tau^2}{m_{B_k}^2}\right)^2 \\ \times \sum_{\beta=1}^{3} \left|(1+\delta)\cdot\delta_{3\beta} - \frac{1}{2\sqrt{2}G_F V_{u_k b}} C^{\phi}_{\nu edu,\beta 33k}(\mu_B)\right|^2\end{aligned} \tag{5.90}$$

where

$$C^{\phi}_{\nu edu,\beta 33k}(\mu_B) \equiv C^{VLL}_{\nu edu,\beta 33k}(\mu_B) - \frac{m_{B_k}^2}{m_\tau(m_{u_k}(\mu_B) + m_b(\mu_B))} C^{SRR}_{\nu edu,\beta 33k}(\mu_B) \tag{5.91}$$

was defined. Here, m_{B_k} and f_{B_k} are the mass and decay constant of the meson, respectively, and V is the CKM matrix. The correction $\delta = 0.007$ accounts for QED running of the SM contribution to $C^{VLL}_{\nu edu}$ from the Z-boson mass scale down to the hadronic scale $\mu = \mu_B$.

I equate the measured decay width with the sum of the contributions in the SM and from ϕ as in

$$\Gamma^{\text{exp}}_{B_c} = \Gamma^{\text{SM}}_{B_c} + \Gamma^{\phi}_{B_c} \,. \tag{5.92}$$

Here, I fix $\tau^{\text{exp}}_{B_c} = 1/\Gamma^{\text{exp}}_{B_c} = 0.510 \pm 0.009$ ps [10,29] at the best-fit value, while $\Gamma^{\phi}_{B_c}$ accounts for contributions to the tree-level process $bc \to \tau\nu$ induced by ϕ. $\Gamma^{\phi}_{B_c}$ can be calculated by subtracting the SM contribution from the rate in eq. (5.90), thereby it also captures interference effects:

$$\begin{aligned}\Gamma^{\phi}_{B_c} = {}& \frac{G_F^2}{8\pi} m_{B_c} f_{B_c}^2 V_{cb}^2 m_\tau^2 \left(1 - \frac{m_\tau^2}{m_{B_c}^2}\right)^2 \\ & \times \left(\sum_{\beta=1}^{3} \left| (1+\delta)\cdot\delta_{3\beta} - \frac{1}{2\sqrt{2} G_F V_{cb}} C^{\phi}_{\nu edu,\beta 332}(\mu_B) \right|^2 - (1+\delta)^2 \right) \,.\end{aligned} \tag{5.93}$$

I do not attempt a direct calculation of $\Gamma^{\text{SM}}_{B_c} = 1/\tau^{\text{SM}}_{B_c}$ which takes into account all SM contributions to the B_c decay width, but instead indirectly infer it from eq. (5.92). The complete expression reads

$$\begin{aligned}\tau^{\text{SM}}_{B_c} = {}& \left[\frac{1}{\tau^{\text{exp}}_{B_c}} - \frac{G_F^2}{8\pi} m_{B_c} f_{B_c}^2 V_{cb}^2 m_\tau^2 \left(1 - \frac{m_\tau^2}{m_{B_c}^2}\right)^2 \right. \\ & \left. \times \left(\sum_{\beta=1}^{3} \left| (1+\delta)\cdot\delta_{3\beta} - \frac{1}{2\sqrt{2} G_F V_{cb}} C^{\phi}_{\nu edu,\beta 332}(\mu_B) \right|^2 - (1+\delta)^2 \right) \right]^{-1} \,.\end{aligned} \tag{5.94}$$

I require that the resulting $\tau^{\text{SM}}_{B_c}$ lies in the interval $[0.4, 0.7]$ ps, following the seminal result in ref. [387] at $1\,\sigma$, and neglect all other uncertainties against the broadness of this range.[18] I use the PDG values $\tau^{\text{exp}}_{B_c} = 0.510$ ps, $m_{B_c} = 6.2745$ GeV, $m_\tau = 1.7769$ GeV, $V_{cb} = 0.0405$ [29] as well as $f_{B_c} = 434$ MeV [410] and the quark masses $m_c(\mu_B) = 0.9023$ GeV and $m_b(\mu_B) = 4.0945$ GeV output by `flavio`, v2.3.

---

[18] More recent calculations of the B_c lifetime in the SM can for instance be found in refs. [408, 409].

The LQ ϕ mainly sources the channel with a tau neutrino ν_τ in the final state, but the muon neutrino channel may also have a non-negligible effect. The latter corresponds to the rightmost term in eqs. (5.96) and (5.98) below. One approximately finds

$$\frac{\tau_{B_c}^{\rm SM}}{\tau_{B_c}^{\rm exp}} = \left[1 - \frac{\Gamma_{B_c}^{\phi}}{\Gamma_{B_c}^{\rm exp}}\right]^{-1} \approx 1 + \frac{\Gamma_{B_c}^{\phi}}{\Gamma_{B_c}^{\rm exp}} \tag{5.95}$$

$$\approx 1 - 0.13\frac{\mathrm{Re}(a_{33}b_{32})}{\hat{m}_\phi^2} + 0.19\frac{|a_{33}b_{32}|^2}{\hat{m}_\phi^4} + 0.01\frac{|a_{23}b_{32}|^2}{\hat{m}_\phi^4} \tag{5.96}$$

$$= 1 - 0.13\frac{|a_{33}b_{32}|}{\hat{m}_\phi^2}\cos\left(\mathrm{Arg}(a_{33}) - \mathrm{Arg}(b_{32})\right) \tag{5.97}$$

$$+ 0.19\frac{|a_{33}b_{32}|^2}{\hat{m}_\phi^4} + 0.01\frac{|a_{23}b_{32}|^2}{\hat{m}_\phi^4} \tag{5.98}$$

upon rearranging eq. (5.92). The latter is also equivalent to the following relation

$$\mathrm{BR}(B_c \to \tau\nu) = \mathrm{BR}(B_c \to \tau\nu)_{\rm SM} - \left(\frac{\tau_{B_c}^{\rm exp}}{\tau_{B_c}^{\rm SM}} - 1\right). \tag{5.99}$$

Thus, imposing an upper bound on the BR, say $\mathrm{BR}(B_c \to \tau\nu) \lesssim 0.3$ [131] or $\lesssim 0.1$ [411], which takes into account the (semi)tauonic contributions in the SM and from NP, is equivalent to $\tau_{B_c}^{\rm SM} \lesssim 0.70$ ps or $\lesssim 0.55$ ps, respectively. Indeed, a BR larger than predicted in the SM implies an effective reduction of the lifetime due to ϕ which must be "compensated" by a larger SM contribution to the lifetime in order to maintain consistency with the experimentally determined value $\tau_{B_c}^{\rm exp}$.

As is illustrated in figure 5.15, a large contribution from the LQ to the lifetime of the B_c meson is incompatible with the imposed experimental bounds. In the plots in the upper (lower) panel, the vertical solid lines indicate (grey-shaded region indicates) where the SM prediction agrees with the measured lifetime of the B_c meson at $1\,\sigma$. In particular, the model can accommodate the current best-fit value in $R(D)_{\rm exp} = 0.339 \pm 0.026 \pm 0.014$ even in the absence of any contribution from ϕ to the B_c lifetime. In the case of larger LQ masses, an inferred SM contribution to the lifetime which is appreciably larger than the experimentally determined one only arises if $R(D)$ and $R(D^\star)$ become smaller than in the SM, respectively, which is consistent with the opposite signs of the respective contributions linear in $|a_{33}b_{32}|$; see eqs. (5.50), (5.51) and (5.98).

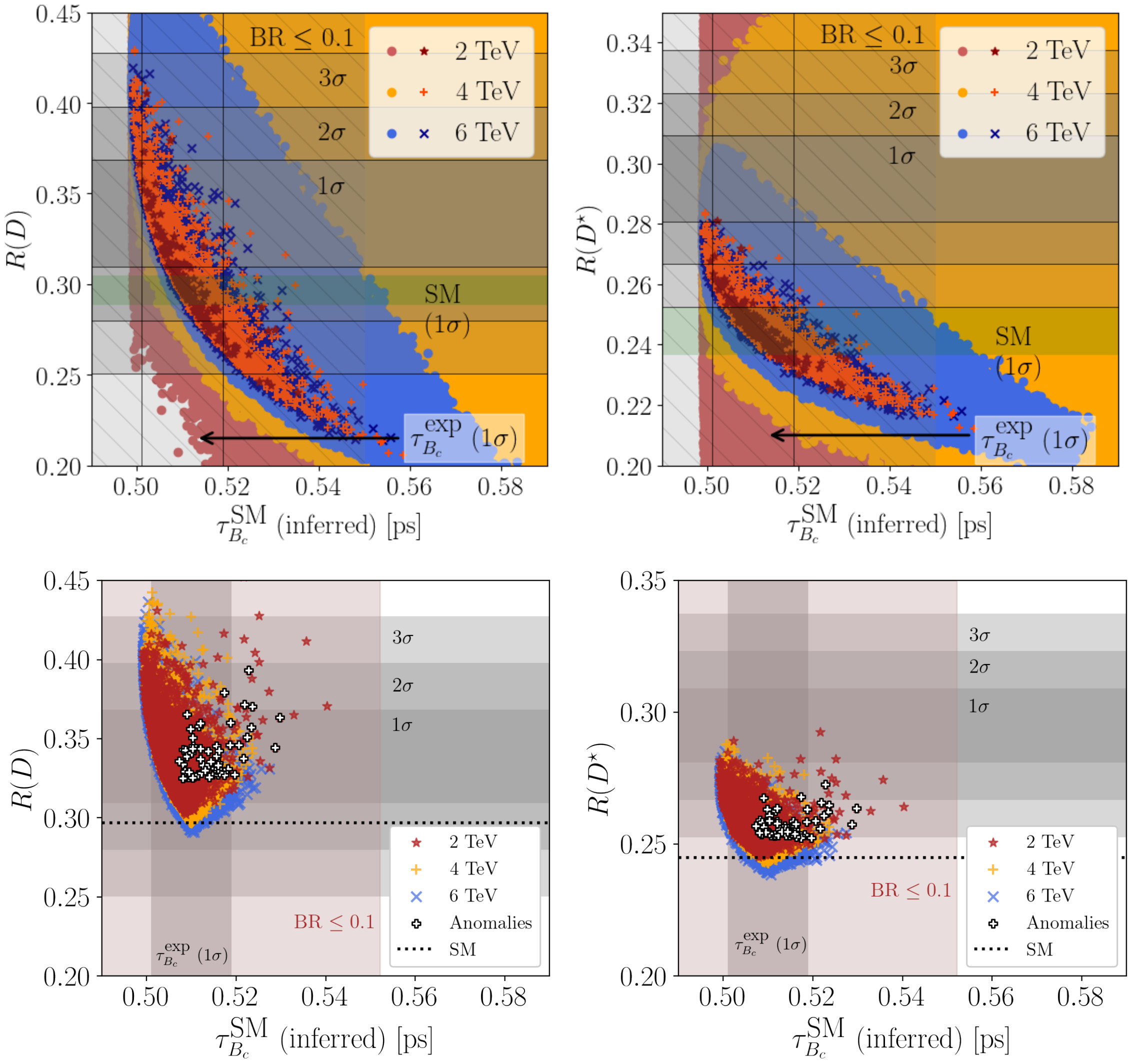

Figure 5.15: **Constraining power and future reach of $\tau_{Bc}^{\rm SM}$ in relation with $R(D)$ and $R(D^\star)$. Top panel:** Results from primary scan. The vertical solid lines indicate the region where the inferred contribution to the B_c lifetime in the SM agrees with the measured lifetime at $1\,\sigma$ [10, 29], and the hatched area marks the region in which the BR of $B_c \to \tau\nu$ remains smaller than 0.1, as is implied by eq. (5.99); see also table 5.4. The round points (geometric shapes) indicate that current experimental bounds are violated (respected); see also the main text of section 5.4.1.1. **Lower panel:** Results from comprehensive scan. The shown sample points respect the experimental bounds from primary constraints; see also section 5.4.1.2. The grey-shaded region represents the $1\,\sigma$ range about the current best-fit value for $\tau_{B_c}^{\rm exp}$, and the red-brown shaded band indicates the region of parameter space that corresponds to $\mathrm{BR}(B_c \to \tau\nu) \leq 0.1$.

Contrariwise, for $\hat{m}_\phi = 2$, the comprehensive scan demonstrates that a SM contribution which substantially exceeds $\tau_{B_c}^{\rm exp} = (0.510 \pm 0.009)$ ps [10, 29] is compatible with a simulta-

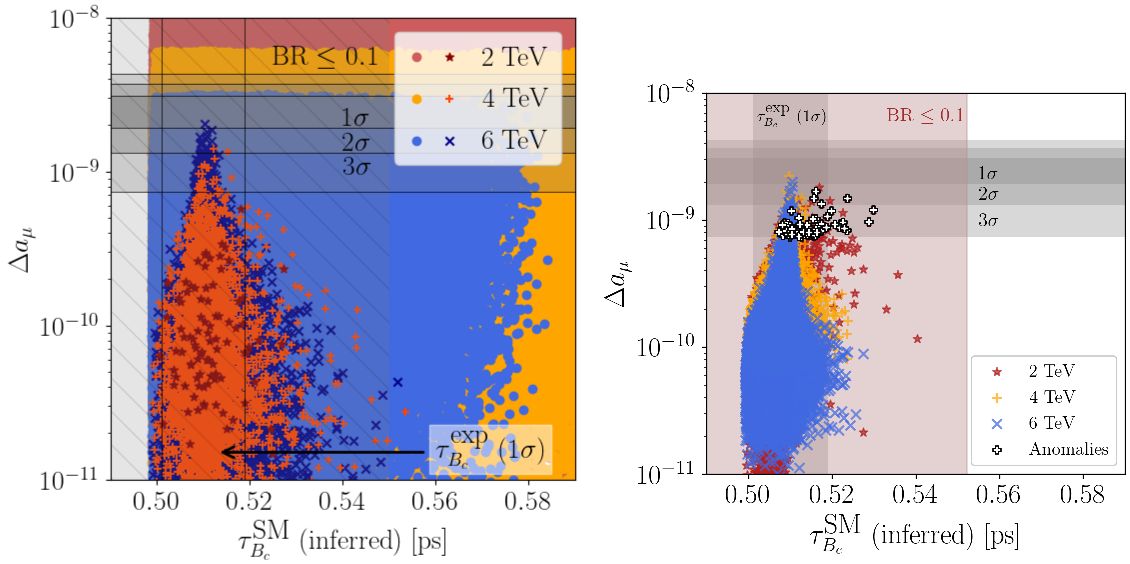

Figure 5.16: **Constraining power and future reach of τ_{Bc}^{SM} in relation with Δa_μ. Left:** Results from primary scan. The vertical solid lines indicate the region compatible with current experimental data on the B_c lifetime at $1\,\sigma$ [10,29], and the hatched areas mark the regions in which the BR of $B_c \to \tau\nu$ remains smaller than 0.1 and 0.3, respectively, as is implied by eq. (5.99); see also table 5.4. The round points (geometric shapes) indicate that current experimental bounds are violated (respected); see also the main text of section 5.4.1.1. **Right:** Results from comprehensive scan. The shown sample points respect the experimental bounds from primary constraints; see also section 5.4.1.2.

neous enhancement of $R(D)$ and $R(D^\star)$ over their respective SM values, which I interpret as mainly due to the channel with a muon neutrino ν_μ in the final state. Furthermore, for almost all sample points found in the comprehensive scan which successfully explain the anomalies in $R(D)$, $R(D^\star)$ and Δa_μ I obtain $|a_{33}b_{32}| \lesssim 1$, thus significantly below the upper bound $|a_{33}b_{32}| \lesssim 1.82$ imposed via the biasing, cf. table 5.6. Hence, a maximally large contribution to the channel with a tau neutrino ν_τ in the final state is not preferred for an accommodation of the anomalies. Note that a similar effect occurs for $R(D)$ and $R(D^\star)$ where an enhancement of up to 40% and 30%, respectively, over the respective SM contributions can in principle be induced via the muon channel in the case of $\hat{m}_\phi = 2$. For $\hat{m}_\phi = 4, 6$, I obtain a maximal enhancement of 10% which is still roughly coincident with the current $1\,\sigma$ region about the respective experimental best-fit values of $R(D)$ and $R(D^\star)$, and should thus not be neglected in the light of more precise data becoming available in the near future.

If Δa_μ is explained at $3\,\sigma$ or better in the model, I find that a substantial deviation of $\tau_{B_c}^{\mathrm{SM}}$ from the measured B_c lifetime is very unlikely for $\hat{m}_\phi = 4, 6$, see figure 5.16. This reflects the way an explanation of $R(D)$ and $R(D^\star)$ competes with an explanation of Δa_μ; see section 5.4.4. Still, according to the results of the comprehensive scan, an enhanced $\tau_{B_c}^{\mathrm{SM}}$ is compatible with an explanation of Δa_μ, since the latter is controlled by the effective parameter $c_{23} \approx a_{23}$ which also drives the muon-neutrino contribution from ϕ to the B_c decay rate and thus implies a larger inferred $\tau_{B_c}^{\mathrm{SM}}$.

Still, a deviation of $\tau_{B_c}^{\mathrm{SM}}$ from the best-fit value of $\tau_{B_c}^{\mathrm{exp}}$ by more than 10 percent is incompatible with the considered constraints. Accordingly, the BR for $B_c \to \tau\nu$ will remain below 0.1 in most cases, and can potentially exceed this limit only to a very small degree. In line with eq. (5.99), imposing the upper bound $\mathrm{BR}(B_c \to \tau\nu) \lesssim 0.1$ ps constrains the B_c lifetime to the hatched (red-brown shaded) region in the upper (lower) panel in figure 5.15, respectively.

5.4.9 $Z \to \tau\tau$

For the discussion of modifications to the effective Z-boson couplings to fermions induced by ϕ, I focus on the case of charged leptons henceforth and define the vector and axial-vector couplings as in

$$g_{e_{V(A)}}^{ij} = g_{e_L}^{ij} \pm g_{e_R}^{ij} \,, \tag{5.100}$$

cf. eq. (2.10). In the model under consideration, charged leptons only couple to up-type quarks at tree level. Following ref. [96], I approximately find

$$\delta g_{e_{A(V)}}^{ii} \equiv \delta g_{e_{i\,A(V)}} \approx \frac{N_c}{32\pi^2} \frac{t_t(t_t - 1 - \ln t_t)}{(t_t - 1)^2} \left(|z_{i3}|^2 \pm |y_{i3}|^2 \right) \,. \tag{5.101}$$

Under the assumption of LFU for the SM couplings, that is

$$g_{e_A}^{\mathrm{SM}} = g_{\mu_A}^{\mathrm{SM}} = g_{\tau_A}^{\mathrm{SM}} \equiv g_A^{\mathrm{SM}} = \sqrt{\rho_\psi} T_3^\psi \,, \tag{5.102}$$

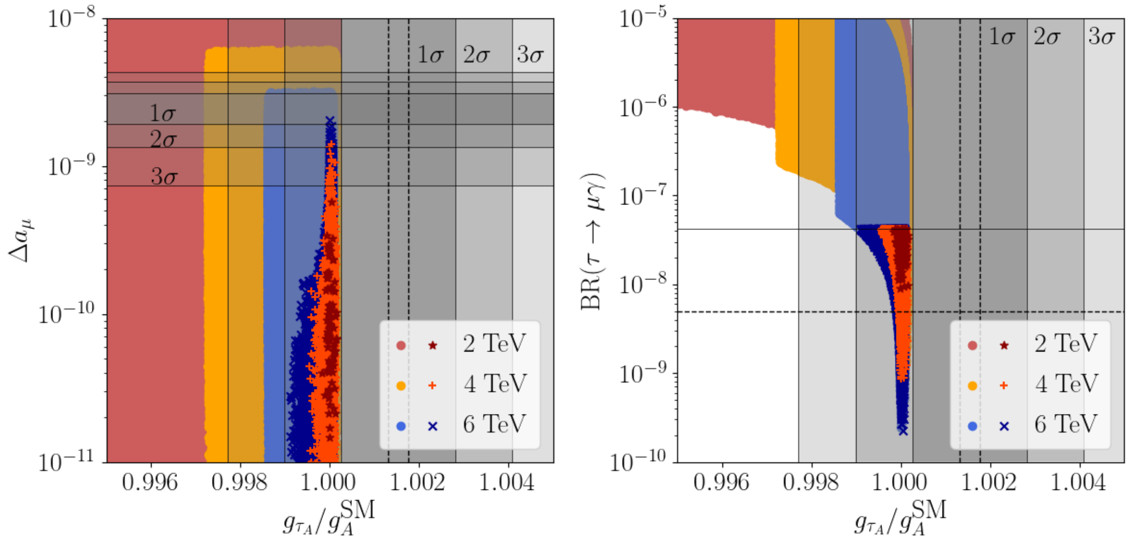

Figure 5.17: **Constraining power and future reach of $g_{\tau_A}/g_A^{\text{SM}}$ as found in the primary scan.** The regions indicated by vertical solid (dashed) lines are compatible with the current experimental world averages for (future sensitivity of) $g_{\tau_A}/g_A^{\text{SM}}$ at the indicated CL [30, 31] (at $3\,\sigma$ [31–33]); see table 5.4. The round points (geometric shapes) indicate that current experimental bounds are violated (respected); see also the main text of section 5.4.1.1.

taking the ratio yields in the case of the tau lepton

$$g_{\tau_A}/g_A^{\text{SM}} \approx 1 - \left\{ \begin{array}{ll} 4.5\,, & \hat{m}_\phi = 2 \\ 1.5\,, & \hat{m}_\phi = 4 \\ 0.8\,, & \hat{m}_\phi = 6 \end{array} \right\} |c_{33}|^2 \times 10^{-4}\,. \tag{5.103}$$

Note that the negative sign of the correction is due to the axial-vector coupling to charged leptons being negative in the SM. This estimate suggests that $g_{\tau_A}/g_A^{\text{SM}}$ is not per se (strongly) correlated with $\Delta a_\mu \propto |a_{23}b_{23}|$, as is further evidenced in figure 5.17. Still, if the experimental constraints are imposed, the axial-vector coupling of Z bosons to tau leptons is necessarily SM-like if Δa_μ is explained at $3\,\sigma$. In particular, the deviation from LFU would be constrained to be much smaller than 0.1%. This correlation is established through the bound on $\text{BR}(\tau \to \mu\gamma) \propto |a_{33}b_{23}|^2$ illustrated by the plot on the right in figure 5.17. It is distinctly visible that a deviation of $g_{\tau_A}/g_A^{\text{SM}}$ from the current best-fit value [30, 31] larger than $2\,\sigma$ is incompatible with the constraint on $\text{BR}(\tau \to \mu\gamma)$. Furthermore, the future search for $\tau \to \mu\gamma$ at Belle II [7] will conclusively test the capability of the model to induce a significant deviation from LFU in axial-vector couplings. Note that the prospective sensitivities of a measurement of Z-boson couplings quoted in table 5.4 are adopted from ref. [31] where it is assumed that the precision of the determination of g_{e_A} will improve by the same factor as $\sin^2\theta_{\text{eff}}$. In addition, if this sensitivity were indeed reached and the current best-fit value for $g_{\tau_A}/g_A^{\text{SM}}$ remained unchanged, the currently observed deviation from the SM value could not be explained within the model.

5.4.10 High-p_T Dilepton Searches

In several recent studies [161, 412–414], constraints on effective operators were derived from LHC data. In ref. [161], the process $q\bar{q} \to \tau\bar{\tau}$ was considered for the LQ ϕ, among other ones, and the ATLAS analysis in ref. [388] was reinterpreted to place a constraint on the LQ couplings for the mass range $\hat{m}_\phi \in [1, 3]$. Reading off from the top-right of figure 4 in ref. [161] and using the fact that the LHC does not distinguish between chiralities, one may infer the upper bound on the LQ coupling involving a RH tau lepton and charm quark

$$|y_{32}| = |b_{32}| < \hat{m}_\phi + 0.6 \ . \tag{5.104}$$

Similarly, in ref. [414] the process $bc \to \tau\nu$ was considered and two analyses [415, 416] by the ATLAS and CMS collaborations were recast to obtain a constraint on the relevant effective charged-current operators. The resulting constraints are quoted in table II in ref. [414], where it is assumed that a single operator dominates. In terms of the effective couplings at the LQ mass scale, they read

$$\sqrt{|a_{33}c_{32}|} < 3.5\,\hat{m}_\phi \quad \text{and} \quad \sqrt{|a_{33}b_{32}|} < 0.70\,\hat{m}_\phi \tag{5.105}$$

where the QCD RG corrections are extracted from `RunDec` [305, 417]. Still, these two constraints are automatically respected in the model if the experimental bounds on other primary observables are imposed.

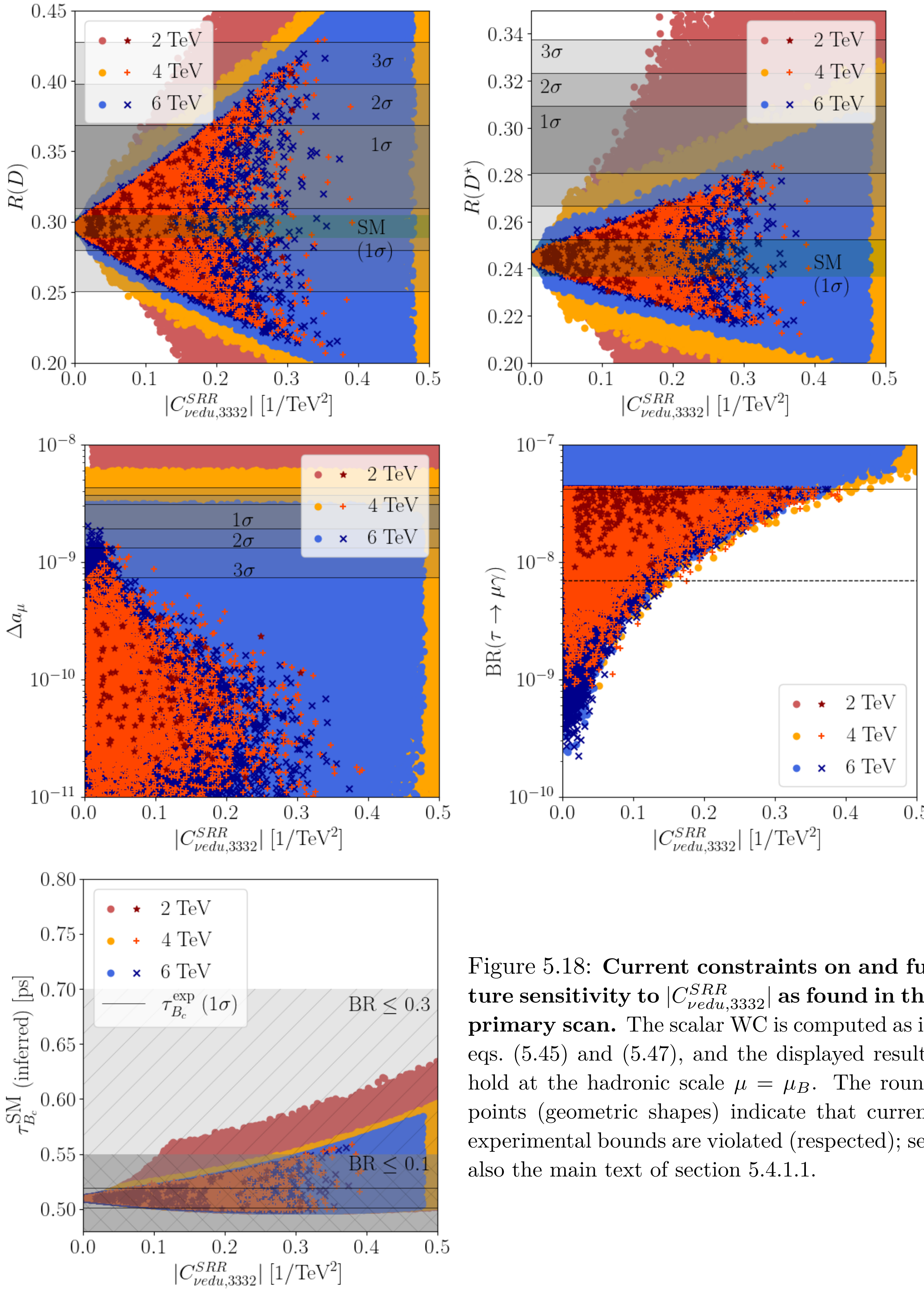

Figure 5.18: **Current constraints on and future sensitivity to $|C_{\nu edu,3332}^{SRR}|$ as found in the primary scan.** The scalar WC is computed as in eqs. (5.45) and (5.47), and the displayed results hold at the hadronic scale $\mu = \mu_B$. The round points (geometric shapes) indicate that current experimental bounds are violated (respected); see also the main text of section 5.4.1.1.

5.4.11 Scalar Charged-Current Wilson Coefficients

Herein I provide a brief discussion on current constraints on and the projected sensitivity to contributions to $|C^{SRR}_{\nu edu,3332}|$ in future experiments. This scalar WC constitutes the dominant contribution to the observables $R(D)$, $R(D^\star)$ and $\tau^{\rm SM}_{B_c}$ in the model. In line with eqs. (5.45) and (5.47), I find $C^{SRR}_{\nu edu,3332} \approx -1.7 x_{33} y_{32}/(2m_\phi^2) \approx -1.7 a_{33} b_{32}/(2m_\phi^2)$ at the hadronic scale $\mu = \mu_B$. The following statements draw from the primary scan, and largely agree with the findings from the comprehensive scan apart from small deviations in the case of $\hat{m}_\phi = 2$.

As can be seen in the top panel in figure 5.18, the achievable deviation of $R(D)$ and $R(D^\star)$ from their respective SM values grows linearly with an increase of the absolute value of $C^{SRR}_{\nu edu,3332}$. Only for magnitudes $|C^{SRR}_{\nu edu,3332}| \gtrsim 0.2/\text{TeV}^2$, a slight deviation from that trend becomes visible. This confirms that the contributions to $R(D)$ and $R(D^\star)$ which are linear in the scalar WC and interfere with the SM, see eqs. (5.50) and (5.51), dominate for smaller LQ coupling values. The top plots also conveniently illustrate that the anomaly is mainly driven by the experimental data for $R(D^\star)$, that is, explaining $R(D^\star)$ at $2\,\sigma$ $(1\,\sigma)$ requires $|C^{SRR}_{\nu edu,3332}| \gtrsim 0.2(0.3)/\text{TeV}^2$.

The centre-left plot in figure 5.18 evidences that a correlation between $\Delta a_\mu \propto |b_{23} c_{23}|$ and $|C^{SRR}_{\nu edu,3332}| \propto |a_{33} b_{32}|$ arises only after imposing the experimental bound on $\text{BR}(\tau \to \mu\gamma) \propto |b_{23} c_{33}|^2 \approx |b_{23} a_{33}|^2$. Indeed, the current constraint requires $|C^{SRR}_{\nu edu,3332}| \lesssim 0.4/\text{TeV}^2$, and the upcoming search for the process at Belle II [7] will potentially strengthen this to $|C^{SRR}_{\nu edu,3332}| \lesssim 0.15/\text{TeV}^2$. Note that an efficient test of the capability of the model to explain Δa_μ still requires a further refinement of that bound, as is visible in the centre-left plot.

Lastly, one can see that $\tau^{\rm SM}_{B_c}$ is slightly less sensitive to $|C^{SRR}_{\nu edu,3332}|$ than $R(D)$ or $R(D^\star)$ are. The distribution of the generated sample points for $\hat{m}_\phi = 2$ features a kink which is localised at the upper boundary of the coloured region at $|C^{SRR}_{\nu edu,3332}| \approx 0.13/\text{TeV}^2$, due to the experimental constraint $|b_{32}| < 2.6$. One can see that $|C^{SRR}_{\nu edu,3332}| \gtrsim 0.3/\text{TeV}^2$ is necessary to have the BR of the decay channel $B_c \to \tau\nu$ exceed 0.1.

List of Secondary Observables					
Observable	Experiment				
	Current constraint/measurement			Future reach	
$\lvert d_\mu \rvert$	$< 1.5 \times 10^{-19}\, e\,\text{cm}$	at 90% C.L.	[418]	$1000\,(60)\,[1] \times 10^{-24}\, e\,\text{cm}$	[34, 35, 40–42]
$g_{\mu_A}/g_A^{\text{SM}}$	0.99986 ± 0.00108	at $1\,\sigma$ level	[30, 31]	$\pm 6.3\,(0.63) \times 10^{-5}$	[31–33]
$R_D^{\mu/e}$	0.995 ± 0.090	at $1\,\sigma$ level	[419]	± 0.00995	[36]
$R_{D^\star}^{e/\mu}$	1.01 ± 0.032	at $1\,\sigma$ level	[420]	± 0.0101	[36]
$\text{BR}(B \to \tau\nu)$	$(1.09 \pm 0.24) \times 10^{-4}$	at $1\,\sigma$ level	[29]	$\pm 9\,(4)\%$ at $5\,(50)$ ab^{-1}	[17]

Table 5.7: **List of secondary observables**. I list the observables that can potentially be used to further constrain and test this model, together with their current experimental constraint and future sensitivity. In the case of the muon EDM d_μ, the future projection without brackets refers to the prospective reach of the Muon $g-2$ experiment at Fermilab [34] and a similar experimental effort at J-PARC [40], while the bracketed values are estimates for experimental proposals [35,41,42] based on the frozen-spin technique. Furthermore, I assume that the precision of measurements of g_{μ_A} will improve by the same factor as $\sin^2\theta_{\text{eff}}$ as in ref. [31]; the (un)bracketed projection refers to the FCC [33] (ILC [32]).

5.4.12 Secondary Observables

In this section, I briefly comment on the results for the secondary observables from the comprehensive scan which are collected in table 5.7. The muon EDM and $\text{BR}(B \to \tau\nu)$ were calculated with the help of `SPheno`, $g_{\mu_A}/g_A^{\text{SM}}$ was obtained from analytic formulae which are analogous to the ones for $g_{\tau_A}/g_A^{\text{SM}}$, and `flavio` was used for $R_D^{\mu/e}$ and $R_{D^\star}^{e/\mu}$.

5.4.12.1 Electric Dipole Moment of the Muon

Similar to the AMM of a charged lepton being sourced by the real part of the relevant dipole operator, EDMs are related to the imaginary part. As the generation of large contributions to Δa_μ is a key motivation for the model, and the LQ couplings can be complex, the occurrence of sizeable results for d_μ is expected. In complete analogy to the reasoning laid out in section 5.4.3.1, the dominant contribution is due to a top-quark mass insertion on the internal line of the relevant one-loop diagram. Using eqs. (2.51) and (5.54), I find

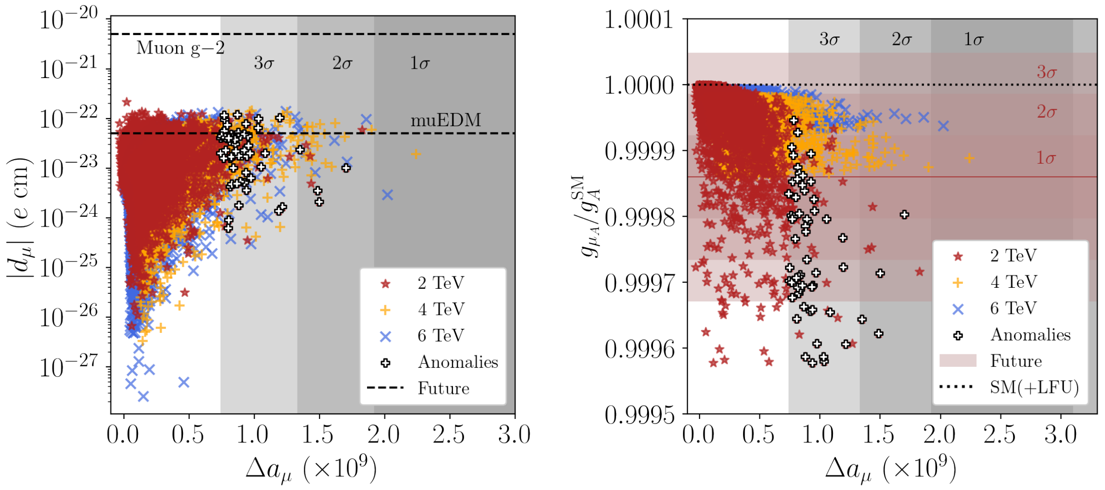

Figure 5.19: **Future reach of secondary leptonic observables in relation with Δa_μ in the comprehensive scan.** The shown sample points respect the experimental bounds from primary constraints; see also section 5.4.1.2. In the left plot, two constraints on the magnitude $|d_\mu|$ of the muon EDM are shown, from the Muon g−2 [34] experiment and the muEDM experiment [35]. For $g_{\mu A}/g_A^{\text{SM}}$, the red-brown shaded regions represent the projected sensitivities at the ILC [32] under the assumption that the current best-fit values [30, 31] shown herein as red-brown solid lines will persist.

$$\begin{aligned} d_\mu &= 2\,\text{Im}(C_{e\gamma}^{22}) \approx \frac{e\,m_t}{32\pi^2 m_\phi^2}(7+4\ln t_t)\,\text{Im}(z_{23}^* y_{23}) \approx -\frac{8}{\hat{m}_\phi^2}\text{Im}(b_{23}c_{23}^*) \times 10^{-9} \\ &\approx -\frac{5}{\hat{m}_\phi^2}\text{Im}(b_{23}c_{23}^*) \times 10^{-22}\,e\,\text{cm} \qquad (5.106) \\ &= -\frac{5}{\hat{m}_\phi^2}|b_{23}c_{23}|\sin\left(\text{Arg}(b_{23}) - \text{Arg}(c_{23})\right) \times 10^{-22}\,e\,\text{cm}\,. \end{aligned}$$

Firstly, note that the contributions to the muon EDM are well below the current bound $|d_\mu| < 1.5 \times 10^{-19}\,e\,\text{cm}$ [34] if the experimental bounds are imposed, see table 5.7 and the left plot in figure 5.19, despite the absence of a CP symmetry in the model. Still, in agreement with the literature regarding correlations between d_μ and solutions to the currently present anomaly in Δa_μ, particularly for the LQ ϕ [276,400], I find that a portion of the viable parameter space can be expected to be probed at the muEDM experiment [35]. Generally, if the anomaly in Δa_μ is accommodated within its $3\,\sigma$ range, one obtains a result $|d_\mu| \in [10^{-25}, 10^{-22}]$. As the biasing requires $\cos(\text{Arg}(a_{23}) - \text{Arg}(b_{23}))$ to lie in a vicinity of -1, see table 5.6, it may favour smallish values for $\sin(\text{Arg}(a_{23}) - \text{Arg}(b_{23}))$, but no preference for either sign of d_u is induced. After all, the impact of the phase difference $\text{Arg}(a_{23}) - \text{Arg}(b_{23})$ seems to be limited, since there is no indication that (comparatively) large contributions to Δa_μ and d_μ would be incompatible.

5.4.12.2 $Z \to \mu\mu$

The presence of sizeable contributions to Δa_μ due to loops containing a top quark triggers the expectation that the process $Z \to \mu\mu$ will also get modified. In complete analogy to section 5.4.9 and under the assumption of LFU for the SM gauge couplings, one finds

$$g_{\mu A}/g_A^{\mathrm{SM}} \approx 1 - \left\{ \begin{array}{ll} 2.3, & \hat{m}_\phi = 2 \\ 0.8, & \hat{m}_\phi = 4 \\ 0.4, & \hat{m}_\phi = 6 \end{array} \right\} |c_{23}|^2 \times 10^{-5} \,. \tag{5.107}$$

The deviation of the best-fit value of the measured axial-vector coupling of the Z boson to a muon-antimuon pair from the SM prediction is currently compatible with zero at $1\,\sigma$; see table 5.7. Moreover, the contributions obtained in the comprehensive scan all fall within this range, thus no constraints can presently be derived from this observable.

Still, the discrepancy between the SM prediction and the current best-fit value can in principle be explained in the model. Furthermore, if the best-fit value persists and the experimental uncertainty shrinks as is projected for the ILC [32], some of the sample points which simultaneously explain all anomalies fall outside the prospective $3\,\sigma$ range, as can be seen in the right plot in figure 5.19. Therefore, upcoming measurements of the axial-vector coupling of the Z boson to muons promise to provide a powerful test of this scenario. Note that a further decrease of the experimental uncertainty by a factor of 10 is expected from the Future Circular Collider (FCC) [33].

Regarding the couplings of the Z boson to electron-positron pairs, the relevant couplings are suppressed by a factor of λ^9, and thus no sizeable BSM contributions to $Z \to ee$ can be expected.

5.4.12.3 Lepton-Flavour Universality Ratios $R_D^{\mu/e}$ and $R_{D^\star}^{e/\mu}$

The LFU ratios $R_D^{\mu/e}$ and $R_{D^\star}^{e/\mu}$ are useful probes for NP effects in $b \to c\ell\nu$ transitions which do not involve the tau lepton,

$$R_D^{\mu/e} = \frac{\mathrm{BR}(B \to D\mu\nu)}{\mathrm{BR}(B \to De\nu)} \equiv \frac{G_2^D}{G_1^D}\,, \qquad R_{D^\star}^{e/\mu} = \frac{\mathrm{BR}(B \to D^\star e\nu)}{\mathrm{BR}(B \to D^\star\mu\nu)} \equiv \frac{G_1^{D^\star}}{G_2^{D^\star}}\,, \tag{5.108}$$

where $G_i^{D^{(\star)}}$ is defined as per eq. (5.149) and (5.150). I obtain the LO estimates

$$\frac{R_D^{\mu/e}}{(R_D^{\mu/e})_{\mathrm{SM}}} \approx 1 + \frac{2}{\hat{m}_\phi^2}\mathrm{Re}(c_{22}^* a_{23}) \times 10^{-3} \tag{5.109}$$

and

$$\frac{R_{D^\star}^{e/\mu}}{(R_{D^\star}^{e/\mu})_{\mathrm{SM}}} \approx 1 - \frac{2}{\hat{m}_\phi^2}\mathrm{Re}(c_{22}^* a_{23}) \times 10^{-3}\,. \tag{5.110}$$

A scalar-operator contribution is induced at the same order in λ, but is numerically suppressed. Note the occurrence of the parameter $a_{23} \approx c_{23}$ which plays a major role for Δa_μ and is biased towards larger values, see table 5.6. Furthermore, $\mathcal{O}(10)$ values can be generated for the magnitudes $|c_{22}| \approx |a_{22}|$ in the comprehensive scan.

The results show that an enhancement or suppression of either LFU ratio by more than 2 percent with respect to the SM expectation is at least very unlikely; see the left plot in figure 5.20. Thus, the model predictions are SM-like and well compatible with currently available data at the $1\,\sigma$ level. Still, this will not be the case anymore for the entire currently viable parameter space if the sensitivity improves as is projected for Belle II [36], regardless of whether the best-fit value will change or not.

5.4.12.4 Leptonic Decay $B \to \tau\nu$

In this model, ϕ contributes to the leptonic decay channel $B \to \tau\nu$ which in the SM is CKM-suppressed due to $|V_{ub}| \sim \lambda^3$; see eq. (5.90) with $u_k = u$ for the full decay width including the contributions from ϕ. I focus on the case of a tau neutrino ν_τ in the final state for which interference with the SM occurs. Indeed, the process $B \to \tau\nu$ also

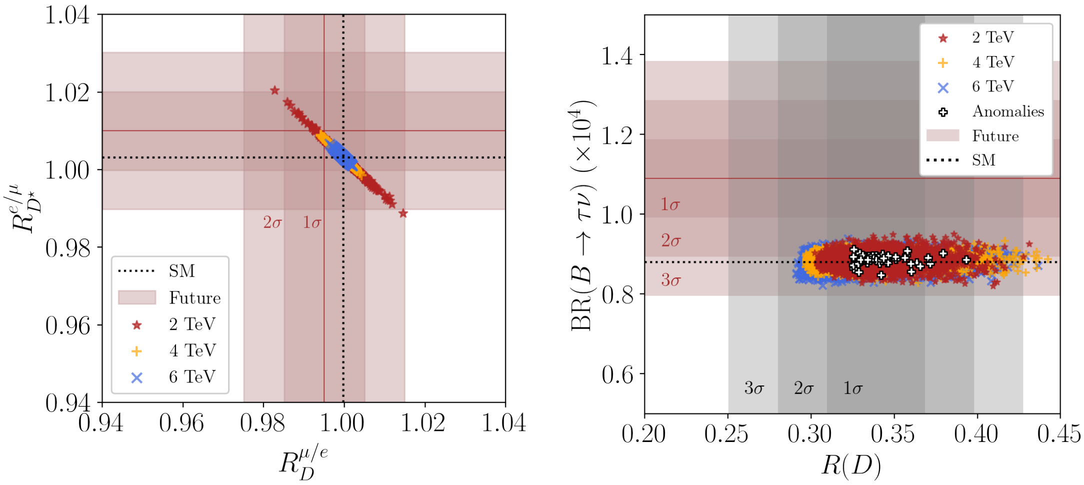

Figure 5.20: **Future reach of secondary hadronic observables in the comprehensive scan.** The shown sample points respect the experimental bounds from primary constraints; see also section 5.4.1.2. The projected sensitivities at Belle II to $R_D^{\mu/e}$ and $R_{D^*}^{e/\mu}$ [36] (5 ab^{-1}) and $\mathrm{BR}(B \to \tau\nu)$ [17] are indicated via the respective red-brown shaded regions. Note that the white crosses are omitted in the left plot since they lie uniformly across the coloured region and would thus obstruct a proper visualisation of the data.

largely depends on the parameter a_{33} and thus provides another probe for the $b \to c\tau\nu$ transitions. The largest contribution arises for the vector-operator WC $C^{VLL}_{\nu edu,3331}$, whereas the scalar-operator WC $C^{SRR}_{\nu edu,3331}$ is suppressed at the scale $\mu = m_\phi$ due to the hierarchy $y_{31}/z_{31} \sim \lambda^2$. This is only partly compensated by the RG evolution down to the hadronic scale $\mu = \mu_B$ and the chirality enhancement of the scalar-operator contribution, which together results in an enhancement factor of roughly 6.5. I find

$$\frac{\mathrm{BR}(B \to \tau\nu)}{\mathrm{BR}(B \to \tau\nu)_{\mathrm{SM}}} \approx 1 - \frac{0.1}{\hat{m}_\phi^2}\mathrm{Re}(a_{33}c_{31}^*)\ . \tag{5.111}$$

In the comprehensive scan, the magnitudes $|c_{31}| \approx |a_{31}|$ can take large $\mathcal{O}(10)$ values. Still, the currently viable parameter space of the model will only be probed by future searches for $B \to \tau\nu$ to an appreciable extent, see the right plot in figure 5.20. This happens despite the dependence on the couplings y_{31} and z_{31} which involve first-generation quarks and thus are protected by the residual symmetry Z_{17}^{diag}; see sections 5.3.3.1 and 5.7.4.

If the current experimental best-fit value persists and the experimental uncertainty decreases as projected at Belle II [17], the model predictions for the BR will remain partly consistent with the data at $2\,\sigma$, but not at $1\,\sigma$. Since these prospective sensitivities to the BR are comparable to the uncertainty of the SM prediction which currently stands at the level of about 10 percent, see [7], one can indeed expect that the decay $B \to \tau\nu$ will provide a useful probe for the model in the near future.

5.5 Conclusions

I have considered an extension of the SM with two Higgs doublets H_u and H_d (in the decoupling limit) and a scalar LQ $\phi \sim (3, 1, -\frac{1}{3})$. The main purpose of ϕ is to explain the flavour anomalies in $R(D)$, $R(D^\star)$ and the AMM of the muon. The interaction structure of this model is constrained by the flavour group $G_f = D_{17} \times Z_{17}$. The three scalars H_u, H_d and ϕ are singlets under the dihedral group, whereas the three generations of SM fermion species transform in doublet and singlet representations, apart from the three RH up-type quarks which are all assigned to singlets. In this way, the masses of the third-generation charged fermions arise without breaking the dihedral group.

The flavour symmetry G_f is broken by the VEVs of four different spurions S, T, U and W which are assigned to doublets of the dihedral group. While the role of S is to (mainly) generate the aimed-at texture of LQ couplings in $\hat{\mathbf{x}}$ and $\hat{\mathbf{y}}$, T and U are responsible for the masses of the second and first generation, respectively, of both down-type quarks and charged leptons. The purpose of the spurion W is to give rise to the mass of the charm quark and to generate the correct size of the Cabibbo angle. The smaller quark mixing angles and the up-quark mass arise automatically due to the spurions S and a combination of T and U, respectively. As dictated by their roles, the VEVs of these spurions are given by the expansion parameter $\lambda \approx 0.2$ taken to some integer power, i.e. $\langle S \rangle \sim \lambda$, $\langle T \rangle \sim \lambda^2$, $\langle U \rangle \sim \lambda^4$ and $\langle W \rangle \sim (\lambda^4, \lambda^5)^t$. A residual symmetry Z_{17}^{diag} given by the diagonal subgroup of a Z_{17} group contained in D_{17} and the external Z_{17} symmetry is preserved by both $\hat{\mathbf{x}}$ and $\hat{\mathbf{y}}$ at LO, which facilitates the achievement of suitable coupling textures and simultaneously avoids too large effects involving first-generation quarks and/or leptons.

The most relevant physical observables were identified analytically, and two numerical studies of the phenomenology of this model were performed. A major distinction was drawn between primary and secondary observables. The former include the anomalies ($R(D)$, $R(D^\star)$ and Δa_μ) and other observables for which the present experimental measurements can (significantly) constrain the parameter space of this model. The latter do not currently provide competitive constraints, but according to short- or mid-term future prospects, increased experimental sensitivity to them will offer an opportunity to probe this model.

In the first ("primary") numerical study I included only the primary observables, and varied the effective LQ coupling coefficients in the charged fermion mass basis as (mostly) independent order-one parameters. This scan, therefore, did not touch upon the viability of the model to explain the charged fermion masses or quark mixing. It identified the bounds on the radiative cLFV decays $\tau \to \mu\gamma$ and $\mu \to e\gamma$ as the most stringent constraints on parameter space, and was used to extract biases on effective LQ parameters to guide a more thorough numerical analysis. A simultaneous reconciliation of all anomalies proved to be very challenging in the primary scan.

In the second ("comprehensive") numerical study, all considered observables were included and the LQ parameters in the interaction basis were (mostly) varied as order-one parameters. A subset of them were fixed in a chi-squared fit in order to reproduce the charged fermion masses and CKM mixing matrix which yielded excellent agreement with experimental data in the case of scenario B. The remaining order-one parameters parametrising the LQ coupling matrices were biased with the help of results from the primary scan. The comprehensive scan demonstrated that this model is compatible with all considered experimental constraints and capable of explaining the observed deviations in $R(D)$, $R(D^\star)$ and Δa_μ from their SM predictions at the 3 σ level for $\hat{m}_\phi = 2$ and 4. Furthermore, even a reconciliation of the three anomalies at the level of 2 σ was shown to be achievable for $\hat{m}_\phi = 2$.

The direct use of the interaction basis turned out to be the main reason for the greater success of the comprehensive scan. For phenomenological purposes, it was found that the effective parameter b_{13} is preferred to be slightly smaller than expected from the construction of the model. Thus, in an improved attempt of model building, one should intend to further suppress the LQ coupling y_{13} by λ or λ^2. In several decay processes, contributions beyond the ones from photon penguins can play an important role, that is, in particular render $\tau \to 3\mu$ and $\tau \to \mu e \bar{e}$ accessible at Belle II. For the primary observables with neutrinos in the final state, i.e. $R(D)$, $R(D^\star)$, $R^{\nu}_{K^\star}$ and the lifetime of the B_c meson, LFV contributions are found to be definitely non-negligible in some instances.

The study laid out in this chapter can be extended in several directions. On the phenomenological side, it seems promising to study the observables $R(J/\psi)$ and $R(\Lambda_c)$ which are closely related to the $b \to c$ transitions analysed so far, as well as the angular distributions of the processes $B \to D^\star e_i \nu$ [133] and the longitudinal polarisation of the tau lepton in $B \to D^\star \tau \nu$ [131]. For some of these, the measured value (slightly) disagrees with the SM expectation, e.g. for $R(J/\psi)$ [130]. It may also be interesting to address other flavour anomalies like those observed in $b \to s$ transitions, that is, in $R(K)$, $R(K^\star)$ and in the process $B_s \to \mu\mu$; see e.g. ref. [421] for a recent concise overview. For this purpose, an additional LQ must be added to the model, for instance the one transforming as $(3, 3, -\frac{1}{3})$ under the SM gauge group; see e.g. refs. [362, 366, 371, 422]. Along the way, this may allow for incorporating a mechanism of neutrino-mass generation, for instance a seesaw mechanism via adding RH neutrinos [196], or a radiative mechanism; see ref. [50] for an extensive review. For simplicity, in the model under consideration it has been assumed that possible diquark couplings of ϕ are forbidden by a baryon-number symmetry. However, it could also be insightful to scrutinise the efficacy of G_f to suppress these couplings beyond the strong existing bounds from searches for proton decay [29]; see e.g. refs. [84, 423] for similar studies.

With non-vanishing neutrino masses, lepton mixing becomes physical and its appropriate description, i.e. two large mixing angles and one small one [38], may require a change in the assignment of the LH lepton doublets to representations of G_f or even the extension or modification of G_f itself. The observed lepton mixing angles are often interpreted as a hint towards the unification of the three generations of LH lepton doublets in an irreducible three-dimensional representation of the flavour symmetry; for reviews see refs. [175–178].

Prime candidates for such a flavour symmetry are members of the group series $\Delta(6\,n^2)$ with $n \geq 2$ integer [424] which were shown to allow for an adequate description of lepton mixing as well as quark mixing, see e.g. refs. [425–429], and of the charged fermion mass hierarchies if accompanied by an appropriate external symmetry; see e.g. the supersymmetric model in ref. [430]. A similarly profound change in the construction of the model might be necessary for an accommodation of $J_{\rm CP} \sim \lambda^6$ in terms of operators which respect (a modified version of) the flavour symmetry G_f. Lastly, one may consider extending G_f by a CP symmetry, given the constraining power regarding the two Majorana phases in the lepton sector [431] (see also refs. [321, 432–438]) and the extent of CP violation in the LQ couplings.

5.6 Appendix: Group Theory of D_{17}

In this appendix, the main features of the non-abelian discrete group D_{17} [374] are summarised. D_{17} is a member of the series of dihedral groups D_n which are non-abelian for $n \geq 3$. D_{17} features 34 distinct elements and ten real irreducible representations: the trivial singlet $\mathbf{1_1}$, a non-trivial singlet $\mathbf{1_2}$ as well as eight doublets, called $\mathbf{2_i}$ with $\mathbf{i} = 1, ..., 8$. All these eight doublets are faithful. Like the other dihedral groups, D_{17} can be described in terms of two generators a and b which satisfy

$$a^{17} = e \; , \quad b^2 = e \; , \quad a\,b\,a = b \tag{5.112}$$

where e denotes the neutral element of the group. Their representation matrices read

$$a(\mathbf{1_1}) = b(\mathbf{1_1}) = 1 \;\text{ and }\; a(\mathbf{1_2}) = 1 \; , \quad b(\mathbf{1_2}) = -1 \tag{5.113}$$

as well as

$$a(\mathbf{2_i}) = \begin{pmatrix} \omega_{17}^{\rm i} & 0 \\ 0 & \omega_{17}^{17-{\rm i}} \end{pmatrix} \;\text{ and }\; b(\mathbf{2_i}) = \begin{pmatrix} 0 & 1 \\ 1 & 0 \end{pmatrix} \; , \tag{5.114}$$

where $\omega_{17} = \exp\left(\frac{2\,\pi\,i}{17}\right)$ is the 17th root of unity. In this model, only the doublets $\mathbf{2_1}$, $\mathbf{2_2}$, $\mathbf{2_3}$ and $\mathbf{2_4}$ are used. Below, the most relevant Kronecker products and Clebsch-Gordan coefficients are presented which have a particularly simple form in the chosen basis. If a

and b are singlets and $(c_1\ \ c_2)^T$, $(d_1\ \ d_2)^T$ are doublets, one has [374]

$$\mathbf{1_1} \times \mathbf{1_1} : a\, b \sim \mathbf{1_1} \ , \tag{5.115a}$$

$$\mathbf{1_1} \times \mathbf{1_2} : a\, b \sim \mathbf{1_2} \ , \tag{5.115b}$$

$$\mathbf{1_2} \times \mathbf{1_2} : a\, b \sim \mathbf{1_1} \ , \tag{5.115c}$$

$$\mathbf{1_1} \times \mathbf{2_i} : \begin{pmatrix} a\, c_1 \\ a\, c_2 \end{pmatrix} \sim \mathbf{2_i} \ , \tag{5.115d}$$

$$\mathbf{1_2} \times \mathbf{2_i} : \begin{pmatrix} a\, c_1 \\ -a\, c_2 \end{pmatrix} \sim \mathbf{2_i} \ , \tag{5.115e}$$

$$\mathbf{2_1} \times \mathbf{2_1} : c_1\, d_2 + c_2\, d_1 \sim \mathbf{1_1} \ , \ \ c_1\, d_2 - c_2\, d_1 \sim \mathbf{1_2} \ , \ \begin{pmatrix} c_1\, d_1 \\ c_2\, d_2 \end{pmatrix} \sim \mathbf{2_2} \ , \tag{5.115f}$$

$$\mathbf{2_1} \times \mathbf{2_2} : \begin{pmatrix} c_2\, d_1 \\ c_1\, d_2 \end{pmatrix} \sim \mathbf{2_1} \ , \ \begin{pmatrix} c_1\, d_1 \\ c_2\, d_2 \end{pmatrix} \sim \mathbf{2_3} \ , \tag{5.115g}$$

$$\mathbf{2_2} \times \mathbf{2_2} : c_1\, d_2 + c_2\, d_1 \sim \mathbf{1_1} \ , \ \ c_1\, d_2 - c_2\, d_1 \sim \mathbf{1_2} \ , \ \begin{pmatrix} c_1\, d_1 \\ c_2\, d_2 \end{pmatrix} \sim \mathbf{2_4} \ , \tag{5.115h}$$

$$\mathbf{2_1} \times \mathbf{2_3} : \begin{pmatrix} c_2\, d_1 \\ c_1\, d_2 \end{pmatrix} \sim \mathbf{2_2} \ , \ \begin{pmatrix} c_1\, d_1 \\ c_2\, d_2 \end{pmatrix} \sim \mathbf{2_4} \ , \tag{5.115i}$$

$$\mathbf{2_2} \times \mathbf{2_3} : \begin{pmatrix} c_2\, d_1 \\ c_1\, d_2 \end{pmatrix} \sim \mathbf{2_1} \ , \ \begin{pmatrix} c_1\, d_1 \\ c_2\, d_2 \end{pmatrix} \sim \mathbf{2_5} \ , \tag{5.115j}$$

$$\mathbf{2_3} \times \mathbf{2_3} : c_1\, d_2 + c_2\, d_1 \sim \mathbf{1_1} \ , \ \ c_1\, d_2 - c_2\, d_1 \sim \mathbf{1_2} \ , \ \begin{pmatrix} c_1\, d_1 \\ c_2\, d_2 \end{pmatrix} \sim \mathbf{2_6} \ , \tag{5.115k}$$

$$\mathbf{2_1} \times \mathbf{2_4} : \begin{pmatrix} c_2\, d_1 \\ c_1\, d_2 \end{pmatrix} \sim \mathbf{2_3} \ , \ \begin{pmatrix} c_1\, d_1 \\ c_2\, d_2 \end{pmatrix} \sim \mathbf{2_5} \ , \tag{5.115l}$$

$$\mathbf{2_2} \times \mathbf{2_4} : \begin{pmatrix} c_2\, d_1 \\ c_1\, d_2 \end{pmatrix} \sim \mathbf{2_2} \ , \ \begin{pmatrix} c_1\, d_1 \\ c_2\, d_2 \end{pmatrix} \sim \mathbf{2_6} \ , \tag{5.115m}$$

$$\mathbf{2_3} \times \mathbf{2_4} : \begin{pmatrix} c_2\, d_1 \\ c_1\, d_2 \end{pmatrix} \sim \mathbf{2_1} \ , \ \begin{pmatrix} c_1\, d_1 \\ c_2\, d_2 \end{pmatrix} \sim \mathbf{2_7} \ , \tag{5.115n}$$

$$\mathbf{2_4} \times \mathbf{2_4} : c_1\, d_2 + c_2\, d_1 \sim \mathbf{1_1} \ , \ \ c_1\, d_2 - c_2\, d_1 \sim \mathbf{1_2} \ , \ \begin{pmatrix} c_1\, d_1 \\ c_2\, d_2 \end{pmatrix} \sim \mathbf{2_8} \ . \tag{5.115o}$$

In addition, it should be pointed out that the Clebsch-Gordan coefficients for combinations involving conjugated fields have a slightly different form, since a complex matrix is chosen for the generator a in the two-dimensional (real) representations $\mathbf{2_i}$. For a being a singlet and $(c_1 \;\; c_2)^T$, $(d_1 \;\; d_2)^T$ being doublets, the combinations involving $c^*_{1,2}$ read e.g.

$$\mathbf{2_i} \times \mathbf{1_1} : \begin{pmatrix} c_2^* \, a \\ c_1^* \, a \end{pmatrix} \sim \mathbf{2_i} \; , \tag{5.116a}$$

$$\mathbf{2_i} \times \mathbf{1_2} : \begin{pmatrix} c_2^* \, a \\ -c_1^* \, a \end{pmatrix} \sim \mathbf{2_i} \; , \tag{5.116b}$$

$$\mathbf{2_1} \times \mathbf{2_1} : c_1^* \, d_1 + c_2^* \, d_2 \sim \mathbf{1_1} \; , \;\; c_1^* \, d_1 - c_2^* \, d_2 \sim \mathbf{1_2} \; , \;\; \begin{pmatrix} c_2^* \, d_1 \\ c_1^* \, d_2 \end{pmatrix} \sim \mathbf{2_2} \; , \tag{5.116c}$$

$$\mathbf{2_1} \times \mathbf{2_2} : \begin{pmatrix} c_1^* \, d_1 \\ c_2^* \, d_2 \end{pmatrix} \sim \mathbf{2_1} \; , \;\; \begin{pmatrix} c_2^* \, d_1 \\ c_1^* \, d_2 \end{pmatrix} \sim \mathbf{2_3} \; . \tag{5.116d}$$

The general form of the Kronecker products and Clebsch-Gordan coefficients can be found in ref. [374].

5.7 Appendix: Lagrangians

In this section, I list the operators contributing to the charged fermion mass matrices M_u, M_d and M_e, and to the LQ couplings $\hat{\mathbf{x}}$ and $\hat{\mathbf{y}}$ as defined in eq. (5.4). I include operators that contribute up to and including order λ^{12} in the symmetry-breaking parameter, and assume the VEVs of the spurions S, T, U and W as given in eq. (5.9). Each operator is accompanied by a complex order-one coefficient. When the operators are listed, they are usually ordered according to the number of spurion insertions. Furthermore, note that the spurions are treated as dimensionless flavour-symmetry breaking fields; thus, no cutoff scale is needed to establish the correct mass dimension of the operators.

Note that for any given operator in the lists below there might be more than one combination of the contained fields which yields an invariant of the flavour symmetry G_f, and thus more than one independent contribution to the charged fermion mass matrices M_u,

M_d and M_e or the LQ couplings $\hat{\mathbf{x}}$ and $\hat{\mathbf{y}}$ from one operator. These instances are signaled via the usage of primed operator efficients, e.g. α_8^d, $(\alpha_8^d)'$ – see eq. (5.141). Generally, I omit all operators which carry insertions of $S\,S^\dagger$, $T\,T^\dagger$, $U\,U^\dagger$ and $W\,W^\dagger$, and products or powers thereof. Typically, these solely duplicate the contribution from the corresponding operators without the respective insertions, but are further suppressed by at least λ^2, λ^4 and $\lesssim \lambda^8$, depending on the spurion involved. There are two exceptions to this rule:

- The up-type quark mass matrix elements $(M_u)_{12}$ and $(M_u)_{22}$ feature the same LO contribution arising from the second operator in eq. (5.117), but the subleading contributions appearing at the relative order λ^2 are not identical due to the first operator in eq. (5.118) which involves the combination $S\,S^\dagger$. This can be seen explicitly in eq. (5.140).
- The combination $W\,W^\dagger$ contains a covariant in $\mathbf{2_4}$ with a non-vanishing VEV, thus some operators with this insertion may yield non-redundant contributions. Nonetheless, they are always suppressed by at least λ^8 compared to the contribution from the respective operator without the insertion.

5.7.1 Up-Quark Sector

In the up-quark sector, I identify four LO operators that generate the up-type quark masses and the three quark mixing angles:

$$\begin{aligned}\mathcal{L}^u_{\text{Yuk,LO}} &= \alpha_1^u\,\overline{Q_{L3}}\,H_u\,u_{R3} + \alpha_2^u\,\overline{Q_L}\,H_u\,u_{R2}\,W \\ &\quad + \alpha_3^u\,\overline{Q_L}\,H_u\,u_{R3}\,(S^\dagger)^2 + \alpha_4^u\,\overline{Q_L}\,H_u\,u_{R1}\,T^2\,U\ .\end{aligned} \tag{5.117}$$

At subleading order, the up-type quark mass matrix receives contributions up to and including λ^{12} from the following operators

$$\begin{aligned}
\mathcal{L}^u_{\text{Yuk,SLO}} = {} & \alpha^u_5 \, \overline{Q_L} \, H_u \, u_{R2} \, S \, S^\dagger \, W + \alpha^u_6 \, \overline{Q_L} \, H_u \, u_{R2} \, (S^\dagger)^4 \, T \\
& + \alpha^u_7 \, \overline{Q_{L3}} \, H_u \, u_{R2} \, (S^\dagger)^2 \, T + \alpha^u_8 \, \overline{Q_{L3}} \, H_u \, u_{R2} \, (W^\dagger)^2 \\
& + \alpha^u_9 \, \overline{Q_L} \, H_u \, u_{R2} \, W^2 \, W^\dagger + \alpha^u_{10} \, \overline{Q_L} \, H_u \, u_{R1} \, T \, U^2 \\
& + \alpha^u_{11} \, \overline{Q_{L3}} \, H_u \, u_{R2} \, S^2 \, W + \alpha^u_{12} \, \overline{Q_L} \, H_u \, u_{R2} \, T^\dagger \, U \, W \\
& + \alpha^u_{13} \, \overline{Q_L} \, H_u \, u_{R2} \, T \, U^\dagger \, W + \alpha^u_{14} \, \overline{Q_L} \, H_u \, u_{R3} \, T^\dagger \, (W^\dagger)^2 \\
& + \alpha^u_{15} \, \overline{Q_L} \, H_u \, u_{R3} \, (S^\dagger)^2 \, T \, U^\dagger + \alpha^u_{16} \, \overline{Q_L} \, H_u \, u_{R3} \, S^2 \, T^\dagger \, W \\
& + \alpha^u_{17} \, \overline{Q_L} \, H_u \, u_{R3} \, S^2 \, U^\dagger \, W + \alpha^u_{18} \, \overline{Q_L} \, H_u \, u_{R2} \, S^2 \, T^\dagger \, W^\dagger \\
& + \alpha^u_{19} \, \overline{Q_L} \, H_u \, u_{R2} \, S^2 \, U^\dagger \, W^\dagger + \alpha^u_{20} \, \overline{Q_L} \, H_u \, u_{R2} \, (S^\dagger)^2 \, (W^\dagger)^2 \\
& + \alpha^u_{21} \, \overline{Q_L} \, H_u \, u_{R3} \, (S^\dagger)^2 \, W \, W^\dagger + \alpha^u_{22} \, \overline{Q_{L3}} \, H_u \, u_{R1} \, S^2 \, T \, U^2 \\
& + \alpha^u_{23} \, \overline{Q_{L3}} \, H_u \, u_{R1} \, (S^\dagger)^4 \, (U^\dagger)^2 + \alpha^u_{24} \, \overline{Q_{L3}} \, H_u \, u_{R3} \, S^4 \, T^\dagger \, W \\
& + \alpha^u_{25} \, \overline{Q_{L3}} \, H_u \, u_{R3} \, (S^\dagger)^4 \, T \, W^\dagger + \alpha^u_{26} \, \overline{Q_{L3}} \, H_u \, u_{R2} \, S^4 \, T^\dagger \, W^\dagger \\
& + \alpha^u_{27} \, \overline{Q_L} \, H_u \, u_{R2} \, (S^\dagger)^4 \, T^2 \, U^\dagger + \alpha^u_{28} \, \overline{Q_L} \, H_u \, u_{R3} \, S^4 \, (T^\dagger)^2 \, W^\dagger \\
& + \alpha^u_{29} \, \overline{Q_L} \, H_u \, u_{R2} \, S^6 \, (T^\dagger)^2 + \alpha^u_{30} \, \overline{Q_L} \, H_u \, u_{R3} \, (S^\dagger)^6 \, T \, W^\dagger \; .
\end{aligned} \tag{5.118}$$

Among these, the first two operators contribute at the relative order λ^2 to the elements $(M_u)_{12}$ and $(M_u)_{22}$ and are thus the most important ones. The operators with the coefficients α^u_6 and α^u_7 are examples of operators which are automatically allowed once the field content of the LO operators is determined. I note that several of the subleading operators yield two independent contributions to the up-type quark mass matrix M_u. The operator with the coefficient α^u_5 induces contributions of order λ^6 to the element $(M_u)_{22}$ and of order λ^7 to the element $(M_u)_{12}$, but with a different relative sign; the one with α^u_{14} gives contributions of order λ^{10} and λ^{11}; the one with α^u_{16} yields contributions of order λ^8 and λ^9; the one with α^u_{18} leads to contributions of order λ^8 and λ^9; finally, the operator with the coefficient α^u_{20} gives rise to two independent contributions of order λ^{10} and λ^{11}, respectively.

5.7.2 Down-Quark Sector

There are three operators which induce the respective dominant contributions to the down-type quark masses:

$$\mathcal{L}^d_{\text{Yuk,LO}} = \alpha^d_1 \, \overline{Q_{L3}} \, H_d \, d_{R3} + \alpha^d_2 \, \overline{Q_L} \, H_d \, d_R \, T + \alpha^d_3 \, \overline{Q_L} \, H_d \, d_R \, U \; . \tag{5.119}$$

At subleading order, I find

$$\begin{aligned} \mathcal{L}^d_{\text{Yuk,SLO}} = {} & \alpha^d_4 \, \overline{Q_L} \, H_d \, d_{R3} \, (S^\dagger)^2 + \alpha^d_5 \, \overline{Q_{L3}} \, H_d \, d_R \, S^2 \, T \\ & + \alpha^d_6 \, \overline{Q_L} \, H_d \, d_R \, T^\dagger \, U^2 + \alpha^d_7 \, \overline{Q_L} \, H_d \, d_R \, T^2 \, U^\dagger \\ & + \alpha^d_8 \, \overline{Q_L} \, H_d \, d_{R3} \, T^\dagger \, (W^\dagger)^2 + \alpha^d_9 \, \overline{Q_L} \, H_d \, d_R \, T \, W \, W^\dagger \\ & + \alpha^d_{10} \, \overline{Q_L} \, H_d \, d_{R3} \, (S^\dagger)^2 \, T \, U^\dagger + \alpha^d_{11} \, \overline{Q_L} \, H_d \, d_{R3} \, S^2 \, T^\dagger \, W \\ & + \alpha^d_{12} \, \overline{Q_L} \, H_d \, d_{R3} \, S^2 \, U^\dagger \, W + \alpha^d_{13} \, \overline{Q_L} \, H_d \, d_R \, S^2 \, (W^\dagger)^2 \\ & + \alpha^d_{14} \, \overline{Q_L} \, H_d \, d_{R3} \, (S^\dagger)^2 \, W \, W^\dagger + \alpha^d_{15} \, \overline{Q_{L3}} \, H_d \, d_R \, S^2 \, T^\dagger \, U^2 \\ & + \alpha^d_{16} \, \overline{Q_L} \, H_d \, d_R \, S^4 \, W + \alpha^d_{17} \, \overline{Q_{L3}} \, H_d \, d_R \, (S^\dagger)^2 \, T^2 \, W^\dagger \\ & + \alpha^d_{18} \, \overline{Q_{L3}} \, H_d \, d_{R3} \, S^4 \, T^\dagger \, W + \alpha^d_{19} \, \overline{Q_{L3}} \, H_d \, d_{R3} \, (S^\dagger)^4 \, T \, W^\dagger \\ & + \alpha^d_{20} \, \overline{Q_{L3}} \, H_d \, d_R \, S^6 \, W + \alpha^d_{21} \, \overline{Q_L} \, H_d \, d_R \, (S^\dagger)^4 \, T^2 \, W^\dagger \\ & + \alpha^d_{22} \, \overline{Q_L} \, H_d \, d_{R3} \, S^4 \, (T^\dagger)^2 \, W^\dagger + \alpha^d_{23} \, \overline{Q_L} \, H_d \, d_{R3} \, (S^\dagger)^6 \, T \, W^\dagger \\ & + \alpha^d_{24} \, \overline{Q_L} \, H_d \, d_R \, S^6 \, T^\dagger \, W^\dagger + \alpha^d_{25} \, \overline{Q_L} \, H_d \, d_R \, (S^\dagger)^7 \, (T^\dagger)^2 \; . \end{aligned} \tag{5.120}$$

The existence of the first operator herein is an immediate consequence of the corresponding operator in the up-quark sector being invariant. Similarly, the second operator with the coefficient α^d_5 is automatically induced once the LO operators which generate the charged fermion mass matrices and the LQ couplings $\hat{\mathbf{x}}$ and $\hat{\mathbf{y}}$ are included.

There are several operators which yield more than one independent contraction: the operator with the coefficient α^d_8 leads to two independent contributions of order λ^{10} and λ^{11} to the down-type quark mass matrix; the one with α^d_9 yields two contributions, both of order λ^{11}; the operator with α^d_{11} gives two contributions of order λ^8 and λ^9; the one with α^d_{13} leads to three contributions of order λ^{10}, λ^{11} and λ^{12}; finally, the operator with the coefficient α^d_{16} implies two contributions of order λ^8 and λ^9.

5.7.3 Charged Lepton Sector

In complete analogy to the down-type quark sector, I identify the corresponding LO operators in the charged lepton sector

$$\mathcal{L}^e_{\text{Yuk,LO}} = \alpha^e_1 \, \overline{L_{L3}} \, H_d \, e_{R3} + \alpha^e_2 \, \overline{L_L} \, H_d \, e_R \, T + \alpha^e_3 \, \overline{L_L} \, H_d \, e_R \, U \ . \tag{5.121}$$

Still, the subleading operators are generally not equivalent:

$$\begin{aligned}
\mathcal{L}^e_{\text{Yuk,SLO}} = {} & \alpha^e_4 \, \overline{L_L} \, H_d \, e_{R3} \, S^\dagger + \alpha^e_5 \, \overline{L_{L3}} \, H_d \, e_R \, S \, T \\
& + \alpha^e_6 \, \overline{L_L} \, H_d \, e_R \, T \, W \, W^\dagger + \alpha^e_7 \, \overline{L_{L3}} \, H_d \, e_R \, S^\dagger \, (T^\dagger)^2 \, W^\dagger \\
& + \alpha^e_8 \, \overline{L_{L3}} \, H_d \, e_R \, S^\dagger \, T^\dagger \, U^\dagger \, W^\dagger + \alpha^e_9 \, \overline{L_L} \, H_d \, e_R \, S^2 \, (W^\dagger)^2 \\
& + \alpha^e_{10} \, \overline{L_L} \, H_d \, e_{R3} \, S \, T^\dagger \, (W^\dagger)^2 + \alpha^e_{11} \, \overline{L_L} \, H_d \, e_R \, S^2 \, (T^\dagger)^3 \\
& + \alpha^e_{12} \, \overline{L_L} \, H_d \, e_R \, S^2 \, T^\dagger \, (U^\dagger)^2 + \alpha^e_{13} \, \overline{L_L} \, H_d \, e_R \, S^4 \, W \\
& + \alpha^e_{14} \, \overline{L_L} \, H_d \, e_{R3} \, S^3 \, T^\dagger \, W + \alpha^e_{15} \, \overline{L_{L3}} \, H_d \, e_R \, (S^\dagger)^3 \, T^\dagger \, W \\
& + \alpha^e_{16} \, \overline{L_{L3}} \, H_d \, e_R \, (S^\dagger)^3 \, U^\dagger \, W + \alpha^e_{17} \, \overline{L_L} \, H_d \, e_R \, (S^\dagger)^2 \, (T^\dagger)^2 \, W^\dagger \\
& + \alpha^e_{18} \, \overline{L_{L3}} \, H_d \, e_R \, S^3 \, (W^\dagger)^2 + \alpha^e_{19} \, \overline{L_{L3}} \, H_d \, e_R \, S^3 \, (T^\dagger)^3 \\
& + \alpha^e_{20} \, \overline{L_{L3}} \, H_d \, e_R \, S^5 \, W + \alpha^e_{21} \, \overline{L_{L3}} \, H_d \, e_{R3} \, S^4 \, T^\dagger \, W \\
& + \alpha^e_{22} \, \overline{L_L} \, H_d \, e_R \, (S^\dagger)^4 \, T^\dagger \, W + \alpha^e_{23} \, \overline{L_L} \, H_d \, e_R \, (S^\dagger)^4 \, U^\dagger \, W \\
& + \alpha^e_{24} \, \overline{L_{L3}} \, H_d \, e_{R3} \, (S^\dagger)^4 \, T \, W^\dagger + \alpha^e_{25} \, \overline{L_{L3}} \, H_d \, e_R \, (S^\dagger)^3 \, T^2 \, W^\dagger \\
& + \alpha^e_{26} \, \overline{L_L} \, H_d \, e_{R3} \, (S^\dagger)^5 \, T \, W^\dagger + \alpha^e_{27} \, \overline{L_L} \, H_d \, e_R \, (S^\dagger)^4 \, T^2 \, W^\dagger \ .
\end{aligned} \tag{5.122}$$

The appearance of the first operator herein has already been commented on in section 5.3.2. The second one with the coefficient α^e_5 also turns out to be an operator that is automatically induced upon fixing the field content of the LO operators which are responsible for the dominant contributions to the charged fermion mass matrices and the LQ couplings $\hat{\mathbf{x}}$ and $\hat{\mathbf{y}}$. I note that only the operator with the coefficient α^e_9 gives rise to two independent contributions to the charged lepton mass matrix M_e: one of order λ^{11} and another one of order λ^{12}, see also eq. (5.142).

5.7.4 Leptoquark Couplings in Interaction Basis

For the LQ couplings, I begin with the LO operators which are responsible for the structure of the (23)-block in the LQ coupling $\hat{\mathbf{x}}$:

$$\mathcal{L}^{\text{int}}_{\hat{\mathbf{x}},\text{LO}} = \beta^L_1\, \overline{L^c_{L3}}\, \phi^\dagger\, Q_{L3} + \beta^L_2\, \overline{L^c_L}\, \phi^\dagger\, Q_{L3}\, S + \beta^L_3\, \overline{L^c_{L3}}\, \phi^\dagger\, Q_L\, S^2 + \beta^L_4\, \overline{L^c_L}\, \phi^\dagger\, Q_L\, S^3\ . \tag{5.123}$$

At subleading order, I find several additional operators

$$\begin{aligned}
\mathcal{L}^{\text{int}}_{\hat{\mathbf{x}},\text{SLO}} = {}& \beta^L_5\, \overline{L^c_{L3}}\, \phi^\dagger\, Q_L\, T\, W^2 + \beta^L_6\, \overline{L^c_L}\, \phi^\dagger\, Q_L\, S^\dagger\, T\, W^\dagger \\
&+ \beta^L_7\, \overline{L^c_L}\, \phi^\dagger\, Q_L\, S^\dagger\, U\, W^\dagger + \beta^L_8\, \overline{L^c_{L3}}\, \phi^\dagger\, Q_L\, S^2\, T^\dagger\, U \\
&+ \beta^L_9\, \overline{L^c_L}\, \phi^\dagger\, Q_L\, S^\dagger\, (T^\dagger)^2\, W + \beta^L_{10}\, \overline{L^c_L}\, \phi^\dagger\, Q_L\, S^\dagger\, T^\dagger\, U^\dagger\, W \\
&+ \beta^L_{11}\, \overline{L^c_L}\, \phi^\dagger\, Q_L\, S\, T\, W^2 + \beta^L_{12}\, \overline{L^c_L}\, \phi^\dagger\, Q_{L3}\, S^\dagger\, T\, W^2 \\
&+ \beta^L_{13}\, \overline{L^c_{L3}}\, \phi^\dagger\, Q_L\, (S^\dagger)^2\, T\, W^\dagger + \beta^L_{14}\, \overline{L^c_{L3}}\, \phi^\dagger\, Q_L\, (S^\dagger)^2\, U\, W^\dagger \\
&+ \beta^L_{15}\, \overline{L^c_{L3}}\, \phi^\dagger\, Q_L\, S^2\, W\, W^\dagger + \beta^L_{16}\, \overline{L^c_L}\, \phi^\dagger\, Q_L\, S^3\, T^\dagger\, U \\
&+ \beta^L_{17}\, \overline{L^c_L}\, \phi^\dagger\, Q_{L3}\, (S^\dagger)^3\, T\, W^\dagger + \beta^L_{18}\, \overline{L^c_L}\, \phi^\dagger\, Q_L\, S\, (T^\dagger)^3\, W^\dagger \\
&+ \beta^L_{19}\, \overline{L^c_L}\, \phi^\dagger\, Q_L\, S^3\, W\, W^\dagger + \beta^L_{20}\, \overline{L^c_L}\, \phi^\dagger\, Q_L\, (S^\dagger)^5\, U^\dagger \\
&+ \beta^L_{21}\, \overline{L^c_L}\, \phi^\dagger\, Q_L\, (S^\dagger)^3\, T^2\, W + \beta^L_{22}\, \overline{L^c_{L3}}\, \phi^\dagger\, Q_{L3}\, S^4\, T^\dagger\, W \\
&+ \beta^L_{23}\, \overline{L^c_{L3}}\, \phi^\dagger\, Q_{L3}\, (S^\dagger)^4\, T\, W^\dagger + \beta^L_{24}\, \overline{L^c_{L3}}\, \phi^\dagger\, Q_L\, (S^\dagger)^4\, T^2\, W \\
&+ \beta^L_{25}\, \overline{L^c_L}\, \phi^\dagger\, Q_{L3}\, S^5\, T^\dagger\, W + \beta^L_{26}\, \overline{L^c_{L3}}\, \phi^\dagger\, Q_L\, S^6\, T^\dagger\, W\ .
\end{aligned} \tag{5.124}$$

All couplings β^L_i are complex order-one coefficients. As was the case in the charged fermion sector, I note that several of these operators induce two respective independent contributions to the LQ coupling $\hat{\mathbf{x}}$. The operator with the coefficient β^L_5 leads to contributions of order λ^{10} and λ^{11}; the one with β^L_6 gives contributions of order λ^7 and λ^8; the operator with β^L_{10} induces two contributions of order λ^{11} and λ^{12}; the one with β^L_{11} yields contributions of order λ^{11} and λ^{12}; the one with β^L_{13} gives rise to two contributions of order λ^8 and λ^9; finally, the operator with the coefficient β^L_{21} leads to two independent contributions of order λ^{11} and λ^{12}.

Lastly, I also list the operators which contribute to the LQ coupling $\hat{\mathbf{y}}$ up to and including order λ^{12}. As expected from the construction of the model, I identify only two LO operators

$$\mathcal{L}^{\text{int}}_{\hat{\mathbf{y}},\text{LO}} = \beta^R_1\, \overline{e^c_{R3}}\, \phi^\dagger\, u_{R2} + \beta^R_2\, \overline{e^c_R}\, \phi^\dagger\, u_{R3}\, S^3 \; . \tag{5.125}$$

Additional operators are found at the subleading level

$$\begin{aligned}
\mathcal{L}^{\text{int}}_{\hat{\mathbf{y}},\text{SLO}} = {} & \beta^R_3\, \overline{e^c_R}\, \phi^\dagger\, u_{R2}\, S\, T + \beta^R_4\, \overline{e^c_{R3}}\, \phi^\dagger\, u_{R3}\, S^2\, T^\dagger \\
& + \beta^R_5\, \overline{e^c_{R3}}\, \phi^\dagger\, u_{R3}\, W^2 + \beta^R_6\, \overline{e^c_R}\, \phi^\dagger\, u_{R1}\, S^\dagger\, (U^\dagger)^2 \\
& + \beta^R_7\, \overline{e^c_R}\, \phi^\dagger\, u_{R1}\, S\, U\, W + \beta^R_8\, \overline{e^c_{R3}}\, \phi^\dagger\, u_{R3}\, (S^\dagger)^2\, W^\dagger \\
& + \beta^R_9\, \overline{e^c_R}\, \phi^\dagger\, u_{R3}\, S^\dagger\, T\, W^\dagger + \beta^R_{10}\, \overline{e^c_R}\, \phi^\dagger\, u_{R3}\, S^\dagger\, (T^\dagger)^2\, W \\
& + \beta^R_{11}\, \overline{e^c_R}\, \phi^\dagger\, u_{R3}\, S^\dagger\, T^\dagger\, U^\dagger\, W + \beta^R_{12}\, \overline{e^c_R}\, \phi^\dagger\, u_{R3}\, S\, T\, W^2 \\
& + \beta^R_{13}\, \overline{e^c_R}\, \phi^\dagger\, u_{R2}\, S^\dagger\, (T^\dagger)^2\, W^\dagger + \beta^R_{14}\, \overline{e^c_R}\, \phi^\dagger\, u_{R2}\, S^\dagger\, T^\dagger\, U^\dagger\, W^\dagger \\
& + \beta^R_{15}\, \overline{e^c_R}\, \phi^\dagger\, u_{R1}\, (S^\dagger)^3\, T\, U + \beta^R_{16}\, \overline{e^c_{R3}}\, \phi^\dagger\, u_{R1}\, (S^\dagger)^2\, T^\dagger\, (U^\dagger)^2 \\
& + \beta^R_{17}\, \overline{e^c_R}\, \phi^\dagger\, u_{R2}\, (S^\dagger)^3\, T^\dagger\, W + \beta^R_{18}\, \overline{e^c_R}\, \phi^\dagger\, u_{R2}\, (S^\dagger)^3\, U^\dagger\, W \\
& + \beta^R_{19}\, \overline{e^c_R}\, \phi^\dagger\, u_{R3}\, S\, (T^\dagger)^3\, W^\dagger + \beta^R_{20}\, \overline{e^c_R}\, \phi^\dagger\, u_{R2}\, S^3\, (W^\dagger)^2 \\
& + \beta^R_{21}\, \overline{e^c_R}\, \phi^\dagger\, u_{R2}\, S^3\, (T^\dagger)^3 + \beta^R_{22}\, \overline{e^c_{R3}}\, \phi^\dagger\, u_{R1}\, S^4\, U^2 \\
& + \beta^R_{23}\, \overline{e^c_R}\, \phi^\dagger\, u_{R3}\, (S^\dagger)^5\, U^\dagger + \beta^R_{24}\, \overline{e^c_R}\, \phi^\dagger\, u_{R2}\, S^5\, W \\
& + \beta^R_{25}\, \overline{e^c_{R3}}\, \phi^\dagger\, u_{R3}\, (S^\dagger)^4\, T\, W + \beta^R_{26}\, \overline{e^c_R}\, \phi^\dagger\, u_{R3}\, (S^\dagger)^3\, T^2\, W \\
& + \beta^R_{27}\, \overline{e^c_{R3}}\, \phi^\dagger\, u_{R2}\, S^4\, T^\dagger\, W + \beta^R_{28}\, \overline{e^c_{R3}}\, \phi^\dagger\, u_{R2}\, (S^\dagger)^4\, T\, W^\dagger \\
& + \beta^R_{29}\, \overline{e^c_R}\, \phi^\dagger\, u_{R2}\, (S^\dagger)^3\, T^2\, W^\dagger \; ,
\end{aligned} \tag{5.126}$$

with all coefficients β^R_i being complex order-one numbers. The presence of the first and the second operator is automatic upon fixing the transformation properties of the fields which are relevant for the LO terms of the charged fermion mass matrices M_u, M_d, M_e and the LQ couplings $\hat{\mathbf{x}}$ and $\hat{\mathbf{y}}$. I note that all listed operators give rise to a single (independent) contribution to $\hat{\mathbf{y}}$.

5.8 Appendix: Mass Matrices and Leptoquark Couplings in Scenario A

For the sake of contrast with section 5.3 where scenario B was focussed on, herein I present the form of the up-type quark mass matrix M_u, the unitary matrices L_u and R_u, and the form of the LQ couplings $\mathbf{x}$, $\mathbf{y}$ and $\mathbf{z}$ as defined in eq. (5.5) in scenario A. As there is no difference between the respective down-quark and charged lepton mass matrices in the two scenarios, they are not explicitly referred to in this section.

5.8.1 Up-Quark Sector

In the absence of an enhancement of the element $(M_u)_{13}$ as is present in scenario B, the effective parametrisation of the up-type quark mass matrix up to and including order λ^{12} reads in scenario A

$$M_u = \begin{pmatrix} f_{11}\,\lambda^8 & f_{12}\,\lambda^5 & f_{13}\,\lambda^8 \\ f_{21}\,\lambda^{10} & f_{22}\,\lambda^4 & f_{23}\,\lambda^2 \\ f_{31}\,\lambda^{12} & f_{32}\,\lambda^4 & f_{33} \end{pmatrix} \left\langle H_u^0 \right\rangle \,, \tag{5.127}$$

where f_{ij} are generally independent, complex order-one numbers, apart from f_{12} and f_{22}, see section 5.3.1.1. Regarding the up-type quark masses, the only difference between scenario A and scenario B is related to subleading corrections to the top-quark mass m_t which appear at order λ^8 in scenario A, but at order λ^6 in scenario B.

The matrices L_u and R_u transforming LH and RH up-type quarks from the interaction to the mass basis read, up to and including order λ^{12},

$$L_u = \begin{pmatrix} 1-\frac{f_{12}^2}{2\,f_{22}^2}\,\lambda^2+\mathcal{O}(\lambda^4) & \frac{f_{12}}{f_{22}}\,\lambda+\mathcal{O}(\lambda^3) & \frac{f_{13}}{f_{33}}\,\lambda^8+\mathcal{O}(\lambda^9) \\ -\frac{f_{12}}{f_{22}}\,\lambda+\mathcal{O}(\lambda^3) & 1-\frac{f_{12}^2}{2\,f_{22}^2}\,\lambda^2+\mathcal{O}(\lambda^4) & \frac{f_{23}}{f_{33}}\,\lambda^2+\mathcal{O}(\lambda^6) \\ \frac{f_{12}f_{23}}{f_{22}f_{33}}\,\lambda^3+\mathcal{O}(\lambda^5) & -\frac{f_{23}}{f_{33}}\,\lambda^2+\mathcal{O}(\lambda^4) & 1-\frac{f_{23}^2}{2\,f_{33}^2}\,\lambda^4+\mathcal{O}(\lambda^8) \end{pmatrix} \tag{5.128}$$

and

$$R_u = \begin{pmatrix} 1+\mathcal{O}(\lambda^{10}) & \frac{f_{11}f_{12}}{f_{22}^2}\,\lambda^5+\mathcal{O}(\lambda^6) & \frac{f_{21}f_{23}+f_{31}f_{33}}{f_{33}^2}\,\lambda^{12}+\wr(\lambda^{12}) \\ -\frac{f_{11}f_{12}}{f_{22}^2}\,\lambda^5+\mathcal{O}(\lambda^6) & 1+\mathcal{O}(\lambda^8) & \frac{f_{32}}{f_{33}}\,\lambda^4+\mathcal{O}(\lambda^6) \\ \frac{f_{11}f_{12}f_{32}}{f_{22}^2 f_{33}}\,\lambda^9+\mathcal{O}(\lambda^{10}) & -\frac{f_{32}}{f_{33}}\,\lambda^4+\mathcal{O}(\lambda^6) & 1+\mathcal{O}(\lambda^8) \end{pmatrix} . \tag{5.129}$$

5.8.2 Quark Mixing

From the matrices L_u and L_d shown in eq. (5.128) and eq. (5.18), respectively, I obtain the following CKM mixing matrix in scenario A

$$V = L_u^\dagger\, L_d = \begin{pmatrix} 1-\frac{f_{12}^2}{2\,f_{22}^2}\,\lambda^2+\mathcal{O}(\lambda^4) & -\frac{f_{12}}{f_{22}}\,\lambda+\mathcal{O}(\lambda^3) & \frac{f_{12}}{f_{22}}V_{32}\,\lambda^3+\mathcal{O}(\lambda^5) \\ \frac{f_{12}}{f_{22}}\,\lambda+\mathcal{O}(\lambda^3) & 1-\frac{f_{12}^2}{2\,f_{22}^2}\,\lambda^2+\mathcal{O}(\lambda^4) & -V_{32}\,\lambda^2+\mathcal{O}(\lambda^4) \\ V_{31}\,\lambda^8+\mathcal{O}(\lambda^9) & V_{32}\,\lambda^2+\mathcal{O}(\lambda^6) & 1-\frac{1}{2}(V_{32})^2\,\lambda^4+\mathcal{O}(\lambda^6) \end{pmatrix} \tag{5.130}$$

with

$$V_{32} \equiv \frac{f_{23}}{f_{33}} - \frac{d_{23}}{d_{33}} \tag{5.131}$$

and

$$V_{31} \equiv \frac{f_{13}}{f_{33}} - \frac{d_{13}}{d_{33}} - \frac{d_{12}}{d_{22}}V_{32}\ . \tag{5.132}$$

Obviously, the element $V_{td} \sim \lambda^8$ is predicted to be further suppressed than the experimentally measured value $|V_{td}| = 0.00854^{+0.00023}_{-0.00016} \sim \lambda^3$ [29]. Furthermore, assuming that the effective parameters d_{ij} and f_{ij} are complex, one can estimate the size of the Jarlskog invariant as in $J_{\text{CP}} \sim \lambda^{11}$, see eq. (2.29), which is in conflict with the measured value, $J_{\text{CP}} = \left(3.00^{+0.15}_{-0.09}\right) \times 10^{-5} \sim \lambda^6$ [29].

In addition, I note that the predicted relation between V_{us}, V_{cb} and V_{ub} is too tight to accommodate all three CKM-matrix elements in accordance with experimental data [29]. One has

$$|V_{us}| \approx \left|\frac{f_{12}}{f_{22}}\right| \lambda \sim \lambda \ \text{ and } \ |V_{cb}| \approx \left|\frac{f_{23}}{f_{33}} - \frac{d_{23}}{d_{33}}\right| \lambda^2 \sim \lambda^2 \tag{5.133}$$

as well as

$$|V_{ub}| \approx \left|\frac{f_{12}}{f_{22}}\left(\frac{f_{23}}{f_{33}} - \frac{d_{23}}{d_{33}}\right)\right| \lambda^3 \approx |V_{us}|\,|V_{cb}|\ , \tag{5.134}$$

so that $|V_{us}| = 0.22650$ and $|V_{cb}| = 0.04053$ [29] imply $|V_{ub}| \approx 0.0092$. Compared to the experimental best-fit value $|V_{ub}| = 0.00361^{+0.00011}_{-0.00009}$ [29], this is by a factor of about 2.5 wrong and clearly outside the range preferred at the level of $3\,\sigma$.

These findings are confirmed with a chi-squared fit – while the charged fermion masses are fitted well at the scale $\mu = 1\,\text{TeV}$ [378], quark mixing cannot be brought into full agreement with experimental data [29].

5.8.3 Leptoquark Couplings

5.8.3.1 Interaction Basis

From the contributions of the operators in eqs. (5.123) and (5.124), I obtain the form of the LQ coupling $\hat{\mathbf{x}}$ up to and including order λ^{12} as in

$$\hat{\mathbf{x}} = \begin{pmatrix} \hat{a}_{11}\,\lambda^9 & \hat{a}_{12}\,\lambda^{12} & \mathfrak{o}(\lambda^{12}) \\ \hat{a}_{21}\,\lambda^8 & \hat{a}_{22}\,\lambda^3 & \hat{a}_{23}\,\lambda \\ \hat{a}_{31}\,\lambda^8 & \hat{a}_{32}\,\lambda^2 & \hat{a}_{33} \end{pmatrix} \tag{5.135}$$

with the effective parameters $\hat{a}_{ij}$ being, in general, complex order-one numbers. Their definitions in terms of the coefficients β_i^L can be found in eq. (5.143). I note that the element $\hat{x}_{13}$ is only generated at an order higher than λ^{12}.

Before adopting the charged fermion mass basis, one may already compare this form of the LQ coupling with the texture laid out in eq. (5.7). The elements in the first column and/or row are well protected by the residual symmetry Z_{17}^{diag}, while each element in the (23)-block has the anticipated order of magnitude in λ.

Similarly, from the contributions of the operators in eqs. (5.125) and (5.126), I obtain the form of the LQ coupling $\hat{\mathbf{y}}$ up to and including order λ^{12} as in

$$\hat{\mathbf{y}} = \begin{pmatrix} \hat{b}_{11}\,\lambda^9 & \hat{b}_{12}\,\lambda^9 & \hat{b}_{13}\,\lambda^9 \\ \hat{b}_{21}\,\lambda^9 & \hat{b}_{22}\,\lambda^3 & \hat{b}_{23}\,\lambda^3 \\ \hat{b}_{31}\,\lambda^{12} & \hat{b}_{32} & \hat{b}_{33}\,\lambda^4 \end{pmatrix} . \tag{5.136}$$

The parameters $\hat{b}_{ij}$ are, in general, complex order-one numbers and are related to the coefficients β_i^R as shown in eq. (5.144).

Comparing this result to the texture in eq. (5.7), one sees that the elements $\hat{y}_{32} \sim 1$ and $\hat{y}_{23} \sim \lambda^3$ are indeed induced at the anticipated order of magnitude, whereas the elements $\hat{y}_{22} \sim \lambda^3$ and $\hat{y}_{33} \sim \lambda^4$ are also rather large. The latter arise from the operators with the coefficients β_3^R and β_4^R in eq. (5.126) which have been identified as being automatically induced upon fixing the LO operators, contributing to the-charged fermion mass matrices and LQ couplings $\hat{\mathbf{x}}$ and $\hat{\mathbf{y}}$, and their particle content. Notably, none of the elements of the first row and/or column of the LQ coupling $\hat{\mathbf{y}}$ is larger than λ^9, reflecting the efficacy of the residual symmetry Z_{17}^{diag}. Couplings to RH electrons and/or up quarks are thus very small.

5.8.3.2 Charged Fermion Mass Basis in Scenario A

In scenario A, i.e. in the absence of an enhancement of the up-quark mass matrix element $(M_u)_{13}$, one obtains the following form for the LQ coupling $\mathbf{z}$ from the unitary matrices L_u and L_e, see eqs. (5.128) and (5.26), and the LQ coupling $\hat{\mathbf{x}}$ in eq. (5.135):

$$\mathbf{z} = L_e^T \, \hat{\mathbf{x}} \, L_u = \begin{pmatrix} c_{11}\,\lambda^9 & c_{12}\,\lambda^{10} & c_{13}\,\lambda^9 \\ c_{21}\,\lambda^4 & c_{22}\,\lambda^3 & c_{23}\,\lambda \\ c_{31}\,\lambda^3 & c_{32}\,\lambda^2 & c_{33} \end{pmatrix} . \tag{5.137}$$

The effective parameters c_{ij} are related to $\hat{a}_{ij}$, e_{ij} and f_{ij} which enter eqs. (5.135), (5.24) and (5.127). Again, the explicit form of these relations can be found in eq. (5.146).

In comparison with eq. (5.35), the strong correlation between the LQ couplings $\mathbf{x}$ and $\mathbf{z}$ can be evidenced in scenario A as in

$$\mathbf{z} = \begin{pmatrix} (a_{11} - \frac{(c_{12}^A)^2}{2\,a_{11}}\,\lambda^2 + c_{11}^A\,\lambda^3)\,\lambda^9 & c_{12}^A\,\lambda^{10} & a_{13}\,\lambda^9 \\ (-\frac{c_{12}^A}{a_{11}}\,(a_{22} + a_{23}\,\tilde{c}) + c_{21}^A\,\lambda)\,\lambda^4 & (a_{22} + a_{23}\,\tilde{c} + c_{22}^A\,\lambda^2)\,\lambda^3 & (a_{23} + c_{23}^A\,\lambda^4)\,\lambda \\ (-\frac{c_{12}^A}{a_{11}}\,(a_{32} + a_{33}\,\tilde{c}) + c_{31}^A\,\lambda)\,\lambda^3 & (a_{32} + a_{33}\,\tilde{c} + c_{32}^A\,\lambda^2)\,\lambda^2 & a_{33} + c_{33}^A\,\lambda^4 \end{pmatrix} \tag{5.138}$$

where a_{ij} are the same parameters as in $\mathbf{x}$ in eq. (5.29). In a manner analogous to scenario B, apart from

$$c^A_{12} = \frac{\hat{a}_{11} f_{12}}{f_{22}} + \mathcal{O}(\lambda) \text{ and } \tilde{c} = \frac{d_{23}}{d_{33}} - \frac{f_{23}}{f_{33}} \,, \tag{5.139}$$

one may take the new effective parameters c^A_{ij} and $\tilde{c}$ to be complex order-one numbers which account for rather involved expressions in the other coefficients.

Lastly, regarding the LQ coupling $\mathbf{y}$, both its form as given in eq. (5.32) and the definition of the effective parameters b_{ij}, given in eq. (5.147), are identical in scenario A and scenario B.

5.9 Appendix: Relations between Lagrangian and Effective Parameters

In the following, I collect the relations between the Lagrangian parameters and the effective ones which appear in the charge fermion mass matrices and LQ couplings. Note that the effective couplings are formally taken to be real herein, whereas complex phases are taken into account for the diagonalisation of the charged fermion mass matrices in the comprehensive scan.

The effective parameters f_{ij} which appear in the up-type quark mass matrix in eq. (5.127) are related as follows to the Lagrangian parameters α_i^u

$$\begin{aligned}
f_{11} &= \alpha_4^u \ , \\
f_{12} &= \alpha_2^u + \alpha_5^u\,\lambda^2 + (\alpha_5^u)'\,\lambda^2 + \alpha_{13}^u\,\lambda^5 + \alpha_{18}^u\,\lambda^3 + \alpha_{19}^u\,\lambda^6 + \alpha_{20}^u\,\lambda^5 + \alpha_{27}^u\,\lambda^7 + \alpha_{29}^u\,\lambda^5 \ , \\
f_{13} &= \alpha_{14}^u\,\lambda^2 + \alpha_{15}^u + \alpha_{16}^u\,\lambda + \alpha_{17}^u\,\lambda^2 + \alpha_{21}^u\,\lambda^3 + \alpha_{28}^u\,\lambda^4 \ , \\
f_{21} &= \alpha_{10}^u \ , \\
f_{22} &= \alpha_2^u + \alpha_5^u\,\lambda^2 - (\alpha_5^u)'\,\lambda^2 + \alpha_6^u\,\lambda^2 + \alpha_9^u\,\lambda^8 + \alpha_{12}^u\,\lambda^7 + (\alpha_{18}^u)'\,\lambda^5 + (\alpha_{20}^u)'\,\lambda^7 \ , \qquad (5.140) \\
f_{23} &= \alpha_3^u + (\alpha_{14}^u)'\,\lambda^9 + (\alpha_{16}^u)'\,\lambda^6 + \alpha_{30}^u\,\lambda^{10} \ , \\
f_{31} &= \alpha_{22}^u + \alpha_{23}^u \ , \\
f_{32} &= \alpha_7^u + \alpha_8^u\,\lambda^5 + \alpha_{11}^u\,\lambda^2 + \alpha_{26}^u\,\lambda^7 \ , \\
f_{33} &= \alpha_1^u + \alpha_{24}^u\,\lambda^{10} + \alpha_{25}^u\,\lambda^{10} \ .
\end{aligned}$$

For the effective parameters d_{ij} appearing in the down-type quark mass matrix in eq. (5.16), I find the following relations to the Lagrangian parameters α_i^d

$$\begin{aligned}
d_{11} &= \alpha_3^d + \alpha_9^d\,\lambda^7 + \alpha_{13}^d\,\lambda^8 \ , \\
d_{12} &= \alpha_7^d + (\alpha_9^d)'\,\lambda^3 + (\alpha_{13}^d)'\,\lambda^2 + \alpha_{16}^d\,\lambda + \alpha_{24}^d\,\lambda^4 + \alpha_{25}^d\,\lambda^3 \ , \\
d_{13} &= \alpha_8^d\,\lambda^2 + \alpha_{10}^d + \alpha_{11}^d\,\lambda + \alpha_{12}^d\,\lambda^2 + \alpha_{14}^d\,\lambda^3 + \alpha_{22}^d\,\lambda^4 \ , \\
d_{21} &= \alpha_6^d \ , \\
d_{22} &= \alpha_2^d + (\alpha_{13}^d)''\,\lambda^9 + (\alpha_{16}^d)'\,\lambda^6 + \alpha_{21}^d\,\lambda^{10} \ , \qquad (5.141) \\
d_{23} &= \alpha_4^d + (\alpha_8^d)'\,\lambda^9 + (\alpha_{11}^d)'\,\lambda^6 + \alpha_{23}^d\,\lambda^{10} \ , \\
d_{31} &= \alpha_{15}^d \ , \\
d_{32} &= \alpha_5^d + \alpha_{17}^d\,\lambda^6 + \alpha_{20}^d\,\lambda^6 \ , \\
d_{33} &= \alpha_1^d + \alpha_{18}^d\,\lambda^{10} + \alpha_{19}^d\,\lambda^{10} \ .
\end{aligned}$$

Similarly, I find the following relations between the effective parameters e_{ij} in the charged lepton mass matrix in eq. (5.24) and the Lagrangian parameters α_i^e

$$\begin{aligned}
e_{11} &= \alpha_3^e + \alpha_6^e\,\lambda^7 + \alpha_9^e\,\lambda^8\ , \\
e_{12} &= \alpha_{12}^e\ , \\
e_{21} &= \alpha_{11}^e + \alpha_{17}^e\,\lambda^2 + \alpha_{22}^e\,\lambda^3 + \alpha_{23}^e\,\lambda^4\ , \\
e_{22} &= \alpha_2^e + (\alpha_9^e)'\,\lambda^9 + \alpha_{13}^e\,\lambda^6 + \alpha_{27}^e\,\lambda^{10}\ , \\
e_{23} &= \alpha_4^e + \alpha_{10}^e\,\lambda^{11} + \alpha_{14}^e\,\lambda^8 + \alpha_{26}^e\,\lambda^{10}\ , \\
e_{31} &= \alpha_7^e + \alpha_8^e\,\lambda^3 + \alpha_{15}^e\,\lambda + \alpha_{16}^e\,\lambda^2 + \alpha_{19}^e\ , \\
e_{32} &= \alpha_5^e + \alpha_{18}^e\,\lambda^9 + \alpha_{20}^e\,\lambda^6 + \alpha_{25}^e\,\lambda^8\ , \\
e_{33} &= \alpha_1^e + \alpha_{21}^e\,\lambda^{10} + \alpha_{24}^e\,\lambda^{10}\ .
\end{aligned} \tag{5.142}$$

I continue with the relations between the effective parameters $\hat{a}_{ij}$ which appear in the LQ coupling $\hat{\mathbf{x}}$, see eq. (5.135), and the coefficients β_i^L

$$\begin{aligned}
\hat{a}_{11} &= \beta_9^L\,\lambda + \beta_{10}^L\,\lambda^2 + \beta_{18}^L\,\lambda^2 + \beta_{20}^L\ , \\
\hat{a}_{12} &= (\beta_{10}^L)'\ , \\
\hat{a}_{21} &= \beta_6^L + \beta_7^L\,\lambda + \beta_{11}^L\,\lambda^3 + \beta_{16}^L\,\lambda + \beta_{19}^L\,\lambda^4 + \beta_{21}^L\,\lambda^3\ , \\
\hat{a}_{22} &= \beta_4^L + (\beta_6^L)'\,\lambda^4 + (\beta_{11}^L)'\,\lambda^9 + (\beta_{21}^L)'\,\lambda^9\ , \\
\hat{a}_{23} &= \beta_2^L + \beta_{12}^L\,\lambda^{11} + \beta_{17}^L\,\lambda^8 + \beta_{25}^L\,\lambda^{10}\ , \\
\hat{a}_{31} &= \beta_5^L\,\lambda^2 + \beta_8^L + \beta_{13}^L\,\lambda + \beta_{14}^L\,\lambda^2 + \beta_{15}^L\,\lambda^3 + \beta_{24}^L\,\lambda^4\ , \\
\hat{a}_{32} &= \beta_3^L + (\beta_5^L)'\,\lambda^9 + (\beta_{13}^L)'\,\lambda^6 + \beta_{26}^L\,\lambda^{10}\ , \\
\hat{a}_{33} &= \beta_1^L + \beta_{22}^L\,\lambda^{10} + \beta_{23}^L\,\lambda^{10}\ .
\end{aligned} \tag{5.143}$$

For the LQ coupling $\hat{\mathbf{y}}$ given in eq. (5.136), one can define the effective parameters $\hat{b}_{ij}$ in terms of the coefficients β_i^R as in

$$\begin{aligned}
\hat{b}_{11} &= \beta_7^R + \beta_{15}^R \; , \\
\hat{b}_{12} &= \beta_{13}^R + \beta_{14}^R \, \lambda^3 + \beta_{17}^R \, \lambda + \beta_{18}^R \, \lambda^2 + \beta_{21}^R \; , \\
\hat{b}_{13} &= \beta_{10}^R \, \lambda + \beta_{11}^R \, \lambda^2 + \beta_{19}^R \, \lambda^2 + \beta_{23}^R \; , \\
\hat{b}_{21} &= \beta_6^R \; , \\
\hat{b}_{22} &= \beta_3^R + \beta_{20}^R \, \lambda^9 + \beta_{24}^R \, \lambda^6 + \beta_{29}^R \, \lambda^8 \; , \\
\hat{b}_{23} &= \beta_2^R + \beta_9^R \, \lambda^4 + \beta_{12}^R \, \lambda^9 + \beta_{26}^R \, \lambda^9 \; , \\
\hat{b}_{31} &= \beta_{16}^R + \beta_{22}^R \; , \\
\hat{b}_{32} &= \beta_1^R + \beta_{27}^R \, \lambda^{10} + \beta_{28}^R \, \lambda^{10} \; , \\
\hat{b}_{33} &= \beta_4^R + \beta_5^R \, \lambda^5 + \beta_8^R \, \lambda^2 + \beta_{25}^R \, \lambda^7 \; .
\end{aligned} \tag{5.144}$$

The effective parameters a_{ij} in the LQ coupling $\mathbf{x}$ in eq. (5.29) read in terms of the effective parameters $\hat{a}_{ij}$, d_{ij} and e_{ij} as follows

$$\begin{aligned}
a_{11} &= \hat{a}_{11} + \mathfrak{o}(\lambda^3) \; , \\
a_{12} &= -\frac{\hat{a}_{22} e_{11} e_{21}}{e_{22}^2} + \frac{\hat{a}_{23} d_{23} e_{11} e_{21}}{d_{33} e_{22}^2} + \frac{\hat{a}_{32} e_{11} e_{21} e_{23}}{e_{22}^2 e_{33}} - \frac{\hat{a}_{33} d_{23} e_{11} e_{21} e_{23}}{d_{33} e_{22}^2 e_{33}} + \mathcal{O}(\lambda) \; , \\
a_{13} &= -\frac{\hat{a}_{23} e_{11} e_{21}}{e_{22}^2} + \frac{\hat{a}_{33} e_{11} e_{21} e_{23}}{e_{22}^2 e_{33}} + \mathcal{O}(\lambda^2) \; , \\
a_{21} &= \hat{a}_{21} + \mathcal{O}(\lambda) \; , \\
a_{22} &= \hat{a}_{22} - \frac{d_{23}}{d_{33}} \left(\hat{a}_{23} - \frac{\hat{a}_{33} e_{23}}{e_{33}} \right) - \frac{\hat{a}_{32} e_{23}}{e_{33}} + \mathcal{O}(\lambda^2) \; , \\
a_{23} &= \hat{a}_{23} - \frac{\hat{a}_{33} e_{23}}{e_{33}} + \mathcal{O}(\lambda^2) \; , \\
a_{31} &= \hat{a}_{31} - \frac{\hat{a}_{32} d_{12}}{d_{22}} - \frac{\hat{a}_{33} d_{13}}{d_{33}} + \frac{\hat{a}_{33} d_{12} d_{23}}{d_{22} d_{33}} + \mathcal{O}(\lambda) \; , \\
a_{32} &= \hat{a}_{32} - \frac{\hat{a}_{33} d_{23}}{d_{33}} + \mathcal{O}(\lambda^2) \; , \\
a_{33} &= \hat{a}_{33} + \mathcal{O}(\lambda^2) \; .
\end{aligned} \tag{5.145}$$

Similarly, one can express the effective parameters c_{ij} in the LQ coupling $\mathbf{z}$ in eq. (5.137) in terms of $\hat{a}_{ij}$, e_{ij} and f_{ij} and find for scenario A

$$\begin{aligned}
c_{11} &= \hat{a}_{11} + \mathcal{O}(\lambda^2)\ , \\
c_{12} &= \frac{\hat{a}_{11} f_{12}}{f_{22}} + \mathcal{O}(\lambda)\ , \\
c_{13} &= -\frac{\hat{a}_{23} e_{11} e_{21}}{e_{22}^2} + \frac{\hat{a}_{33} e_{11} e_{21} e_{23}}{e_{22}^2 e_{33}} + \mathcal{O}(\lambda^2)\ , \\
c_{21} &= -\frac{f_{12}}{e_{33} f_{22} f_{33}} \left(\hat{a}_{33} e_{23} f_{23} - \hat{a}_{23} e_{33} f_{23} - \hat{a}_{32} e_{23} f_{33} + \hat{a}_{22} e_{33} f_{33}\right) + \mathcal{O}(\lambda^2)\ , \\
c_{22} &= \hat{a}_{22} - \frac{\hat{a}_{32} e_{23}}{e_{33}} - \left(\hat{a}_{23} - \frac{\hat{a}_{33} e_{23}}{e_{33}}\right) \frac{f_{23}}{f_{33}} + \mathcal{O}(\lambda^2)\ , \\
c_{23} &= \hat{a}_{23} - \frac{\hat{a}_{33} e_{23}}{e_{33}} + \mathcal{O}(\lambda^2)\ , \\
c_{31} &= \frac{f_{12}(\hat{a}_{33} f_{23} - \hat{a}_{32} f_{33})}{f_{22} f_{33}} + \mathcal{O}(\lambda^2)\ , \\
c_{32} &= \hat{a}_{32} - \frac{\hat{a}_{33} f_{23}}{f_{33}} + \mathcal{O}(\lambda^2)\ , \\
c_{33} &= \hat{a}_{33} + \mathcal{O}(\lambda^2)\ .
\end{aligned} \tag{5.146}$$

The effective parameters b_{ij} in the LQ coupling $\mathbf{y}$ given in eq. (5.32) read for scenario A in terms of $\hat{b}_{ij}$, e_{ij} and f_{ij}

$$\begin{aligned}
b_{11} &= \hat{b}_{11} + \mathfrak{o}(\lambda^3)\ , \\
b_{12} &= \hat{b}_{12} - \frac{\hat{b}_{22} e_{21}}{e_{22}} - \frac{\hat{b}_{32} e_{31}}{e_{33}} + \frac{\hat{b}_{32} e_{21} e_{32}}{e_{22} e_{33}} + \mathcal{O}(\lambda^2)\ , \\
b_{13} &= \hat{b}_{13} - \frac{\hat{b}_{23} e_{21}}{e_{22}} + \mathcal{O}(\lambda^2)\ , \\
b_{21} &= -\frac{\hat{b}_{22} f_{11} f_{12}}{f_{22}^2} + \frac{\hat{b}_{32} e_{22} e_{23} f_{11} f_{12}}{e_{33}^2 f_{22}^2} + \frac{\hat{b}_{32} e_{32} f_{11} f_{12}}{e_{33} f_{22}^2} + \mathcal{O}(\lambda)\ , \\
b_{22} &= \hat{b}_{22} - \frac{\hat{b}_{32}(e_{22} e_{23} + e_{32} e_{33})}{e_{33}^2} + \mathcal{O}(\lambda^2)\ , \\
b_{23} &= \hat{b}_{23} + \mathcal{O}(\lambda^4)\ , \\
b_{31} &= -\frac{\hat{b}_{32} f_{11} f_{12}}{f_{22}^2} + \mathcal{O}(\lambda)\ , \\
b_{32} &= \hat{b}_{32} + \mathcal{O}(\lambda^6)\ , \\
b_{33} &= \hat{b}_{33} + \frac{\hat{b}_{32} f_{32}}{f_{33}} + \mathcal{O}(\lambda^2)\ .
\end{aligned} \tag{5.147}$$

5.10 Appendix: Formulae for $R(D)$ and $R(D^\star)$

I define

$$\frac{R(D)}{R(D)_{\mathrm{SM}}} \equiv \frac{G_3^D}{G_2^D + G_1^D}, \qquad \frac{R(D^\star)}{R(D^\star)_{\mathrm{SM}}} \equiv \frac{G_3^{D^\star}}{G_2^{D^\star} + G_1^{D^\star}} \tag{5.148}$$

with

$$\begin{aligned} G_\alpha^D \approx \sum_{\beta=1}^{3} \Bigg(& \left\{ \begin{array}{cc} 1, & \alpha = 1 \\ 0.500, & \alpha = 2 \\ 0.500, & \alpha = 3 \end{array} \right\} \left| \tilde{V}_{cb} G_F \delta_{\alpha\beta} - C^{VLL}_{\nu edu,\beta\alpha 32}(\mu_B) \right|^2 \\ & + \left\{ \begin{array}{c} 0.596 \\ 0.593 \\ 1.120 \end{array} \right\} \left| C^{SRR}_{\nu edu,\beta\alpha 32}(\mu_B) \right|^2 + \left\{ \begin{array}{c} 0.272 \\ 0.272 \\ 0.662 \end{array} \right\} \left| C^{TRR}_{\nu edu,\beta\alpha 32}(\mu_B) \right|^2 \\ & - \left\{ \begin{array}{c} 0.000 \\ 0.079 \\ 1.563 \end{array} \right\} \mathrm{Re} \left(\left(\tilde{V}_{cb} G_F \delta_{\alpha\beta} - C^{VLL}_{\nu edu,\beta\alpha 32}(\mu_B) \right) C^{SRR*}_{\nu edu,\beta\alpha 32}(\mu_B) \right) \\ & - \left\{ \begin{array}{c} 0.000 \\ 0.084 \\ 0.959 \end{array} \right\} \mathrm{Re} \left(\left(\tilde{V}_{cb} G_F \delta_{\alpha\beta} - C^{VLL}_{\nu edu,\beta\alpha 32}(\mu_B) \right) C^{TRR*}_{\nu edu,\beta\alpha 32}(\mu_B) \right) \Bigg) \end{aligned} \tag{5.149}$$

and

$$
\begin{aligned}
G_\alpha^{D^\star} \approx \sum_{\beta=1}^{3} \Bigg(& \begin{Bmatrix} 0.501, & \alpha=1 \\ 0.499, & \alpha=2 \\ 1.000, & \alpha=3 \end{Bmatrix} \left|\tilde{V}_{cb} G_F \delta_{\alpha\beta} - C^{VLL}_{\nu edu,\beta\alpha 32}(\mu_B)\right|^2 \\
& + \begin{Bmatrix} 0.039 \\ 0.039 \\ 0.053 \end{Bmatrix} \left|C^{SRR}_{\nu edu,\beta\alpha 32}(\mu_B)\right|^2 + \begin{Bmatrix} 6.372 \\ 6.364 \\ 15.347 \end{Bmatrix} \left|C^{TRR}_{\nu edu,\beta\alpha 32}(\mu_B)\right|^2 \\
& - \begin{Bmatrix} 0.000 \\ -0.012 \\ -0.139 \end{Bmatrix} \mathrm{Re}\left(\left(\tilde{V}_{cb} G_F \delta_{\alpha\beta} - C^{VLL}_{\nu edu,\beta\alpha 32}(\mu_B)\right) C^{SRR*}_{\nu edu,\beta\alpha 32}(\mu_B)\right) \\
& - \begin{Bmatrix} -0.001 \\ -0.261 \\ -5.620 \end{Bmatrix} \mathrm{Re}\left(\left(\tilde{V}_{cb} G_F \delta_{\alpha\beta} - C^{VLL}_{\nu edu,\beta\alpha 32}(\mu_B)\right) C^{TRR*}_{\nu edu,\beta\alpha 32}(\mu_B)\right) \Bigg) .
\end{aligned}
\tag{5.150}
$$

Here, $\tilde{V}_{cb} \equiv (1+\delta)\cdot 2\sqrt{2}V_{cb}$, and α (β) denotes the flavour of the charged lepton (neutrino) in the final state. The numbers in the first (second) [third] entry of the vectors in curly brackets encode the hadronic form factors employed by `flavio` [11–13] since v2.0, and the integrated-out phase space for $\alpha = 1$ (2) [3]. These numbers can be compared to the ones that are found in ref. [439]. The correction $\delta = 0.007$ accounts for QED running of the SM contribution to $C^{VLL}_{\nu edu}$ from the Z-boson mass scale down to the hadronic scale $\mu = \mu_B = 4.8$ GeV. I employ the PDG value $V_{cb} = 0.0405$ [29]. Using the values $R(D)_{\mathrm{SM}} = 0.297 \pm 0.008$ and $R(D^\star)_{\mathrm{SM}} = 0.245 \pm 0.008$ output by `flavio`, v2.3, I find that the results obtained from the expressions above deviate from those obtained from `flavio` only by up to 0.5% in the ranges of $R(D^{(\star)})$ displayed in the plots in section 5.4.

5.11 Appendix: Matching Results for Leptonic Lagrangian

The one-loop contributions to the WCs in the effective leptonic Lagrangian can be grouped according to the type of diagrams. Firstly, the results for short-distance contributions from

Z-penguin diagrams read[19]

$$
\begin{aligned}
C^{VLL,Z}_{ee,ijkl} &\approx \frac{3\sqrt{2}G_F(1-2s^2_W)}{64\pi^2} t_t(1+\ln t_t)\left(\delta_{il}z^*_{k3}z_{j3} + \delta_{ij}z^*_{k3}z_{l3} + \delta_{kl}z^*_{i3}z_{j3} + \delta_{jk}z^*_{i3}z_{l3}\right) \ , \\
C^{VRR,Z}_{ee,ijkl} &\approx \frac{3\sqrt{2}G_F s^2_W}{32\pi^2} t_t(1+\ln t_t)\left(\delta_{il}y^*_{k3}y_{j3} + \delta_{ij}y^*_{k3}y_{l3} + \delta_{kl}y^*_{i3}y_{j3} + \delta_{jk}y^*_{i3}y_{l3}\right) \ , \\
C^{VLR,Z}_{ee,ijkl} &\approx -\frac{3\sqrt{2}G_F}{16\pi^2} t_t(1+\ln t_t)\left((1-2s^2_W)\delta_{ij}y^*_{k3}y_{l3} + 2s^2_W\delta_{kl}z^*_{i3}z_{j3}\right) \ ,
\end{aligned}
\tag{5.151}
$$

with the Fermi constant G_F and the sine of the weak mixing angle signified by s_W. Secondly, the results for short-distance contributions from photon-penguin diagrams read

$$
\begin{aligned}
C^{VLL,\gamma}_{ee,ijkl} &= \frac{\alpha_{\text{em}}}{96\pi m^2_\phi}\sum_m (5+4\ln t_{u_m})\left(\delta_{il}z^*_{km}z_{jm} + \delta_{kl}z^*_{im}z_{jm} + \delta_{ij}z^*_{km}z_{lm} + \delta_{jk}z^*_{im}z_{lm}\right) \ , \\
C^{VRR,\gamma}_{ee,ijkl} &= \frac{\alpha_{\text{em}}}{96\pi m^2_\phi}\sum_m (5+4\ln t_{u_m})\left(\delta_{il}y^*_{km}y_{jm} + \delta_{kl}y^*_{im}y_{jm} + \delta_{ij}y^*_{km}y_{lm} + \delta_{jk}y^*_{im}y_{lm}\right) \ , \\
C^{VLR,\gamma}_{ee,ijkl} &= \frac{\alpha_{\text{em}}}{24\pi m^2_\phi}\sum_m (5+4\ln t_{u_m})\left(\delta_{ij}y^*_{km}y_{lm} + \delta_{kl}z^*_{im}z_{jm}\right) \ ,
\end{aligned}
\tag{5.152}
$$

with the fine-structure constant α_{em}. Thirdly, the results for short-distance contributions from box diagrams read

$$
\begin{aligned}
C^{VLL,\text{box}}_{ee,ijkl} &= \frac{3}{256\pi^2 m^2_\phi}\sum_{m,n} z_{jm}z_{ln}\left(z^*_{in}z^*_{km} + z^*_{im}z^*_{kn}\right) \ , \\
C^{VRR,\text{box}}_{ee,ijkl} &= \frac{3}{256\pi^2 m^2_\phi}\sum_{m,n} y_{jm}y_{ln}\left(y^*_{in}y^*_{km} + y^*_{im}y^*_{kn}\right) \ , \\
C^{VLR,\text{box}}_{ee,ijkl} &= \frac{3}{64\pi^2 m^2_\phi}\sum_{m,n} y_{ln}z_{jm}y^*_{kn}z^*_{im} \ .
\end{aligned}
\tag{5.153}
$$

Lastly, the short-distance contributions from Higgs-penguin diagrams are neglected due to the small Yukawa couplings to the charged leptons.

5.12 Appendix: Effective Coupling Constants for $\mu - e$ Conversion

The effective coupling constants for $\mu - e$ conversion in nuclei used herein read

---

[19] Note that the masses of the external leptons are set to zero here, thus the contributions are proportional to the square of the internal quark mass, that is, there are two mass insertions on the internal line. The contribution with an internal top quark is by far the dominant one.

$$\begin{aligned}
\tilde{g}_{LS}^{(N)} &= \sum_i G_S^{q_i,N} \left(C_{eq,12ii}^{SRR} + C_{eq,12ii}^{SRL} \right) \\
\tilde{g}_{RS}^{(N)} &= \sum_i G_S^{q_i,N} \left(C_{eq,21ii}^{SRR*} + C_{eq,21ii}^{SRL*} \right) \\
\tilde{g}_{LV}^{(p)} &= 2 \left(C_{eu,1211}^{VLL} + C_{eu,1211}^{VLR} \right) + \left(C_{ed,1211}^{VLL} + C_{ed,1211}^{VLR} \right) \\
\tilde{g}_{RV}^{(p)} &= 2 \left(C_{eu,1211}^{VRR} + C_{ue,1112}^{VLR} \right) + \left(C_{ed,1211}^{VRR} + C_{de,1112}^{VLR} \right) \\
\tilde{g}_{LV}^{(n)} &= \left(C_{eu,1211}^{VLL} + C_{eu,1211}^{VLR} \right) + 2 \left(C_{ed,1211}^{VLL} + C_{ed,1211}^{VLR} \right) \\
\tilde{g}_{RV}^{(n)} &= \left(C_{eu,1211}^{VRR} + C_{ue,1112}^{VLR} \right) + 2 \left(C_{ed,1211}^{VRR} + C_{de,1112}^{VLR} \right)
\end{aligned} \tag{5.154}$$

with $N = p, n$.

Chapter 6

Conclusion and Future Directions

In this thesis, I have demonstrated that it is indeed possible to investigate the origin behind the observed flavour structure of nature in several ways. Specifically, a class of models in which neutrino masses are radiatively generated is studied in chapter 3, which represents an intermediate avenue between model-based and model-independent analyses. While chapter 4 demonstrates the fruitfulness of the latter approach, a thorough investigation of a concrete new-physics model is detailed in chapter 5.

After having reviewed some technical aspects of flavour physics in and beyond the SM in chapter 2, I continued with the above-mentioned study of a simplified model containing a singly-charged scalar singlet $h \sim (1,1,1)$ under the assumption that this particle generates the main contribution to Majorana neutrino masses. Since the antisymmetric coupling y_h of h to two LH lepton doublets is the only renormalisable interaction with SM fermions, this extension of the SM can be very predictive. In particular, the minimal scenario of adding one copy of h to the SM particle content yields only two possible structures for the neutrino mass matrix, and it allows for the straightforward derivation of a necessary condition for the elements of y_h^{ij} in terms of experimental neutrino data.

Indeed, in this case it is not necessary to specify the mechanism of how the breaking of lepton-number conservation is achieved, which may involve further new particles, effective interactions, strongly coupled dynamics or other features. Several well-known models of radiative neutrino mass generation, that is, the Zee model [60–62], the Zee-Babu model [63–65] and the KNT model [66] are different realisations of this minimal scenario. In the regime where NP effects at low energy are only induced by h to an appreciable extent, the results of the study of the simplified model can be expected to agree with the predictions obtained from complete models to a good degree.

With the prospect of more data on leptonic CP violation becoming available, e.g. at Hyper-Kamiokande [116] or DUNE [117], as well as further insights into the mass ordering in the neutrino sector for instance at JUNO [118], the constraints on the couplings y_h^{ij} are set to become more stringent in the near future. Overall, the feasibility to quantitatively study a specific class of neutrino mass models lays the ground to repeat this exercise for other BSM particles.

Following a somewhat different approach, in chapter 4 I formalise the extraction of information about NP via a careful investigation of experimental data on decay processes mediated by the transition $b \to s\nu\nu$. It is studied how current bounds on and future sensitivities to the observables $\mathrm{BR}(B \to K\nu\nu)$, $\mathrm{BR}(B \to K^*\nu\nu)$ and $\mathrm{BR}(B \to X_s\nu\nu)$ as well as $F_L(B \to K^*\nu\nu)$ can be used to constrain different effective operators, under the conservative assumption that Belle II will not detect a deviation from the respective SM expectations.

Since I make use of the most general set of dimension-6 operators in LEFT which contribute to $b \to s\nu\nu$ [192,298] including massive sterile neutrinos, except for the dimension-5 neutrino dipole operators, the results can be applied to any concrete model which introduces NP at or above the electroweak scale and contributes to at least one of the considered operators. The results show that one can expect the currently established bounds on the WCs associated with the different operators to be considerably strengthened, and that the constraining power of the considered observables is (partly) complimentary. Therefore, a case can be made for model-independent studies of other rare processes, or for a further refinement of the one laid out in this thesis, for instance with regard to subleading contributions to the inclusive decay mode $B \to X_s\nu\nu$.

Lastly, in chapter 5 I demonstrated that one can successfully explain the charged fermion masses in the SM as well as quark mixing together with currently observed anomalies in $R(D)$ and $R(D^\star)$ and of the AMM of the muon via a model which makes use of the discrete flavour symmetry $G_f = D_{17} \times Z_{17}$. The presence of two Higgs doublets H_u and H_d (in the decoupling limit) and the enlargement of the SM particle content by a scalar LQ $\phi \sim (3, 1, -\frac{1}{3})$ is assumed. The flavour symmetry is intact at high energies, but gets broken by the non-zero VEVs of several spurion fields. It was found that the most stringent constraints on the viable parameter space of the model currently arise from the non-observation of the radiative cLFV decays $\tau \to \mu\gamma$ and $\mu \to e\gamma$. A successful accommodation of the anomalies in $R(D)$ and $R(D^\star)$ and of the AMM of the muon proved to be very challenging in an unbiased scan with only the most relevant observables included.

Therefore, biases were extracted in order to target preferred regions in parameter space in a more comprehensive scan. This allowed for an explanation of $R(D)$, $R(D^\star)$ and the AMM of the muon at a CL of $3\,\sigma$ for the LQ masses $\hat{m}_\phi = 2$ and 4, and even at $2\,\sigma$ in the case of $\hat{m}_\phi = 2$, while all considered experimental bounds were respected and a successful fit to the charged fermion masses and quark mixing was achieved. Signals in several cLFV $\mu \to e$ transitions were found to be a typical signature of explaining the AMM of the muon.

Key avenues to further improve the model are the incorporation of lepton mixing and non-zero neutrino masses as well as predicting $J_{\rm CP} \sim \lambda^6$ in terms of operators respecting the flavour symmetry G_f, which might in fact necessitate a modification or enlargement of G_f, and/or a change of the transformation properties of the particles contained in the model. Other refinements could consist in forbidding operators which violate the conservation of baryon number in terms of the flavour symmetry, and suppressing the coupling between ϕ, a RH electron and a RH top quark by a further factor of λ or λ^2. The latter has proven crucial for a simultaneous amelioration of the anomalies in $R(D)$, $R(D^\star)$ and Δa_μ. On the phenomenological side, an incorporation of further observables related to the underlying $b \to c$ transitions would be desirable, for instance $R(J/\psi)$ [130], $R(\Lambda_c)$, angular distributions in $B \to D^\star e_i \nu$ [133] and the longitudinal tau-lepton polarisation in $B \to D^\star \tau \nu$ [131]. For an extended version of the model, one might also attempt an explanation of the observed anomalies in $b \to s$ transitions, that is, $R(K)$, $R(K^\star)$ and $B_s \to \mu\mu$.

The quest to shed light on the inner workings of the flavour structure of nature is pursued on many frontiers, both theoretically and experimentally, and the prospects for major breakthroughs in the next decades are good. The approach of simplified models will prove useful for navigating further efforts to decipher the origin of neutrino masses, which may be seen as the most pressing open question in the field of flavour physics. On the experimental side, precise measurements of rare processes as well as a further investigation and clarification of the situation regarding currently observed anomalies will be absolutely crucial. Together with efforts in model building as well as EFT-based studies performed in the theory community, with examples laid out in this thesis, we can expect to at least catch a further glimpse of what constitutes the fundamental structures of our universe.

References

[1] Belle-II collaboration, *Search for $B^+ \to K^+\nu\bar{\nu}$ decays with an inclusive tagging method at the Belle II experiment*, in *55th Rencontres de Moriond on Electroweak Interactions and Unified Theories*, 5, 2021 [`2105.05754`].

[2] S. Bifani, S. Descotes-Genon, A. Romero Vidal and M.-H. Schune, *Review of Lepton Universality tests in B decays*, *J. Phys. G* **46** (2019) 023001 [`1809.06229`].

[3] W. Altmannshofer and J. Zupan, *Snowmass White Paper: Flavor Model Building*, in *2022 Snowmass Summer Study*, 3, 2022 [`2203.07726`].

[4] W. Skiba, *Effective Field Theory and Precision Electroweak Measurements*, in *Theoretical Advanced Study Institute in Elementary Particle Physics: Physics of the Large and the Small*, pp. 5–70, 2011, DOI [`1006.2142`].

[5] A. Bharucha, D.M. Straub and R. Zwicky, *$B \to V\ell^+\ell^-$ in the Standard Model from light-cone sum rules*, *JHEP* **08** (2016) 098 [`1503.05534`].

[6] N. Gubernari, A. Kokulu and D. van Dyk, *$B \to P$ and $B \to V$ Form Factors from B-Meson Light-Cone Sum Rules beyond Leading Twist*, *JHEP* **01** (2019) 150 [`1811.00983`].

[7] Belle-II collaboration, *The Belle II Physics Book*, *PTEP* **2019** (2019) 123C01 [`1808.10567`].

[8] Belle-II collaboration, *Search for $B^+ \to K^+\nu\bar{\nu}$ Decays Using an Inclusive Tagging Method at Belle II*, *Phys. Rev. Lett.* **127** (2021) 181802 [`2104.12624`].

[9] M.L. Waskom, *seaborn: statistical data visualization*, *Journal of Open Source Software* **6** (2021) 3021.

[10] HFLAV collaboration, *Averages of b-hadron, c-hadron, and τ-lepton properties as of 2018*, *Eur. Phys. J. C* **81** (2021) 226 [`1909.12524`].

[11] D.M. Straub, *flavio: a Python package for flavour and precision phenomenology in the Standard Model and beyond*, `1810.08132`.

[12] D. Straub, P. Stangl, M. Kirk, J. Kumar, C. Niehoff, E. Gurler et al., *flav-io/flavio: v2.3.1*, Oct., 2021. 10.5281/zenodo.5543714.

[13] M. Bordone, M. Jung and D. van Dyk, *Theory determination of $\bar{B} \to D^{(*)}\ell^-\bar{\nu}$ form factors at $\mathcal{O}(1/m_c^2)$*, *Eur. Phys. J. C* **80** (2020) 74 [`1908.09398`].

[14] Belle collaboration, *Measurement of $\mathcal{R}(D)$ and $\mathcal{R}(D^*)$ with a semileptonic tagging method*, *Phys. Rev. Lett.* **124** (2020) 161803 [`1910.05864`].

[15] LHCb collaboration, *Measurement of the ratio of the $B^0 \to D^{*-}\tau^+\nu_\tau$ and $B^0 \to D^{*-}\mu^+\nu_\mu$ branching fractions using three-prong τ-lepton decays*, *Phys. Rev. Lett.* **120** (2018) 171802 [`1708.08856`].

[16] LHCb collaboration, *Test of Lepton Flavor Universality by the measurement of the $B^0 \to D^{*-}\tau^+\nu_\tau$ branching fraction using three-prong τ decays*, *Phys. Rev. D* **97** (2018) 072013 [`1711.02505`].

[17] Belle-II collaboration, *Snowmass Whitepaper: The Belle II Detector Upgrade Program*, in *2022 Snowmass Summer Study*, 3, 2022 [`2203.11349`].

[18] Muon g-2 collaboration, *Measurement of the Positive Muon Anomalous Magnetic Moment to 0.46 ppm*, *Phys. Rev. Lett.* **126** (2021) 141801 [`2104.03281`].

[19] T. Aoyama et al., *The anomalous magnetic moment of the muon in the Standard Model*, *Phys. Rept.* **887** (2020) 1 [`2006.04822`].

[20] Muon g-2 collaboration, *Muon (g-2) Technical Design Report*, `1501.06858`.

[21] Belle collaboration, *Search for lepton-flavor-violating tau decays to $\ell\gamma$ modes at Belle*, `2103.12994`.

[22] MEG collaboration, *Search for the lepton flavour violating decay $\mu^+ \to \mathrm{e}^+\gamma$ with the full dataset of the MEG experiment*, *Eur. Phys. J. C* **76** (2016) 434 [`1605.05081`].

[23] MEG II collaboration, *The Search for $\mu^+ \to \mathrm{e}^+\gamma$ with 10^{-14} Sensitivity: the Upgrade of the MEG Experiment*, `2107.10767`.

[24] Belle collaboration, *Search for $\boldsymbol{B \to h\nu\bar{\nu}}$ decays with semileptonic tagging at Belle*, *Phys. Rev. D* **96** (2017) 091101 [`1702.03224`].

[25] COMET collaboration, *COMET Phase-I Technical Design Report*, *PTEP* **2020** (2020) 033C01 [`1812.09018`].

[26] Mu2e collaboration, *Mu2e Technical Design Report*, `1501.05241`.

[27] A. Blondel et al., *Research Proposal for an Experiment to Search for the Decay $\mu \to eee$*, `1301.6113`.

[28] K. Hayasaka et al., *Search for Lepton Flavor Violating τ Decays into Three Leptons with 719 Million Produced $\tau^+\tau^-$ Pairs*, *Phys. Lett. B* **687** (2010) 139 [`1001.3221`].

[29] Particle Data Group collaboration, *Review of Particle Physics*, *PTEP* **2020** (2020) 083C01.

[30] ALEPH, DELPHI, L3, OPAL, SLD, LEP Electroweak Working Group, SLD Electroweak Group, SLD Heavy Flavour Group collaboration, *Precision electroweak measurements on the Z resonance*, *Phys. Rept.* **427** (2006) 257 [`hep-ex/0509008`].

[31] A. Crivellin, C. Greub, D. Müller and F. Saturnino, *Scalar Leptoquarks in Leptonic Processes*, *JHEP* **02** (2021) 182 [`2010.06593`].

[32] H. Baer et al., eds., *The International Linear Collider Technical Design Report - Volume 2: Physics*, `1306.6352`.

[33] FCC collaboration, *FCC-ee: The Lepton Collider: Future Circular Collider Conceptual Design Report Volume 2*, *Eur. Phys. J. ST* **228** (2019) 261.

[34] Muon g-2 collaboration, *The muon EDM in the g-2 experiment at Fermilab*, *EPJ Web Conf.* **118** (2016) 01005.

[35] A. Adelmann et al., *Search for a muon EDM using the frozen-spin technique*, `2102.08838`.

[36] Belle-II collaboration, *Semileptonic B-Meson decays at Belle II*, *PoS* **HQL2018** (2018) 012.

[37] A. Freitas, *TASI 2020 Lectures on Precision Tests of the Standard Model*, `2012.11642`.

[38] I. Esteban, M. Gonzalez-Garcia, M. Maltoni, T. Schwetz and A. Zhou, *The fate of hints: updated global analysis of three-flavor neutrino oscillations*, `2007.14792`.

[39] S. Descotes-Genon, A. Khodjamirian and J. Virto, *Light-cone sum rules for $B \to K\pi$ form factors and applications to rare decays*, *JHEP* **12** (2019) 083 [`1908.02267`].

[40] T.P. Gorringe and D.W. Hertzog, *Precision Muon Physics*, *Prog. Part. Nucl. Phys.* **84** (2015) 73 [`1506.01465`].

[41] Y.K. Semertzidis et al., *Sensitive search for a permanent muon electric dipole moment*, in *KEK International Workshop on High Intensity Muon Sources (HIMUS 99)*, 12, 1999, DOI [`hep-ph/0012087`].

[42] F.J.M. Farley, K. Jungmann, J.P. Miller, W.M. Morse, Y.F. Orlov, B.L. Roberts et al., *A New method of measuring electric dipole moments in storage rings*, *Phys. Rev. Lett.* **93** (2004) 052001 [`hep-ex/0307006`].

[43] Super-Kamiokande collaboration, *Evidence for oscillation of atmospheric neutrinos*, *Phys. Rev. Lett.* **81** (1998) 1562 [`hep-ex/9807003`].

[44] SNO collaboration, *Measurement of the rate of $\nu_e + d \rightarrow p + p + e^-$ interactions produced by ^8B solar neutrinos at the Sudbury Neutrino Observatory*, *Phys. Rev. Lett.* **87** (2001) 071301 [`nucl-ex/0106015`].

[45] SNO collaboration, *Direct evidence for neutrino flavor transformation from neutral current interactions in the Sudbury Neutrino Observatory*, *Phys. Rev. Lett.* **89** (2002) 011301 [`nucl-ex/0204008`].

[46] Muon g-2 collaboration, *Final Report of the Muon E821 Anomalous Magnetic Moment Measurement at BNL*, *Phys. Rev. D* **73** (2006) 072003 [`hep-ex/0602035`].

[47] S. Weinberg, *Baryon and Lepton Nonconserving Processes*, *Phys.Rev.Lett.* **43** (1979) 1566.

[48] E. Ma, *Neutrino Mass: Mechanisms and Models*, `0905.0221`.

[49] S.M. Boucenna, S. Morisi and J.W.F. Valle, *The low-scale approach to neutrino masses*, *Adv. High Energy Phys.* **2014** (2014) 831598 [`1404.3751`].

[50] Y. Cai, J. Herrero-García, M.A. Schmidt, A. Vicente and R.R. Volkas, *From the trees to the forest: a review of radiative neutrino mass models*, *Front.in Phys.* **5** (2017) 63 [`1706.08524`].

[51] K. Babu and C.N. Leung, *Classification of effective neutrino mass operators*, *Nucl.Phys.* **B619** (2001) 667 [`hep-ph/0106054`].

[52] A. de Gouvea and J. Jenkins, *A Survey of Lepton Number Violation Via Effective Operators*, *Phys. Rev.* **D77** (2008) 013008 [`0708.1344`].

[53] A. de Gouvea, J. Herrero-Garcia and A. Kobach, *Neutrino Masses, Grand Unification, and Baryon Number Violation*, *Phys.Rev.* **D90** (2014) 016011 [`1404.4057`].

[54] P.W. Angel, N.L. Rodd and R.R. Volkas, *Origin of neutrino masses at the LHC: $\Delta L = 2$ effective operators and their ultraviolet completions*, *Phys.Rev.* **D87** (2013) 073007 [`1212.6111`].

[55] Y. Cai, J.D. Clarke, M.A. Schmidt and R.R. Volkas, *Testing Radiative Neutrino Mass Models at the LHC*, *JHEP* **02** (2015) 161 [`1410.0689`].

[56] J. Gargalionis and R.R. Volkas, *Exploding operators for Majorana neutrino masses and beyond*, *JHEP* **01** (2021) 074 [`2009.13537`].

[57] F. del Aguila, A. Aparici, S. Bhattacharya, A. Santamaria and J. Wudka, *Effective Lagrangian approach to neutrinoless double beta decay and neutrino masses*, *JHEP* **1206** (2012) 146 [`1204.5986`].

[58] M. Gustafsson, J.M. No and M.A. Rivera, *Lepton number violating operators with standard model gauge fields: A survey of neutrino masses from 3-loops and their link to dark matter*, *JHEP* **11** (2020) 070 [`2006.13564`].

[59] J. Herrero-García and M.A. Schmidt, *Neutrino mass models: New classification and model-independent upper limits on their scale*, *Eur. Phys. J. C* **79** (2019) 938 [`1903.10552`].

[60] A. Zee, *A Theory of Lepton Number Violation, Neutrino Majorana Mass, and Oscillation*, *Phys. Lett.* **93B** (1980) 389.

[61] T.P. Cheng and L.-F. Li, *Neutrino Masses, Mixings and Oscillations in $SU(2) \times U(1)$ Models of Electroweak Interactions*, *Phys. Rev.* **D22** (1980) 2860.

[62] L. Wolfenstein, *A theoretical pattern for neutrino oscillations*, *Nuclear Physics B* **175** (1980) 93 .

[63] A. Zee, *Quantum Numbers of Majorana Neutrino Masses*, *Nucl. Phys.* **B264** (1986) 99.

[64] A. Zee, *Charged Scalar Field and Quantum Number Violations*, *Phys. Lett.* **161B** (1985) 141.

[65] K.S. Babu, *Model of 'Calculable' Majorana Neutrino Masses*, *Phys. Lett.* **B203** (1988) 132.

[66] L.M. Krauss, S. Nasri and M. Trodden, *A Model for neutrino masses and dark matter*, *Phys. Rev. D* **67** (2003) 085002 [`hep-ph/0210389`].

[67] W.-S. Hou, R.S. Willey and A. Soni, *Implications of a Heavy Top Quark and a Fourth Generation on the Decays* $B \to Kl^+l^-, K\nu\nu^-$, *Phys. Rev. Lett.* **58** (1987) 1608.

[68] G. Buchalla and A.J. Buras, *QCD corrections to rare K and B decays for arbitrary top quark mass*, *Nucl. Phys. B* **400** (1993) 225.

[69] Y. Grossman, Z. Ligeti and E. Nardi, *New limit on inclusive* $B \to X_s$ *anti-neutrino neutrino decay and constraints on new physics*, *Nucl. Phys. B* **465** (1996) 369 [`hep-ph/9510378`].

[70] P. Colangelo, F. De Fazio, P. Santorelli and E. Scrimieri, *Rare* $B \to K^{(*)}$ *neutrino anti-neutrino decays at B factories*, *Phys. Lett. B* **395** (1997) 339 [`hep-ph/9610297`].

[71] D. Melikhov, N. Nikitin and S. Simula, *Right-handed currents in rare exclusive* $B \to (K, K^*)$ *neutrino anti-neutrino decays*, *Phys. Lett. B* **428** (1998) 171 [`hep-ph/9803269`].

[72] C.S. Kim, Y.G. Kim and T. Morozumi, *New physics effects in* $B \to K^{(*)}$ *neutrino neutrino decays*, *Phys. Rev. D* **60** (1999) 094007 [`hep-ph/9905528`].

[73] T.M. Aliev, A. Ozpineci and M. Savci, *Rare* $B \to K^\star \nu\bar{\nu}$ *decay beyond standard model*, *Phys. Lett. B* **506** (2001) 77 [`hep-ph/0101066`].

[74] W. Altmannshofer, A.J. Buras, D.M. Straub and M. Wick, *New strategies for New Physics search in* $B \to K^*\nu\bar{\nu}$, $B \to K\nu\bar{\nu}$ *and* $B \to X_s\nu\bar{\nu}$ *decays*, *JHEP* **04** (2009) 022 [`0902.0160`].

[75] W. Altmannshofer, P. Paradisi and D.M. Straub, *Model-Independent Constraints on New Physics in* $b \to s$ *Transitions*, *JHEP* **04** (2012) 008 [`1111.1257`].

[76] A.J. Buras, J. Girrbach-Noe, C. Niehoff and D.M. Straub, $B \to K^{(*)}\nu\bar{\nu}$ *decays in the Standard Model and beyond*, *JHEP* **02** (2015) 184 [`1409.4557`].

[77] R. Bause, H. Gisbert, M. Golz and G. Hiller, *Interplay of dineutrino modes with semileptonic rare* $\boldsymbol{B}$*-decays*, `2109.01675`.

[78] C.D. Froggatt and H.B. Nielsen, *Hierarchy of Quark Masses, Cabibbo Angles and CP Violation*, *Nucl. Phys. B* **147** (1979) 277.

[79] M. Bauer and M. Neubert, *Minimal Leptoquark Explanation for the* $R_{D^{(*)}}$ *,* R_K *, and* $(g-2)_\mu$ *Anomalies*, *Phys. Rev. Lett.* **116** (2016) 141802 [`1511.01900`].

[80] Y. Cai, J. Gargalionis, M.A. Schmidt and R.R. Volkas, *Reconsidering the One Leptoquark solution: flavor anomalies and neutrino mass*, *JHEP* **10** (2017) 047 [`1704.05849`].

[81] I. de Medeiros Varzielas and G. Hiller, *Clues for flavor from rare lepton and quark decays*, *JHEP* **06** (2015) 072 [`1503.01084`].

[82] G. Hiller, D. Loose and K. Schönwald, *Leptoquark Flavor Patterns & B Decay Anomalies*, *JHEP* **12** (2016) 027 [`1609.08895`].

[83] I. de Medeiros Varzielas and S.F. King, $R_{K^{(*)}}$ *with leptoquarks and the origin of Yukawa couplings*, *JHEP* **11** (2018) 100 [`1807.06023`].

[84] I. de Medeiros Varzielas and J. Talbert, *Simplified Models of Flavourful Leptoquarks*, *Eur. Phys. J. C* **79** (2019) 536 [`1901.10484`].

[85] R. Barbieri and R. Ziegler, *Quark masses, CKM angles and Lepton Flavour Universality violation*, *JHEP* **07** (2019) 023 [`1904.04121`].

[86] D. Marzocca, S. Trifinopoulos and E. Venturini, *From B-meson anomalies to Kaon physics with scalar leptoquarks*, *Eur. Phys. J. C* **82** (2022) 320 [`2106.15630`].

[87] T. Felkl, J. Herrero-Garcia and M.A. Schmidt, *The Singly-Charged Scalar Singlet as the Origin of Neutrino Masses*, *JHEP* **05** (2021) 122 [`2102.09898`].

[88] T. Felkl, J. Herrero-Garcia and M.A. Schmidt, *Erratum to: The Singly-Charged Scalar Singlet as the Origin of Neutrino Masses*, *JHEP* **05** (2022) 73 [`2102.09898`].

[89] T. Felkl, S.L. Li and M.A. Schmidt, *A tale of invisibility: constraints on new physics in $b \to s\nu\nu$*, *JHEP* **12** (2021) 118 [`2111.04327`].

[90] I. Bigaran, T. Felkl, C. Hagedorn and M.A. Schmidt, *Flavour anomalies meet flavour symmetry*, `2207.06197`.

[91] M.D. Schwartz, *Quantum Field Theory and the Standard Model*, Cambridge University Press (3, 2014).

[92] S. Willenbrock, *Symmetries of the standard model*, in *Theoretical Advanced Study Institute in Elementary Particle Physics: Physics in $D \geqq 4$*, pp. 3–38, 10, 2004 [`hep-ph/0410370`].

[93] H.K. Dreiner, H.E. Haber and S.P. Martin, *Two-component spinor techniques and Feynman rules for quantum field theory and supersymmetry*, *Phys. Rept.* **494** (2010) 1 [`0812.1594`].

[94] C.C. Nishi, *Simple derivation of general Fierz-like identities*, *Am. J. Phys.* **73** (2005) 1160 [`hep-ph/0412245`].

[95] M.D. Schwartz, *Quantum Field Theory and the Standard Model*, Cambridge University Press (2014).

[96] P. Arnan, D. Becirevic, F. Mescia and O. Sumensari, *Probing low energy scalar leptoquarks by the leptonic W and Z couplings*, *JHEP* **02** (2019) 109 [`1901.06315`].

[97] Y. Grossman and P. Tanedo, *Just a Taste: Lectures on Flavor Physics*, in *Proceedings, Theoretical Advanced Study Institute in Elementary Particle Physics : Anticipating the Next Discoveries in Particle Physics (TASI 2016): Boulder, CO, USA, June 6-July 1, 2016*, pp. 109–295, 2018, DOI [`1711.03624`].

[98] C. Jarlskog, *Commutator of the Quark Mass Matrices in the Standard Electroweak Model and a Measure of Maximal CP Nonconservation*, *Phys. Rev. Lett.* **55** (1985) 1039.

[99] Y. Nir, *Flavour physics and CP violation*, *CERN Yellow Rep. School Proc.* **5** (2020) 79.

[100] S. Koren, *A Note on Proton Stability in the Standard Model*, *Universe* **8** (2022) 308 [`2204.01741`].

[101] M. Ardu and G. Pezzullo, *Introduction to Charged Lepton Flavor Violation*, *Universe* **8** (2022) 299 [`2204.08220`].

[102] U. Egede, S. Nishida, M. Patel and M.-H. Schune, *Electroweak Penguin Decays of b-Flavoured Hadrons*, `2205.05222`.

[103] A. Khodjamirian and A.V. Rusov, *$B_s \to K\ell\nu_\ell$ and $B_{(s)} \to \pi(K)\ell^+\ell^-$ decays at large recoil and CKM matrix elements*, *JHEP* **08** (2017) 112 [`1703.04765`].

[104] J. Gao, C.-D. Lü, Y.-L. Shen, Y.-M. Wang and Y.-B. Wei, *Precision calculations of $B \to V$ form factors from soft-collinear effective theory sum rules on the light-cone*, *Phys. Rev. D* **101** (2020) 074035 [`1907.11092`].

[105] R.R. Horgan, Z. Liu, S. Meinel and M. Wingate, *Lattice QCD calculation of form factors describing the rare decays $B \to K^*\ell^+\ell^-$ and $B_s \to \phi\ell^+\ell^-$*, *Phys. Rev. D* **89** (2014) 094501 [`1310.3722`].

[106] HPQCD collaboration, *Rare decay $B \to K\ell^+\ell^-$ form factors from lattice QCD*, *Phys. Rev. D* **88** (2013) 054509 [`1306.2384`].

[107] R.R. Horgan, Z. Liu, S. Meinel and M. Wingate, *Rare B decays using lattice QCD form factors*, *PoS* **LATTICE2014** (2015) 372 [`1501.00367`].

[108] J.A. Bailey et al., *$B \to Kl^+l^-$ Decay Form Factors from Three-Flavor Lattice QCD*, *Phys. Rev. D* **93** (2016) 025026 [`1509.06235`].

[109] F. Reines and C.L. Cowan, *Detection of the free neutrino*, *Phys. Rev.* **92** (1953) 830.

[110] C.L. Cowan, F. Reines, F.B. Harrison, H.W. Kruse and A.D. McGuire, *Detection of the free neutrino: a confirmation*, *Science* **124** (1956) 103.

[111] G. Danby, J.-M. Gaillard, K. Goulianos, L.M. Lederman, N. Mistry, M. Schwartz et al., *Observation of high-energy neutrino reactions and the existence of two kinds of neutrinos*, *Phys. Rev. Lett.* **9** (1962) 36.

[112] K. Kodama, N. Ushida, C. Andreopoulos, N. Saoulidou, G. Tzanakos, P. Yager et al., *Observation of tau neutrino interactions*, *Physics Letters B* **504** (2001) 218.

[113] A. Suzuki, *Antineutrino Science in KamLAND*, *Eur. Phys. J. C* **74** (2014) 3094 [`1409.4515`].

[114] T2K collaboration, *Observation of Electron Neutrino Appearance in a Muon Neutrino Beam*, *Phys. Rev. Lett.* **112** (2014) 061802 [`1311.4750`].

[115] NOvA collaboration, *First Measurement of Neutrino Oscillation Parameters using Neutrinos and Antineutrinos by NOvA*, *Phys. Rev. Lett.* **123** (2019) 151803 [`1906.04907`].

[116] HYPER-KAMIOKANDE collaboration, *Hyper-Kamiokande Design Report*, `1805.04163`.

[117] DUNE collaboration, *Long-Baseline Neutrino Facility (LBNF) and Deep Underground Neutrino Experiment (DUNE): Conceptual Design Report, Volume 1: The LBNF and DUNE Projects*, `1601.05471`.

[118] JUNO collaboration, *Neutrino Physics with JUNO*, *J. Phys. G* **43** (2016) 030401 [`1507.05613`].

[119] M.V. Smirnov, Z.J. Hu, S.J. Li and J.J. Ling, *The possibility of leptonic CP-violation measurement with JUNO*, *Nucl. Phys. B* **931** (2018) 437 [`1802.03677`].

[120] C. Dvorkin et al., *Neutrino Mass from Cosmology: Probing Physics Beyond the Standard Model*, `1903.03689`.

[121] PLANCK collaboration, *Planck 2018 results. VI. Cosmological parameters*, *Astron. Astrophys.* **641** (2020) A6 [`1807.06209`].

[122] KATRIN collaboration, *KATRIN: Status and Prospects for the Neutrino Mass and Beyond*, `2203.08059`.

[123] J.M. Yao, J. Meng, Y.F. Niu and P. Ring, *Beyond-mean-field approaches for nuclear neutrinoless double beta decay in the standard mechanism*, `2111.15543`.

[124] LHCb collaboration, *Measurement of the ratio of branching fractions $\mathcal{B}(\bar{B}^0 \to D^{*+}\tau^-\bar{\nu}_\tau)/\mathcal{B}(\bar{B}^0 \to D^{*+}\mu^-\bar{\nu}_\mu)$*, *Phys. Rev. Lett.* **115** (2015) 111803 [`1506.08614`].

[125] Belle collaboration, *Measurement of the branching ratio of $\bar{B} \to D^{(*)}\tau^-\bar{\nu}_\tau$ relative to $\bar{B} \to D^{(*)}\ell^-\bar{\nu}_\ell$ decays with hadronic tagging at Belle*, *Phys. Rev. D* **92** (2015) 072014 [`1507.03233`].

[126] Belle collaboration, *Measurement of the τ lepton polarization and $R(D^*)$ in the decay $\bar{B} \to D^*\tau^-\bar{\nu}_\tau$*, *Phys. Rev. Lett.* **118** (2017) 211801 [`1612.00529`].

[127] Belle collaboration, *Measurement of the τ lepton polarization and $R(D^*)$ in the decay $\bar{B} \to D^*\tau^-\bar{\nu}_\tau$ with one-prong hadronic τ decays at Belle*, *Phys. Rev. D* **97** (2018) 012004 [`1709.00129`].

[128] BaBar collaboration, *Evidence for an excess of $\bar{B} \to D^{(*)}\tau^-\bar{\nu}_\tau$ decays*, *Phys. Rev. Lett.* **109** (2012) 101802 [`1205.5442`].

[129] BaBar collaboration, *Measurement of an Excess of $\bar{B} \to D^{(*)}\tau^-\bar{\nu}_\tau$ Decays and Implications for Charged Higgs Bosons*, *Phys. Rev. D* **88** (2013) 072012 [`1303.0571`].

[130] LHCb collaboration, *Measurement of the ratio of branching fractions $\mathcal{B}(B_c^+ \to J/\psi\tau^+\nu_\tau)/\mathcal{B}(B_c^+ \to J/\psi\mu^+\nu_\mu)$*, *Phys. Rev. Lett.* **120** (2018) 121801 [`1711.05623`].

[131] R. Alonso, B. Grinstein and J. Martin Camalich, *Lifetime of B_c^- Constrains Explanations for Anomalies in $B \to D^{(*)}\tau\nu$*, *Phys. Rev. Lett.* **118** (2017) 081802 [`1611.06676`].

[132] M. Blanke, A. Crivellin, S. de Boer, T. Kitahara, M. Moscati, U. Nierste et al., *Impact of polarization observables and $B_c \to \tau\nu$ on new physics explanations of the $b \to c\tau\nu$ anomaly*, *Phys. Rev. D* **99** (2019) 075006 [`1811.09603`].

[133] C. Bobeth, M. Bordone, N. Gubernari, M. Jung and D. van Dyk, *Lepton-flavour non-universality of $\bar{B} \to D^*\ell\bar{\nu}$ angular distributions in and beyond the Standard Model*, *Eur. Phys. J. C* **81** (2021) 984 [`2104.02094`].

[134] LHCb collaboration, *Observation of the decay $\Lambda_b^0 \to \Lambda_c^+\tau^-\overline{\nu}_\tau$*, `2201.03497`.

[135] D.M. Asner et al., *Belle II Executive Summary*, `2203.10203`.

[136] G. Buchalla, A.J. Buras and M.E. Lautenbacher, *Weak decays beyond leading logarithms*, *Rev. Mod. Phys.* **68** (1996) 1125 [`hep-ph/9512380`].

[137] LHCb collaboration, *Test of lepton universality with $B^0 \to K^{*0}\ell^+\ell^-$ decays*, *JHEP* **08** (2017) 055 [`1705.05802`].

[138] LHCb collaboration, *Search for lepton-universality violation in $B^+ \to K^+\ell^+\ell^-$ decays*, *Phys. Rev. Lett.* **122** (2019) 191801 [`1903.09252`].

[139] LHCb collaboration, *Test of lepton universality in beauty-quark decays*, *Nature Phys.* **18** (2022) 277 [`2103.11769`].

[140] LHCb collaboration, *Branching Fraction Measurements of the Rare $B_s^0 \to \phi\mu^+\mu^-$ and $B_s^0 \to f_2'(1525)\mu^+\mu^-$- Decays*, *Phys. Rev. Lett.* **127** (2021) 151801 [`2105.14007`].

[141] Belle collaboration, *Test of Lepton-Flavor Universality in $B \to K^*\ell^+\ell^-$ Decays at Belle*, *Phys. Rev. Lett.* **126** (2021) 161801 [`1904.02440`].

[142] BELLE collaboration, *Test of lepton flavor universality and search for lepton flavor violation in $B \to K\ell\ell$ decays*, *JHEP* **03** (2021) 105 [`1908.01848`].

[143] M. Nowakowski, E.A. Paschos and J.M. Rodriguez, *All electromagnetic form-factors*, *Eur. J. Phys.* **26** (2005) 545 [`physics/0402058`].

[144] C. Itzykson and J.B. Zuber, *Quantum Field Theory*, International Series In Pure and Applied Physics, McGraw-Hill, New York (1980).

[145] S. Borsanyi et al., *Leading hadronic contribution to the muon magnetic moment from lattice QCD*, *Nature* **593** (2021) 51 [`2002.12347`].

[146] M. Cè et al., *Window observable for the hadronic vacuum polarization contribution to the muon $g-2$ from lattice QCD*, `2206.06582`.

[147] C. Alexandrou et al., *Lattice calculation of the short and intermediate time-distance hadronic vacuum polarization contributions to the muon magnetic moment using twisted-mass fermions*, `2206.15084`.

[148] C.T.H. Davies et al., *Windows on the hadronic vacuum polarisation contribution to the muon anomalous magnetic moment*, `2207.04765`.

[149] R.H. Parker, C. Yu, W. Zhong, B. Estey and H. Müller, *Measurement of the fine-structure constant as a test of the standard model*, *Science* **360** (2018) 191.

[150] L. Morel, Z. Yao, P. Cladé and S. Guellati-Khelifa, *Determination of the fine-structure constant with an accuracy of 81 parts per trillion*, *Nature* **588** (2020) 61.

[151] D. Bryman, V. Cirigliano, A. Crivellin and G. Inguglia, *Testing Lepton Flavor Universality with Pion, Kaon, Tau, and Beta Decays*, `2111.05338`.

[152] A. Crivellin, M. Hoferichter and C.A. Manzari, *Fermi Constant from Muon Decay Versus Electroweak Fits and Cabibbo-Kobayashi-Maskawa Unitarity*, *Phys. Rev. Lett.* **127** (2021) 071801 [`2102.02825`].

[153] K.N. Abazajian et al., *Light Sterile Neutrinos: A White Paper*, `1204.5379`.

[154] M. Drewes, *The Phenomenology of Right Handed Neutrinos*, *Int. J. Mod. Phys. E* **22** (2013) 1330019 [`1303.6912`].

[155] M. Sajjad Athar et al., *Status and perspectives of neutrino physics*, *Prog. Part. Nucl. Phys.* **124** (2022) 103947 [`2111.07586`].

[156] V. Kuzmin, V. Rubakov and M. Shaposhnikov, *On anomalous electroweak baryon-number non-conservation in the early universe*, *Physics Letters B* **155** (1985) 36.

[157] MicroBooNE collaboration, *Search for an Excess of Electron Neutrino Interactions in MicroBooNE Using Multiple Final-State Topologies*, *Phys. Rev. Lett.* **128** (2022) 241801 [`2110.14054`].

[158] MicroBooNE collaboration, *Search for Neutrino-Induced Neutral-Current Δ Radiative Decay in MicroBooNE and a First Test of the MiniBooNE Low Energy Excess under a Single-Photon Hypothesis*, *Phys. Rev. Lett.* **128** (2022) 111801 [`2110.00409`].

[159] B. Dasgupta and J. Kopp, *Sterile Neutrinos*, *Phys. Rept.* **928** (2021) 1 [`2106.05913`].

[160] I. Dorner, S. Fajfer, A. Greljo, J.F. Kamenik and N. Konik, *Physics of leptoquarks in precision experiments and at particle colliders*, *Phys. Rept.* **641** (2016) 1 [`1603.04993`].

[161] A. Angelescu, D. Bečirević, D.A. Faroughy and O. Sumensari, *Closing the window on single leptoquark solutions to the B-physics anomalies*, *JHEP* **10** (2018) 183 [`1808.08179`].

[162] A. Angelescu, D. Bečirević, D.A. Faroughy, F. Jaffredo and O. Sumensari, *Single leptoquark solutions to the B-physics anomalies*, *Phys. Rev. D* **104** (2021) 055017 [`2103.12504`].

[163] O. Popov, M.A. Schmidt and G. White, *R_2 as a single leptoquark solution to $R_{D^{(*)}}$ and $R_{K^{(*)}}$*, *Phys. Rev. D* **100** (2019) 035028 [`1905.06339`].

[164] T. Markkanen, A. Rajantie and S. Stopyra, *Cosmological Aspects of Higgs Vacuum Metastability*, *Front. Astron. Space Sci.* **5** (2018) 40 [`1809.06923`].

[165] B. Horn, *The Higgs field and early universe cosmology: a (brief) review*, *MDPI Physics* **2** (2020) 503 [`2007.10377`].

[166] M.B. Hindmarsh, M. Lüben, J. Lumma and M. Pauly, *Phase transitions in the early universe*, *SciPost Phys. Lect. Notes* **24** (2021) 1 [`2008.09136`].

[167] L. Lavoura and J.P. Silva, *Fundamental CP violating quantities in a* $SU(2) \otimes U(1)$ *model with many Higgs doublets*, *Phys. Rev. D* **50** (1994) 4619 [`hep-ph/9404276`].

[168] C. Froggatt and H. Nielsen, *Hierarchy of quark masses, cabibbo angles and* CP *violation*, *Nuclear Physics B* **147** (1979) 277.

[169] L. Calibbi, F. Goertz, D. Redigolo, R. Ziegler and J. Zupan, *Minimal axion model from flavor*, *Phys. Rev. D* **95** (2017) 095009 [`1612.08040`].

[170] Y. Ema, K. Hamaguchi, T. Moroi and K. Nakayama, *Flaxion: a minimal extension to solve puzzles in the standard model*, *JHEP* **01** (2017) 096 [`1612.05492`].

[171] F. Arias-Aragon and L. Merlo, *The Minimal Flavour Violating Axion*, *JHEP* **10** (2017) 168 [`1709.07039`].

[172] Q. Bonnefoy, P. Cox, E. Dudas, T. Gherghetta and M.D. Nguyen, *Flavoured Warped Axion*, *JHEP* **04** (2021) 084 [`2012.09728`].

[173] P. Cox, T. Gherghetta and M.D. Nguyen, *Light sterile neutrinos and a high-quality axion from a holographic Peccei-Quinn mechanism*, *Phys. Rev. D* **105** (2022) 055011 [`2107.14018`].

[174] E. Goudzovski et al., *New Physics Searches at Kaon and Hyperon Factories*, `2201.07805`.

[175] H. Ishimori, T. Kobayashi, H. Ohki, Y. Shimizu, H. Okada and M. Tanimoto, *Non-Abelian Discrete Symmetries in Particle Physics*, *Prog. Theor. Phys. Suppl.* **183** (2010) 1 [`1003.3552`].

[176] S.F. King and C. Luhn, *Neutrino Mass and Mixing with Discrete Symmetry*, *Rept. Prog. Phys.* **76** (2013) 056201 [`1301.1340`].

[177] F. Feruglio and A. Romanino, *Lepton flavor symmetries*, *Rev. Mod. Phys.* **93** (2021) 015007 [`1912.06028`].

[178] W. Grimus and P.O. Ludl, *Finite flavour groups of fermions*, *J. Phys. A* **45** (2012) 233001 [`1110.6376`].

[179] T.W.B. Kibble, *Topology of cosmic domains and strings*, *Journal of Physics A: Mathematical and General* **9** (1976) 1387.

[180] F. Feruglio, *Are neutrino masses modular forms?*, in *From My Vast Repertoire ...: Guido Altarelli's Legacy*, A. Levy, S. Forte and G. Ridolfi, eds., pp. 227–266 (2019), DOI [`1706.08749`].

[181] R. Penco, *An Introduction to Effective Field Theories*, `2006.16285`.

[182] J.L. Barrow et al., *Theories and Experiments for Testable Baryogenesis Mechanisms: A Snowmass White Paper*, `2203.07059`.

[183] G. Elor et al., *New Ideas in Baryogenesis: A Snowmass White Paper*, in *2022 Snowmass Summer Study*, 3, 2022 [`2203.05010`].

[184] A. Achúcarro et al., *Inflation: Theory and Observations*, `2203.08128`.

[185] B. Grzadkowski, M. Iskrzynski, M. Misiak and J. Rosiek, *Dimension-Six Terms in the Standard Model Lagrangian*, *JHEP* **10** (2010) 085 [`1008.4884`].

[186] A. Kobach, *Baryon Number, Lepton Number, and Operator Dimension in the Standard Model*, *Phys. Lett.* **B758** (2016) 455 [`1604.05726`].

[187] F. del Aguila, S. Bar-Shalom, A. Soni and J. Wudka, *Heavy Majorana Neutrinos in the Effective Lagrangian Description: Application to Hadron Colliders*, *Phys. Lett. B* **670** (2009) 399 [`0806.0876`].

[188] S. Bhattacharya and J. Wudka, *Dimension-seven operators in the standard model with right handed neutrinos*, *Phys. Rev. D* **94** (2016) 055022 [`1505.05264`].

[189] Y. Liao and X.-D. Ma, *Operators up to Dimension Seven in Standard Model Effective Field Theory Extended with Sterile Neutrinos*, *Phys. Rev. D* **96** (2017) 015012 [`1612.04527`].

[190] M. Chala and A. Titov, *One-loop matching in the SMEFT extended with a sterile neutrino*, *JHEP* **05** (2020) 139 [`2001.07732`].

[191] T. Li, X.-D. Ma and M.A. Schmidt, *General neutrino interactions with sterile neutrinos in light of coherent neutrino-nucleus scattering and meson invisible decays*, *JHEP* **07** (2020) 152 [`2005.01543`].

[192] E.E. Jenkins, A.V. Manohar and P. Stoffer, *Low-Energy Effective Field Theory below the Electroweak Scale: Operators and Matching*, *JHEP* **03** (2018) 016 [`1709.04486`].

[193] S. Weinberg, *Phenomenological lagrangians*, *Physica A: Statistical Mechanics and its Applications* **96** (1979) 327.

[194] R. Machleidt and D.R. Entem, *Chiral effective field theory and nuclear forces*, *Phys. Rept.* **503** (2011) 1 [`1105.2919`].

[195] N. Hermansson-Truedsson, *Chiral Perturbation Theory at NNNLO*, *Symmetry* **12** (2020) 1262 [`2006.01430`].

[196] P. Minkowski, *$\mu \to e\gamma$ at a Rate of One Out of 10^9 Muon Decays?*, *Phys. Lett. B* **67** (1977) 421.

[197] T. Yanagida, *Horizontal Symmetry and Masses of Neutrinos*, *Conf.Proc.* **C7902131** (1979) 95.

[198] M. Gell-Mann, P. Ramond and R. Slansky, *Complex Spinors and Unified Theories*, *Conf.Proc.* **C790927** (1979) 315.

[199] R.N. Mohapatra and G. Senjanovic, *Neutrino Mass and Spontaneous Parity Violation*, *Phys.Rev.Lett.* **44** (1980) 912.

[200] S.L. Glashow, *The Future of Elementary Particle Physics*, *NATO Sci. Ser. B* **61** (1980) 687.

[201] M. Magg and C. Wetterich, *Neutrino Mass Problem and Gauge Hierarchy*, *Phys.Lett.* **B94** (1980) 61.

[202] J. Schechter and J. Valle, *Neutrino Masses in $SU(2) \times U(1)$ Theories*, *Phys.Rev.* **D22** (1980) 2227.

[203] G. Lazarides, Q. Shafi and C. Wetterich, *Proton Lifetime and Fermion Masses in an SO(10) Model*, *Nucl.Phys.* **B181** (1981) 287.

[204] C. Wetterich, *Neutrino Masses and the Scale of B-L Violation*, *Nucl. Phys.* **B187** (1981) 343.

[205] R.N. Mohapatra and G. Senjanovic, *Neutrino Masses and Mixings in Gauge Models with Spontaneous Parity Violation*, *Phys. Rev.* **D23** (1981) 165.

[206] R. Foot, H. Lew, X. He and G.C. Joshi, *Seesaw Neutrino Masses Induced by a Triplet of Leptons*, *Z.Phys.* **C44** (1989) 441.

[207] P. Fileviez Perez and M.B. Wise, *On the Origin of Neutrino Masses*, *Phys. Rev. D* **80** (2009) 053006 [`0906.2950`].

[208] S.S.C. Law and K.L. McDonald, *The simplest models of radiative neutrino mass*, *Int. J. Mod. Phys. A* **29** (2014) 1450064 [`1303.6384`].

[209] C. Klein, M. Lindner and S. Ohmer, *Minimal Radiative Neutrino Masses*, *JHEP* **03** (2019) 018 [`1901.03225`].

[210] E. Ma, *Pathways to naturally small neutrino masses*, *Phys. Rev. Lett.* **81** (1998) 1171 [`hep-ph/9805219`].

[211] F. Bonnet, M. Hirsch, T. Ota and W. Winter, *Systematic study of the d=5 Weinberg operator at one-loop order*, *JHEP* **1207** (2012) 153 [`1204.5862`].

[212] D. Aristizabal Sierra, A. Degee, L. Dorame and M. Hirsch, *Systematic classification of two-loop realizations of the Weinberg operator*, *JHEP* **03** (2015) 040 [`1411.7038`].

[213] R. Cepedello, M. Hirsch and J.C. Helo, *Loop neutrino masses from $d = 7$ operator*, *JHEP* **07** (2017) 079 [`1705.01489`].

[214] R. Cepedello, R.M. Fonseca and M. Hirsch, *Systematic classification of three-loop realizations of the Weinberg operator*, *JHEP* **10** (2018) 197 [`1807.00629`].

[215] G. Anamiati, O. Castillo-Felisola, R.M. Fonseca, J.C. Helo and M. Hirsch, *High-dimensional neutrino masses*, *JHEP* **12** (2018) 066 [`1806.07264`].

[216] Y. Farzan, S. Pascoli and M.A. Schmidt, *Recipes and Ingredients for Neutrino Mass at Loop Level*, *JHEP* **03** (2013) 107 [`1208.2732`].

[217] S.S.C. Law and K.L. McDonald, *A Class of Inert N-tuplet Models with Radiative Neutrino Mass and Dark Matter*, *JHEP* **09** (2013) 092 [`1305.6467`].

[218] D. Restrepo, O. Zapata and C.E. Yaguna, *Models with radiative neutrino masses and viable dark matter candidates*, *JHEP* **11** (2013) 011 [`1308.3655`].

[219] F. Bonnet, D. Hernandez, T. Ota and W. Winter, *Neutrino masses from higher than d=5 effective operators*, *JHEP* **10** (2009) 076 [`0907.3143`].

[220] M.B. Krauss, D. Meloni, W. Porod and W. Winter, *Neutrino Mass from a d=7 Effective Operator in an SU(5) SUSY-GUT Framework*, *JHEP* **05** (2013) 121 [`1301.4221`].

[221] M. Gustafsson, J.M. No and M.A. Rivera, *Predictive Model for Radiatively Induced Neutrino Masses and Mixings with Dark Matter*, *Phys. Rev. Lett.* **110** (2013) 211802 [`1212.4806`].

[222] T. Geib, S.F. King, A. Merle, J.M. No and L. Panizzi, *Probing the Origin of Neutrino Masses and Mixings via Doubly Charged Scalars: Complementarity of the Intensity and the Energy Frontiers*, *Phys. Rev. D* **93** (2016) 073007 [`1512.04391`].

[223] J. Herrero-García, T. Ohlsson, S. Riad and J. Wirén, *Full parameter scan of the Zee model: exploring Higgs lepton flavor violation*, *JHEP* **04** (2017) 130 [`1701.05345`].

[224] M. Nebot, J.F. Oliver, D. Palao and A. Santamaria, *Prospects for the Zee-Babu Model at the CERN LHC and low energy experiments*, *Phys. Rev.* **D77** (2008) 093013 [`0711.0483`].

[225] T. Ohlsson, T. Schwetz and H. Zhang, *Non-standard neutrino interactions in the Zee-Babu model*, *Phys.Lett.* **B681** (2009) 269 [`0909.0455`].

[226] J. Herrero-Garcia, M. Nebot, N. Rius and A. Santamaria, *The Zee-Babu Model revisited in the light of new data*, *Nucl.Phys.* **B885** (2014) 542 [`1402.4491`].

[227] A. Ahriche, C.-S. Chen, K.L. McDonald and S. Nasri, *Three-loop model of neutrino mass with dark matter*, *Phys. Rev. D* **90** (2014) 015024 [`1404.2696`].

[228] C.-S. Chen, K.L. McDonald and S. Nasri, *A Class of Three-Loop Models with Neutrino Mass and Dark Matter*, *Phys. Lett. B* **734** (2014) 388 [`1404.6033`].

[229] J.A. Casas and A. Ibarra, *Oscillating neutrinos and* $\mu \to e, \gamma$, *Nucl. Phys. B* **618** (2001) 171 [`hep-ph/0103065`].

[230] I. Cordero-Carrión, M. Hirsch and A. Vicente, *Master Majorana neutrino mass parametrization*, *Phys. Rev. D* **99** (2019) 075019 [`1812.03896`].

[231] I. Cordero-Carrión, M. Hirsch and A. Vicente, *General parametrization of Majorana neutrino mass models*, *Phys. Rev. D* **101** (2020) 075032 [`1912.08858`].

[232] I. Esteban, M.C. Gonzalez-Garcia, A. Hernandez-Cabezudo, M. Maltoni and T. Schwetz, *Global analysis of three-flavour neutrino oscillations: synergies and tensions in the determination of* θ_{23}, δ_{CP}, *and the mass ordering*, *JHEP* **01** (2019) 106 [`1811.05487`].

[233] X.-G. He and S.K. Majee, *Implications of Recent Data on Neutrino Mixing and Lepton Flavour Violating Decays for the Zee Model*, *JHEP* **03** (2012) 023 [`1111.2293`].

[234] T. Matsui, T. Nomura and K. Yagyu, *Flavor Dependent* $U(1)$ *Symmetric Zee Model with a Vector-like Lepton*, `2102.09247`.

[235] K. Babu and C. Macesanu, *Two loop neutrino mass generation and its experimental consequences*, *Phys.Rev.* **D67** (2003) 073010 [`hep-ph/0212058`].

[236] K.L. McDonald and B. McKellar, *Evaluating the two loop diagram responsible for neutrino mass in Babu's model*, `hep-ph/0309270`.

[237] A. Crivellin, F. Kirk, C.A. Manzari and L. Panizzi, *Searching for Lepton Flavour (Universality) Violation and Collider Signals from a Singly-Charged Scalar Singlet*, `2012.09845`.

[238] ATLAS collaboration, *Search for electroweak production of charginos and sleptons decaying into final states with two leptons and missing transverse momentum in $\sqrt{s} = 13$ TeV pp collisions using the ATLAS detector*, *Eur. Phys. J. C* **80** (2020) 123 [`1908.08215`].

[239] Q.-H. Cao, G. Li, K.-P. Xie and J. Zhang, *Searching for Weak Singlet Charged Scalar at the Large Hadron Collider*, *Phys. Rev. D* **97** (2018) 115036 [`1711.02113`].

[240] MEG II collaboration, *The design of the MEG II experiment*, *Eur. Phys. J. C* **78** (2018) 380 [`1801.04688`].

[241] BaBar collaboration, *Searches for Lepton Flavor Violation in the Decays $\tau^\pm \to e^\pm \gamma$ and $\tau^\pm \to \mu^\pm \gamma$*, *Phys. Rev. Lett.* **104** (2010) 021802 [`0908.2381`].

[242] SINDRUM collaboration, *Search for the Decay $\mu^+ \to e^+ e^+ e^-$*, *Nucl. Phys. B* **299** (1988) 1.

[243] Mu3e collaboration, *Technical design of the phase I Mu3e experiment*, `2009.11690`.

[244] E. Gersabeck and A. Pich, *Tau and charm decays*, *Comptes Rendus Physique* **21** (2020) 75.

[245] M.S. Bilenky and A. Santamaria, *One loop effective Lagrangian for a standard model with a heavy charged scalar singlet*, *Nucl. Phys. B* **420** (1994) 47 [`hep-ph/9310302`].

[246] A. Pich, *Precision Tau Physics*, *Prog. Part. Nucl. Phys.* **75** (2014) 41 [`1310.7922`].

[247] L. Berthier and M. Trott, *Towards consistent Electroweak Precision Data constraints in the SMEFT*, *JHEP* **05** (2015) 024 [`1502.02570`].

[248] A.K. Alok, A. Dighe, S. Gangal and J. Kumar, *The role of non-universal Z couplings in explaining the V_{us} anomaly*, `2010.12009`.

[249] A.M. Coutinho, A. Crivellin and C.A. Manzari, *Global Fit to Modified Neutrino Couplings and the Cabibbo-Angle Anomaly*, *Phys. Rev. Lett.* **125** (2020) 071802 [`1912.08823`].

[250] M. Kirk, *The Cabibbo anomaly versus electroweak precision tests – an exploration of extensions of the Standard Model*, *Phys. Rev. D* **103** (2021) 035004 [`2008.03261`].

[251] A. Crivellin, F. Kirk, C.A. Manzari and M. Montull, *Global Electroweak Fit and Vector-Like Leptons in Light of the Cabibbo Angle Anomaly*, `2008.01113`.

[252] B. Capdevila, A. Crivellin, C.A. Manzari and M. Montull, *Explaining $b \to s\ell^+\ell^-$ and the Cabibbo Angle Anomaly with a Vector Triplet*, *Phys. Rev. D* **103** (2021) 015032 [`2005.13542`].

[253] M. Endo and S. Mishima, *Muon $g - 2$ and CKM unitarity in extra lepton models*, *JHEP* **08** (2020) 004 [`2005.03933`].

[254] A. Crivellin and M. Hoferichter, *β Decays as Sensitive Probes of Lepton Flavor Universality*, *Phys. Rev. Lett.* **125** (2020) 111801 [`2002.07184`].

[255] B. Belfatto, R. Beradze and Z. Berezhiani, *The CKM unitarity problem: A trace of new physics at the TeV scale?*, *Eur. Phys. J. C* **80** (2020) 149 [`1906.02714`].

[256] Flavour Lattice Averaging Group collaboration, *FLAG Review 2019: Flavour Lattice Averaging Group (FLAG)*, *Eur. Phys. J. C* **80** (2020) 113 [`1902.08191`].

[257] HFLAV collaboration, *Averages of b-hadron, c-hadron, and τ-lepton properties as of 2018*, `1909.12524`.

[258] C.Y. Seng, M. Gorchtein and M.J. Ramsey-Musolf, *Dispersive evaluation of the inner radiative correction in neutron and nuclear β decay*, *Phys. Rev.* **D100** (2019) 013001 [`1812.03352`].

[259] C.-Y. Seng, X. Feng, M. Gorchtein and L.-C. Jin, *Joint lattice QCD–dispersion theory analysis confirms the quark-mixing top-row unitarity deficit*, *Phys. Rev. D* **101** (2020) 111301 [`2003.11264`].

[260] A. Pich, *Challenges for tau physics at the TeraZ*, `2012.07099`.

[261] FCC collaboration, *FCC Physics Opportunities*, *Eur. Phys. J.* **C79** (2019) 474.

[262] Super Charm-Tau Factory collaboration, *The Super Charm-Tau Factory in Novosibirsk*, *PoS* **LeptonPhoton2019** (2019) 062.

[263] Q. Luo, W. Gao, J. Lan, W. Li and D. Xu, *Progress of Conceptual Study for the Accelerators of a 2-7GeV Super Tau Charm Facility at China*, in *10th International Particle Accelerator Conference*, p. MOPRB031, 2019, DOI.

[264] I. Brivio and M. Trott, *The Standard Model as an Effective Field Theory*, *Phys. Rept.* **793** (2019) 1 [`1706.08945`].

[265] J. Erler, *Electroweak Precision Tests of the SM*, 2019 [`1908.07346`].

[266] CEPC Study Group collaboration, *CEPC Conceptual Design Report: Volume 2 - Physics & Detector*, `1811.10545`.

[267] Y. Farzan and M. Tortola, *Neutrino oscillations and Non-Standard Interactions*, *Front. in Phys.* **6** (2018) 10 [`1710.09360`].

[268] B. Dev, "NSI and Neutrino Mass Models at DUNE." `https://indico.fnal.gov/event/18430/contributions/47239/attachments/29448/36310/dev_pondd.pdf`, 2018.

[269] J. Tang and W. Winter, *Physics with near detectors at a neutrino factory*, *Phys. Rev. D* **80** (2009) 053001 [`0903.3039`].

[270] S. Bertolini and A. Santamaria, *The doublet majoron model and solar neutrino oscillations*, *Nuclear Physics B* **310** (1988) 714.

[271] S.M. Bilenky and S.T. Petcov, *Massive neutrinos and neutrino oscillations*, *Rev. Mod. Phys.* **59** (1987) 671.

[272] A. Pich, A. Santamaría and J. Bernabéu, *$\mu^- \to e^-\gamma$ decay in the scalar triplet model*, *Physics Letters B* **148** (1984) 229.

[273] Y. Kuno and Y. Okada, *Muon decay and physics beyond the standard model*, *Rev. Mod. Phys.* **73** (2001) 151 [`hep-ph/9909265`].

[274] A. Crivellin, S. Najjari and J. Rosiek, *Lepton Flavor Violation in the Standard Model with general Dimension-Six Operators*, *JHEP* **04** (2014) 167 [`1312.0634`].

[275] SINDRUM II collaboration, *A Search for muon to electron conversion in muonic gold*, *Eur. Phys. J. C* **47** (2006) 337.

[276] A. Crivellin, M. Hoferichter and P. Schmidt-Wellenburg, *Combined explanations of $(g-2)_{\mu,e}$ and implications for a large muon EDM*, *Phys. Rev. D* **98** (2018) 113002 [`1807.11484`].

[277] R. Kitano, M. Koike and Y. Okada, *Detailed calculation of lepton flavor violating muon electron conversion rate for various nuclei*, *Phys. Rev. D* **66** (2002) 096002 [`hep-ph/0203110`].

[278] R.K. Kutschke, *The Mu2e Experiment at Fermilab*, in *31st International Symposium on Physics In Collision*, 12, 2011 [`1112.0242`].

[279] COMET collaboration, *COMET/PRISM muon to electron conversion at J-PARC*, *AIP Conf. Proc.* **1182** (2009) 694.

[280] Y. Kuno, *PRISM/PRIME*, *Nucl. Phys. B Proc. Suppl.* **149** (2005) 376.

[281] S.R. Moore, K. Whisnant and B.-L. Young, *Second-order corrections to the muon anomalous magnetic moment in alternative electroweak models*, *Phys. Rev. D* **31** (1985) 105.

[282] J.P. Leveille, *The second-order weak correction to (g - 2) of the muon in arbitrary gauge models*, *Nuclear Physics B* **137** (1978) 63.

[283] M. Lindner, M. Platscher and F.S. Queiroz, *A Call for New Physics : The Muon Anomalous Magnetic Moment and Lepton Flavor Violation*, *Phys. Rept.* **731** (2018) 1 [`1610.06587`].

[284] T. Blum, A. Denig, I. Logashenko, E. de Rafael, B.L. Roberts, T. Teubner et al., *The Muon (g-2) Theory Value: Present and Future*, `1311.2198`.

[285] I. Bigaran and R.R. Volkas, *Getting chirality right: Single scalar leptoquark solutions to the $(g-2)_{e,\mu}$ puzzle*, *Phys. Rev. D* **102** (2020) 075037 [`2002.12544`].

[286] R.H. Parker, C. Yu, W. Zhong, B. Estey and H. Müller, *Measurement of the fine-structure constant as a test of the standard model*, *Science* **360** (2018) 191 [`https://science.sciencemag.org/content/360/6385/191.full.pdf`].

[287] N. Chakrabarty, C.-W. Chiang, T. Ohata and K. Tsumura, *Charged scalars confronting neutrino mass and muon $g-2$ anomaly*, *JHEP* **12** (2018) 104 [`1807.08167`].

[288] T. Nomura and H. Okada, *Zee-Babu type model with $U(1)_{L_\mu - L_\tau}$ gauge symmetry*, *Phys. Rev. D* **97** (2018) 095023 [`1803.04795`].

[289] T. Suzuki, D.F. Measday and J.P. Roalsvig, *Total Nuclear Capture Rates for Negative Muons*, *Phys. Rev. C* **35** (1987) 2212.

[290] CDF collaboration, *High-precision measurement of the W boson mass with the CDF II detector*, *Science* **376** (2022) 170.

[291] Belle collaboration, *Search for $B \to h^{(*)}\nu\bar{\nu}$ with the full Belle $\Upsilon(4S)$ data sample*, *Phys. Rev. D* **87** (2013) 111103 [`1303.3719`].

[292] BaBar collaboration, *Search for $B \to K^{(*)}\nu\bar{\nu}$ and invisible quarkonium decays*, *Phys. Rev. D* **87** (2013) 112005 [`1303.7465`].

[293] T.E. Browder, N.G. Deshpande, R. Mandal and R. Sinha, *Impact of $B \to K\nu\bar{\nu}$ measurements on beyond the Standard Model theories*, *Phys. Rev. D* **104** (2021) 053007 [`2107.01080`].

[294] X.G. He and G. Valencia, *$R^{\nu}_{K^{(*)}}$ and non-standard neutrino interactions*, *Phys. Lett. B* **821** (2021) 136607 [`2108.05033`].

[295] S. Descotes-Genon, S. Fajfer, J.F. Kamenik and M. Novoa-Brunet, *Implications of $b \to s\mu\mu$ anomalies for future measurements of $B \to K^{(*)}\nu\bar{\nu}$ and $K \to \pi\nu\bar{\nu}$*, *Phys. Lett. B* **809** (2020) 135769 [`2005.03734`].

[296] L. Calibbi, A. Crivellin and T. Ota, *Effective Field Theory Approach to $b \to s\ell\ell^{(\prime)}$, $B \to K^{(*)}\nu\overline{\nu}$ and $B \to D^{(*)}\tau\nu$ with Third Generation Couplings*, *Phys. Rev. Lett.* **115** (2015) 181801 [`1506.02661`].

[297] S. Fukae, C.S. Kim, T. Morozumi and T. Yoshikawa, *A Model independent analysis of the rare B decay $B \to X_s l^+ l^-$*, *Phys. Rev. D* **59** (1999) 074013 [`hep-ph/9807254`].

[298] J. Aebischer, M. Fael, C. Greub and J. Virto, *B physics Beyond the Standard Model at One Loop: Complete Renormalization Group Evolution below the Electroweak Scale*, *JHEP* **09** (2017) 158 [`1704.06639`].

[299] A.G. Beda, V.B. Brudanin, V.G. Egorov, D.V. Medvedev, V.S. Pogosov, M.V. Shirchenko et al., *The results of search for the neutrino magnetic moment in GEMMA experiment*, *Adv. High Energy Phys.* **2012** (2012) 350150.

[300] Borexino collaboration, *Limiting neutrino magnetic moments with Borexino Phase-II solar neutrino data*, *Phys. Rev. D* **96** (2017) 091103 [`1707.09355`].

[301] C. Giunti and A. Studenikin, *Neutrino electromagnetic interactions: a window to new physics*, *Rev. Mod. Phys.* **87** (2015) 531 [`1403.6344`].

[302] J. Gratrex, M. Hopfer and R. Zwicky, *Generalised helicity formalism, higher moments and the $B \to K_{J_K}(\to K\pi)\bar{\ell}_1\ell_2$ angular distributions*, *Phys. Rev. D* **93** (2016) 054008 [`1506.03970`].

[303] J. Brod, M. Gorbahn and E. Stamou, *Two-Loop Electroweak Corrections for the $K \to \pi\nu\bar{\nu}$ Decays*, *Phys. Rev. D* **83** (2011) 034030 [`1009.0947`].

[304] E.E. Jenkins, A.V. Manohar and P. Stoffer, *Low-Energy Effective Field Theory below the Electroweak Scale: Anomalous Dimensions*, *JHEP* **01** (2018) 084 [`1711.05270`].

[305] K.G. Chetyrkin, J.H. Kuhn and M. Steinhauser, *RunDec: A Mathematica package for running and decoupling of the strong coupling and quark masses*, *Comput. Phys. Commun.* **133** (2000) 43 [`hep-ph/0004189`].

[306] ALEPH collaboration, *Measurements of* $\mathrm{BR}(b \to \tau^- \bar{\nu}_\tau X)$ *and* $\mathrm{BR}(b \to \tau^- \bar{\nu}_\tau D^{*\pm} X)$ *and upper limits on* $\mathrm{BR}(B^- \to \tau^- \bar{\nu}_\tau)$ *and* $\mathrm{BR}(b \to s\nu\bar{\nu})$, *Eur. Phys. J. C* **19** (2001) 213 [`hep-ex/0010022`].

[307] M. Jacob and G.C. Wick, *On the General Theory of Collisions for Particles with Spin*, *Annals Phys.* **7** (1959) 404.

[308] D. Das, G. Hiller and I. Nisandzic, *Revisiting* $B \to K^*(\to K\pi)\nu\bar{\nu}$ *decays*, *Phys. Rev. D* **95** (2017) 073001 [`1702.07599`].

[309] S.-L. Li, *Invisible and semi-invisible meson decay in low energy effective field theory including sterile neutrinos*, honours thesis, The University of New South Wales, 2020.

[310] W. Altmannshofer, P. Ball, A. Bharucha, A.J. Buras, D.M. Straub and M. Wick, *Symmetries and Asymmetries of* $B \to K^* \mu^+ \mu^-$ *Decays in the Standard Model and Beyond*, *JHEP* **01** (2009) 019 [`0811.1214`].

[311] C. Bobeth, G. Hiller and D. van Dyk, *General analysis of* $\bar{B} \to \bar{K}^{(*)} \ell^+ \ell^-$ *decays at low recoil*, *Phys. Rev. D* **87** (2013) 034016 [`1212.2321`].

[312] PARTICLE DATA GROUP collaboration, *Review of Particle Physics*, *PTEP* **2020** (2020) 083C01.

[313] J. Chay, H. Georgi and B. Grinstein, *Lepton energy distributions in heavy meson decays from QCD*, *Physics Letters B* **247** (1990) 399.

[314] A.H. Hoang, Z. Ligeti and A.V. Manohar, *B decay and the Upsilon mass*, *Phys. Rev. Lett.* **82** (1999) 277 [`hep-ph/9809423`].

[315] C.W. Bauer, Z. Ligeti, M. Luke, A.V. Manohar and M. Trott, *Global analysis of inclusive B decays*, *Phys. Rev. D* **70** (2004) 094017 [`hep-ph/0408002`].

[316] SIMBA collaboration, *Precision Global Determination of the $B \to X_s\gamma$ Decay Rate*, *Phys. Rev. Lett.* **127** (2021) 102001 [`2007.04320`].

[317] V. Shtabovenko, R. Mertig and F. Orellana, *New Developments in FeynCalc 9.0*, *Comput. Phys. Commun.* **207** (2016) 432 [`1601.01167`].

[318] V. Shtabovenko, R. Mertig and F. Orellana, *FeynCalc 9.3: New features and improvements*, *Comput. Phys. Commun.* **256** (2020) 107478 [`2001.04407`].

[319] T. Li, X.-D. Ma and M.A. Schmidt, *Implication of $K \to \pi\nu\bar{\nu}$ for generic neutrino interactions in effective field theories*, *Phys. Rev. D* **101** (2020) 055019 [`1912.10433`].

[320] P.F. Harrison, D.H. Perkins and W.G. Scott, *Tri-bimaximal mixing and the neutrino oscillation data*, *Phys. Lett. B* **530** (2002) 167 [`hep-ph/0202074`].

[321] P.F. Harrison and W.G. Scott, *Symmetries and generalizations of tri-bimaximal neutrino mixing*, *Phys. Lett. B* **535** (2002) 163 [`hep-ph/0203209`].

[322] Z.-z. Xing, *Nearly tri bimaximal neutrino mixing and CP violation*, *Phys. Lett. B* **533** (2002) 85 [`hep-ph/0204049`].

[323] P.F. Harrison and W.G. Scott, *Permutation symmetry, tri-bimaximal neutrino mixing and the S_3 group characters*, *Phys. Lett. B* **557** (2003) 76 [`hep-ph/0302025`].

[324] M. Davier, A. Hoecker, B. Malaescu and Z. Zhang, *Reevaluation of the hadronic vacuum polarisation contributions to the Standard Model predictions of the muon $g-2$ and $\alpha(m_Z^2)$ using newest hadronic cross-section data*, *Eur. Phys. J. C* **77** (2017) 827 [`1706.09436`].

[325] A. Keshavarzi, D. Nomura and T. Teubner, *Muon $g-2$ and $\alpha(M_Z^2)$: a new data-based analysis*, *Phys. Rev. D* **97** (2018) 114025 [`1802.02995`].

[326] G. Colangelo, M. Hoferichter and P. Stoffer, *Two-pion contribution to hadronic vacuum polarization*, *JHEP* **02** (2019) 006 [`1810.00007`].

[327] M. Hoferichter, B.-L. Hoid and B. Kubis, *Three-pion contribution to hadronic vacuum polarization*, *JHEP* **08** (2019) 137 [`1907.01556`].

[328] M. Davier, A. Hoecker, B. Malaescu and Z. Zhang, *A new evaluation of the hadronic vacuum polarisation contributions to the muon anomalous magnetic moment and to* $\boldsymbol{\alpha}(\mathbf{m_Z^2})$, *Eur. Phys. J. C* **80** (2020) 241 [`1908.00921`].

[329] A. Keshavarzi, D. Nomura and T. Teubner, $g-2$ *of charged leptons,* $\alpha(M_Z^2)$ *, and the hyperfine splitting of muonium*, *Phys. Rev. D* **101** (2020) 014029 [`1911.00367`].

[330] A. Kurz, T. Liu, P. Marquard and M. Steinhauser, *Hadronic contribution to the muon anomalous magnetic moment to next-to-next-to-leading order*, *Phys. Lett. B* **734** (2014) 144 [`1403.6400`].

[331] Fermilab Lattice, LATTICE-HPQCD, MILC collaboration, *Strong-Isospin-Breaking Correction to the Muon Anomalous Magnetic Moment from Lattice QCD at the Physical Point*, *Phys. Rev. Lett.* **120** (2018) 152001 [`1710.11212`].

[332] Budapest-Marseille-Wuppertal collaboration, *Hadronic vacuum polarization contribution to the anomalous magnetic moments of leptons from first principles*, *Phys. Rev. Lett.* **121** (2018) 022002 [`1711.04980`].

[333] RBC, UKQCD collaboration, *Calculation of the hadronic vacuum polarization contribution to the muon anomalous magnetic moment*, *Phys. Rev. Lett.* **121** (2018) 022003 [`1801.07224`].

[334] D. Giusti, V. Lubicz, G. Martinelli, F. Sanfilippo and S. Simula, *Electromagnetic and strong isospin-breaking corrections to the muon* $g-2$ *from Lattice QCD+QED*, *Phys. Rev. D* **99** (2019) 114502 [`1901.10462`].

[335] PACS collaboration, *Hadronic vacuum polarization contribution to the muon $g-2$ with 2+1 flavor lattice QCD on a larger than (10 fm)^4 lattice at the physical point*, *Phys. Rev. D* **100** (2019) 034517 [`1902.00885`].

[336] Fermilab Lattice, LATTICE-HPQCD, MILC collaboration, *Hadronic-vacuum-polarization contribution to the muon's anomalous magnetic moment from four-flavor lattice QCD*, *Phys. Rev. D* **101** (2020) 034512 [`1902.04223`].

[337] A. Gérardin, M. Cè, G. von Hippel, B. Hörz, H.B. Meyer, D. Mohler et al., *The leading hadronic contribution to $(g-2)_\mu$ from lattice QCD with $N_\mathrm{f}=2+1$ flavours of O(a) improved Wilson quarks*, *Phys. Rev. D* **100** (2019) 014510 [`1904.03120`].

[338] C. Aubin, T. Blum, C. Tu, M. Golterman, C. Jung and S. Peris, *Light quark vacuum polarization at the physical point and contribution to the muon $g-2$*, *Phys. Rev. D* **101** (2020) 014503 [`1905.09307`].

[339] D. Giusti and S. Simula, *Lepton anomalous magnetic moments in Lattice QCD+QED*, *PoS* **LATTICE2019** (2019) 104 [`1910.03874`].

[340] K. Melnikov and A. Vainshtein, *Hadronic light-by-light scattering contribution to the muon anomalous magnetic moment revisited*, *Phys. Rev. D* **70** (2004) 113006 [`hep-ph/0312226`].

[341] P. Masjuan and P. Sanchez-Puertas, *Pseudoscalar-pole contribution to the $(g_\mu - 2)$: a rational approach*, *Phys. Rev. D* **95** (2017) 054026 [`1701.05829`].

[342] G. Colangelo, M. Hoferichter, M. Procura and P. Stoffer, *Dispersion relation for hadronic light-by-light scattering: two-pion contributions*, *JHEP* **04** (2017) 161 [`1702.07347`].

[343] M. Hoferichter, B.-L. Hoid, B. Kubis, S. Leupold and S.P. Schneider, *Dispersion relation for hadronic light-by-light scattering: pion pole*, *JHEP* **10** (2018) 141 [`1808.04823`].

[344] A. Gérardin, H.B. Meyer and A. Nyffeler, *Lattice calculation of the pion transition form factor with $N_f = 2+1$ Wilson quarks*, *Phys. Rev. D* **100** (2019) 034520 [1903.09471].

[345] J. Bijnens, N. Hermansson-Truedsson and A. Rodríguez-Sánchez, *Short-distance constraints for the HLbL contribution to the muon anomalous magnetic moment*, *Phys. Lett. B* **798** (2019) 134994 [1908.03331].

[346] G. Colangelo, F. Hagelstein, M. Hoferichter, L. Laub and P. Stoffer, *Longitudinal short-distance constraints for the hadronic light-by-light contribution to $(g-2)_\mu$ with large-N_c Regge models*, *JHEP* **03** (2020) 101 [1910.13432].

[347] V. Pauk and M. Vanderhaeghen, *Single meson contributions to the muon's anomalous magnetic moment*, *Eur. Phys. J. C* **74** (2014) 3008 [1401.0832].

[348] I. Danilkin and M. Vanderhaeghen, *Light-by-light scattering sum rules in light of new data*, *Phys. Rev. D* **95** (2017) 014019 [1611.04646].

[349] F. Jegerlehner, *The Anomalous Magnetic Moment of the Muon*, vol. 274, Springer, Cham (2017), 10.1007/978-3-319-63577-4.

[350] M. Knecht, S. Narison, A. Rabemananjara and D. Rabetiarivony, *Scalar meson contributions to a μ from hadronic light-by-light scattering*, *Phys. Lett. B* **787** (2018) 111 [1808.03848].

[351] G. Eichmann, C.S. Fischer and R. Williams, *Kaon-box contribution to the anomalous magnetic moment of the muon*, *Phys. Rev. D* **101** (2020) 054015 [1910.06795].

[352] P. Roig and P. Sanchez-Puertas, *Axial-vector exchange contribution to the hadronic light-by-light piece of the muon anomalous magnetic moment*, *Phys. Rev. D* **101** (2020) 074019 [1910.02881].

[353] G. Colangelo, M. Hoferichter, A. Nyffeler, M. Passera and P. Stoffer, *Remarks on higher-order hadronic corrections to the muon g−2*, *Phys. Lett. B* **735** (2014) 90 [1403.7512].

[354] T. Blum, N. Christ, M. Hayakawa, T. Izubuchi, L. Jin, C. Jung et al., *Hadronic Light-by-Light Scattering Contribution to the Muon Anomalous Magnetic Moment from Lattice QCD*, *Phys. Rev. Lett.* **124** (2020) 132002 [`1911.08123`].

[355] T. Aoyama, M. Hayakawa, T. Kinoshita and M. Nio, *Complete Tenth-Order QED Contribution to the Muon g-2*, *Phys. Rev. Lett.* **109** (2012) 111808 [`1205.5370`].

[356] T. Aoyama, T. Kinoshita and M. Nio, *Theory of the Anomalous Magnetic Moment of the Electron*, *Atoms* **7** (2019) 28.

[357] A. Czarnecki, W.J. Marciano and A. Vainshtein, *Refinements in electroweak contributions to the muon anomalous magnetic moment*, *Phys. Rev. D* **67** (2003) 073006 [`hep-ph/0212229`].

[358] C. Gnendiger, D. Stöckinger and H. Stöckinger-Kim, *The electroweak contributions to* $(g-2)_\mu$ *after the Higgs boson mass measurement*, *Phys. Rev. D* **88** (2013) 053005 [`1306.5546`].

[359] A. Crivellin, D. Müller and T. Ota, *Simultaneous explanation of R(*$D^{(*)}$*) and* $b{\to}s\mu^+\,\mu^-$*: the last scalar leptoquarks standing*, *JHEP* **09** (2017) 040 [`1703.09226`].

[360] D. Buttazzo, A. Greljo, G. Isidori and D. Marzocca, *B-physics anomalies: a guide to combined explanations*, *JHEP* **11** (2017) 044 [`1706.07808`].

[361] D. Marzocca, *Addressing the B-physics anomalies in a fundamental Composite Higgs Model*, *JHEP* **07** (2018) 121 [`1803.10972`].

[362] I. Bigaran, J. Gargalionis and R.R. Volkas, *A near-minimal leptoquark model for reconciling flavour anomalies and generating radiative neutrino masses*, *JHEP* **10** (2019) 106 [`1906.01870`].

[363] A. Crivellin, D. Müller and F. Saturnino, *Flavor Phenomenology of the Leptoquark Singlet-Triplet Model*, *JHEP* **06** (2020) 020 [`1912.04224`].

[364] S. Balaji and M.A. Schmidt, *Unified SU(4) theory for the* $R_{D^{(*)}}$ *and* $R_{K^{(*)}}$ *anomalies*, *Phys. Rev. D* **101** (2020) 015026 [`1911.08873`].

[365] S. Saad and A. Thapa, *Common origin of neutrino masses and $R_{D^{(*)}}$, $R_{K^{(*)}}$ anomalies*, *Phys. Rev. D* **102** (2020) 015014 [`2004.07880`].

[366] S. Saad, *Combined explanations of $(g-2)_\mu$, $R_{D^{(*)}}$, $R_{K^{(*)}}$ anomalies in a two-loop radiative neutrino mass model*, *Phys. Rev. D* **102** (2020) 015019 [`2005.04352`].

[367] V. Gherardi, D. Marzocca and E. Venturini, *Low-energy phenomenology of scalar leptoquarks at one-loop accuracy*, *JHEP* **01** (2021) 138 [`2008.09548`].

[368] M. Bordone, O. Catà, T. Feldmann and R. Mandal, *Constraining flavour patterns of scalar leptoquarks in the effective field theory*, *JHEP* **03** (2021) 122 [`2010.03297`].

[369] D. Marzocca and S. Trifinopoulos, *Minimal Explanation of Flavor Anomalies: B-Meson Decays, Muon Magnetic Moment, and the Cabibbo Angle*, *Phys. Rev. Lett.* **127** (2021) 061803 [`2104.05730`].

[370] J. Julio, S. Saad and A. Thapa, *Marriage between neutrino mass and flavor anomalies*, `2203.15499`.

[371] S.-L. Chen, W.-w. Jiang and Z.-K. Liu, *Combined explanations of B-physics anomalies, $(g-2)_{e,\mu}$ and neutrino masses by scalar leptoquarks*, `2205.15794`.

[372] W. Grimus and L. Lavoura, *A Discrete symmetry group for maximal atmospheric neutrino mixing*, *Phys. Lett. B* **572** (2003) 189 [`hep-ph/0305046`].

[373] W. Grimus and L. Lavoura, *$S_3 \times Z_2$ model for neutrino mass matrices*, *JHEP* **08** (2005) 013 [`hep-ph/0504153`].

[374] A. Blum, C. Hagedorn and M. Lindner, *Fermion Masses and Mixings from Dihedral Flavor Symmetries with Preserved Subgroups*, *Phys. Rev. D* **77** (2008) 076004 [`0709.3450`].

[375] C.S. Lam, *Symmetry of Lepton Mixing*, *Phys. Lett. B* **656** (2007) 193 [`0708.3665`].

[376] L.J. Hall and M.B. Wise, *Flavor Changing Higgs - Boson Couplings*, *Nucl. Phys. B* **187** (1981) 397.

[377] J.F. Donoghue and L.F. Li, *Properties of Charged Higgs Bosons*, *Phys. Rev. D* **19** (1979) 945.

[378] Z.-z. Xing, H. Zhang and S. Zhou, *Updated Values of Running Quark and Lepton Masses*, *Phys. Rev. D* **77** (2008) 113016 [`0712.1419`].

[379] H.E. Haber and Y. Nir, *Multiscalar Models With a High-energy Scale*, *Nucl. Phys. B* **335** (1990) 363.

[380] ATLAS collaboration, *Search for new phenomena in pp collisions in final states with tau leptons, b-jets, and missing transverse momentum with the ATLAS detector*, *Phys. Rev. D* **104** (2021) 112005 [`2108.07665`].

[381] ATLAS collaboration, *Search for pairs of scalar leptoquarks decaying into quarks and electrons or muons in $\sqrt{s}$ = 13 TeV pp collisions with the ATLAS detector*, *JHEP* **10** (2020) 112 [`2006.05872`].

[382] CMS collaboration, *Search for new particles in events with energetic jets and large missing transverse momentum in proton-proton collisions at $\sqrt{s}$ = 13 TeV*, *JHEP* **11** (2021) 153 [`2107.13021`].

[383] J. Aebischer, J. Kumar and D.M. Straub, *Wilson: a Python package for the running and matching of Wilson coefficients above and below the electroweak scale*, *Eur. Phys. J. C* **78** (2018) 1026 [`1804.05033`].

[384] W. Porod, F. Staub and A. Vicente, *A Flavor Kit for BSM models*, *Eur. Phys. J.* **C74** (2014) 2992 [`1405.1434`].

[385] W. Porod and F. Staub, *SPheno 3.1: Extensions including flavour, CP-phases and models beyond the MSSM*, *Comput. Phys. Commun.* **183** (2012) 2458 [`1104.1573`].

[386] S. Banerjee et al., *Snowmass 2021 White Paper: Charged lepton flavor violation in the tau sector*, in *2022 Snowmass Summer Study*, 3, 2022 [`2203.14919`].

[387] M. Beneke and G. Buchalla, *The B_c Meson Lifetime*, *Phys. Rev. D* **53** (1996) 4991 [`hep-ph/9601249`].

[388] ATLAS collaboration, *Search for additional heavy neutral Higgs and gauge bosons in the ditau final state produced in 36 fb^{-1} of pp collisions at $\sqrt{s} = 13$ TeV with the ATLAS detector*, *JHEP* **01** (2018) 055 [`1709.07242`].

[389] A. Alloul, N.D. Christensen, C. Degrande, C. Duhr and B. Fuks, *FeynRules 2.0 - A complete toolbox for tree-level phenomenology*, *Comput. Phys. Commun.* **185** (2014) 2250 [`1310.1921`].

[390] T. Hahn, *Generating Feynman diagrams and amplitudes with FeynArts 3*, *Comput. Phys. Commun.* **140** (2001) 418 [`hep-ph/0012260`].

[391] T. Hahn and M. Perez-Victoria, *Automatized one loop calculations in four-dimensions and D-dimensions*, *Comput. Phys. Commun.* **118** (1999) 153 [`hep-ph/9807565`].

[392] T. Hahn, S. Paßehr and C. Schappacher, *FormCalc 9 and Extensions*, *PoS* **LL2016** (2016) 068 [`1604.04611`].

[393] H.H. Patel, *Package-X: A Mathematica package for the analytic calculation of one-loop integrals*, *Comput. Phys. Commun.* **197** (2015) 276 [`1503.01469`].

[394] P.W. Angel, Y. Cai, N.L. Rodd, M.A. Schmidt and R.R. Volkas, *Testable two-loop radiative neutrino mass model based on an $LLQd^cQd^c$ effective operator*, *JHEP* **1310** (2013) 118 [`1308.0463`].

[395] S. Eidelman and M. Passera, *Theory of the tau lepton anomalous magnetic moment*, *Mod. Phys. Lett. A* **22** (2007) 159 [`hep-ph/0701260`].

[396] BELLE-II collaboration, *First Results and Prospects for τ Lepton Physics at Belle II*, *PoS* **CHARM2020** (2021) 042 [`2111.13385`].

[397] R. Parker, C. Yu, W. Zhong, B. Estey and H. Mãeller, *Measurement of the fine-structure constant as a test of the standard model*, *Science* **360** (2018) 191.

[398] L. Morel, Z. Yao, P. Cladé and S. Guellati-Khélifa, *Determination of the fine-structure constant with an accuracy of 81 parts per trillion*, *Nature* **588** (2020) 61.

[399] P. Athron, C. Balázs, D.H.J. Jacob, W. Kotlarski, D. Stöckinger and H. Stöckinger-Kim, *New physics explanations of a_μ in light of the FNAL muon $g-2$ measurement*, *JHEP* **09** (2021) 080 [`2104.03691`].

[400] I. Bigaran and R.R. Volkas, *Reflecting on chirality: CP-violating extensions of the single scalar-leptoquark solutions for the (g-2)e,μ puzzles and their implications for lepton EDMs*, *Phys. Rev. D* **105** (2022) 015002 [`2110.03707`].

[401] T.S. Kosmas, S. Kovalenko and I. Schmidt, *Nuclear muon- e- conversion in strange quark sea*, *Phys. Lett. B* **511** (2001) 203 [`hep-ph/0102101`].

[402] P. Wintz, *Results of the SINDRUM-II experiment*, *Conf. Proc. C* **980420** (1998) 534.

[403] SINDRUM II collaboration, *Improved limit on the branching ratio of $\mu \to e$ conversion on lead*, *Phys. Rev. Lett.* **76** (1996) 200.

[404] SINDRUM II collaboration, *A Search for muon to electron conversion in muonic gold*, *Eur. Phys. J. C* **47** (2006) 337.

[405] N. Teshima, *Status of the DeeMe Experiment, an Experimental Search for μ-e Conversion at J-PARC MLF*, *PoS* **NuFact2019** (2020) 082 [`1911.07143`].

[406] L. Calibbi, X. Marcano and J. Roy, *Z lepton flavour violation as a probe for new physics at future e^+e^- colliders*, `2107.10273`.

[407] M. González-Alonso and J. Martin Camalich, *Global Effective-Field-Theory analysis of New-Physics effects in (semi)leptonic kaon decays*, *JHEP* **12** (2016) 052 [`1605.07114`].

[408] J. Aebischer and B. Grinstein, *Standard Model prediction of the B_c lifetime*, *JHEP* **07** (2021) 130 [`2105.02988`].

[409] J. Aebischer and B. Grinstein, *A novel determination of the B_c lifetime*, `2108.10285`.

[410] HPQCD collaboration, *B-meson decay constants: a more complete picture from full lattice QCD*, *Phys. Rev. D* **91** (2015) 114509 [`1503.05762`].

[411] A.G. Akeroyd and C.-H. Chen, *Constraint on the branching ratio of $B_c \to \tau\bar{\nu}$ from LEP1 and consequences for $R(D^{(*)})$ anomaly*, *Phys. Rev. D* **96** (2017) 075011 [`1708.04072`].

[412] J. Fuentes-Martin, A. Greljo, J. Martin Camalich and J.D. Ruiz-Alvarez, *Charm Physics Confronts High-p_T Lepton Tails*, `2003.12421`.

[413] A. Angelescu, D.A. Faroughy and O. Sumensari, *Lepton Flavor Violation and Dilepton Tails at the LHC*, *Eur. Phys. J. C* **80** (2020) 641 [`2002.05684`].

[414] A. Greljo, J. Martin Camalich and J.D. Ruiz-Álvarez, *Mono-τ Signatures at the LHC Constrain Explanations of B-decay Anomalies*, *Phys. Rev. Lett.* **122** (2019) 131803 [`1811.07920`].

[415] ATLAS collaboration, *Search for High-Mass Resonances Decaying to $\tau\nu$ in pp Collisions at $\sqrt{s}$=13 TeV with the ATLAS Detector*, *Phys. Rev. Lett.* **120** (2018) 161802 [`1801.06992`].

[416] CMS collaboration, *Search for a W' boson decaying to a τ lepton and a neutrino in proton-proton collisions at $\sqrt{s}$ = 13 TeV*, *Phys. Lett. B* **792** (2019) 107 [`1807.11421`].

[417] F. Herren and M. Steinhauser, *Version 3 of RunDec and CRunDec*, *Comput. Phys. Commun.* **224** (2018) 333 [`1703.03751`].

[418] Muon (g-2) collaboration, *An Improved Limit on the Muon Electric Dipole Moment*, *Phys. Rev. D* **80** (2009) 052008 [`0811.1207`].

[419] Belle collaboration, *Measurement of the decay $B \to D\ell\nu_\ell$ in fully reconstructed events and determination of the Cabibbo-Kobayashi-Maskawa matrix element $|V_{cb}|$*, *Phys. Rev. D* **93** (2016) 032006 [`1510.03657`].

[420] Belle collaboration, *Measurement of the CKM matrix element $|V_{cb}|$ from $B^0 \to D^{*-}\ell^+\nu_\ell$ at Belle*, *Phys. Rev. D* **100** (2019) 052007 [`1809.03290`].

[421] A. Crivellin and J. Matias, *Beyond the Standard Model with Lepton Flavor Universality Violation*, in *1st Pan-African Astro-Particle and Collider Physics Workshop*, 4, 2022 [`2204.12175`].

[422] F.F. Freitas, J.a. Gonçalves, A.P. Morais, R. Pasechnik and W. Porod, *On interplay between flavour anomalies and neutrino properties*, `2206.01674`.

[423] J. Davighi, A. Greljo and A.E. Thomsen, *Leptoquarks with Exactly Stable Protons*, `2202.05275`.

[424] J.A. Escobar and C. Luhn, *The Flavor Group* $\Delta(6\,n^2)$, *J. Math. Phys.* **50** (2009) 013524 [`0809.0639`].

[425] R. de Adelhart Toorop, F. Feruglio and C. Hagedorn, *Discrete Flavour Symmetries in Light of T2K*, *Phys. Lett. B* **703** (2011) 447 [`1107.3486`].

[426] R. de Adelhart Toorop, F. Feruglio and C. Hagedorn, *Finite Modular Groups and Lepton Mixing*, *Nucl. Phys. B* **858** (2012) 437 [`1112.1340`].

[427] S.F. King, T. Neder and A.J. Stuart, *Lepton mixing predictions from* $\Delta(6\,n^2)$ *family symmetry*, *Phys. Lett. B* **726** (2013) 312 [`1305.3200`].

[428] C. Hagedorn, A. Meroni and E. Molinaro, *Lepton mixing from* $\Delta(3\,n^2)$ *and* $\Delta(6\,n^2)$ *and CP*, *Nucl. Phys. B* **891** (2015) 499 [`1408.7118`].

[429] G.-J. Ding, S.F. King and T. Neder, *Generalised CP and* $\Delta(6\,n^2)$ *family symmetry in semi-direct models of leptons*, *JHEP* **12** (2014) 007 [`1409.8005`].

[430] C. Hagedorn and J. König, *Lepton and quark masses and mixing in a SUSY model with* $\Delta(384)$ *and CP*, *Nucl. Phys. B* **953** (2020) 114953 [`1811.09262`].

[431] F. Feruglio, C. Hagedorn and R. Ziegler, *Lepton Mixing Parameters from Discrete and CP Symmetries*, *JHEP* **07** (2013) 027 [`1211.5560`].

[432] M. Holthausen, M. Lindner and M.A. Schmidt, *CP and Discrete Flavour Symmetries*, *JHEP* **04** (2013) 122 [`1211.6953`].

[433] M.-C. Chen, M. Fallbacher, K.T. Mahanthappa, M. Ratz and A. Trautner, *CP Violation from Finite Groups*, *Nucl. Phys. B* **883** (2014) 267 [`1402.0507`].

[434] W. Grimus and M.N. Rebelo, *Automorphisms in gauge theories and the definition of CP and P*, *Phys. Rept.* **281** (1997) 239 [`hep-ph/9506272`].

[435] G. Ecker, W. Grimus and H. Neufeld, *Spontaneous CP Violation in Left-right Symmetric Gauge Theories*, *Nucl. Phys. B* **247** (1984) 70.

[436] G. Ecker, W. Grimus and H. Neufeld, *A Standard Form for Generalized CP Transformations*, *J. Phys. A* **20** (1987) L807.

[437] H. Neufeld, W. Grimus and G. Ecker, *Generalized CP Invariance, Neutral Flavor Conservation and the Structure of the Mixing Matrix*, *Int. J. Mod. Phys. A* **3** (1988) 603.

[438] W. Grimus and L. Lavoura, *A Nonstandard CP transformation leading to maximal atmospheric neutrino mixing*, *Phys. Lett. B* **579** (2004) 113 [`hep-ph/0305309`].

[439] R. Fleischer, R. Jaarsma and G. Tetlalmatzi-Xolocotzi, *Mapping out the Space for New Physics with Leptonic and Semileptonic $B_{(c)}$ Decays*, `2104.04023`.